Etude de la performance acoustique des écrans antibruit de faible hauteur pour le tramway : optimisation numérique par méthode de gradient et approches expérimentales

Alexandre Jolibois

UNIVERSITÉ PARIS-EST

École doctorale Sciences, Ingénierie et Environnement

Thèse de doctorat

Spécialité : Mécanique

Alexandre JOLIBOIS

A study on the acoustic performance of tramway low height noise barriers: gradient-based numerical optimization and experimental approaches

---

Étude de la performance acoustique des écrans antibruit de faible hauteur pour le tramway : optimisation numérique par méthode de gradient et approches expérimentales

---

Soutenue publiquement le 25 novembre 2013 devant un jury composé de :

M. Marc BONNET	Rapporteur
M. Jérome DEFRANCE	Examinateur
M. Denis DUHAMEL	Directeur de thèse
M. Jens FORSSÉN	Rapporteur
M. Philippe JEAN	Examinateur
M. Judicaël PICAUT	Président du jury
M. Victor W. SPARROW	Examinateur

Remerciements

Je devrais certainement commencer par remercier le ciel et les circonstances peu ordinaires qui m'ont permis d'effectuer cette thèse en partenariat entre trois institutions que j'admire chacune profondément : le laboratoire Navier de l'école des Ponts ParisTech, le Graduate Program in Acoustics de l'université américaine de Penn State et le Centre Scientifique et Technique du Bâtiment, plus particulièrement l'équipe d'acoustique environnementale et urbaine de Grenoble. Ce fut un honneur de passer du temps au sein de ces trois environnements, si stimulants et si agréables à vivre.

Je tiens à remercier du fond du cœur mon directeur de thèse, Denis Duhamel, pour ses qualités scientifiques et humaines exceptionnelles, en tant que professeur et en tant que chercheur.
Je tiens également à remercier :
- Victor Sparrow, qui a suivi attentivement ma formation et mon travail à Penn State, et à qui je dois beaucoup de mes connaissances en acoustique.
- mes deux encadrants au CSTB, Jérôme Defrance et Philippe Jean, pour leur énergie, leur enthousiasme, et pour la confiance qu'ils m'ont accordée pour mener à bien ce projet.
- Jens Forssén et Marc Bonnet, qui m'ont fait l'honneur d'être rapporteurs de ce mémoire, ainsi que Judicaël Picaut, dont la présence honore également ce jury.
- le ministère de l'écologie, du développement durable et de l'énergie pour le financement de ce projet au travers de la formation doctorale des Ingénieurs des Ponts, des Eaux et des Forêts.

Je tiens également à adresser des remerciements particuliers à de nombreux employés du CSTB qui ont fourni un travail considérable pour m'aider dans la partie expérimentale de ce travail. Concernant les mesures sur maquette: Hélène Koreneff, pour l'aide très précieuse que tu m'as fournie pour effectuer les mesures, ainsi que Jean-François Buisson et Bruno Baggetto pour la construction des maquettes. Concernant le prototype d'écran antibruit en taille réelle, je veux remercier :
- Jean-François Buisson, pour avoir construit le prototype et supervisé sa mise en place. Ce fut un travail titanesque et je te remercie de t'être investi à ce point dans ce projet.
- une fois encore, Hélène Koreneff, pour l'aide très précieuse que tu m'as fournie pour sa préparation.
- Frank Vivien, Grégory Ruinat, Julien Maillard et Pascal Ducruet pour l'aide à sa mise en place.
- Hélène Koreneff et Grégory Ruinat à nouveau pour la journée (éprouvante !) de mesures.
Un grand merci également à la mairie de Saint-Martin-d'Hères pour nous avoir accordé l'autorisation d'installer le prototype et d'effectuer nos mesures, ainsi qu'à la SEMITAG pour leur coopération.

Je repense également à tous les collègues de bureau que j'ai eus lors de ces trois années, notamment aux discussions scientifiques passionnées et aux moments de convivialité : à Penn State, Kieran Poulain, Sang Cho, Andrew Christian, Amanda Lind, Joyce Rosenbaum, Beom-Soo Kim, Joe Salamone, Rachel Romond, Denise Miller, Kim Riegel et plus particulièrement ma très chère amie Whitney Coyle ; Tim Jensen, Guillaume Perrin, Laurent Charpin, Natalia Kotelnikova, Mathieu Rivallain, Daniel Patrault, Ha Le au laboratoire Navier ; Xavier Vuylsteke, Jan Jagla, Corentin Coguenanff, Christophe Rougier, Simon Bailhache, Nicolas Picard et Jérémy Rouch au CSTB Grenoble.

Enfin, je veux exprimer ma plus sincère gratitude à ma famille, sans laquelle je n'aurais jamais pu accomplir ce travail :
- Mon frère Emmanuel. Tu es parmi les scientifiques les plus brillants que je connaisse, et je te remercie d'avoir partagé un peu de ton immense savoir avec moi.
- Mon père Georges, qui pour moi restera le seul véritable "docteur Jolibois".
- Enfin et surtout ma mère Catherine, pour tout l'amour et la confiance que tu m'as toujours accordés.

Étude de la performance acoustique des écrans antibruit de faible hauteur pour le tramway : optimisation numérique par méthode de gradient et approches expérimentales

Résumé

Le bruit est devenu une nuisance importante en zone urbaine au point que selon l'Organisation Mondiale de la Santé, 40% de la population européenne est exposée à des niveaux de bruit excessifs, principalement dû aux transports terrestres. Il devient donc nécessaire de trouver de nouveaux moyens de lutter contre le bruit en zone urbaine.

Dans ce travail, on étudie une solution possible à ce problème : un écran bas antibruit. Il s'agit d'un écran de hauteur inférieure à un mètre placé près d'une source, conçu pour réduire le niveau de bruit pour les piétons et les cyclistes à proximité. Ce type de protection est étudié numériquement et expérimentalement. Nous nous intéressons particulièrement aux écrans adaptés au bruit du tramway puisque dans ce cas les sources sont proches du sol et peuvent être atténuées efficacement.

La forme ainsi que le traitement de surface de l'écran sont optimisés par une méthode de gradient couplée à une méthode 2D d'éléments finis de frontière. Les variables à optimiser sont les coordonnées de nœuds de contrôle et les paramètres servant à décrire l'impédance de surface. Les sensibilités sont calculées efficacement par la méthode de l'état adjoint.

Les formes générées par l'algorithme d'optimisation sont assez irrégulières mais induisent une nette amélioration par rapport à des formes simples, d'au moins 5 dB(A). Il est également montré que l'utilisation de traitement absorbant du côté source de l'écran peut améliorer la performance sensiblement. Ce dernier point est confirmé par des mesures effectuées sur modèle réduit.

De plus, un prototype à l'échelle 1 d'écran bas antibruit a été construit et testé en conditions réelles, le long d'une voie de tramway à Grenoble. Les mesures montrent que la protection réduit le niveau de 10 dB(A) pour un récepteur proche situé à hauteur d'oreilles. Ces résultats semblent donc confirmer l'applicabilité de ces protections pour réduire efficacement le bruit en zone urbaine.

Mots-clés : Écrans antibruit de faible hauteur, Bruit de tramway, Conception optimale par méthode de gradient, Éléments finis de frontière, Mesures sur modèles réduits, Mesures sur prototype en conditions réelles

A study of the acoustic performance of tramway low height noise barriers: gradient-based numerical optimization and experimental approaches

Abstract

Noise has become a main nuisance in urban areas to the point that according to the World Health Organization 40% of the European population is exposed to excessive noise levels, mainly due to ground transportation. There is therefore a need to find new ways to mitigate noise in urban areas.

In this work, a possible device to achieve this goal is studied: a low-height noise barrier. It consists of a barrier typically less than one meter high placed close to a source, designed to decrease the noise level for nearby pedestrians and cyclists. This type of device is studied both numerically and experimentally. Tramway noise barriers are especially studied since the noise sources are in this case very close to the ground and can therefore be attenuated efficiently.

The shape and the surface treatment of the barrier are optimized using a gradient-based method coupled to a 2D boundary element method (BEM). The optimization variables are the node coordinates of a control mesh and the parameters describing the surface impedance. Sensitivities are calculated efficiently using the adjoint state approach.

Numerical results show that the shapes generated by the optimization algorithm tend to be quite irregular but provide a significant improvement of more than 5 dB(A) compared to simpler shapes. Utilizing an absorbing treatment on the source side of the barrier is shown to be efficient as well. This second point has been confirmed by scale model measurements.

In addition, a full scale low height noise barrier prototype has been built and tested in situ close to a tramway track in Grenoble. Measurements show that the device provides more than 10 dB(A) of attenuation for a close receiver located at the typical height of human ears. These results therefore seem to confirm the applicability of such protections to efficiently decrease noise exposure in urban areas.

Keywords: Low-height noise barriers, Tramway noise, Gradient-based optimal design, Boundary element method, Scale model measurements, In situ measurements of a prototype device

Long résumé en français

En tant qu'outil principal pour le contrôle du bruit en milieu extérieur, les écrans antibruit ont été largement étudiés dans la seconde moitié du $20^{\text{ème}}$ siècle, d'un point de vue pratique mais aussi dans une perspective de recherche. Ces écrans ont surtout été utilisés pour réduire le bruit à proximité des autoroutes et des voies de trains en milieu rural et péri-urbain. Cependant, il devient de plus en plus important de réduire le bruit non seulement le long des grands axes routiers et ferroviaires mais également au cœur des zones urbaines, puisque le bruit est une des nuisances principales pour les habitants des villes. En effet, de nombreuses sources de bruit sont présentes au sein des villes, notamment à cause de tous les moyens de transport qui y coexistent : trafic routier, bus, transports guidés comme le métro mais aussi le tramway. Concevoir des écrans antibruit adaptés à ce type d'environnement, notamment pour qu'ils puissent être implémentés près d'un moyen de transport urbain bruyant, semble donc prometteur dans un objectif de réduction du bruit en milieu urbain. Ces protections doivent être bien sûr suffisamment petites pour pouvoir être intégrées facilement à un environnement confiné comme l'espace urbain, d'où le nom d'écran de faible hauteur ou encore d'écran bas. L'application de ces protections à la réduction du bruit du tramway semble particulièrement intéressante d'une part parce que ce moyen de transport peu polluant a connu un regain d'intérêt cette dernière décennie dans plusieurs grandes villes en Europe et à travers le monde, et d'autre part parce que les sources de bruit du tramway sont principalement situées près du sol et donc seraient plus efficacement atténuées par un écran bas. Ce travail a donc pour principal objectif d'étudier les écrans antibruit de faible hauteur adaptés au tramway, du point de vue de la conception aidée par simulation numérique, mais aussi expérimentalement.

A la différence des cas plus classiques d'implémentation d'écrans antibruit, au sein d'un espace urbain les distances entre source et récepteur peuvent être de l'ordre de quelques mètres seulement. Ceci suggère que les effets météorologiques lors de la propagation du son peuvent être négligés dans ce contexte. L'efficacité d'un écran bas en terme de réduction du bruit est donc principalement contrôlée par la géométrie des objets dans son voisinage proche (comme la caisse du tramway par exemple, qui peut induire le phénomène de réflexions multiples), les propriétés acoustiques du sol et les caractéristiques de l'écran lui-même, c'est-à-dire sa géométrie et les propriétés acoustiques des matériaux à sa surface. A cause de cette dépendance et des phénomènes complexes de réflexion et de diffraction mis en jeu, optimiser l'écran de manière

numérique pourra certainement apporter un gain significatif à son efficacité.

La méthode des éléments finis de frontières (BEM) est une des rares méthodes numériques capable de rendre compte avec précision de tels effets, et a donc été choisie pour calculer le champ acoustique autour de l'écran, et par conséquent son efficacité. Le logiciel MICADO développé au CSTB a été utilisé dans ce but. De plus, comme les algorithmes d'optimisation nécessitent de nombreux calculs de champs (et donc de nombreux calculs BEM), des hypothèses simplificatrices peuvent être faites pour accélérer le temps de calcul, tout en gardant un niveau de précision acceptable. Le sol est donc considéré comme rigide, et la présence du tramway est modélisée comme un baffle vertical infini, ce qui revient mathématiquement à introduire un écran image. La taille du maillage est considérablement réduite avec cette approche, tout comme le temps de calcul. La plage de fréquences d'étude est de 100 à 2500 Hz, ce qui couvre une grande partie du spectre d'émission du tramway. De plus, si l'on suppose que l'écran est suffisamment long et de section constante, on peut se placer dans un cadre bi-dimensionnel moyennant une modélisation de la source comme ligne source cohérente. Il est cependant connu que l'approximation 2D est valide pour calculer l'atténuation en bande fine pour un point source en 3D, ce qui est précisément ce qui est utilisé dans la fonction objectif choisie. Ceci dit, une fois l'optimisation terminée, ces approximations ne sont plus nécessaires et le calcul de l'efficacité peut se faire de manière plus précise.

Dans ce travail, à la fois la forme et le traitement de surface de l'écran sont optimisés. Bien que dans certains cas il soit possible de décrire la forme d'un écran à l'aide d'un petit nombre de paramètres correspondant à des caractéristiques particulières (succession d'aspérités de hauteur différentes par exemple), il a été choisi de représenter la forme de l'écran d'une manière très générale, par un ensemble quelconque de points de contrôle, et les variables à optimiser sont donc les coordonnées de ces points. Une contrainte doit être cependant rajoutée pour s'assurer que la courbe décrivant la forme de l'écran ne se replie pas sur elle-même, et doit donc être injective. En ce qui concerne le traitement de surface, deux types de traitements sont considérés dans ce travail : une couche de matériau poreux, qui absorbe le son efficacement en hautes fréquences, et un traitement réactif, efficace dans des bandes de fréquences particulières correspondant aux résonances du traitement. De plus, on considère deux types de matériaux poreux : un matériau de type fibreux - par exemple de la laine de verre - et du béton de chanvre, matériau plus durable fabriqué à partir de fibres végétales. On modélise l'effet de ces traitements par une admittance de surface, qui est décrite soit par le modèle de Delany et Bazley pour le matériau fibreux, soit par un modèle hybride de matériau poreux (Johnson-Zwikker-Kosten) pour le béton de chanvre. Le traitement réactif choisi est un résonateur à panneau micro-perforé, dont on décrit l'admittance par le modèle de Crandall-Sivian-Fok.

L'optimisation des coordonnées des points de contrôle et des paramètres qui décrivent l'admittance des différents traitements est effectuée par un algorithme de gradient. La dérivée de la fonction objectif par rapport à tous ces paramètres est calculée efficacement en utilisant la méthode de l'état adjoint adaptée au problème de la diffraction acoustique. Ce type d'algorithme ne peut trouver qu'une solution locale du problème d'optimisation, cependant le nombre d'itérations et

donc d'évaluations de la fonction objectif est bien plus faible avec ce type de méthode qu'avec des méthodes d'optimisation globale, comme par exemple les algorithmes génétiques. La méthode d'optimisation choisie sert donc à *améliorer* la performance à partir d'un écran initial choisi, plutôt qu'à trouver *la* solution optimale du problème. De plus, comme les contraintes à appliquer aux paramètres de forme sont différentes de celles appliquées aux paramètres d'admittance, il a été choisi d'utiliser deux types d'algorithme de gradient différents : la méthode SQP (Sequential Quadratic Programming) pour les paramètres d'admittance, et une version adaptée de la méthode de la plus grande pente (steepest descent) pour les paramètres de forme. En effet, bien que la méthode SQP converge plus rapidement, il est plus aisé d'implémenter la contrainte d'injectivité de la courbe avec la méthode de la plus grande pente.

Tout d'abord, l'algorithme d'optimisation proposé est appliqué au cas des écrans rigides, ce qui serait le cas s'il était fabriqué par exemple en béton. En effet, bien que les traitements acoustiques peuvent être efficaces pour améliorer la performance acoustique de l'écran, ils peuvent avoir un coût environnemental important et nécessiter une mise en œuvre particulière, par opposition aux matériaux rigides dont la mise en œuvre est généralement plus aisée. Plusieurs formes ont été choisies comme points de départ de l'algorithme d'optimisation de forme, notamment un simple écran droit et un écran en forme de T. Dans tous les cas, l'algorithme a convergé rapidement, en seulement quelques dizaines d'itérations au maximum. Alors que les écrans de départ à géométrie simple avaient une efficacité assez faible - atténuation inférieure à 6 dB(A) - les écrans à forme optimisée ont une efficacité significativement plus élevée - de 11 à 14 dB(A). Cette augmentation est due à une amélioration de l'atténuation aux moyennes et hautes fréquences, au-delà de 500 Hz. Les formes optimisées présentent de fortes irrégularités sur la partie de l'écran directement exposée à la radiation de la source et aux réflexions sur le tramway. Des calculs supplémentaires du champ d'intensité semblent montrer que cette augmentation de l'atténuation est due à une redirection de l'énergie acoustique vers le haut, ce qui diminue la diffraction vers la zone d'ombre de l'écran. Ces irrégularités semblent donc agir contre le phénomène de réflexions multiples entre l'écran et le tramway.

Dans un second temps, l'algorithme d'optimisation de forme a été appliqué dans le cas d'écrans recouverts de traitement absorbant poreux de type laine de verre. A nouveau, la convergence est rapide et l'optimisation de forme induit une amélioration de 5 dB(A) d'atténuation, et l'efficacité totale prédite atteint 20 dB(A). La géométrie est cependant moins altérée du côté de la source mais plus dans la partie haute de l'écran, par rapport au cas des écrans rigides. Cette observation semble suggérer que lorsque les réflexions multiples entre l'écran et le tramway sont fortement atténuées par un matériau absorbant, l'optimisation de forme peut tout de même permettre d'améliorer l'efficacité en jouant sur les effets de diffraction qui sont prépondérants dans la zone haute de l'écran. Des résonateurs aux paramètres bien choisis peuvent également augmenter l'atténuation aux fréquences moyennes. De plus, des performances similaires sont obtenues lorsque l'optimisation est effectuée en remplaçant le matériau fibreux par du béton de chanvre.

Puis, une fois les solutions d'écrans optimisés trouvées, on peut effectuer des calculs plus

précis en enlevant les hypothèses simplificatrices qui avaient été faites pour diminuer le temps de calcul pendant l'optimisation. Le tramway peut donc être remplacé par une caisse de géométrie plus réaliste, le sol peut être potentiellement absorbant et plusieurs modèles de sources sont considérés en plus du modèle de ligne source cohérente : un point source en 3D, une série de point sources incohérents (qui approxime une ligne source incohérente finie) sur une longueur égale à celle d'un tramway - soit 43 mètres pour le Alstom Citadis 402 implanté à Grenoble - et enfin une ligne source incohérente infinie. Ces sources sont modélisées par une approche BEM 2.5D, et à cause de la complexification importante du modèle, les calculs sont effectués jusqu'à 1800 Hz seulement. Tout d'abord, au vu de la grande différence dans les prévisions entre la ligne source incohérente finie et infinie, et puisque considérer une source finie semble bien plus réaliste, les résultats obtenus par la ligne incohérente infinie ne sont pas retenus puisque apparemment peu pertinents dans notre cas.

Pour tous les autres modèles de source, les calculs montrent que la perte par insertion est réduite d'environ 1 dB(A) quand la caisse du tramway est modélisée plus précisément, et de 2 à 4 dB(A) quand le sol est fortement absorbant. Lorsque l'incohérence spatiale de la source est prise en compte (modèle de ligne source incohérent finie), l'atténuation est sensiblement diminuée surtout en basses fréquences. Malgré cela, les pertes par insertion globales restent importantes, surtout lorsque le sol est rigide : de 9 à 12 dB(A) d'atténuation pour les écrans optimisés rigides, et de 16 à 19 dB(A) pour les écrans de forme et de traitement optimisés.

En complément des simulations numériques, une méthode pour mesurer l'atténuation d'un écran de faible hauteur près d'un tramway en utilisant des modèles réduits (à l'échelle 1/10) a été développée et validée dans des cas simples. On utilise une source impulsive, de type source étincelle, et une méthode de fenêtrage temporel pour rejeter les réflexions parasites. Le spectre de la source utilisée est exploitable de 200 à 1800 Hz en échelle réelle (soit 2 kHz à 18 kHz à l'échelle de la maquette). Les matériaux poreux de type fibreux sont reproduits dans la maquette par des couches de feutrine. A titre d'exemple, cette méthode est appliquée à un écran en forme de T recouvert de quantités différentes d'absorbant. La correspondance entre calculs BEM et les mesures est bonne. Notamment les mesures ont confirmé la faible efficacité d'un simple écran rigide, ainsi que l'intérêt d'utiliser un traitement absorbant sur le côté source. Cependant, il est à noter que la BEM tend à sous-estimer légèrement l'atténuation en basses et hautes fréquences.

Enfin, un prototype d'écran antibruit de faible hauteur a été construit et installé en conditions réelles près d'une voie de tramway de l'agglomération Grenobloise. Le prototype, en forme de Gamma, a été fabriqué grâce à des éléments de bois aggloméré, dont le côté exposé au tramway est recouvert de laine de verre, pour une longueur totale de 22 mètres. Le prototype a été installé temporairement dans un quartier résidentiel assez calme de Saint-Martin-d'Hères au milieu duquel passe le tramway à des vitesses qui peuvent être importantes - jusqu'à 60 km/h - et donc les mesures ont pu être faites avec un bon rapport signal sur bruit. Une série de mesures au passage avec et sans l'écran ont été faites à 1.5 m du sol et à 3 m du rail, soit à une position

représentant un piéton à proximité du tramway. La vitesse des tramways lors de leur passage a été également mesurée grâce à un microphone auxiliaire placé très près du rail.

Les mesures montrent qu'il y a une variabilité importante dans les niveaux au passage entre les différents trams, même lorsque qu'une correction de niveau due à la vitesse est appliquée. Cependant, l'atténuation de l'écran est en moyenne supérieure à 10 dB(A), durant tout le passage, et ceci bien que la longueur de l'écran soit seulement la moitié de celle du tram. Une analyse en fréquence des enregistrements a également été faite, et a montré que la perte par insertion entre 200 et 2500 Hz est d'environ 13 dB(A). Enfin, une comparaison a été effectuée entre les mesures et des calculs BEM simplifiés et a montré que les prévisions donnent de bonnes estimations de la performance réelle, à environ 3 dB(A) près, malgré le fait que l'environnement soit fortement idéalisé dans les calculs. Des calculs supplémentaires suggèrent cependant que l'atténuation obtenue en conditions réelles avec un tel écran pourrait être améliorée sensiblement par une meilleure conception.

Pour conclure, on peut dire que la conception d'écrans antibruit de faible hauteur pour le milieu urbain, en tant que sujet relativement récent dans la communauté du contrôle du bruit environnemental, représente un défi important puisque ce type de protections pourrait changer radicalement la façon d'habiter l'espace urbain. En se basant sur les résultats issus de l'étude d'optimisation numérique ainsi que sur les mesures collectées au cours de ce travail, on peut affirmer que les écrans de faible hauteur peuvent être des solutions efficaces pour réduire le bruit du tramway, même pour des récepteurs proches, typiquement des piétons et des cyclistes, mais aussi pour les bâtiments environnants. Il est probable que les écrans de faible hauteur soient aussi efficaces pour atténuer n'importe quelle source de bruit urbaine, pourvu que les sources soient relativement proches du sol et que l'écran puisse être placé suffisamment près. Il semblerait aussi qu'il soit particulièrement important de bien concevoir un écran bas, puisque son efficacité dépend fortement de sa forme et des traitements qui lui sont appliqués, notamment lorsqu'il est entouré d'autres objets qui peuvent induire un phénomène de réflexions multiples. Dans cette perspective, les méthodes d'optimisation comme celle proposée dans ce travail sont donc des outils extrêmement utiles d'aide à la conception de telles protections.

Contents

Contents **xi**

List of Figures **xvii**

Introduction **1**

1 What is a noise barrier and how does it work ? **5**

1.1 Introduction 5

1.1.1 First pass on noise barriers 6

1.1.2 Tramway noise 7

1.1.3 Objectives of this chapter 7

1.2 Measure of the efficiency of a noise barrier 8

1.2.1 General comments on the physical description of a sound field 8

1.2.2 Definition of the insertion loss in the frequency domain 8

1.2.3 The equivalent sound pressure level $L_{\mathrm{Aeq,T}}$ 11

1.3 Human response to noise 12

1.4 Physical effects influencing a noise barrier efficiency 13

1.4.1 Meteorological effects 13

1.4.2 Ground effect 14

1.4.3 Multiple reflections and diffuse field 15

1.4.4 Shape and material distribution over the barrier 15

1.5 Review of prediction methods 16

1.6 A few examples of surface treatment models 17

1.6.1 Delany and Bazley layer model 18

1.6.2 Hemp concrete layer 18

1.6.3 Micro-perforated panel resonator (MPPR) model 19

1.7 Review of noise barriers designs and performance assessment 20

1.7.1 Common designs (highway and train noise barriers) 20

1.7.2 Complex noise barriers 21

1.7.3 Low-height noise barriers 22

1.8 Conclusion 23

2 Review of the forward scattering problem and the integral equation method 25
2.1 Initial scattering problem . . . 25
2.1.1 Properties of the Green's function . . . 27
2.2 Weak formulation of the scattering problem . . . 27
2.2.1 Dirichlet-Neumann operator . . . 28
2.2.2 Equivalent scattering problem in a bounded domain . . . 29
2.3 Integral equations derived from the scattering problem . . . 30
2.3.1 Single and double layer potentials . . . 30
2.3.1.1 Definition . . . 30
2.3.1.2 Behavior close to the boundary Γ . . . 31
2.3.2 Integral representation theorem . . . 33
2.3.3 Kirchhoff-Helmholtz integral theorem and Jean's equation . . . 34
2.4 Issues for geometries with corners . . . 36
2.4.1 Angle correction in the Kirchhoff Helmholtz integral equation . . . 36
2.4.2 Singular behavior of the pressure field close to a corner . . . 37
2.5 Extension to the 3D sound field with infinite geometry in one dimension . . . 40
2.6 Conclusion . . . 41

3 Review of optimization methods and their application to scatterer shape design and inverse scattering 43
3.1 Introduction . . . 43
3.2 General considerations . . . 44
3.2.1 Form of the considered optimization problem . . . 44
3.2.1.1 Constraints . . . 45
3.2.2 Continuous vs. discrete representation of the search space . . . 46
3.2.3 Optimality conditions for gradient-based optimization . . . 46
3.2.4 A few comments regarding practical applications . . . 47
3.3 Overview of some common optimization algorithms . . . 47
3.3.1 Derivative free optimization methods . . . 47
3.3.2 Sensitivity-based (gradient-based) methods . . . 48
3.3.2.1 Gradient calculation . . . 48
3.3.2.2 Line search methods . . . 51
3.3.2.3 Examples of general methods: the Sequential Quadratic Programming (SQP) and the interior-point algorithm . . . 52
3.3.3 Global search methods . . . 52
3.3.4 General comments on the utility of global minimum finding . . . 53
3.4 A review of shape and admittance optimization applications in acoustic scattering 54
3.4.1 Admittance eduction . . . 54
3.4.2 Optimized design of admittance . . . 55
3.4.3 Scatterer shape optimization and reconstruction . . . 55
3.4.3.1 Topological approaches . . . 56
3.4.4 Conclusion of the review . . . 56

3.5 Details of the chosen optimization algorithm . . . 56
3.6 Conclusion . . . 58

4 Shape and admittance sensitivity expressions 59
4.1 Barrier implementation and modeling assumptions . . . 59
4.1.1 Physical assumptions and geometry . . . 59
4.1.2 Objective function . . . 60
4.2 Formal definitions of the gradient with respect to the admittance and the shape . 61
4.2.1 Field derivative . . . 61
4.2.2 Boundary field derivative . . . 62
4.2.3 Shape derivative . . . 63
4.3 Derivation of the sensitivity expressions . . . 64
4.3.1 General expressions . . . 64
4.3.1.1 Adjoint state equation . . . 65
4.3.1.2 Shape derivative expression . . . 67
4.3.1.3 Admittance derivative expression . . . 68
4.3.2 Derivatives with respect to shape and admittance parameters . . . 69
4.3.2.1 Derivative with respect to an admittance parameter . . . 69
4.3.2.2 Derivative with respect to a node coordinate . . . 70
4.3.3 Derivatives of the broadband objective function . . . 72
4.4 Numerical implementation . . . 72
4.4.1 Numerical evaluation of the sensitivity expressions from BEM solutions . 72
4.4.1.1 Sensitivity with respect to a node coordinate . . . 73
4.4.1.2 Sensitivity with respect to an admittance parameter . . . 74
4.4.2 Mesh refinement close to corners . . . 74
4.4.3 Validation . . . 75
4.4.3.1 Shape parameters . . . 76
4.4.3.2 Admittance parameters . . . 78
4.5 Conclusion . . . 78

5 Application to the shape optimization of rigid barriers 79
5.1 Introduction . . . 79
5.2 Results . . . 80
5.3 Efficiency of smoothed and randomly perturbed shapes . . . 84
5.4 Influence of the modeling approximations . . . 85
5.4.1 Effect of the tramway cross-section and of the ground impedance in 2D . 85
5.4.2 Effect of the source modeling . . . 88
5.5 Conclusion . . . 91

6 Application to coupled admittance and shape optimization of barriers with acoustic treatments 97
6.1 Considered acoustic treatments . . . 97
6.2 Shape optimization of a barrier covered entirely with a fibrous absorbing treatment 98

6.3 Shape optimization of absorbing source side and reactive treatment optimization on top . . . 100
6.4 Results with hemp concrete as the absorbing treatment . . . 102
6.4.1 Uniform porous treatment . . . 103
6.4.2 Porous and reactive treatment . . . 104
6.5 Performance of some optimized designs using more advanced modeling . . . 106
6.6 Conclusion . . . 108

7 Scale model measurements of tramway low-height noise barriers performances 109
7.1 Introduction . . . 109
7.2 Theoretical issues related to scale change . . . 110
7.2.1 Physical quantities similarities . . . 110
7.2.2 Air absorption . . . 111
7.3 Description of the experimental protocol . . . 111
7.3.1 Choice of the source: electrostatic spark source . . . 112
7.3.2 Measurement room and signal selection by time windowing . . . 113
7.3.3 Receiver locations and microphones . . . 114
7.3.4 Scale model representation of the tramway . . . 116
7.3.5 Data acquisition system and sampling frequency . . . 116
7.3.6 Measurement set-up overview and insertion loss calculation . . . 117
7.3.6.1 Insertion loss calculation . . . 118
7.4 Simple validation tests . . . 119
7.4.1 Reflection on a rigid ground . . . 119
7.4.2 Diffraction by a straight wall . . . 120
7.5 Porous absorbing materials at the reduced scale: felt layers . . . 121
7.6 Measured performance of a T-shape barrier with absorbing treatment . . . 123
7.6.1 Comparisons between measurements and BEM calculations . . . 124
7.7 Conclusion . . . 125

8 In situ measurements of a full scale low height barrier prototype 127
8.1 Preliminary considerations . . . 127
8.1.1 Choice of the implementation site . . . 127
8.1.2 Choice of the design . . . 129
8.2 Performed measurements . . . 131
8.2.1 Speed measurement from auxiliary microphone signal . . . 132
8.3 Measurement analysis and barrier effect . . . 134
8.3.1 Pass-by equivalent level and speed dependence . . . 134
8.3.2 Analysis of the $L_{\mathrm{Aeq,T}}$ time histories . . . 136
8.3.3 Spectral analysis and third-octave insertion losses . . . 138
8.3.3.1 Effect of noise on insertion loss evaluation and considered frequency range . . . 138
8.3.3.2 Measured third-octave insertion losses . . . 140

8.4 Comparison with BEM calculations . . . 142
8.4.1 Numerical comparison of the barrier prototype with other designs . . . 144
8.5 Conclusion . . . 145

9 Conclusions **147**
9.1 Summary of findings . . . 147
9.2 Future work . . . 151

Appendix **153**
A Tangential differential operators . . . 153
B Uniqueness of Jean's integral equation solution . . . 154
C Static kernels properties and regularization of the Kirchhoff-Hemholtz integral equation . . . 156
C.1 Integral properties of static kernels . . . 156
C.2 Regularization using static kernels . . . 157
D Shape optimization algorithm details . . . 161
D.1 Loop detection algorithm . . . 162
E Shape derivative of a boundary integral defined on a piecewise smooth curve . . . 163
F Derivatives of considered admittance models with respect to the parameters . . . 164
G Shape smoothing algorithm . . . 165
H Uncertainty evaluation of linear regression parameters . . . 167

References **169**

Publication list **181**

List of Figures

1.1 Definition of the incident and total field 8
1.2 Examples of situations with multiple reflections 15

2.1 Scattering problem geometry 26
2.2 Definition of the half sphere S_R containing the boundary Γ 28
2.3 Corner in the boundary 36
2.4 Corner singularity - test geometry 38
2.5 Corner singularity - pressure values and slope close to the corner 38
2.6 Three dimensional geometry for 2.5 D calculation 40

3.1 Shape and admittance optimization algorithm outline 58

4.1 Tramway noise spectra 59
4.2 Barrier geometry 59
4.3 State and adjoint state definition 67
4.4 Schematics for admittance parameters derivatives 69
4.5 MICADO barrier representation 71
4.6 Node displacement velocity field 71
4.7 Geometry for validation of shape sensitivity 75

5.1 Shape optimization of rigid barriers - starting geometries 80
5.2 Comparison of initial and optimized geometries 81
5.3 Comparison of third octave IL between initial and optimized shapes 81
5.4 Objective function evolution 82
5.5 Intensity map comparison - initial and optimized medium and small wall 83
5.6 Effect of smoothing optimized geometries 84
5.7 Effect of random perturbations 85
5.8 Cases to assess the effect of the rigid ground and infinite baffle approximations . 86
5.9 Third-octave IL for the cases of figure 5.8 and four geometries 87
5.10 Considered 2.5D source models 89
5.11 Comparison of medium wall and T-shape rigid initial and optimized geometries . 91

5.12 Combined effect of approximations - third-octave IL - small wall 94
5.13 Combined effect of approximations - third-octave IL - medium wall 94
5.14 Combined effect of approximations - third-octave IL - T-shape 95
5.15 Combined effect of approximations - third-octave IL - Gamma-shape 95

6.1 Shape-optimized fully absorbing barrier (fibrous layer) - comparison of initial and optimized geometries 99
6.2 Shape-optimized fully absorbing barrier (fibrous layer) - third octave IL 99
6.3 Shape-optimized fully absorbing barrier (fibrous layer) - comparison between rigid and absorbing shape-optimized barriers 100
6.4 Shape-optimized porous source side and optimized MPPR on top - comparison of initial and optimized geometries 100
6.5 Shape-optimized porous source side and optimized MPPR on top - third-octave IL 102
6.6 Shape-optimized absorbing source side and optimized MPPR on top - MPPR admittance 102
6.7 Comparison of acoustic properties of a a fiberglass-type material and hemp concrete 103
6.8 Shape-optimized fully absorbing barrier (hemp concrete) - comparison of initial and optimized geometries 104
6.9 Shape-optimized fully absorbing barrier (hemp concrete) - third octave IL 104
6.10 Shape-optimized hemp concrete source side and optimized MPPR on top - comparison of initial and optimized geometries 105
6.11 Shape-optimized hemp concrete source side and optimized MPPR on top - third-octave IL 105
6.12 Simplified and more advanced models schematics 106
6.13 Comparison between simplified and more advanced model - considered optimized designs 107
6.14 Comparison between simplified and more advanced model - third-octave IL . . . 107

7.1 Air absorption effect 111
7.2 Grozier spark source 112
7.3 Spark source signal and spectrum 113
7.4 Overview of the experimental set up 113
7.5 Example of windowing 114
7.6 Time window definition 115
7.7 Scale model source and receiver positions 115
7.8 Simple tramway scale model 116
7.9 Fireface UFX soundboard 116
7.10 Spark signal spectrum and aliasing 117
7.11 Measurement set up schematic 117
7.12 Measurement geometrical configuration 118
7.13 Measurement test case - reflection on a rigid ground - geometry 119

7.14 Measurement test case - reflection on a rigid ground - measurement/calculation comparison . . . 119
7.15 Measurement test case - diffraction by a straight wall - geometry . . . 120
7.16 Measurement test case - diffraction by a straight wall - measurement/calculation comparison . . . 120
7.17 Felt layers - Delany-Bazley parameters identification - geometry . . . 121
7.18 Felt layers - measured/curve-fitted relative SPL comparison . . . 122
7.19 Four layers of felt - absorption coefficient . . . 123
7.20 T-shape barrier - scale model . . . 123
7.21 T-shape barrier - geometrical configuration . . . 123
7.22 T-shape barrier - considered treatments . . . 124
7.23 T-shape - rigid case - receiver signal . . . 124
7.24 T-shape barrier - BEM/measurement third-octave insertion losses comparisons . 126

8.1 Implementation site . . . 128
8.2 Low-height barrier prototype - schematics . . . 129
8.3 Low-height barrier prototype - view of the prototype . . . 130
8.4 Low-height barrier prototype - cross-section and joint system . . . 130
8.5 Receiver locations . . . 131
8.6 Measurement devices . . . 131
8.7 Close and far trams . . . 132
8.8 Speed measurement from tram pass-by time histories . . . 133
8.9 Dimensions of the Alstom Citadis 402 tram . . . 134
8.10 Pass-by level measurement . . . 134
8.11 Pass-by equivalent levels and speeds . . . 135
8.12 Example of speed correction on time and level . . . 137
8.13 Comparison of corrected time histories - mean and dispersion . . . 137
8.14 Schematic of the prototype during the pass-by of a close tram - top view . . . 138
8.15 Example of tram pass-by and background noise spectrum . . . 140
8.16 Measured third-octave insertion losses . . . 141
8.17 Shadow zone for far trams . . . 141
8.18 Geometries used in the BEM calculations . . . 142
8.19 Comparison of calculated and measured third octave insertion losses . . . 143
8.20 Numerical evaluation of the prototype relative performance - considered designs . 144
8.21 Numerical evaluation of the prototype relative performance - third-octave insertion losses . . . 146

A.1 Shape smoothing filtering window . . . 166
A.2 Shape smoothing example . . . 166

Introduction

Noise exposure is still an important nuisance in 21st century society, especially in urban areas where many sources of noise coexist, including traffic, trains, but also tramways which have been developing recently in several cities. Urban environments are also characterized by the fact that receivers - pedestrians and cyclists - can be very close to noise sources and therefore exposed to high levels, even though urban noise sources are by themselves not as loud as other more traditional environmental noise sources.

Noise barriers are a common strategy to decrease noise levels in a given area, however typical solutions - commonly built along highways and train tracks - are not applicable in urban areas. This is why the concept of low-height noise barriers has been developed: due to the very confined environment one could find in a dense city, noise barriers need to be adapted to fit to this environment, and therefore should be small - typically less than one meter high - and well-integrated to the urban landscape. Besides, low height noise barriers seem like a particularly appropriate way to mitigate tramway noise, since in this case most sources are close to the ground and have very little spatial variability (as opposed to traffic noise), and safety requirements are such that a device could be set up very close to a tramway track. The purpose of this work is therefore to study a low height noise barrier meant to attenuate tramway noise, from a numerical and experimental standpoint.

One can indeed raise the question of how to design such a device to make it as efficient as possible in terms of acoustic efficiency. Indeed, because of the tramway itself being so close to the barrier, one expects multiple reflections to happen, which suggests that the design of the barrier - its shape and its surface treatment - will have a significant influence on its efficiency. Optimizing the design is therefore likely to provide good improvement of the barrier noise reduction.

For this purpose, it is necessary to develop an efficient optimization method coupled with a numerical tool able to predict the efficiency of a given design accurately. The method will also have to be general enough to explore a vast set of possible designs, and fast enough to provide solutions in a reasonable computation time. Such a general method can then be applied in different configurations involving for instance different choices of surface treatments. In addition, extra calculations can be made to check the performance of the optimized noise barriers in a more realistic situation.

Moreover, performing such a numerical optimization should allow us to determine what key

features of a low height barrier are essential to attenuate tramway noise efficiently. It would then be possible to choose an appropriate design for an actual full scale low height barrier prototype. Building and setting up such a prototype would provide insight regarding the feasibility and the actual in situ performance of low height barriers for tramway noise reduction applications.

It should also be pointed out that this work is the continuation of another Ph.D. dissertation completed by the author at the Pennsylvania State University [1]. This work was also concerned with tramway low height noise barriers optimization, but focused essentially on surface treatments. The author acknowledges that a portion of the present document is indeed very similar to what has been presented in [1]. Nevertheless, the reader is encouraged to look at this previous work as well to be convinced of the originality of the present document.

This dissertation is organized as follows. Chapter 1 reviews parts of the accumulated knowledge of noise barriers in general, and low height noise barriers in particular. More specifically physical effects that may influence the acoustic performance of a noise reducing device are reviewed, and corresponding modeling assumptions for the context of a tramway low height noise barrier are proposed. Common numerical prediction methods are reviewed as well, and arguments are given towards the choice of using the boundary element method (BEM) to calculate the device performance.

Chapter 2 presents the foundations of the BEM which is the integral equation method to solve the forward scattering problem. Important results regarding the weak formulation of the problem are recalled, as well as some numerical issues regarding geometrical singularities. These results will be directly applied in chapter 4.

Chapter 3 reviews optimization methods to tackle the optimization problem at stake, which is the minimization of an objective function depending on the solution of a boundary value problem. Arguments are given towards the interest of using a sensitivity-based optimization method coupled with the adjoint state approach, which allows one to use a large number of variables without significant increase of computation time. A general algorithm to optimize both the shape and the surface treatment of the barrier is presented.

In chapter 4, the calculation model - including the different physical assumptions - used in the optimization and the considered objective function are summarized, and the expressions of the sensitivities of the objective function with respect to all parameters are derived, implemented numerically and validated.

Chapter 5 presents optimized designs obtained with the algorithm, assuming the barrier is made of a rigid material such as concrete. Extra numerical calculations are made to further analyze the generated optimized shapes. The optimization algorithm is then applied in chapter 6 in a more general context, in which both shape and admittance parameters are optimized at the same time. Optimized solutions coupling shape-optimized absorbing porous layers and micro-perforated panel resonators are presented, and again extra calculations are performed and discussed.

Chapter 7 presents an experimental method to measure the insertion loss of a low height barrier design in the presence of a tramway using scale models. The method is applied to study

experimentally the effect of an absorbing treatment on a simple T-shape barrier.

Chapter 8 presents a full scale low height barrier prototype which has been set up next to a tramway track in Grenoble. Measurements of pass-by levels with and without the device are presented and analyzed, and arguments are given towards the feasibility of such devices.

Finally, in chapter 9, conclusions are drawn and suggestions for future work are discussed.

Chapter 1

What is a noise barrier and how does it work ?

1.1 Introduction

Along with the industrialization of society, the growth of urban areas as well as the development of transportation infrastructures, noise has become a serious nuisance in 21st century society. Working in an office building or in a plant, wandering in a city, or even traveling across a country or across the world oceans, noise always surrounds and possibly annoys us. Noise can even represent a danger to human health, especially to more fragile populations (elderly and children), which is all the more problematic since damage induced by noise can be irreversible. More specifically, it is clear that noise generated by means of transportation is a major issue, especially in urban areas where many noise sources coexist (namely cars, urban trains, tramways, buses, aircrafts...). Indeed, according to the World Health Organization [2, 3]:

> About 40% of the population in EU countries is exposed to road traffic noise at levels exceeding 55 dB(A), 20% is exposed to levels exceeding 65 dB(A) during the daytime and more than 30% is exposed to levels exceeding 55 dB(A) at night.
>
> Impairment of early childhood development and education caused by noise may have lifelong effects on academic achievement and health. Studies and statistics on the effects of chronic exposure to aircraft noise on children have found consistent evidence that noise exposure harms cognitive performance.
>
> At least one million healthy life years are lost every year from traffic-related noise in the western part of Europe.

It also seems clear that a large infrastructure such as a highway or a high speed train track can induce disorders in the wildlife that inhabits its surrounding environment, since it interferes with the ecosystem by its presence itself and by the noise it generates, which can be significant several kilometers away from the infrastructure. Environmental noise is hence considered as a serious issue, from a social, environmental or public health perspective.

However, environmental noise, which can be defined as any sound field that reaches and can potentially annoy or harm a human or animal receiver, is extremely difficult to control since the extent of a noise source is usually small compared to the extent of the area where the generated

noise can be heard: for instance, in a city, one single car radiates noise that can be heard several blocks away.

One should also point out that environmental noise usually involves propagation in a complex and unsteady physical "medium", such as a city or the atmosphere itself, where many physical effects come into play in the sound propagation. This makes environmental noise control an even more difficult task. Nevertheless, there are mainly three means of actions for engineers to control noise:

- **reducing the source radiated power**: this implies a better design of pieces of machinery, trains, cars, plants and any sources of sound.
- **protecting the receiver from the noise**: a common example of this strategy is to build houses with high performance windows to isolate the inside from the outside.
- **preventing the propagation by modifying the propagation path**

One way to implement this third strategy is to use a screen between the source and the receiver, which is commonly called a *noise barrier* or noise protection. In this work, we are particularly interested in noise protections adapted to an urban context, since noise is considered one of the most important nuisances in cities, and since the proportion of city dwellers in the worldwide population keeps increasing, as it has been for centuries. This trend is certainly going to remain the same in the near future and therefore it makes sense to imagine new ways to tackle the issue of noise exposure in urban areas.

1.1.1 First pass on noise barriers

Noise barriers were first built in the middle of the 20^{th} century, in the United States and in Europe, quickly followed by Japan along with its rapid highway network development. The main application of such screens initially was road traffic noise mitigation, since screens were mostly built along highways passing by inhabited areas, dense suburbs or quiet countryside areas. Barriers were also built to mitigate railway noise in the same context, or noise from HVAC (heating, ventilation and air conditioning) heavy machinery, usually located on buildings roofs.

Typical highway or train noise protections can be divided into two main types: noise berms - also known as earth mounds or natural barriers, made out of natural materials - and noise walls - also known as noise screens and widely referred to as the general expression *noise barriers*, which are manufactured engineering structures. There are however many limitations to the design of noise barriers: materials used have to be durable, resistant to weather conditions, and even salt in case of highway treatment against heavy snow. Concrete is therefore most commonly chosen because of its durability, its easy maintenance and easy implementation on site during the construction, although metal, masonry, wood or even brick are also commonly used materials. Further, some more sophisticated materials with good sound absorption properties, such as porous concrete, have been used as well.

As we have mentioned earlier, the main application of noise barriers since the beginning of their development has been mitigation of highway and train track noise. Nevertheless, another recent development suggests one could use noise reducing devices at the heart of urban areas in order to mitigate the noise exposure of urban inhabitants [4–15] - one can also refer to the European project HOSANNA which was also concerned with noise reduction in urban areas [16–19]. This type of device should be easy to implement in a constrained environment, such as a city canyon or along a urban train track, which would typically require its height to be limited. This is why those devices have been referred to as *low-height noise barriers*, "low height" typically meaning less than one meter high. They could be used for instance to acoustically isolate pedestrians walking on pavements from the traffic noise coming from the street, or to reduce the noise received by cyclists riding really close to a heavy traffic driveway. Low-height barriers could even decrease noise reaching buildings, for instance in case of elevated railroads inside cities.

1.1.2 Tramway noise

Many sources of noise coexist in urban environments, including road traffic (from light and heavy vehicles), urban trains, but also tramways. For many decades, urban noise studies were mostly concerned with road traffic and trains, which were considered as the main sources of noise in urban areas, but tramway noise has become a concern as well. Indeed, based on the fact that a tramway is an environmentally-friendly non-polluting means of transport which helps reduce the traffic congestion in city centers, there has been a renewed development of this means of transportation in the past decade, for instance in several European cities (including Paris, Brussels and London). Tramway has hence become a significant urban noise source.

Back in the seventies and eighties, several studies had already reported significant levels and annoyance due to tramways [20–22]. Along with the more recent tramway development, researchers have characterized physical emission levels of tramway-induced noise and vibration [23–26] and annoyance [24, 27]. Tramway noise is all the more problematic since pedestrians and cyclists can be close to trams on a regular basis, and because the power levels of tramway noise sources are significant (above 90 dB(A) for typical urban speeds [26]), the noise level at nearby receiver locations can be quite high, well above 80 dB(A).

However it has been shown that noise sources for modern tramway are mostly located close to the ground [26]. This suggests that a properly designed low-height noise barrier can be efficient against tramway noise, even for receivers close to the tram track. This is why this work will be mostly concerned with tramway noise mitigation using a low-height noise barrier.

1.1.3 Objectives of this chapter

Although they might look like rather simple manufactured objects, noise barriers - including low height noise barriers - involve many physical phenomena in the way they attenuate sound and have been the topic of many research studies. We therefore intend in this introductory chapter to briefly review the physical and mathematical tools involved in the accurate description of the effect a noise barrier has on a sound wave, and therefore in the assessment of its efficiency.

We will also present a broad overview of the accumulated knowledge concerning noise barrier design, which will eventually help us identify what approach can be followed to explore further the potential of low height urban noise barriers, more specifically tramway noise barriers.

1.2 Measure of the efficiency of a noise barrier

1.2.1 General comments on the physical description of a sound field

Physically, a sound propagating in a fluid (such as air) can be described as the "small" perturbations of the thermodynamic variables describing the fluid: pressure p, temperature T, particle velocity $\mathbf{v}$, and density ρ. We will use the subscript $_0$ to refer to the mean values: p_0 (also referred to as the atmospheric pressure), T_0, ρ_0 (also referred to as the ambient density) and $\mathbf{v}_0$ (also referred to as the mean flow or simply the *wind*). Basically the zeroth order quantities describe the acoustic medium in which the propagation occurs, and the first order quantities are used to describe the acoustic field itself. Further, the adiabatic sound speed c_0, assuming air is a perfect gas, is given by:

$$c_0 = \sqrt{\frac{\gamma\, p_0}{\rho_0}} = \sqrt{\frac{\gamma\, R\, T_0}{M}}$$

where γ is the ratio of specific heats, M is the molecular mass of air, $R = 8.314\,\mathrm{J/(mol.K)}$ is the universal gas constant and T_0 is expressed in Kelvin. Typically one can take $\gamma = 1.4$ and $M = 28.97\ 10^{-3}\,\mathrm{kg/mol}$. At a temperature of 20°C, the sound speed is about $c_0 = 343\,\mathrm{m/s}$.

In typical outdoor propagation situations, knowing the acoustic pressure field p only is sufficient (other variables could be derived from it and the relevant properties of the medium), so it will be the main physical quantity we will look at. The sound field is then a scalar function of a receiver point $\mathbf{x}$ and time t: $p(\mathbf{x}, t)$. Since the frequency content of a signal usually contains easier information to interpret, one usually looks at the acoustic signal as a function of frequency $p(\mathbf{x}, f)$ instead of time, the transformation from one to the other simply being a Fourier transform.

1.2.2 Definition of the insertion loss in the frequency domain

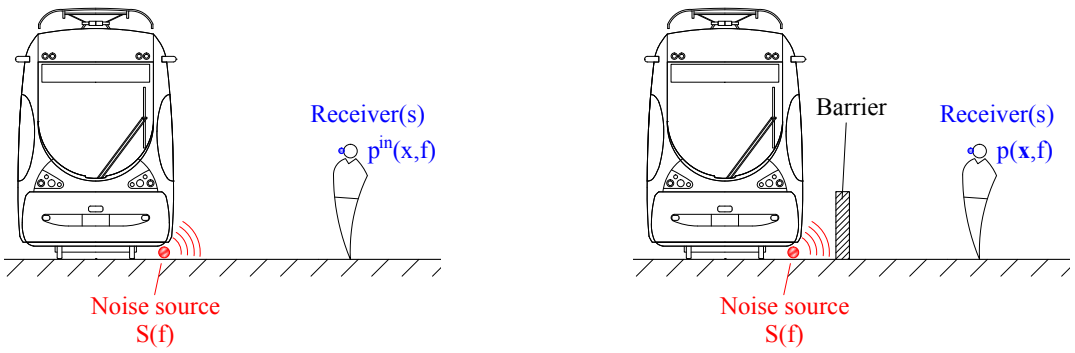

Figure 1.1: Schematic of a noise barrier implementation. Definition of the incident field p^{in} (left) and the total field p, which is the sum of the incident and the diffracted field $p = p^{\mathrm{in}} + p^{\mathrm{sc}}$ (right).

One can then imagine a typical situation where there is a source of sound - for instance a tramway - and some receivers - a pedestrian walking by (see figure 1.1). The source frequency content is described by a certain function S which depends on frequency f. This information is typically related to the power spectrum of the source (measured for instance with a power spectral density), which is a continuous function of frequency, but in practice one will use a discrete version of this spectrum at a set of frequencies f_n, or band-averaged values (most typically octave or third octave bands). In environmental noise applications, this power source function is typically A-weighted to take into account the filtering of the human ear, defined for instance in the International standard IEC 61672:2003 (which implies that the A-weighting filter is already included in the function S). Besides, noise sources are typically modeled as "point" sources, whereas in reality sources are always somewhat extended in space, as it would be the case for a vibrating structure for instance. Real sources also do not usually radiate energy equally in all directions, and should therefore be described as well by directivity functions. In this work however, we will consider omni-directional sources only, which is a rather strong approximation which should be kept in mind.

Then, to evaluate the noise at the receiver locations, we want to know the pressure field at the considered receiver points which consists of a discrete set of points (R_m). The pressure field at a given point and at a given frequency f_n is the complex number $p(R_m, f_n)$.

Now, let us imagine furthermore that in the design phase of a project, one wants to predict how efficient a barrier will be in terms of noise reduction. The relevant reference situation in that case is the sound field that would exist at the receiver points without any barrier constructed, but with the same sources of sound and in the same environment. We will call this the *incident field* $p^{\text{in}}(R_m, f_n)$ (see figure 1.1, left part).

Then, assuming that there is a barrier present (see figure 1.1, right part) and assuming we can predict how the sound field will be modified by the presence of the barrier, we can compute the actual sound pressure field, simply called the *total field* and written as $p(R_m, f_n)$. We will call the difference between those two fields the *scattered field* $p^{\text{sc}} = p - p^{\text{in}}$ (also called the *diffracted field*), which is precisely the field the barrier "adds" to the existing field and therefore tells us how much the barrier modifies the propagation of the sound.

To have a quantitative measure that tells us how efficient the barrier is in mitigating the incoming noise, we will define an average attenuation across the receivers at a given frequency:

$$A(f) = \frac{P(f)}{P^{\text{in}}(f)} \qquad \text{with} \quad \begin{cases} P(f) = \sqrt{\sum_m |p(R_m, f)|^2} \\ P^{\text{in}}(f) = \sqrt{\sum_m |p^{\text{in}}(R_m, f)|^2} \end{cases}$$

P and P^{in} are the root-mean-square (RMS) total and incident pressure across the receivers. One can also convert the attenuation to a dB scale, which one can refer to as the frequency dependent *insertion loss*:

$$\text{IL}(f) = -10 \log\big(A(f)^2\big)$$

The minus sign is there so that when $|P| \ll |P^{\text{in}}|$, the logarithm is largely negative and the *loss* is actually a high positive number. Also, we took the magnitude squared of the pressure field so that what we compute is really a ratio of acoustic energy. This number tells how many dBs are "lost" on average across the receivers due to the barrier at a given frequency.

However, the attenuation is usually a function that strongly varies with frequency, due for instance to constructive or destructive interference effects. To have one single number to evaluate the benefit of the noise reduction device, one therefore needs to average across a certain frequency range, say between f_{min} and f_{max}. One possibility would be to evaluate the total acoustic energy by integration over frequency of the spectral acoustic energy, which is approximately proportional to the RMS pressure squared, and take the ratio of the incident and total energies (AER):

$$\text{AER} = \Big(\int_{f_{\text{min}}}^{f_{\text{max}}} P(f)^2 \,\mathrm{d}f\Big) \Big/ \Big(\int_{f_{\text{min}}}^{f_{\text{max}}} P^{\text{in}}(f)^2 \,\mathrm{d}f\Big)$$

The integration is replaced in practice by a discrete summation based on a finite number of frequencies, as follows:

$$\text{AER} \approx \Big(\sum_n P(f_n)^2 \,\Delta f_n\Big) \Big/ \Big(\sum_n P^{\text{in}}(f_n)^2 \,\Delta f_n\Big)$$

where Δf_n is a frequency bandwidth associated with f_n. However, there is a major problem with using this number: it strongly depends on the modeling of the source. Indeed, assuming a given frequency content for a 3D point source, if the same frequency content is applied to a 2D line source and the pressure field evaluated with a 2D method, the AER in those two cases would be significantly different. This is due to the fact that a 3D point source and a 2D line source have by themselves different "frequency content". This is problematic since most of the time the prediction model to assess the efficiency of a noise barrier is based on 2D modeling in order to keep computation time reasonable.

However, it has been shown [28, 29] that the attenuation at a given frequency $A(f_n)$ is similar whether the source is represented by a point source with an infinitely long barrier or by a 2D line source. Constructing a broadband efficiency from the attenuations therefore reduces the error related to the 2D modeling. But, at each frequency the attenuation does not depend on the source spectral content. Hence to take into account the noise spectrum of the considered source, we define a broadband attenuation weighted by the S function, as so:

$$A_{\text{bb}} = \frac{\sum_n S_n \, A(f_n)^2}{\sum_n S_n} \tag{1.1}$$

Typically the frequencies f_n at which the attenuation is evaluated will be be taken equally spaced in a third-octave band. In this case the coefficient S_n can be taken as $S_n = 10^{L_w}$ with L_w the source power level in the considered third octave band. The same coefficient is then assigned to all the frequencies of this band, but one needs to have the same number of frequencies per band (typically 20 per third-octave band) to preserve the repartition of energy on the spectrum.

One can finally define from the broadband attenuation a broadband insertion loss in dB(A) as: $\mathrm{IL_{bb}} = -10 \log A_{\mathrm{bb}}$. An efficient barrier has a high broadband insertion loss, and therefore this parameter is the one we will use as the quantitative *efficiency* of a given noise barrier.

1.2.3 The equivalent sound pressure level $L_{\mathbf{Aeq,T}}$

Let us recall that we introduced the insertion loss as a frequency domain quantity and therefore at each frequency it is implicitly assumed that the generated noise is "steady", and does not present radical changes with time. However, most sources of noise, especially tramway noise, are by definition unsteady since they are related to the passage of a tramway. Therefore, when a frequency domain steady-state description is not possible, the equivalent sound pressure level L_{eq} is used. This level is related to the mean squared pressure $p^2_{\mathrm{rms,T}}(\mathbf{x})$, which is a time-average squared pressure value over a given period of time T and at a given receiver point $\mathbf{x}$:

$$p^2_{\mathrm{rms,T}}(\mathbf{x}) = \frac{1}{T} \int_0^T p(\mathbf{x}, t)^2 \, dt$$

where $[0, T]$ is the time interval of the noise event we are interested in. For instance, this could be night time (to calculate the L_{night}), or the pass-by of a tram. The equivalent sound pressure level is then defined as:

$$L_{\mathrm{eq,T}}(\mathbf{x}) = 10 \, \log \frac{p^2_{\mathrm{rms,T}}(\mathbf{x})}{p^2_{\mathrm{ref}}}$$

with $p_{\mathrm{ref}} = 20 \, \mu\mathrm{Pa}$ in air. However, in environmental noise assessment, it makes more sense to consider A-weighted quantities. One way to do this is to apply the A-weighting filter on the pressure signal $p(\mathbf{x}, t)$ to generate $p_A(\mathbf{x}, t)$, for instance using a time domain filter. From this signal the A-weighted mean squared pressure $p^2_{\mathrm{A,rms,T}}(\mathbf{x})$ can be calculated and then the A-weighted equivalent sound pressure level:

$$L_{\mathrm{Aeq,T}}(\mathbf{x}) = 10 \, \log \frac{p^2_{\mathrm{A,rms,T}}(\mathbf{x})}{p^2_{\mathrm{ref}}}$$

This metric is the most commonly used for in situ noise exposure measurements, and will be used extensively in chapter 8. Let us also point out that it would then be straightforward to define an insertion loss from the $L_{\mathrm{Aeq,T}}$: one can measure or predict $L^{\mathrm{in}}_{\mathrm{Aeq,T}}(\mathbf{x})$ before the barrier (or any mitigation device for which we want to estimate the efficiency) was built and the same $L_{\mathrm{Aeq,T}}(\mathbf{x})$ with the barrier, so that the "equivalent" insertion loss becomes:

$$\mathrm{IL_{Aeq}}(\mathbf{x}) = L^{\mathrm{in}}_{\mathrm{Aeq,T}}(\mathbf{x}) - L_{\mathrm{Aeq,T}}(\mathbf{x})$$

This is a possible metric to measure the performance of a noise barrier, typically used in standard measurement (again this will be used in chapter 8). Although, in the context of numerical simulations involving noise barriers, since we are mostly going to use frequency domain prediction methods we will rather use the insertion loss as defined in section 1.2.2.

1.3 Human response to noise

Interest in the assessment and prediction of environmental noise fundamentally started because of concerns to its effects on human health, especially sleep quality, or more generally human well-being, including mood and performance at work. The latter lead to the assessment of *annoyance* due to noise exposure, which is one of the main purpose of psychoacoustics. It could also be mentioned that all animals [30, 31] and not only humans are affected by noise.

The difficulty is to quantify a purely subjective judgment, and to correlate it to predictable physical parameters, such as the $L_{\mathrm{Aeq,T}}$ introduced in 1.2.3 or the insertion loss related to some noise control device. Indeed, most of the time it is questionable to state that such physical quantities will correlate directly with the change in people's subjective opinions concerning their noise exposure. For instance it has been shown that depending on the type of source - railway, aircraft or road traffic -, for the same $L_{\mathrm{Aeq,T}}$, the human subjective annoyance would be different [32]. Another study [33], focusing on a well-being degradation in noisy areas, showed that the situation of living in a place where there are windows showing the source of noise can lead to a more intense depression feeling than the equivalent noise exposure situation, which notably includes same $L_{\mathrm{Aeq,T}}$, without windows.

Besides, noise exposure is known to interfere with all human activities and therefore becomes more annoying during the evening and the night when people devote themselves to leisure activities and relaxing, including sleep. This led to the 5 and 10 dB penalty used in the community level metric L_{den} which has now become the most widely spread metric to assess noise exposure. A review of many relevant effects on annoyance and correlation with metrics can be found in [34].

More than just causing a feeling of annoyance, noise has significant direct effects on human health, especially on sleep quality [35, 36]. Depending on the nature of the ambient noise during sleep, sleep depth and therefore performance and mood during the day can be significantly degraded. Apart from the fact that the louder the noise, the poorer the sleep quality, it has been established that the nature of the noise, especially its intermittent character, has a significant influence on sleep quality. For instance, the pass-by of a truck on its own causes increased body movements, which are known to be correlated to sleep shallowness, and of course could even lead to awakening and therefore interruption of the sleep cycle.

However, some psycho-social effects seem to be relevant as well, even during sleep since humans can still discriminate sounds while sleeping, and therefore the subjective attitude towards certain sources of noise can affect the physiological response, as well as the character of the source: in a recent study [37], it has been shown that railway noise affects sleep more than traffic noise.

Even though environmental noise is really concerned about reducing negative health effects of noise (namely feeling of annoyance and degradation of sleep quality), in the remainder of this work we will focus on a purely physical description of the noise and the noise reduction by noise barriers, with the fundamental assumption that purely physical quantities such as the insertion loss exactly correlates with the feeling of noise exposure reduction by human beings. This is a quite dramatic simplification, as we have seen, but commonly accepted in the noise barriers

performance research community, which is understandable since otherwise the problem of noise reduction would rapidly become impossible to handle.

1.4 Physical effects influencing a noise barrier efficiency

We review here the different physical effects involved in the propagation of sound in outdoor environments in general, including when a noise barrier is present. This will allow us to identify what phenomena are the most relevant to low height noise barriers acoustic performance. Regarding outdoor sound propagation in general, one can refer to comprehensive descriptions in two books written by Attenborough et al. [38] and Salomons [39], or in the excellent review paper by Embleton [40].

1.4.1 Meteorological effects

The propagation of sound from a known noise source to a receiver in a typical outdoor environment, for instance from a highway to a nearby house, with or without the presence of obstacles such as noise barriers, is a complex problem to solve. One of the difficulties is that the atmospheric conditions, which define the medium where the sound propagates, have an influence on the sound field and therefore on the performance of a noise barrier, as measured experimentally in [41].

The first effect is the refraction of sound due to local inhomogeneities of the ambient temperature and mean wind fields, which modifies the local speed of sound. This causes a wave propagating in the medium to bend, typically upward or downward, depending on the sign of the vertical sound speed gradient. This effect can be of importance for the assessment of noise barriers performance, since in a downward refracting case, the sound could go above the barrier and then back down, hence decreasing the shielding effect of the barrier. In fact, on a sunny day - in which the temperature typically decrease with height - upwards refraction naturally happens, whereas downward refraction can happen on an unclouded night. The presence of wind can either strengthen or weaken this effect, depending on the propagation being downwind or upwind. Insertion losses of barriers in the presence of wind have been studied numerically and in wind tunnel experiments [42, 43], and it has been shown that they decrease in downwind conditions. Besides, in a noise barrier context, the presence of the screen will also affect the wind field [44, 45], which would typically worsen the downwind propagation effect.

Inhomogeneities of the ambient temperature and wind fields can be caused as well by turbulent fluctuations, which can cause scattering of the acoustic energy, with two main consequences in a noise barrier context: the wave tends to lose spatial coherence during its propagation - which decreases the strength of interference effects - and sound can be backscattered to a region where there is supposedly little energy such as the shadow zone created by a noise barrier, which typically limits its insertion loss. The main theoretical framework to describe backscattering is due to Daigle [46] who introduced the concept of scattering volume and cross section. Several studies which followed this framework showed that turbulent back scattering has a significant effect at higher frequencies, typically above 4 kHz [47–49].

Nevertheless, an important point is that meteorological effects - temperature and wind-induced refraction, as well as turbulence - are considered to possibly have a significant influence at rather large distances [40], or a high enough frequency (several kHz for turbulent backscattering), and indeed most of the studies cited in this section considered a distance of about 100 m and more between source and receiver. Atmospheric absorption effects are also known to be negligible at low enough frequencies and small enough ranges (extra attenuation typically less than 3 dB for ranges less than 100 m and frequencies below 3000 Hz [40]). Therefore, when the distance between source and receiver is small, say below 20 m - which would be the case for an urban low-height barrier - and assuming a typical environmental noise frequency range (100 to 3000 Hz), the performance of a noise reduction device might therefore be mostly controlled by other effects, such as the ground properties, the presence of surrounding objects and the features of the device itself. However, if one was to extrapolate results obtained at short ranges to larger ranges, those meteorological effects should be considered.

1.4.2 Ground effect

The ground is always present in realistic situations and should be considered. Basically, when assumed completely flat, it can be modeled as an infinite plane over which the sound can reflect. This reflection can be easily described by image source theory when it is assumed perfectly reflecting (rigid), but is more complicated when the ground is absorbing, as most outdoor ground surfaces are [40, 50]. How absorbing the ground is can be typically quantified with an impedance.

The problem of predicting the sound field due to a point source above an impedance plane has been tackled theoretically for several decades [51–54]. These studies showed that the pressure field is this case is given by a free-field contribution emanating from the source (S) plus a free-field contribution emanating from the image source (S') plus a extra contribution due to the finite impedance of the ground, expressed as a Fourier integral, and which also depends on the source and receiver positions. A popular approximate expression is the so-called Weyl - Van der Pol solution (from the names of the two scientists who first derived this expression in electromagnetism [55, 56]), which can be found in many references [38, 40]. Using this solution, one can show that the main effect of a finite impedance ground is to limit interference effects between direct and reflected sound, and also to cause a shift in interference dips [40].

One can also ask the question of the influence of the ground impedance on a noise barrier insertion loss. It has first been pointed out that a ground finite impedance can provide on its own an attenuation, which the presence of the barrier can decrease, to the point that the insertion loss becomes negative [57]. It has also been pointed out that simple empirical expressions (see in section 1.5), which do not take into account the ground effect, can in some cases over-predict the attenuation [58]. Similar conclusions were drawn by Hutchins et al. in the case of thin reflective barriers [59] as well as for more complicated shapes [60]. The main conclusion of these studies is that as a general rule, the insertion loss of a noise reduction device is smaller with an absorbing ground than a rigid ground, and that the ground impedance on the source side matters more than on the receiver side. Also, the authors state that the ground impedance has a larger effect on the barrier efficiency than the barrier impedance. One can however point out these results

were found for a typical highway barrier configuration, and may not be applied directly in other situations, such as a low-height tramway noise barrier context.

1.4.3 Multiple reflections and diffuse field

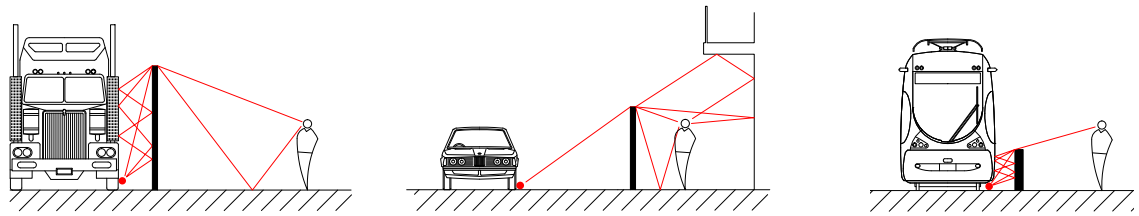

Figure 1.2: Examples of configurations where multiple reflections can influence a noise barrier efficiency. Left: heavy truck traveling close to a highway noise barrier - center: barrier implemented close to a building - right: low-height barrier close to a tramway.

In some situations, for instance in most urban environments, extra objects are present around the site where a noise barrier is implemented, and those objects can induce many more reflections compared to the case where the barrier only is present. This is the case for instance for heavy trucks traveling close to a highway barrier, for a barrier close to a building facade, and for a barrier close to a tramway (see figure 1.2). This could even happen in a street canyon or between parallel noise barriers. Those reflections tend to decrease the efficiency of noise protections and should therefore be taken into account in numerical prediction schemes modeling barriers in such situations, for instance considering a set of image sources or a radiosity-based scattering scheme [61, 62]. Implementation of barriers in urban canyons have also been investigated numerically and with scale models, either for hard barriers [63, 64] or absorbent barriers [8, 65]. Both calculations and measurements show that in those situations, rigid barriers do not have a significant noise reduction effect, but with an absorbing treatment the efficiency of the barriers is a lot higher.

1.4.4 Shape and material distribution over the barrier

Finally, the design of the barrier itself - namely its shape and the materials covering it - may have an effect on its efficiency. Actually, from simple theoretical considerations, one can state that this effect exists. However, one should raise the question of the relative importance of the influence of the barrier design compared to all the other effects mentioned in this section.

It has already been pointed out in section 1.4.2 that in a typical highway noise barrier configuration, the impedance coverage of the barrier has a smaller effect than the ground impedance [60]. Also in a highway context, May and Osman [66] measured as well that there was not a significant difference in performance between a thin reflective and absorptive screen. However, when a T-profile is considered, they measured that an absorptive treatment on the top yielded an improvement of a few dB(A). Similar results were found by Watts et al. [67].

Moreover, in a railway barrier context, Morgan et al. [68] found - based on scale measurements - that different shapes had significantly different insertion losses, and that the barrier impedance had a great effect as well: for a rigid ground, insertion losses were between 14 and

23 dB(A), whereas for an absorbing ground, they ranged between 10 and 20 dB(A). It was also found that going from rigid to absorbing ground does seem to decrease the insertion loss (as stated in section 1.4.2), but however in this context the shape and material distribution can still make the insertion loss vary by 10 dB(A), which means that the design of the barrier itself has a significant effect.

In a low-height tramway noise barrier context, the presence of the tramway is similar to the presence of the train in [68] - it causes multi reflections - and therefore it is likely that the barrier shape and admittance will be significant as well, even in the presence of an absorbing ground. This also suggests that seeking to optimize the design of the barrier will be worth it, in the sense that significant improvement can be obtained in the barrier efficiency by careful design.

1.5 Review of prediction methods

From reviewing the different effects that could come into play in the efficiency of a low-height noise barrier close to a tramway, one can now decide which prediction method can be used to evaluate the efficiency of a low height barrier. It has been found that meteorological effects - related to inhomogeneities in the ambient properties describing the propagation medium, namely the speed of sound - are probably negligible since short range propagation only will be considered. On the other hand, reflections and scattering effects due to the barrier itself, the ground or the surrounding geometrical features - such as the tramway - will have an important effect and therefore the chosen prediction method should be able to render diffraction effects by arbitrarily complicated geometries accurately. It should also be able to take into account the acoustic properties (the admittance) of the surface of the different obstacles. We will now briefly review some of the common methods in outdoor sound propagation prediction which will allow us to decide which one seems the most appropriate in our context.

Diffraction effects from an infinite screen have first been described using analytical formula derived from Sommerfeld's geometrical theory of diffraction [69], which was then extended by McDonald [70], Keller [71] and Pierce [72, 73]. Considerations of reflections on the ground [57, 74–76] and finite barrier effects [77, 78] have also been studied with these analytical expressions. Apart from this approach, several empirical formulae predicting the efficiency of a noise barrier based on the so-called Fresnel number have been derived, the most famous being Maekawa's curve [79], which was then extended by Kurze and Anderson [80] and Menounou [81]. All those expressions, although useful and used in many engineering methods, are valid in highly idealized contexts, especially for a flat screen and a straight diffraction edge. They are not general enough to model a barrier for our application.

In terms of numerical methods, mainly two main families of methods have been developed in the second half of the 20^{th} century: long-range and short-range methods. Indeed, as mentioned in section 1.4, propagation at large distances (more than 100 m) is significantly influenced by meteorological effects, whereas the sound field at short ranges is mostly influences by geometrical features close to the source (obstacles, ground), but little by meteorological conditions. It therefore makes sense that different types of numerical methods were developed for those two applications. Nevertheless, those two types of methods can be coupled, as for instance in the

Harmonoise reference model [82].

Long-range propagation mostly uses ray tracing [83, 84] and the Parabolic Equation (PE) method [39, 85, 86], which is based on an approximation of the Helmholtz equation with non-uniform speed of sound. It is possible to some extent to take into account terrain and obstacles - such as a noise barrier - in the PE by approximate methods [87, 88], but again these would not be valid for an arbitrary geometry.

Concerning short range propagation, most commonly used methods for taking into account complex geometry are finite element methods (FEM), finite-difference time-domain methods (FDTD) and boundary element methods (BEM). The FEM and the FDTD can include quite naturally physical effects as well as complex geometries, with appropriate meshing of the domain, but have a rather high computational cost since a volume mesh is required. The FEM is hence not widely used in outdoor sound propagation simulations, although the FDTD has been applied successfully [29, 89, 90]. On the other hand, the BEM is able to represent complex geometries accurately, since only the boundaries of the obstacles are meshed, and to model the ground effect via an appropriate choice of the Green's function. It usually assumes a uniform speed of sound, although there have been attempts to consider a linear sound speed profile [91, 92]. The computation cost of the BEM is limited since only the boundary is meshed, although it is still rather high due to the non-sparsity of the matrices. It can however be greatly reduced using the so-called Fast Multipole method, which will not be detailed here (one can refer to the introductory paper by Coifman et al. [93]).

From this brief review, the BEM clearly seems like the most appropriate method for our application. It will be explained in more details in chapter 2.

1.6 A few examples of surface treatment models

As mentioned earlier, the acoustic properties of a surface treatment can have a significant influence on the efficiency of a noise barrier, and therefore one should be able to model the effect of a surface on the sound field. A more comprehensive review can be found in [1], and we simply recall here a few models that will be used in this work.

The classical approach to model the effect of a surface is to force the local impedance to match that of the given surface, which mathematically corresponds to apply a so-called Robin boundary condition at the surface location. However, instead of the classical specific acoustic impedance Z (ratio of pressure to particle velocity), it is usually more convenient to consider the normalized admittance β, which is simply the inverse of the normalized impedance Z/Z_0, with $Z_0 = \rho_0 c_0$ is the specific acoustic impedance of air - one therefore has $\beta = Z_0/Z$, which would for instance go to zero for a rigid material. As we will see in chapter 2, in a BEM formalism the admittance of any surface β is readily taken into account, and therefore being able to model β is the only requirement to predict the effect of the surface treatment on the sound field.

Most construction materials can be assumed acoustically rigid (for instance concrete, steel, heavy wood...), but acoustic surface treatments can be used as well to increase the efficiency of a noise barrier (as mentioned in section 1.4). Those treatments can be generally divided in two categories: porous materials - which rely on energy dissipation through viscothermal dissipation

effects - and reactive treatments - which rely on destructive interference effects, usually using one or several resonators. Examples of porous materials include fibrous materials, foams, porous concrete, or natural materials like vegetation or hemp concrete. Reactive treatments on the other hand include reverberation chambers (exhaust mufflers), quarter-wavelength resonators or micro-perforated panel resonators (MPPR).

We give here three examples of possible treatments which will be used in this work, more specifically in chapter 6.

1.6.1 Delany and Bazley layer model

In a noise barriers application, the most common type of treatment is porous since it can provide absorption over a broad range of frequencies. Many models exist to express the admittance of such a treatment (see for instance [1] for a review of some of these models), however the most common one is the Delany and Bazley model [94], which has the main advantage to depend on one parameter σ/f, with σ the airflow resistivity of the medium - usually expressed in kPa.s/m^2 - which corresponds to the pressure drop across a porous sample normalized by its thickness and the airflow velocity through it. Due to its simplicity, this model has been extensively used to model many materials, including soils [50], although it should be recalled it was initially derived for fibrous materials and for a given range of validity ($\sigma/f \in [1, 100]$). The expression for the normalized impedance z_{DB} and wavenumber k_{DB} are (within the $e^{-\mathrm{i}\omega t}$ convention):

$$\begin{cases} z_{\mathrm{DB}} = 1 + 0.0511 \left(\dfrac{\sigma}{f}\right)^{0.75} + \mathrm{i}\, 0.0768 \left(\dfrac{\sigma}{f}\right)^{0.73} \\ \dfrac{k_{\mathrm{DB}}}{k_0} = 1 + 0.0858 \left(\dfrac{\sigma}{f}\right)^{0.7} + \mathrm{i}\, 0.175 \left(\dfrac{\sigma}{f}\right)^{0.59} \end{cases} \tag{1.2}$$

where σ is here in Pa.s/m^2 and $k_0 = \omega/c_0$ is the wavenumber in air . The normalized admittance β_{DBL} of a rigid-backed layer of material of thickness d is then:

$$\beta_{\mathrm{DBL}} = \frac{1}{z_{\mathrm{DB}}} \tanh(-\mathrm{i} k_{\mathrm{DB}} d) \tag{1.3}$$

1.6.2 Hemp concrete layer

Porous materials can be made out of many different basic components such as polymeric foams, plastic fibers, glass fibers, wool fibers, tire wastes, plastic grains, and so on. Some of these components, other than being hazardous and therefore requiring appropriate packaging, are not sustainable. However, porous materials with good acoustic properties can also be made from wood fibers binded together [95], which is the case of *hemp concrete*. Specifically Glé et al. [96, 97] studied different ways to manufacture hemp concrete for acoustic applications and proposed a porous material model which matches well to experimental data. They expressed the impedance in terms of the dynamic density ρ_e, calculated with the Johnson model [98], and dynamic bulk density K_e, calculated with the Zwikker and Kosten model [99]. Within this

model, the normalized admittance β_{HC} of a hemp concrete layer is given by:

$$\beta_{\mathrm{HC}} = \frac{1}{z_{\mathrm{HC}}} \tanh(-\mathrm{i}k_{\mathrm{HC}}d) \tag{1.4}$$

with:

$$k_{\mathrm{HC}} = \omega\sqrt{\frac{\rho_e}{K_e}} \qquad \text{and} \qquad z_{\mathrm{HC}} = \frac{1}{\rho_0 c_0}\sqrt{\rho_e K_e}$$

and

$$\begin{cases} \rho_e = \dfrac{\alpha_\infty \rho_0}{\phi}\left(1 + \mathrm{i}\,\dfrac{8}{\lambda^2}\sqrt{1 - \mathrm{i}\,\dfrac{4\alpha_\infty^2 \mu \rho_0 \omega}{\sigma^2 \Lambda^2 \phi^2}}\right) \\ K_e = \dfrac{\rho_0 c_0^2}{\phi}\left[1 + 2(\gamma-1)\,\dfrac{J_1(\lambda\sqrt{\mathrm{i}\,\mathrm{Pr}})}{\lambda\sqrt{\mathrm{i}\,\mathrm{Pr}}\,J_0(\lambda\sqrt{\mathrm{i}\,\mathrm{Pr}})}\right]^{-1} \end{cases}$$

where J_0 and J_1 are the Bessel functions of zeroth and first order, and the parameter λ is defined by:

$$\lambda = \sqrt{\frac{8\alpha_\infty \rho_0 \omega}{\sigma\phi}}$$

This model therefore requires four parameters to describe the porous material (porosity ϕ, flow resistivity σ, tortuosity α_∞ and viscous characteristic length Λ) and the thickness of the layer d, as well as physical characteristics of air (dynamic viscosity μ, air density ρ_0, sound speed c_0, specific heats ratio γ and Prandtl number Pr). For a typical ratio of water, hemp and binder, the authors give the following values for the porous parameters: $\phi = 0.73$, $\sigma = 19.3\,\mathrm{kPa.s/m^2}$, $\alpha_\infty = 3.0$, $\Lambda = 23\,\mu\mathrm{m}$ and $d = 10\,\mathrm{cm}$. The physical properties of air can be taken assuming for instance a temperature of 20°C: density $\rho_0 = 1.21$ kg/m^3, sound speed $c_0 = 343\,\mathrm{m/s}$, dynamic viscosity $\mu = 1.81\ 10^{-5}$ Pa.s, ratio of specific heats $\gamma = 1.4$ and Prandtl number $\mathrm{Pr} = 0.7$.

1.6.3 Micro-perforated panel resonator (MPPR) model

Some reactive treatments have been considered in noise barrier applications [100–107] but their use is still limited. One possible treatment, which has the main advantage to cover a wide range of behaviors thanks to its four design parameters, is the micro-perforated panel resonator (MPPR). This treatment simply consists of thin sheet of heavy material perforated by a grid of holes and coupled to a cavity, and has been studied by many authors [100, 108–112]. One possible model for its impedance, taking into account viscous and thermal effects in the holes, radiation mass and interaction effects, is the model one can refer to as the Crandall-Sivian-Fok model - following the work of Crandall [113], Sivian [114] and Fok [115, 116] - which has been used by Melling [110] and Asdrubali et al. [100]. According to this model, given a panel of porosity s, of hole radius a_0, of panel thickness l_0 and of cavity depth D, the normalized impedance is:

$$z_{\mathrm{MPPR}} = -\mathrm{i}\,\frac{k_0 l_0}{s}\left(\frac{1}{\Theta(x')} + \frac{16}{3\pi}\,\frac{a_0}{l_0}\,\frac{\Psi(\xi)}{\Theta(x)}\right) + \mathrm{i}\,\mathrm{cotan}\,(k_0 D) \tag{1.5}$$

with
$$\begin{cases} k_0 = \dfrac{2\pi f}{c_0} \;\; ; \;\; \xi = \sqrt{s} \;\; ; \;\; x = a_0\sqrt{\dfrac{2\pi f\,\rho_0}{\mu}} \;\; ; \;\; x' = a_0\sqrt{\dfrac{2\pi f\,\rho_0}{\mu'}} \;\; ; \;\; \mu' = \mu\left(1+\dfrac{\gamma-1}{\sqrt{\mathrm{Pr}}}\right)^2 \\ \Theta(w) = 1 - \dfrac{2}{w\sqrt{\mathrm{i}}}\dfrac{J_1(w\sqrt{\mathrm{i}})}{J_0(w\sqrt{\mathrm{i}})} \qquad \Psi(\xi) = \displaystyle\sum_{m=0}^{8} u_m\,\xi^m \end{cases}$$

with the coefficients u_m given by $u_0 = 1$, $u_1 = -1.4092$, $u_2 = 0$, $u_3 = 0.33818$, $u_4 = 0$, $u_5 = 0.06793$, $u_6 = -0.02287$, $u_7 = 0.03015$ and $u_8 = -0.01641$ (values for air physical parameters are given in section 1.6.2). μ' is an equivalent viscosity representing both viscous and thermal effects, and the intermediate variables x and x' are the so-called *perforate constants* and correspond to ratios between the radius of the hole and either the viscous or thermo-viscous penetration depth. Finally, the Fok's function [115, 116] $\Psi(\xi)$ is a correction to take into account interaction effects between the different holes, directly related to the porosity. The normalized admittance is then simply $\beta_{\mathrm{MPPR}} = 1/z_{\mathrm{MPPR}}$.

1.7 Review of noise barriers designs and performance assessment

1.7.1 Common designs (highway and train noise barriers)

As stated earlier, engineers have been developing noise barriers for many decades now, and therefore there are quite a variety of common designs, mostly implemented along highways, but also along train tracks. We here review some of the main designs and state a few results about their relative performance. The assessment of a noise barrier efficiency has been typically done using three approaches: numerical calculations (most of the time using 2D BEM), scale model measurements or in situ measurements.

Numerical studies are useful since they allow one to compare many different designs easily. Namely, for implementation as a highway noise barrier, the most commonly assessed noise wall shapes are: straight thin wall, T-shape, Y-shape, arrow-shape, wedge barriers and straight wall with added cylindrical top [117–119]. From those studies it seems like the T-shape is the most efficient. Further, the presence of absorptive treatment on top seems to provide a few extra dB of attenuation, although this benefit is largely diminished when sources sufficiently far away are considered.

Railway noise barriers have been studied extensively as well [120, 121]. Since they are typically implemented close to the sources of noise and therefore to the train body, multiple reflections can occur and consequently an absorptive treatment on the source side of the barrier as well its shape may have a significant effect.

Scale model measurements can be performed as well to assess the efficiency of a design, since it is still relatively cheap to build a model say at a 1/20 scale of a highway or railway noise barrier. Many different shapes have been tested indeed, for highway barriers [122] and train barriers [123]. Those different studies show that insertion losses measured from scale models usually agree rather well with BEM calculations.

Fewer full scale tests have been performed. Thin straight screen and T-shape profiles imple-

mented along highways have been assessed in [66], and again the T-shape seems indeed more efficient (by a couple of dB). Watts et al. [67, 124, 125] also pointed out the advantage of the T-shape for highway noise barriers and good agreement with BEM calculations (although their measurements were made under somewhat controlled environments, not actual field sites). Adding multiple-edges is also shown to add some attenuation, although the effect seems less important than for the T-shape.

1.7.2 Complex noise barriers

Although noise barrier research has been going on for several decades, the research community is still active in this area. We will not give here a comprehensive review but rather emphasize a few interesting results. For more details, we refer the reader to the excellent review paper by Ekici [126] (although since this paper was published ten years ago, it is probably not completely up to date). In addition, as for the more common designs, one can point out that performance assessment of new designs has been essentially based on numerical simulations.

A first idea that was investigated to increase the efficiency of an already implemented screen is to add extra diffracting edges on the side of the noise barrier, which is referred to as a multiple-edge device. Several measurements - both on scale models and at full scale - of added parallel panels were performed by Watts et al. [67, 127]. Their results show that extra diffracting edges do provide a consistent improvement in efficiency above a certain limiting frequency (typically related to the dimensions of the multiple edge device). Oblique panels covered with absorptive materials have also been studied and optimized numerically by Baulac et al. [128] in a highway context, which can yield a good improvement of 5 dB(A) compared to a straight screen.

Another possible improvement of a typical highway straight screen is to add geometrical complexity (or even "randomize") the top diffracting edge, by using so-called *thnadners*. A type of thnadners had been studied by May and Osman [122], although their considered designs did not show a significant improvement. On the other hand, other experimental and numerical studies showed that random profile of the top diffracting edge induced consistent improvement of the noise barrier, especially at high frequencies [129–131]. The effect at play here is believed to be the loss of coherence of the secondary sources located at the edge of the barrier, which in turns decreases the level of the diffracted signal.

Another possible approach to increase the efficiency of a straight screen is to add a designed object at the top edge, among which cylinders have received significant attention. Numerical investigations indeed suggested that using an acoustically soft impedance on the cylinder was particularly efficient in increasing the barrier insertion loss [119, 132–134]. Besides, although it is difficult to achieve a perfectly soft boundary condition over a wide frequency range, attempts have been made to design a device made of several resonators which would approximate a soft surface, such as the so-called "waterwheel" design [132, 133]. Improvement is noticed although such a device may also have a negative insertion loss outside of the design band.

Interference-type devices to be placed on top of a screen have also been considered, both with BEM simulations and full scale measurements [124, 135]. The idea of this device is to force part of the incident wave to follow longer paths by a set of tubes, and then interfere destructively

with the rest of the wave. The measured improvement was reported however not to be as good as traditional top devices (such as the T-shape or cylinder caps), and it is argued that the performance could be largely dependent on the source and receiver positions.

Using destructive interference to attenuate the wave on a top device is also the idea of reactive admittance barriers, which is somewhat similar to the idea of approximating a soft impedance with several tuned resonators. Several approaches have been followed to this end: build a top device with a designed network of Helmholtz-like quarter-wavelength resonators [102], cover the top of T-shape barrier with wells of possibly different depths [103, 104], construct the top of a T-shape barrier as a QRD diffuser [105, 106] and possibly add perforated sheets in the wells to further improve the design at low frequencies [106, 107]. Those different studies reported improvement which can be of the order 2-3 dB(A) for a typical traffic noise spectrum.

1.7.3 Low-height noise barriers

Finally we describe some results previously obtained in the relatively recent field of low height noise barriers. As stated in section 1.1.1, this type of noise reduction device - which is typically limited to be less than one meter high - is really meant to be implemented in an urban context, close to the noise sources (cars, urban trains, tramways, ...), in order to reduce the noise level reaching close receivers such as pedestrians or cyclists during a pass by.

A simple type of low-height barrier (pedestrian restraints) has been considered by Horoshenkov et al. to mitigate noise in an urban canyon [8]. They showed with scale modeling that this type of device can provide more than 8 dB(A) of attenuation for the pedestrians if it is covered with absorptive treatment, considering light and heavy vehicles traffic noise.

Thorsson [9, 10] also considered low height barriers of simple shape (straight wall, half cylinder and T-shape) and optimized the admittance distribution - either by an equivalent source method [9] or a direct optimization method [10] - to increase the insertion loss at selected frequencies at different heights. His results suggest a large improvement is achievable (more than 10 dB), and that even when the ground is treated the benefit of optimizing the barrier admittance was still significant (10 dB of extra attenuation due to the barrier optimized admittance). However one should point out that the obtained admittances are not realistic and that only a few low frequencies were considered.

Ding et al. [14] modeled a porous low-height barrier meant to attenuate traffic noise with an advanced time-domain method, and showed that significant insertion loss is obtained (which can reach 10 dB(A), depending on the type of vehicle and receiver locations).

We finally mention Baulac's and Koussa's Ph.D. theses [4, 11] completed at the *Centre Scientifique et Technique du Bâtiment* (CSTB), since a significant part of their work concerned low height noise barriers. Baulac considered a typical urban traffic noise situation and optimized the shape and the treatment (mostly absorbing) of a low-height barrier using BEM simulations and genetic algorithms [6]. She showed that an insertion loss of 10 dB(A) is achievable. Simpler shapes have also been studied with scale modeling and showed that numerical simulations were in good agreement with the BEM [5].

Koussa, whose work was concerned with the use of natural materials for noise control, also

studied numerically and experimentally a type of low height noise barrier made of many rocks of different sizes (gabions) [13]. The insertion loss he obtained, depending on the gabions arrangement, ranged from 5 to 10 dB(A), which confirmed the applicability of such a barrier. He also studied numerically a so-called *sonic crystal* low height noise barrier for tramway noise mitigation made of parallel cylinders of different diameters. Those barriers can provide up to 6 dB(A) of attenuation by themselves, although when a rigid screen is added behind the sonic crystal the efficiency reaches 10 dB(A), and more than 15 dB(A) when both the cylinders and the screen are absorbent [11]. Koussa et al. [12] also considered parallel arrangements of hollow cylinders and found similar insertion losses.

1.8 Conclusion

Noise barriers have been studied extensively in the past few decades, along with their industrial development and the rapid expansion of highways and railway track networks in many industrialized countries. Several physical effects which can influence the efficiency of those type of noise control devices have been identified, including diffraction, atmospheric refraction, turbulent scattering and acoustic properties of the ground. For typical highway noise barriers, it has been found that meteorological effects have a significant impact when long ranges (more than 100 m) are considered, but they can probably be neglected at short ranges (less than 10 m), which would be typically the case in an urban environment. The ground characteristics however still remain important in this context.

Moreover, the presence of other reflectors of sound in the vicinity of the device, such as buildings or a train body, induces a multiple reflection phenomenon which can negatively impact the performance of a barrier, and therefore should be taken into account. However an absorbing treatment on the barrier and well-designed barrier shapes can be efficient in limiting this effect. On the other hand, in a typical highway configuration in which sources and potential reflectors are sufficiently far away from the device, the acoustic treatment of the barrier has a smaller effect. Nevertheless, adding a designed cap - either absorbing or using destructive interference effects - on a thin vertical screen can improve the performance significantly, even in the highway case.

In the context of urban low-height barriers, especially close to a tramway which would be the source of multiple reflections, it would therefore makes sense that a well-designed acoustic treatment and barrier shape may yield a significant improvement in the efficiency of the device. Besides, since the reflection and diffraction effects might be complex in this case, it is also natural to seek improvement in the design by an optimization algorithm, coupled to a numerical prediction method, as opposed to a trial-and-error approach. Due to the complex geometries and treatments the method will have to handle, the boundary element method seems like the most natural solution, although any other method that aims to solve as accurately as possible the complete diffraction problem would be appropriate as well.

Chapter 2

Review of the forward scattering problem and the integral equation method

In this chapter, we give the mathematical foundations of the integral equation method to the acoustic scattering exterior problem, which naturally yields the boundary element method (BEM). This chapter is essentially a review (which is by no means comprehensive) of known results about the acoustic scattering problem formalism and its resolution using the integral equation method. Some of these results will be used explicitly in the rest of this work (especially in chapter 4), but the author's intention is essentially to give a somewhat detailed introduction to this method, emphasizing a few points that are not perhaps very well-known.

Although the integral equation framework can be tackled in 3D, we will present the formalism in 2D since this is the type of calculations that we will be mostly using to predict the performance noise barriers in this work. The general framework of the integral equation method given here is essentially taken from the comprehensive treatment by Terrasse and Abboud [136]. Besides, we will also focus more specifically on the integral equation approach proposed by Jean [120], which has been been implemented in the software MICADO, since we are going to use this software extensively in the rest of this work.

2.1 Initial scattering problem

The atmosphere is assumed homogeneous with a uniform speed of sound c_0. The problem at stake is the resolution of the pressure field in two dimensions in the presence of a point source located at point (S), of one of several obstacles which will induce scattering of the incident field and of a rigid ground represented as an infinite horizontal baffle (see figure 2.1). Generally speaking, the baffle representing the ground could also have a finite impedance, but this case will not be considered in this work. The problem is solved in the frequency domain so that the frequency f is fixed and $k = 2\pi f/c_0$ is the wavenumber. The time convention is $\mathrm{e}^{-\mathrm{i}\omega t}$.

Let Γ be the planar curve (or the set of curves) defining the boundary of the obstacles (it

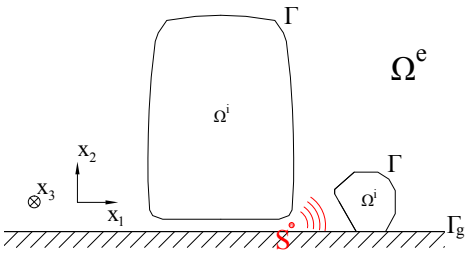

Figure 2.1: Typical geometrical configuration of the scattering problem. Cartesian coordinates are defined such that x_1 is the horizontal coordinate, x_2 the vertical coordinate (and x_3 the direction normal to the vertical plane). The ground is assumed to lie at $x_2 = 0$. One or several scattering bodies delimit the domain into a bounded interior domain Ω^i and an unbounded exterior domain Ω^e. The curve (or set of curves) delimiting Ω^i are referred to as the boundary Γ. (S) is the point where the source is located.

can be the noise barrier alone or the barrier and the tramway body for instance), and Γ_g the remaining part of the rigid ground (parts of the ground which are not rigid are taken into account as part of Γ). Γ separates the half-infinite domain in two open sets, the interior domain Ω^i and the exterior domain Ω^e. Let $\mathbf{n}$ be the normal vector exterior to the boundary (pointing towards Ω^e), defined on Γ and Γ_g. The source is assumed to lie in the exterior domain and therefore we consider an exterior problem. Besides, we will assume that the acoustic behavior at each point of the boundary Γ can be described by a normalized admittance β (which is typically a piecewise continuous function defined on Γ).

Under those hypotheses, the total pressure field p in the exterior domain satisfies the following scattering problem:

$$\begin{cases} -\left(\nabla^2 + k^2\right) p = \delta(S,.) \quad \text{in } \Omega^e \\ \dfrac{\partial p}{\partial n} + \mathrm{i}k\,\beta\, p = 0 \quad \text{on } \Gamma \\ \dfrac{\partial p}{\partial n} = 0 \quad \text{on } \Gamma_g \\ + \quad \text{radiation condition} \end{cases} \tag{2.1}$$

$\delta(S,.)$ is the Dirac delta function located at point (S) and $\partial p/\partial n = \mathbf{n}\cdot\nabla p$ is the normal derivative on the boundary. The Sommerfeld's radiation condition, which ensures the fact that all waves radiate outwardly at infinity, is given in 2D by:

$$\frac{\partial p}{\partial r} - \mathrm{i}k\, p = o\left(\frac{1}{\sqrt{r}}\right)$$

Associated with this problem, one can define the associated half-space problem (obtained by removing the boundary Γ but keeping the influence of the ground Γ_g), of which the solution is the half-space Green's function $G(\mathbf{x},\mathbf{y})$, that is the field at point $\mathbf{y}$ due to the radiation of a point source at point $\mathbf{x}$, $\mathbf{x} = (x_1, x_2)$ and $\mathbf{y} = (y_1, y_2)$ being two arbitrary points. In the presence of a rigid ground in 2D, the expression for the Green's function is:

$$G(\mathbf{x},\mathbf{y}) = \frac{\mathrm{i}}{4}\left(H_0^{(1)}\left[k\sqrt{(y_1-x_1)^2+(y_2-x_2)^2}\right] + H_0^{(1)}\left[k\sqrt{(y_1-x_1)^2+(y_2+x_2)^2}\right]\right)$$

with $H_0^{(1)}$ is the Hankel function of order zero of the first kind. If the ground had been assumed

impedant, a correction term should be added to this expression (as mentioned in section 1.4.2). One can naturally define four partial derivatives with respect to each coordinate of the two considered points: $\partial G/\partial x_1$, $\partial G/\partial x_2$ and so on. Similarly, we write the gradient with respect to the coordinates of $\mathbf{x}$ and $\mathbf{y}$ as $\nabla_{\mathbf{x}}$ and $\nabla_{\mathbf{y}}$.

The total field p solution of (2.1) can be broken down as $p = p^{\text{in}} + p^{\text{sc}}$ where $p^{\text{in}} = G(S, .)$, referred to as the *incident field*, is the field emitted by the source without influence of the scattering objects Γ. p^{sc}, referred to as the *scattered field*, then satisfies the following problem:

$$\begin{cases} -\left(\nabla^2 + k^2\right) p^{\text{sc}} = 0 \ \text{ in } \Omega^e \\ \dfrac{\partial p^{\text{sc}}}{\partial n} + \mathrm{i}k\,\beta\, p^{\text{sc}} = h^{\text{in}} \ \text{ on } \Gamma \qquad \text{with } \ h^{\text{in}} = -\dfrac{\partial p^{\text{in}}}{\partial n}\Big|_{\Gamma} - \mathrm{i}k\beta\, p^{\text{in}}|_{\Gamma} \\ \dfrac{\partial p^{\text{sc}}}{\partial n} = 0 \quad \text{on } \Gamma_g \\ + \quad \text{radiation condition} \end{cases} \tag{2.2}$$

where h^{in} corresponds to the influence of the incident field on the scattering surface Γ and the notation $|_{\Gamma}$ refers to the evaluation of a function on the surface Γ.

2.1.1 Properties of the Green's function

The Green's function satisfies by definition the following equation:

$$-\left(\nabla_{\mathbf{y}}^2 + k^2\right) G(\mathbf{x}, \mathbf{y}) = \delta(\mathbf{y} - \mathbf{x}) + \delta(\mathbf{y} - \mathbf{x}')$$

with $\mathbf{x}' = (x_1, -x_2)$. G also satisfies the fundamental reciprocity property $G(\mathbf{x}, \mathbf{y}) = G(\mathbf{y}, \mathbf{x})$. From this property follows similar relationships on the gradients of G:

$$\nabla_{\mathbf{y}} G(\mathbf{x}, \mathbf{y}) = \nabla_{\mathbf{y}} G(\mathbf{y}, \mathbf{x}) \qquad \nabla_{\mathbf{x}} G(\mathbf{x}, \mathbf{y}) = \nabla_{\mathbf{x}} G(\mathbf{y}, \mathbf{x}) \tag{2.3}$$

This means that regardless of the position of a point as an argument in G (first or second argument), the gradient with respect to a point coordinate will be the same. This can be extended to the Laplacian with respect to each argument: $\nabla_{\mathbf{y}}^2 G(\mathbf{x}, \mathbf{y}) = \nabla_{\mathbf{y}}^2 G(\mathbf{y}, \mathbf{x})$ and $\nabla_{\mathbf{x}}^2 G(\mathbf{x}, \mathbf{y}) = \nabla_{\mathbf{x}}^2 G(\mathbf{y}, \mathbf{x})$.

2.2 Weak formulation of the scattering problem

The theoretical study of problem (2.1), especially considerations about the existence and uniqueness of a solution to the problem, is more convenient using a weak formulation. It will be helpful as well for calculations of the shape derivative, as we will see in chapter 4. This type of formulations is typically obtained by multiplying the equation by a test function and making appropriate transformations of the integrals to find how the boundary conditions intervene. However, although this kind of approach usually does not cause any trouble in bounded domains, it cannot be applied directly to the problem (2.1) because of convergence issues at infinity. One therefore needs to consider a problem on a bounded domain, the solution of which will be the same

as the initial problem (2.1). This is achieved using a so-called "transparent" boundary condition, which mathematically uses the Dirichlet-Neumann operator. We here briefly introduce the methodology to build a well-posed weak formulation for the scattering problem.

2.2.1 Dirichlet-Neumann operator

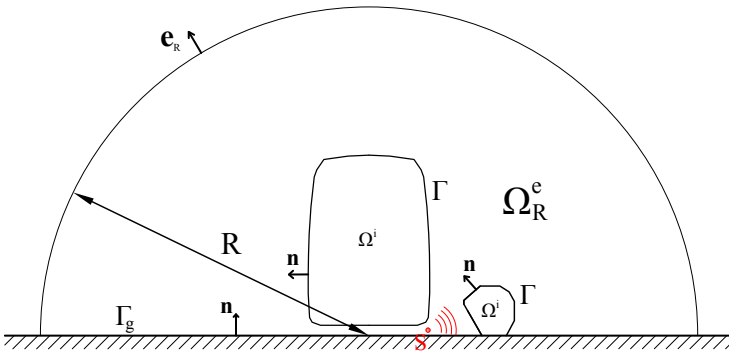

Figure 2.2: Schematic representing the half sphere S_R containing the boundary Γ and definition of the truncated exterior domain $\Omega_R^e = \Omega^e \cap B_R$. The normal vector $\mathbf{n}$ defined on $\Gamma \cup \Gamma_g$ points towards Ω_R^e whereas the normal vector $\mathbf{e}_R$ defined on S_R points outwards Ω_R^e.

Let S_R be the half-sphere of radius R located above the ground Γ_g and assumed sufficiently large that all the scattering surface Γ lies inside S_R (see in figure 2.2). One could point out that in 2D S_R is actually a half-circle but for simplicity we will keep using the term "half-sphere". Let u be a solution of the Helmholtz equation outside S_R which satisfies the radiation condition and is smooth up to S_R. Using separation of variables between the two naturally defined polar coordinates r and θ, u can be written as a series of outgoing cylindrical waves, as follows:

$$u(r,\theta) = \sum_{n=0}^{\infty} \alpha_n \frac{H_n^{(1)}(kr)}{H_n^{(1)}(kR)} \cos(n\theta) \qquad \text{with} \quad \alpha_n = \frac{2}{\pi\, \epsilon_n} \int_0^{\pi} u(R,\theta)\, \cos(n\theta)\, \mathrm{d}\theta$$

with $H_n^{(1)}$ is the Hankel function of the first kind of order n and $\epsilon_n = (2,1,1,1,...)$. Hankel functions of the second kind are ignored because they do not satisfy the radiation condition, and only cosine angular functions are used since here the problem is defined on the half space only with a rigid ground. The normal derivative of u is then given by:

$$\frac{\partial u}{\partial r} = \sum_{n=0}^{\infty} k\alpha_n \frac{H_n^{(1)'}(kr)}{H_n^{(1)}(kR)} \cos(n\theta)$$

where $'$ is the derivative with respect to the argument. One can therefore conclude that u and its normal derivative are related on S_R as follows:

$$\left.\frac{\partial u}{\partial r}\right|_{S_R} = T\big(u|_{S_R}\big) \qquad \text{with} \quad T: \ \sum_{n=0}^{\infty} \alpha_n \cos(n\theta) \mapsto \sum_{n=0}^{\infty} k \frac{H_n^{(1)'}(kR)}{H_n^{(1)}(kR)} \alpha_n \cos(n\theta)$$

T is the so-called Dirichlet-Neumann operator.

2.2.2 Equivalent scattering problem in a bounded domain

Let B_R be the half-ball of radius R (its boundary is the half-sphere S_R) and $\Omega_R^e = \Omega^e \cap B_R$ be the truncated exterior domain (see again in figure 2.2). Now, let us consider the following scattering problem:

$$\begin{cases} -(\nabla^2 + k^2)\, p_R = \delta(S,.) \quad \text{in } \Omega_R^e \\ \dfrac{\partial p_R}{\partial n} + \mathrm{i}k\,\beta\, p_R = 0 \quad \text{on } \Gamma \\ \dfrac{\partial p_R}{\partial n} = 0 \quad \text{on } \Gamma_g \\ \dfrac{\partial p_R}{\partial r} = T(p_R) \quad \text{on } S_R \end{cases} \tag{2.4}$$

One can show that the problems (2.1) and (2.4) are equivalent in the bounded domain B_R, which means that $p|_{B_R} = p_R$ and that p_R can be extended to be equal to p [136, p. 97]. This is basically related to the fact that p and p_R both satisfy the Helmholtz equation and the same boundary conditions on Γ and Γ_g, and they have the same traces and the same normal derivatives on S_R. The boundary condition involving the Dirichlet-Neumann operator therefore acts as a "transparent" boundary condition.

The main difference however between problems (2.1) and (2.4) is that (2.4) is posed on a bounded domain, and therefore there are no issues of convergence at infinity. It is now possible to write down a weak formulation of the problem, basically by multiplying each equation of (2.4) by a sufficiently smooth test function q and integrating over the corresponding domains. Following this process and replacing p_R by p (which is legitimate since they are equal), one can write:

$$(\forall q) \quad \int_{\Omega_R^e} (\nabla^2 + k^2)\, p\, q + q(S) + \int_\Gamma \Big(\frac{\partial p}{\partial n} + \mathrm{i}k\beta\, p\Big)\, q + \int_{\Gamma_g} \frac{\partial p}{\partial n}\, q - \int_{S_R} \Big(\frac{\partial p}{\partial r} - T(p)\Big)\, q = 0 \tag{2.5}$$

Integration by parts of the Laplacian term yields:

$$\int_{\Omega_R^e} \nabla^2 p\, q = -\int_{\Omega_R^e} \nabla p \cdot \nabla q - \int_{\Gamma \cup \Gamma_g} \frac{\partial p}{\partial n}\, q + \int_{S_R} \frac{\partial p}{\partial r}\, q$$

The sign is different in front of the integral on $\Gamma \cup \Gamma_g$ and S_R because the normal vectors are defined differently (see in figure 2.2). Equation (2.5) can therefore be rewritten as:

$$(\forall q) \quad -\int_{\Omega_R^e} \nabla p \cdot \nabla q + k^2 \int_{\Omega_R^e} p\, q + q(S) + \int_\Gamma \mathrm{i}k\beta\, p\, q + \int_{S_R} T(p)\, q = 0 \tag{2.6}$$

Under this form, one can notice that an appropriate space for both the solution p and the test function q is $V = H^1(\Omega_R^e)$. Let us define the bilinear form $\mathcal{A}$ on $V \times V$ and the linear form b on V defined as:

$$\begin{cases} \mathcal{A}(p,q) = \displaystyle\int_{\Omega_R^e} \nabla p \cdot \nabla q - k^2 \int_{\Omega_R^e} p\, q - \int_\Gamma \mathrm{i}k\beta\, p\, q - \int_{S_R} T(p)\, q \\ b(q) = q(S) \end{cases}$$

One can then rewrite the weak formulation (2.6) as follows:

$$\begin{cases} \text{Find } p \in V \text{ such that:} \\ (\forall q \in V) \quad \mathcal{A}(p,q) = b(q) \end{cases}$$

Under this form, one can show that there exists a unique solution $p \in V$ to the problem (2.6) [136]. This formalism could also be used to numerically solve the scattering problem using finite elements, however the boundary element method uses a different approach to numerically solve for the pressure field.

2.3 Integral equations derived from the scattering problem

The idea of the integral equation formalism is to represent the scattered field p^{sc} as a "potential", that is an integral expression of source distributions existing on Γ. Such a representation is ensured by the so-called integral representation theorem [136, p. 189], which is reproduced here.

2.3.1 Single and double layer potentials

2.3.1.1 Definition

Let us first introduce the integral operators that will be used in the rest of this chapter. Given a function p defined on Γ and a point $\mathbf{x}$ in the interior of $\Omega^e \cup \Omega^i$, we define the single layer S and double layer D potentials as follows:

$$\begin{aligned} Sp &: \mathbf{x} \mapsto \int_\Gamma G(\mathbf{x},\mathbf{y})\, p(\mathbf{y})\, \mathrm{d}\Gamma(\mathbf{y}) \\ Dp &: \mathbf{x} \mapsto \int_\Gamma \frac{\partial G}{\partial n_y}(\mathbf{x},\mathbf{y})\, p(\mathbf{y})\, \mathrm{d}\Gamma(\mathbf{y}) \end{aligned}$$

with $\partial/\partial n_y = \mathbf{n}(\mathbf{y}) \cdot \nabla_{\mathbf{y}}$ is the normal derivative with respect to $\mathbf{y}$. One can point out that p is in general scalar valued but using the same definition it could be as well vector-valued. Besides, the argument of the operators S and D should typically be piecewise continuous for the integrals to be well-defined [137].

Although the Green's function is unbounded when $\mathbf{y} = \mathbf{x}$, the integrals are well defined even for $\mathbf{x} \in \Gamma$. Indeed, for a given point $\mathbf{x} \in \Gamma$, defining $\rho = ||\mathbf{y} - \mathbf{x}||$, one has for $\mathbf{y}$ approaching $\mathbf{x}$:

$$G(\mathbf{x},\mathbf{y}) = \frac{\mathrm{i}}{4} J_0(k\rho) - \frac{1}{4} N_0(k\rho) + O(1) = -\frac{1}{2\pi} \log \rho + O(1)$$

where the asymptotic behavior of N_0 the Neumann function of order 0 has been used and since J_0 is bounded at 0. The second term due to the ground has been neglected as well since it is always bounded (except at points belonging to the ground Γ_g and to Γ, at which the two terms in the Green's function are equal and have therefore the same behavior). Therefore, for $\mathbf{x} \in \Gamma$, $G(\mathbf{x},\mathbf{y})$ behaves as $\log \rho$ and is therefore integrable on Γ when multiplied by p since p is piecewise continuous.

Similarly, the kernel involved in the double layer potential is integrable even for $\mathbf{x} \in \Gamma$. Indeed, the gradient of G with respect to $\mathbf{y}$ is given by:

$$\begin{cases} \nabla_{\mathbf{y}} G(\mathbf{x},\mathbf{y}) = -\dfrac{\mathrm{i}k}{4} H_1^{(1)}(k\rho)\,\mathbf{e}_\rho + \mathbf{O}(1) = \dfrac{k}{4} N_1^{(1)}(k\rho)\,\mathbf{e}_\rho + \mathbf{O}(1) = -\dfrac{1}{2\pi\rho}\,\mathbf{e}_\rho + \mathbf{O}(1) \\ \text{with} \quad \mathbf{e}_\rho = \dfrac{\mathbf{y}-\mathbf{x}}{\rho} \end{cases}$$

$\mathbf{e}_\rho$ is the unit vector pointing towards $\mathbf{y}$ from $\mathbf{x}$. The asymptotic behavior of N_1 (Neumann function of order 1) has been used as well. Now, assuming the curve Γ is smooth, the normal is continuous along Γ and therefore one has $\mathbf{n}(\mathbf{y}) = \mathbf{n}(\mathbf{x}) + \mathbf{O}(\rho)$. Besides, the vector $\mathbf{e}_\rho$ tends to the tangent vector $\mathbf{t}(\mathbf{x})$ as $\mathbf{y}$ goes to $\mathbf{x}$ and therefore $\mathbf{e}_\rho = \mathbf{t}(\mathbf{x}) + \mathbf{O}(\rho)$. Since the vectors $\mathbf{n}(\mathbf{x})$ and $\mathbf{t}(\mathbf{x})$ are orthogonal by definition, this implies $\mathbf{n}(\mathbf{y}) \cdot \mathbf{e}_\rho = \mathbf{n}(\mathbf{x}) \cdot \mathbf{t}(\mathbf{x}) + \ O(\rho) = O(\rho)$. Therefore one has:

$$\frac{\partial G}{\partial n_y}(\mathbf{x},\mathbf{y}) = \nabla G_{\mathbf{y}}(\mathbf{x},\mathbf{y}) \cdot \mathbf{n}(\mathbf{y}) = -\frac{1}{2\pi\rho}\,\mathbf{n}(\mathbf{y}) \cdot \mathbf{e}_\rho + \ O(1) = O(1)$$

The kernel $\partial G/\partial n_y$ is therefore bounded, which of course implies it is integrable when multiplied by p (again since p is assumed piecewise continuous).

One can point out that the single and double layer potentials are well-defined as well in 3D since the kernels are integrable. Indeed in 3D both the Green's function and its normal derivative behaves as $1/\rho$ when $\mathbf{y}$ approaches $\mathbf{x}$, which is integrable on a surface in 3D.

The single and double layer potentials are therefore defined as well on Γ. We are now recalling important properties about their behaviors close to Γ.

2.3.1.2 Behavior close to the boundary Γ

The single layer potential Sp is continuous across Γ, but its normal derivative is discontinuous. Indeed, assuming the curve Γ is smooth, one can show that:

$$\begin{cases} \dfrac{\partial (Sp)}{\partial n}\Big|^e = -\dfrac{1}{2}\,p + D^* p \\ \dfrac{\partial (Sp)}{\partial n}\Big|^i = +\dfrac{1}{2}\,p + D^* p \end{cases} \qquad \text{with} \quad D^* p = \int_\Gamma \frac{\partial G}{\partial n_x}(\mathbf{x},\mathbf{y})\,p(\mathbf{y})\,\mathrm{d}\Gamma(\mathbf{y})$$

with $|^e$ and $|^i$ referring to the exterior and interior traces of a function. The operator D^* is the *pseudo-adjoint*[1] of the operator D, in the sense that given two functions p and q defined on Γ, one has:

$$\begin{aligned} \int_\Gamma Dp\,q &= \int_\Gamma \int_\Gamma \nabla_{\mathbf{y}} G(\mathbf{x},\mathbf{y}) \cdot \mathbf{n}(\mathbf{y})\,p(\mathbf{y})\,q(\mathbf{x})\,\mathrm{d}\Gamma(\mathbf{y})\,\mathrm{d}\Gamma(\mathbf{x}) \\ &= \int_\Gamma \int_\Gamma \underbrace{\nabla_{\mathbf{x}} G(\mathbf{y},\mathbf{x})}_{=\nabla_{\mathbf{x}} G(\mathbf{x},\mathbf{y})} \cdot \mathbf{n}(\mathbf{x})\,p(\mathbf{x})\,q(\mathbf{y})\,\mathrm{d}\Gamma(\mathbf{y})\,\mathrm{d}\Gamma(\mathbf{x}) = \int_\Gamma D^* q\,p \end{aligned}$$

[1] D^* is not strictly speaking the adjoint operator of D, since this would require to use an actual scalar product - that is a sesquilinear form involving a conjugation -, which is not what is done here.

where we simply exchanged the two variables $\mathbf{x}$ and $\mathbf{y}$ to go from the first to the second line and where we used equation (2.3). Furthermore, because of the symmetry of the Green's function, one can show that the operator S is *symmetrical* (it is equal to its pseudo-adjoint), in the following sense:

$$\int_\Gamma Sp\, q = \int_\Gamma Sq\, p$$

Also, the operator D^* typically requires a continuous argument in order to be well-defined [137, 138].

On the other hand, Dp is discontinuous across Γ but its normal derivative is continuous if p is $C^{1,\alpha}$ (Hölder differentiable) [138]:

$$\begin{cases} Dp|^e = \dfrac{1}{2}\, p + Dp \\ Dp|^i = -\dfrac{1}{2}\, p + Dp \\ \dfrac{\partial (Dp)}{\partial n}\Big|^e = \dfrac{\partial (Dp)}{\partial n}\Big|^i = Np \end{cases}$$

N can therefore formally be written as:

$$Np(\mathbf{x}) = \int_\Gamma \frac{\partial^2 G}{\partial n_x\, \partial n_y}(\mathbf{x}, \mathbf{y})\, p(\mathbf{y})\, \mathrm{d}\Gamma(\mathbf{y})$$

However, under this form, the integral is not defined since the kernel is $\partial^2 G / \partial n_x \partial n_y$ (referred to as the *hypersingular* kernel) is not integrable on Γ. A more accurate definition for N is the following [136]:

$$Np = -\mathrm{rot}_\Gamma\, S(\mathbf{rot}_\Gamma p) + k^2\, S(p\mathbf{n}) \cdot \mathbf{n} \tag{2.7}$$

where rot_Γ and $\mathbf{rot}_\Gamma$ are tangential differential operators, that is differential operators acting along the boundary Γ. A short introduction to those operators is given in appendix A. This expression is derived by consideration of the velocity field associated with the pressure field given by the double layer potential, and as it is expressed in terms of single layer potentials raises no issues of integrability due to the assumed smoothness of the argument.

In a variational context and in 2D, the expression for the operator N can take an even more practical form. Given a function q defined on Γ, and applying an integration by parts as described in appendix A, one has:

$$\begin{aligned} \int_\Gamma Np\, q &= -\int_\Gamma q\, \mathrm{rot}_\Gamma\, S(\mathbf{rot}_\Gamma p) + \int_\Gamma k^2\, S(p\mathbf{n}) \cdot q\mathbf{n} \\ &= -\int_\Gamma S(\mathbf{rot}_\Gamma p) \cdot \mathbf{rot}_\Gamma q + \int_\Gamma k^2\, S(p\mathbf{n}) \cdot q\mathbf{n} \\ &= -\int_\Gamma S\Big(\frac{\partial p}{\partial t}\Big)\, \frac{\partial q}{\partial t} + \int_\Gamma k^2\, S(p\mathbf{n}) \cdot q\mathbf{n} \end{aligned}$$

where $\partial / \partial t = \mathbf{t} \cdot \nabla$ is the tangential derivative along the curve Γ ($\mathbf{t}$ is the unit tangent vector along Γ). Under this form, one can notice that N is also a symmetrical operator since S is symmetrical.

2.3.2 Integral representation theorem

Now consider a function $\hat{p}$ satisfying the homogeneous Helmholtz equation both in Ω^e and Ω^i as well as the radiation condition:

$$\begin{cases} -(\nabla^2 + k^2)\hat{p} = 0 & \text{in } \Omega^e \\ -(\nabla^2 + k^2)\hat{p} = 0 & \text{in } \Omega^i \\ \quad + \text{radiation condition} \end{cases}$$

It is also assumed that $\hat{p}$ is smooth up to the delimiting boundary Γ, but with possible jumps of its value of its normal derivative across Γ. We define the jumps at the boundary as:

$$\mu = \hat{p}|^i - \hat{p}|^e \qquad \lambda = \frac{\partial \hat{p}}{\partial n}\Big|^i - \frac{\partial \hat{p}}{\partial n}\Big|^e$$

The integral representation theorem states that under those hypotheses, the function $\hat{p}$ is the sum of a single layer and double layer potential. More specifically, one has:

$$\begin{cases} \hat{p} = S\lambda - D\mu \\ \nabla\hat{p} = \nabla S\lambda + \mathbf{rot}\, S(\mathbf{rot}_\Gamma \mu) - k^2\, S(\mu \mathbf{n}) \end{cases} \quad \text{in } \ \Omega^i \cup \Omega^e \tag{2.8}$$

Further one has the following relationships between the interior and exterior traces at the boundary Γ:

$$\begin{cases} \dfrac{1}{2}\left(\hat{p}|^i + \hat{p}|^e\right) = S\lambda - D\mu \\ \dfrac{1}{2}\left(\dfrac{\partial \hat{p}}{\partial n}\Big|^i + \dfrac{\partial \hat{p}}{\partial n}\Big|^e\right) = D^*\lambda - N\mu \end{cases} \quad \text{in } \ \Gamma \tag{2.9}$$

Those last two equations are also known as the *trace relationships*.

This means that a solution of the homogeneous Helmholtz equation can be written as an integral potential. However, the distributions λ and μ are not known a priori. In order to solve for them, one needs to ensure that the boundary condition of a scattering problem is verified, which will impose that the distributions satisfy one or several integral equations. The resolution of these equations can then be used to calculate the field at any point in space using the integral representation formula given in equation (2.8).

One can use this approach to solve the scattering problem (2.1) but the theorem can be applied to the scattered field p^{sc} only since the total field does not satisfy the homogeneous Helmholtz equation. Besides, before applying the theorem one needs to define the represented field both on Ω^e and Ω^i, which means that the scattered field solution of the problem (2.2) must first be extended to Ω^i. This extension is not unique and therefore several different integral equations can be obtained.

Finally, one can point out that these equations are valid even for $k = 0$, which can be helpful in some regularization techniques of the integral equations (see in appendix C for more details).

2.3.3 Kirchhoff-Helmholtz integral theorem and Jean's equation

We first apply the integral representation theorem to show that one can derive the well-known Kirchhoff-Helmholtz integral relationships. To do so, we define $\hat{p}$ to be equal to p^{sc} - the solution of the problem (2.2) - in Ω^e and $-p^{\text{in}}$ in Ω^i. $\hat{p}$ satisfies the hypotheses of the theorem (the source is assumed to lie in Ω^e and therefore the incident field satisfies the homogeneous Helmholtz equation in Ω^i). The distributions λ and μ are here simply given by:

$$\begin{aligned}\lambda &= -\frac{\partial p^{\text{sc}}}{\partial n}\Big|_\Gamma - \frac{\partial p^{\text{in}}}{\partial n}\Big|_\Gamma = -\frac{\partial p}{\partial n}\Big|_\Gamma = \mathrm{i}k\beta\, p_\Gamma \\ \mu &= -p^{\text{sc}}|_\Gamma - p^{\text{in}}|_\Gamma = -p_\Gamma\end{aligned}$$

where p_Γ is the total field on the boundary Γ and the boundary condition of the problem (2.1) has been used. Therefore, at any receiver point $\mathbf{x} \in \Omega^e$, one has:

$$p^{\text{sc}}(\mathbf{x}) = Dp_\Gamma(\mathbf{x}) + S(\mathrm{i}k\beta p_\Gamma)(\mathbf{x}) = \int_\Gamma \Big(\frac{\partial G}{\partial n_y}(\mathbf{x},\mathbf{y}) + \mathrm{i}k\beta(\mathbf{y})\, G(\mathbf{x},\mathbf{y})\Big)\, p_\Gamma(\mathbf{y})\, \mathrm{d}\Gamma(\mathbf{y})$$

There is essentially one unknown here, the pressure field on the boundary p_Γ. Now one can write the integral equations satisfied by p_Γ by applying equation (2.9):

$$\begin{cases} \dfrac{1}{2}\,(p^{\text{sc}}|_\Gamma - p^{\text{in}}|_\Gamma) = Dp_\Gamma + S(\mathrm{i}k\beta p_\Gamma) \\ \dfrac{1}{2}\Big(\dfrac{\partial p^{\text{sc}}}{\partial n}\Big|_\Gamma - \dfrac{\partial p^{\text{in}}}{\partial n}\Big|_\Gamma\Big) = D^*(\mathrm{i}k\beta p_\Gamma) + Np_\Gamma \end{cases}$$

Recalling that $p^{\text{sc}} = p - p^{\text{in}}$ and using once again the boundary condition, those two equations can be rewritten as:

$$\frac{1}{2}\, p_\Gamma - Dp_\Gamma - S(\mathrm{i}k\beta p_\Gamma) = p^{\text{in}}|_\Gamma \tag{2.10}$$

$$-\frac{1}{2}\,\mathrm{i}k\beta p_\Gamma - D^*(\mathrm{i}k\beta p_\Gamma) - Np_\Gamma = \frac{\partial p^{\text{in}}}{\partial n}\Big|_\Gamma \tag{2.11}$$

Those two integral equations are most commonly used to solve the scattering problem (2.1) since the unknown distribution has a clear physical meaning (it is the value of the total pressure field on the boundary Γ). Many other integral equations could be derived but the physical interpretation of the distributions would be different (which is the case in the so-called indirect boundary element method).

It is well-known however that equation (2.10) on its own does not admit a unique solution at the so-called singular frequencies, which are the eigenfrequencies of a corresponding interior problem. A popular approach to circumvent this issue is the Burton and Miller's approach [139], which consists in considering a linear combination of equation (2.10) and (2.11). Given α a real number, one can consider the equation (2.11)+$\mathrm{i}k\alpha$ (2.10):

$$\frac{1}{2}\,\mathrm{i}k(\alpha-\beta)p_\Gamma - D^*(\mathrm{i}k\beta p_\Gamma) - Np_\Gamma - \mathrm{i}k\alpha\, Dp_\Gamma - \mathrm{i}k\alpha\, S(\mathrm{i}k\beta p_\Gamma) = \frac{\partial p^{\text{in}}}{\partial n}\Big|_\Gamma + \mathrm{i}k\alpha\, p^{\text{in}}|_\Gamma$$

α is usually taken to be 1, but any non zero real number ensures uniqueness of the solution of the new equation [139].

Instead of considering a constant coefficient α, yet another approach followed by Hamdi [140] and Jean [120], is to replace α by the normalized admittance β. The equation one obtains is:

$$Np_\Gamma + D^*(\mathrm{i}k\beta p_\Gamma) + \mathrm{i}k\beta\, Dp_\Gamma + \mathrm{i}k\beta\, S(\mathrm{i}k\beta p_\Gamma) = h^{\mathrm{in}} \tag{2.12}$$

with h^{in} defined as in problem (2.2). This equation has the main advantage to be strongly symmetrical. Indeed, if one considers a variational form of this equation by multiplying this equation by an arbitrary function q_Γ and integrating over Γ, one obtains:

$$(\forall q_\Gamma) \qquad \int_\Gamma Np_\Gamma\, q_\Gamma + \int_\Gamma D^*(\mathrm{i}k\beta p_\Gamma)\, q_\Gamma + \int_\Gamma \mathrm{i}k\beta q_\Gamma\, Dp_\Gamma + \int_\Gamma S(\mathrm{i}k\beta p_\Gamma)\, \mathrm{i}k\beta q_\Gamma = \int_\Gamma h^{\mathrm{in}}\, q_\Gamma \tag{2.13}$$

Because of the symmetry and pseudo-adjoint properties of the different operators recalled in section (2.3.1.2), equation (2.13) is symmetrical in p_Γ and q_Γ, which is a significant advantage regarding numerical implementation.

If one assumes that the real part of β is nonzero everywhere, following the same approach as done by Burton and Miller [139], one can show that equation (2.12) has a unique solution for all wavenumbers (see in appendix B). Besides, Jean pointed out that even in the case of an entirely rigid barrier ($\beta = 0$ everywhere on Γ), the results do not seem to undergo the problem of singular frequencies, as long as the mesh is sufficiently fine [120], and therefore the results are accurate even in the case of a rigid barrier.

Classical finite element discretization techniques can be applied to equation (2.13), which is what has been implemented in the software MICADO developed at the CSTB. By representing the fields in terms of their nodal values and shape functions (which are assumed linear in MICADO), equation (2.13) can be rewritten as:

$$\mathbf{q}_\Gamma^T\, [\mathbf{A}]\, \mathbf{p}_\Gamma = \mathbf{q}_\Gamma^T\, \mathbf{h}^{\mathrm{in}}$$

where $\mathbf{p}_\Gamma$, $\mathbf{q}_\Gamma$ and $\mathbf{h}^{\mathrm{in}}$ respectively correspond to the nodal values of the total pressure field p, arbitrary weighting function q and source term h^{in} on the boundary, $[\mathbf{A}]$ is a symmetric matrix which is the discretized equivalent of the different operators involved in equation (2.13) and ^{T} refers to the transpose of a vector. This equation should be true for arbitrary values of $\mathbf{q}_\Gamma$, and therefore this yields:

$$[\mathbf{A}]\, \mathbf{p}_\Gamma = \mathbf{h}^{\mathrm{in}} \tag{2.14}$$

Equation (2.14) is the one implemented and solved in the BEM software MICADO by classical matrix inversion techniques (either by direct inversion or using an iterative solver). Once p_Γ is known one can therefore calculate the pressure field everywhere using the integral representation given in equation (2.8) and the total field is obtained by adding the incident field.

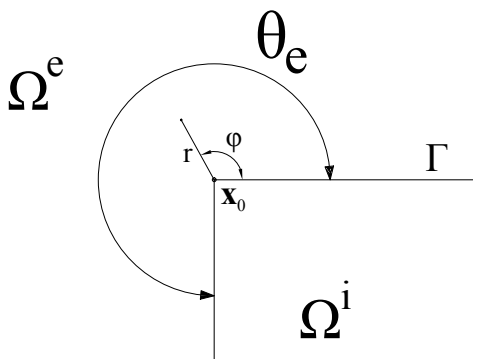

Figure 2.3: Schematic of a non regular point $\mathbf{x}_0$ in the boundary Γ (a "corner"). One can define a local polar coordinate system r and ϕ at the corner, with ϕ ranging between 0 and θ_e.

2.4 Issues for geometries with corners

2.4.1 Angle correction in the Kirchhoff Helmholtz integral equation

All the results derived in section 2.3 assumed that the curve Γ was sufficiently smooth, typically C^1. This is not true in general since a scatterer such as a noise barrier may have corners (in 2D) or edges (in 3D), at which the normal vector may be discontinuous and the Kirchhoff-Helmholtz integral relationships modified. Indeed, at a corner, equation (2.10) should be replaced by:

$$\frac{\theta_e}{2\pi} p_\Gamma - Dp_\Gamma - S(\mathrm{i}k\beta p_\Gamma) = p^{\mathrm{in}}|_\Gamma$$

with θ_e the exterior angle formed by the curve Γ at the current point (see in figure 2.3). θ_e is therefore equal to $1/2$ where the curve is smooth. The normal vector at a corner is undefined and therefore the second relationship (2.11) holds only in a distribution sense. Nevertheless, in several circumstances, the coefficient θ_e will have no influence on the result. For instance, when the equation is regularized by an interior function p^0 as done in appendix C.2, the obtained integral equation holding for p^0 should be modified as follows:

$$\frac{\theta_i}{2\pi} p^0_\Gamma + D^0 p^0_\Gamma - S^0 \frac{\partial p^0}{\partial n}\Big|_\Gamma = 0$$

with θ_i is the interior angle, which satisfies $\theta_e + \theta_i = 2\pi$. Therefore when the two equations are summed together, the angle terms cancel out (as long as $p^0_\Gamma(\mathbf{x}) = p_\Gamma(\mathbf{x})$). Furthermore, as pointed out by Jean [120], if a variational approach is used and if the points at which the curve Γ is not regular - where neither θ_e nor θ_i are equal to $1/2$ - represent a zero-measure set (which would be true in most practical applications since the geometry would contain only a finite number of corners), the functions θ_e and θ_i will be equal to $1/2$ almost everywhere and therefore there will be no influence of the points where the angle is not equal to $1/2$ on the second integration.

2.4.2 Singular behavior of the pressure field close to a corner

The presence of a corner also induces a singularity of the pressure gradient around in its vicinity. This phenomenon is actually relevant in any elliptic boundary value problem. A comprehensive treatment of this phenomenon is given in [141], we here expose some simple results relevant to our case.

Close to a corner point $\mathbf{x}_0$, one can locally describe the pressure field using a local polar coordinate scheme r and ϕ (see in figure 2.3). We would like to describe the behavior of the pressure field as r approaches 0. It is known that the pressure field is continuous in the exterior domain as well as along the boundary Γ, and therefore remains bounded even close to a corner. As a bounded solution of the Helmholtz equation, in 2D, the local pressure field can be described as a series of cylindrical waves:

$$p(r,\phi) - p(\mathbf{x}_0) = \sum_n J_n(kr) \left[\tilde{\alpha}_n \cos(n\phi) + \tilde{\beta}_n \sin(n\phi)\right]$$

where J_n is the Bessel function of order n (Neumann functions have been discarded since they are unbounded as r approaches 0). The indexes n are positive but unknown for now and not necessarily integers. The Bessel functions can be approximated as r goes to zero, for any nonzero positive value of n, as [142]:

$$J_n(kr) \sim \frac{1}{\Gamma(n+1)} \frac{(kr)^n}{2^n} \propto r^n$$

So that the pressure field can be rewritten as:

$$p(r,\phi) - p(\mathbf{x}_0) \sim \sum_n r^n \left[\alpha_n \cos(n\phi) + \beta_n \sin(n\phi)\right] \tag{2.15}$$

Now, assuming for simplicity that the boundary Γ is rigid, the boundary condition on Γ implies that:

$$\frac{\partial p}{\partial \phi}(r, \phi = 0) = 0 \quad \text{and} \quad \frac{\partial p}{\partial \phi}(r, \phi = \theta_e) = 0$$

The first condition implies $\beta_n = 0$ and the second defines the values of n:

$$\sin(n\theta_e) = 0 \quad \Leftrightarrow \quad (\exists m \in \mathbb{N} - \{0\}) \;\; n = m\,\frac{\pi}{\theta_e} \tag{2.16}$$

One can now define the so-called *singularity exponent* $\lambda = \pi/\theta_e$. Since $\theta_e < 2\pi$, λ is always greater than $1/2$. Given equation (2.15) and the values of n given in equation (2.16), one finally has the following asymptotic behavior for the pressure and its gradient:

$$p(r,\phi) - p(\mathbf{x}_0) \propto r^\lambda + O(r^{2\lambda}) \qquad \nabla p(r,\phi) \propto r^{\lambda-1} + O(r^{2\lambda-1})$$

This states that the pressure field essentially behaves as r^λ as r approaches 0. From this statement, one can already conclude that when $\lambda > 1$ (that is when $\theta_e < \pi$), the pressure field is therefore at least C^1 (continuously differentiable), which implies that the pressure field and its

gradient (which is related to the velocity field) are regular even when approaching the corner.

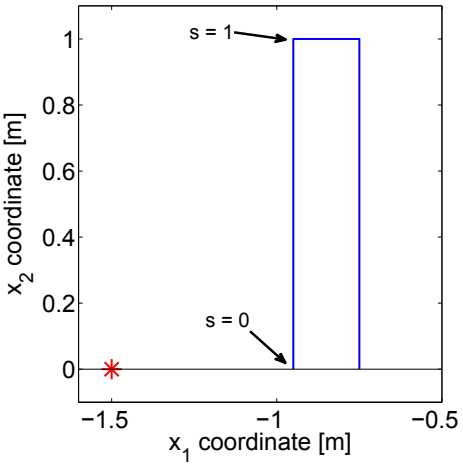

Figure 2.4: Test geometry for the numerical study of corner singularities (dimensions are in meters). The red star is the source location, in blue the scatterer Γ (assumed rigid) and in black the rigid ground. The curvilinear abscissa s is defined to be 0 at the bottom-left corner and increasing following the blue line in the clockwise direction. The corner point which we will focus on is located at $s = 1\,\mathrm{m}$.

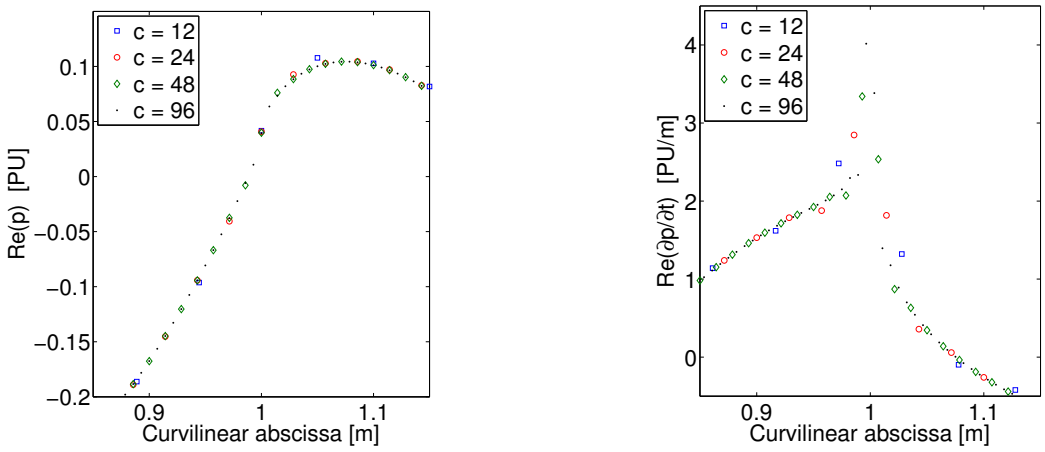

Figure 2.5: Boundary pressure values p_Γ (in arbitrary pressure unit [PU]) and tangential derivatives $\partial p/\partial t$ (in PU/m) as a function of curvilinear abscissa s (in meters) calculated with the BEM (MICADO) for the configuration given in figure 2.4, at 500 Hz, and for different values of the criterion c (number of elements per wavelength). Left plot: pressure values. Right plot: tangential derivatives.

On the other hand, in the case of an exterior angle larger than π, the singularity exponent λ is smaller than 1, which implies that the pressure field is only $C^{0,\lambda}$ in this case. This means that the pressure field is still continuous and bounded (r^λ goes to zero) but the pressure gradient is unbounded although integrable (and even square-integrable) in the neighborhood of the corner as well as along the boundary Γ. When evaluated on the boundary Γ, the normal derivative has a similar behavior as the pressure itself due to the boundary condition, which implies that the tangential derivative only is unbounded.

From a theoretical standpoint, even if the pressure field is continuous but its gradient unbounded and integrable, there are no issues to evaluate the three operators S, D and D^* at the corner since their arguments, as taken in the integral equations given in section 2.3.3, are at

least $C^{0,\lambda}$. On the other hand, there is an issue regarding the operator N which requires the argument to be $C^{1,\alpha}$, a condition which is not met at the corner point. Nevertheless, it is likely that a regularization of the integral equation as described in section C.2 and/or a variational approach as proposed by Jean [120] may circumvent this issue to some extent.

The fact that the solution is less regular close to a corner compared to points where the curve Γ is smooth can induce inaccuracy in some numerical calculations involving the boundary field, since the numerical approximation of the solution is usually piecewise continuous in the case of constant elements, or continuous and piecewise C^1 in the case of linear and quadratic elements, and therefore cannot resolve properly the exact behavior of the solution close to a corner. This will be especially true when evaluating the tangential derivative which is known to be unbounded close to the corner. However, when evaluating the scattered field at a receiver point far from the boundary, it is likely that local inaccuracies close to corners will not have a strong influence on the result.

As an example of this phenomenon, the boundary pressure nodal values are calculated using the software MICADO developed by Jean [120] (which uses linear elements) for a simple test geometry with corners (see in figure 2.4), at 500 Hz. The top left corner corresponds to a curvilinear abscissa of $s = 1\,\mathrm{m}$, which is the point we will focus on. The refinement of the mesh is varied by changing the minimum number of elements per wavelength c (which is one of the input parameters of MICADO). The nodal values of the boundary pressure close to the corner are presented in figure 2.5, left part. Although the value exactly at the corner is essentially the same regardless of the mesh fineness, the convergence of pressure values in the vicinity of the corner is much slower, to the point that there is still a difference of about 3% in the field 1 cm (less than 2% of the wavelength) away from the corner in the solutions calculated with $c = 48$ and $c = 96$. Furthermore, one can notice that with $c = 12$, which is usually assumed to be a relatively fine meshing, the behavior of the solution is not well resolved.

This phenomenon is even more obvious when looking at the tangential derivative, calculated as the difference of successive nodal values divided by the length of the element (see in figure 2.5, right part). As the mesh size decreases, the tangential derivative values right before and after the corner keep increasing, as they should since they theoretically are unbounded. Again, when $c = 12$, the tangential derivative is not well resolved, which means that numerical calculations involving the tangential derivative cannot be accurate close to a corner, unless the mesh is extremely fine. For instance, let us assume one wishes to evaluate the following integral:

$$I = \int_{s=0.5\,\mathrm{m}}^{1\,\mathrm{m}} \left| \frac{\partial p}{\partial t} \right|^2 \mathrm{d}s$$

The result will be strongly dependent on the mesh and therefore cannot be accurate (see in table 2.1). One can notice that with $c = 12$ the error on the integral I is at least 8% (it is probably larger since the value at $c = 96$ is probably not converged).

Despite this local inaccuracy, one should however point out that when evaluating the pressure field far from the boundary - which is the most common application of the BEM -, convergence is achieved a lot faster. For instance, again using MICADO, for a receiver point located at $(x_1 = 3\,\mathrm{m}\,,\, x_2 = 1\,\mathrm{m})$ (following the same coordinate system as given in figure 2.4), the error is

less than 2% with $c = 6$ and drops to less than 1% with $c = 12$. The singular behavior of the pressure field will cause an issue only when one is interested in the fine description of the field close to a corner (this will be the case when evaluating corner node sensitivities, as we will see in chapter 4).

Table 2.1: Numerical evaluation of the integral I as a function of the mesh criterion c and element size h (in cm). The estimated relative error (with respect to the estimated value at $c = 96$) is also shown.

c	h [cm]	I	Error [%]
12	5.7	1.8512	8.4
24	2.8	1.9865	1.7
48	1.4	1.9915	1.5
96	0.7	2.0212	-

2.5 Extension to the 3D sound field with infinite geometry in one dimension

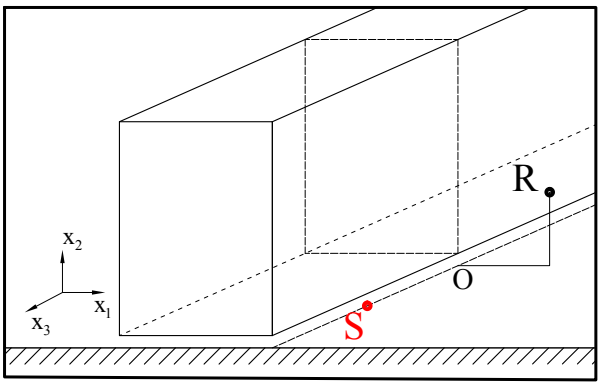

Figure 2.6: Considered geometry for three dimensional calculation of the sound field assuming an infinitely extending geometry in one dimension (2.5 D modeling). The point (R) has coordinates $(x_1, x_2, 0)$ and (S) has coordinates $(0, 0, x_3)$ in the (x_1, x_2, x_3) coordinate system, referenced to the origin (O).

In the previous sections, the diffraction problem in the presence of a noise barrier has been presented in two dimensions, which implicitly assumes on one hand that the geometry is infinitely extended in the dimension perpendicular to the vertical plane containing the source and receiver, and on the other hand that the source is an infinite coherent line source. However, it is possible to calculate the three dimensional field - still assuming an infinite geometry extension - for instance due to a point source which can be offset compared to the vertical plane containing the receiver (see figure 2.6), thanks to a method proposed by Duhamel [28, 143] (this type of approach is referred to as 2.5 D modeling). The result was first derived assuming rigid boundary conditions in [28], but we give here the generalized result in the case of a finite admittance boundary condition [143] described by a generic function of frequency β. Let $p_{2D}(x_1, x_2, k, \gamma)$ be the pressure field in two dimensions (assuming an infinite coherent line source) at a given wavenumber k (which corresponds to frequency $f = kc_0/2\pi$) and with an admittance distribution γ, and $p_{3D}(x_1, x_2, x_3, K, \beta)$ the pressure field in three dimensions at the wavenumber K (which corresponds to frequency $F = Kc_0/2\pi$) and with the corresponding admittance distribution

$\beta(K)$. It turns out that p_{3D} can be expressed as the following Fourier integral [143]:

$$p_{3D}\big(x_1, x_2, x_3, K, \beta(K)\big) = \frac{1}{2\pi}\int_{-\infty}^{\infty} p_{2D}\left(x_1, x_2, \sqrt{K^2-\alpha^2}, \frac{\beta(K)}{\sqrt{1-\alpha^2/K^2}}\right) e^{-\mathrm{i}\alpha x_3}\,\mathrm{d}\alpha \quad (2.17)$$

Using simple symmetry properties of the integrand, one can show that this expression can also be written as:

$$p_{3D}\big(x_1, x_2, x_3, K, \beta(K)\big) = \frac{1}{\pi}\int_{0}^{\infty} p_{2D}\left(x_1, x_2, \sqrt{K^2-\alpha^2}, \frac{\beta(K)}{\sqrt{1-\alpha^2/K^2}}\right) \cos(\alpha x_3)\,\mathrm{d}\alpha \quad (2.18)$$

Equation (2.18) expresses the fact that the 3D sound field can be calculated from a set of 2D sound fields, calculated at different frequencies and at different admittances. As α varies from 0 to K, the frequency at which the 2D calculations are made varies from F to 0. When $\alpha > K$, the wavenumber at which the 2D calculation is made becomes imaginary, which requires specific attention in how to solve the 2D problem. Duhamel nevertheless pointed out that the range of imaginary wavenumbers necessary to achieve good convergence of the integral is small [28, 143]. Jean even states that at a high enough frequency, the imaginary wavenumbers can be simply ignored if great accuracy is not required, such as in the estimation of a broadband A-weighted quantity [144]. In this case the integration is only performed from 0 to K in equation (2.18).

This formalism also allows to calculate the sound field in the case of an infinitely extended but incoherent line source (meaning that the cross-correlation of the source distribution along the line is given by a Dirac delta function, as explained in [28]). The mean-square value of the sound field is independent of x_3 in this case and is given by:

$$p^2_{3D,\text{ inc. line, rms}}\big(x_1, x_2, K, \beta(K)\big) = \frac{1}{\pi}\int_{0}^{\infty} \left|p_{2D}\left(x_1, x_2, \sqrt{K^2-\alpha^2}, \frac{\beta(K)}{\sqrt{1-\alpha^2/K^2}}\right)\right|^2 \mathrm{d}\alpha$$

From the knowledge of a fine 2D spectrum, this approach therefore allows one to consider one or several point sources as well as an infinite incoherent line source, as long as the different sources are all on the same line along the x_3 direction (sources on another line would require another 2D spectrum). Several point sources may be summed incoherently and therefore one can also approximately model a finite length incoherent line source, which might be a more realistic model for a rail track for instance.

This method has been implemented in MICADO as well. Using those different source models, it has been found that depending on which model is used, the predicted attenuation can vary significantly [144]: insertion losses are typically a lot smaller when the spatial incoherence of the sources is considered, which also means that the performance based solely on 2D results is usually overestimated.

2.6 Conclusion

In this chapter, we have briefly introduced the theoretical framework of the integral equation method to solve the exterior acoustic scattering problem. The formalism has been mostly

presented in two dimensions, although most results can be extended to the three dimensions case. We have also presented the equivalent weak formulation of the scattering problem which will be helpful in the derivation of the shape sensitivity expressions (see in chapter 4). The integral equation derived by Jean and implemented in the BEM software MICADO has been presented as well, since this will be the main tool of calculation in the rest of this work, along with some regularization techniques.

The issue of decreased regularity of the solution close to a geometrical singularity (a corner) has been raised as well. Although this does not cause significant inaccuracy in most applications (typically for the calculation of the pressure field in the exterior domain), in a shape optimization context this will induce some extra error in the evaluation of the sensitivity, as we will see in chapter 4.

Finally, the 2.5D approach, which has been briefly presented here and is implemented in MICADO as well, will be used to make some more realistic predictions of noise barrier performances, as we will see in chapter 5 and chapter 6.

Chapter 3

Review of optimization methods and their application to scatterer shape design and inverse scattering

3.1 Introduction

As it has been shown in chapter 1, in a noise barrier application (such as a low height noise barrier close to a tramway), the acoustic treatments and the geometrical features of the different surfaces surrounding the propagation medium - what we referred to as the *boundary* in chapter 2 - will influence the acoustic field and therefore the efficiency of a noise barrier (the amount of noise reduction the device can achieve in a given receiver zone). Because of this dependence, it is possible to change the efficiency by varying the parameters describing the admittance and the shape of the boundary, which includes the noise barrier, which means one can even *optimize* the design of a barrier to improve its performance.

Optimization relies on a prediction method (which calculates the efficiency given a set of parameters), which intrinsically requires some simplification of the situation under consideration in order to be mathematically modeled. This can make the results of such a process questionable when applying it to real life situations. However, an important feature of optimization methods is that they can help identify what parameters influence the efficiency the most, which is valuable information before designing and building a possibly expensive device such as a noise barrier.

Besides, instead of improving the efficiency of a device by changing its shape, one could also wish to *identify* the shape of a boundary - or scattering surface - based on some known typically measured quantity such as the far field diffraction pattern: this is referred to as *inverse scattering*. The same approach can be followed, except that this time the function to minimize will not be an efficiency, but a difference between measured data and predicted data. A similar approach can be followed to identify the *admittance* of a surface, which has been referred to as *admittance eduction*.

First, we will review some general optimization strategies and associated mathematical results. We will then point out a few examples of how these strategies have been applied in the

context of scattering surface optimization, which in turn will allow us to choose an appropriate approach with application to tramway low-height noise barriers.

3.2 General considerations

3.2.1 Form of the considered optimization problem

First, one needs to define a real-valued criterion which characterizes the performance of the device under consideration, which is referred to as the *objective function* e. By convention, this criterion is chosen to be better when it decreases, and therefore we wish to minimize it (if one wants to maximize a criterion, one can simply consider minus this criterion to make it a function to minimize). Typically, in our context we choose a weighted attenuation provided by the barrier, which is a positive quantity typically ranging between 0 and 1, and can be expressed as a function of the acoustic pressure field values $p(R)$ at the different receiver locations.

One criterion only is used, and therefore we are considering a mono-objective optimization. In many cases however, several independent criteria are indeed relevant to describe the performance of a device, for instance noise reduction and cost, as done by Baulac [4] and Leissing et al. [145]. Indeed cost is always an issue when building a noise reduction device but unfortunately it can be difficult to model. Specific methods exist to deal with a multi-objective optimization, but they will not be detailed here. One can for instance consider a weighted sum of the different criteria, so that the problem reduces to a classical mono-objective optimization problem.

Moreover, we consider a set of generic, typically real-valued parameters $x_1, ..., x_N$ - gathered in the vector $\mathbf{x} = (x_1, ..., x_N)$ - which influence the objective function. For our application, those parameters can be categorized in two types:

- **admittance parameters**: geometrical and physical inputs of the admittance models describing the admittance (a few examples have been given in section 1.6)
- **shape parameters**: variables describing the shape of the scattering surface

Shape parameters can be of various types, for instance it could directly be the coordinates of a set of nodes which control the shape - referred to as *control nodes* - or any type of variable describing a geometrical feature, such as well depths or tilting angles (as done by Baulac et al. to describe multiple-edge barriers [128]).

The parameters only influence the objective function indirectly (or implicitly), since the weighted attenuation simply depends on the pressure field p, which we will call the *state*, following Allaire [146]. The state, as the solution of a boundary value problem - in which the admittance and boundary shape intervene in the boundary condition - depends on the parameters, but again in an implicit fashion. One can write the boundary value problem in the general form $L[p] = b$ with L an operator (linear in our context) and b a generic right hand side related to the source term (this equation would be for instance equation (2.12) introduced in chapter 2). In a sound diffraction problem, both the operator and the right hand side can depend on the boundary condition and therefore on the parameters $\mathbf{x}$. The boundary value problem can

be hence written as:

$$L(\mathbf{x})[p] = b(\mathbf{x}) \tag{3.1}$$

Equation (3.1) is referred to as the *state equation*. As the solution of equation (3.1), the state p is a function of the parameters $\mathbf{x}$, since indeed one can formally write $p(\mathbf{x}) = L(\mathbf{x})^{-1}\, b(\mathbf{x})$. The inverse of the operator is usually not known explicitly, and therefore the function $p(\mathbf{x})$ is an implicit function. The objective function, which can depend on the parameters $\mathbf{x}$ explicitly as well as the state, can hence be written as $e\big(\mathbf{x}, p(\mathbf{x})\big)$.

3.2.1.1 Constraints

The goal is hence to minimize the function e by modifying the values of the parameters $\mathbf{x}$. However, parameters usually cannot take arbitrary values but instead satisfy a set of *constraints*, for instance due to the geometrical feasibility of the shape of the scatterer or so that the parameters stay within a range of physically achievable values. For instance, in a low-height noise barrier application, the height of the barrier will be limited typically to 1 m, which means that all the vertical coordinate above the ground of all nodes should be less than 1 m. In general, constraints can take complicated forms, but first one can assume so-called *bound* constraints. Given two vectors $\mathbf{l}$ and $\mathbf{u}$ respectively of lower and upper bounds for the parameters, the bound constraints can be written as:

$$\mathbf{l} \leqslant \mathbf{x} \leqslant \mathbf{u} \tag{3.2}$$

with the inequalities applying element-wise.

In a shape optimization application, other geometrical constraints can arise, related to the mathematical feasibility of the surface - or the curve in 2D - describing the boundary. Let us assume for simplicity the 2D case (which will be the main focus of this work). The curve - or the set of curves when dealing with several scatterers - describing the boundary should also be *injective*, meaning in particular that the boundary should not present any loops or should not fold over itself, or that the disjoint parts of the boundary should not intersect. The easiest way to deal with this constraint is to ensure that the representation of the shape (that is the choice of parameters describing the shape) will always meet such a requirement. This can be done with bound constraints in some cases, for instance when part of the geometry is described as a set of wells, as done in [128].

However, if one wishes to describe the shape with control nodes (assuming for instance linear interpolation between the nodes to generate the whole curve), preventing the presence of loops is not as straightforward. A method to deal with this issue is presented in appendix D.1.

Finally, the optimization problem under consideration can be summarized as follows:

$$\min_{\mathbf{x}} e\big(\mathbf{x}, p(\mathbf{x})\big) \qquad \text{s.t.} \quad \begin{cases} \mathbf{l} \leqslant \mathbf{x} \leqslant \mathbf{u} \\ \Gamma(\mathbf{x}) \text{ is injective} \end{cases} \tag{3.3}$$

where $\Gamma(\mathbf{x})$ is the boundary shape corresponding to the shape parameters of $\mathbf{x}$. This problem falls into the general category of constrained nonlinear optimization problems.

3.2.2 Continuous vs. discrete representation of the search space

Under the form given in (3.3), the optimization problem is not complete yet: one still needs to define the *search space*, that is the set which the parameters $\mathbf{x}$ belong to. This basically raises the question of how to represent the parameters. This question is extremely important since it strongly determines which type of optimization method can be used.

One can first assume that the parameters can vary continuously, and therefore the search space can be here identified to $\mathbb{R}^N$. Under the assumption of sufficient smoothness of the state with respect to $\mathbf{x}$ and of the objective function with respect to the state, one can naturally introduce the notion of *sensitivity* (or derivative, or gradient) which quantifies how much the state and the objective function are changed when a parameter is varied, which is valuable information in an optimization context. Sensitivity-based optimization methods, as detailed in [147], are particularly well-suited in this case, although one could also use derivative-free optimization methods such as the Nelder-Mead method [148]. The main drawback of this kind of approach is that it can only find a local solution of the problem (3.3), since only a neighborhood of the initial guess is searched. Considering several randomly chosen starting points can nevertheless help in exploring the domain in a more "global" way.

However, one could follow a different approach and allow each parameter to take only a set of discrete values, for instance corresponding to a set of existing commercially available materials or products, or by approximating a continuous search space with a discretization. In this case, one cannot define the derivative, and therefore the optimization will have to do without this information. Evolutionary optimization methods, such as genetic algorithms, are particularly well-suited for this purpose, although they do not necessarily require a discrete search space. These methods intrinsically allow a more global search of the set of possible values, but because one cannot use the sensitivity information any more, the number of evaluations required to solve the problem (3.3) would be much larger than in the previous case, particularly if there is a large number of parameters [146].

For our application, it has been chosen to use a continuous search space for the purpose of being as general as possible. Indeed, admittance parameters - which usually are geometrical characteristics of a device or physical properties properties of a material - as well as shape parameters - would they be control node coordinates or geometrical features - are more naturally described with continuous parameters. Besides, as we will see, the sensitivity information can be obtained efficiently in this context, and therefore it makes sense to take advantage of the speed of gradient-based optimization methods, which intrinsically require a continuous representation of the parameters.

3.2.3 Optimality conditions for gradient-based optimization

Assuming a continuous search space - which means $\mathbf{x} \in \mathbb{R}^N$ - and a sufficiently smooth objective function and state equation, one can characterize a solution $\mathbf{x}^*$ of the problem (3.3) (again meaning here a local solution) by some conditions that should be satisfied at this point. First, if there was no constraint, the objective function should be *stationary* at a local solution, which means any variation of the parameters away from the solution should not modify the value of e

to the first order. This implies:

$$(\forall i \in [1:N]) \qquad \frac{\mathrm{d}e}{\mathrm{d}x_i}\big(\mathbf{x}^*, p(\mathbf{x}^*)\big) = 0$$

with $\mathrm{d}/\mathrm{d}x_i$ is here the *total* derivative - as opposed to $\partial/\partial x_i$ which is the partial derivative, meaning the derivative taken while assuming other arguments are kept constant.

However, in general, in the presence of constraints, the stationary condition should be modified to the so-called Karush-Kuhn-Tucker (KKT) conditions [147] which require the introduction of a set of Lagrange multipliers. The KKT conditions are however not sufficient to guarantee a local minimum: since they are only based on first order derivatives, those conditions would be valid both at a local maximum and a local minimum. Introduction of second order conditions, mostly related to the positiveness of the Hessian, can help characterize a local minimum as opposed to a maximum [147].

3.2.4 A few comments regarding practical applications

However, one should point out that those necessary optimality conditions are usually not directly solved in practice. Instead, iterative approaches are followed, starting from an initial guess of the solution $\mathbf{x}^0$ and recursively proceeding as follows: from the current estimate $\mathbf{x}^k$, build a new estimation $\mathbf{x}^{k+1}$ based on the available information at $\mathbf{x}^k$, typically the gradient or the Hessian, as we will see in the next section. One can also point out that evolutionary optimization methods do follow an iterative process as well, but at every step a whole "population" of points are considered, instead of just one. From this general statement it makes sense that evolutionary methods fundamentally need many more function evaluations than gradient-based methods. Therefore, when a function evaluation is expensive - as in the case here, since one has to solve several diffraction problems in order to calculate the attenuation provided by the barrier - evolutionary methods will require a much larger computation time. On the other hand, these methods will be well-suited in cases where function evaluations are fast but gradient calculations are time consuming.

3.3 Overview of some common optimization algorithms

We briefly review here some common optimization algorithms that can be used to tackle optimization problems such as the one under consideration.

3.3.1 Derivative free optimization methods

A popular continuous search space method is the so-called Nelder-Mead local search [148]. Although this algorithm is a continuous search space method, it does not require the knowledge of the gradient. Instead, at each iteration, one considers a set of points - which makes this method somewhat similar to an evolutionary optimization method - which forms a "simplex", and from the knowledge of the objective function value at each point, the algorithm replaces

the "worst" point with a new one by deforming the simplex (using a contraction, expansion or reflection of the worst point with respect to the center of the other points).

Due to its simplicity this algorithm has been widely used, for instance by Baulac et al. [128] in the context of multiple edge highway noise barriers, in which the authors coupled a genetic algorithm to a Nelder-Mead local search in order to improve its efficiency.

3.3.2 Sensitivity-based (gradient-based) methods

As stated in section 3.2, the sensitivity of the objective function with respect to changes of each parameter at a given point is a valuable piece of information in an optimization algorithm. This information can then be exploited in specific methods to reach a local solution in an efficient manner. However, for the derivative to make sense, one needs the objective function to be smooth enough, although in most physics-based calculations and for simple enough objective functions, this assumption is usually satisfied. Again one can point out that, although sensitivity-based methods are limited to local minimum finding, on can add some randomness in the search by considering several random starting points in order to make the search more global.

In this section we are assuming the general framework of an iterative method as briefly explained in section 3.2.4. Basically, given an estimate $\mathbf{x}^k$ of the solution, we assumed the state $p(\mathbf{x}^k)$ is known as well as the objective function value $e\big(\mathbf{x}^k, p(\mathbf{x}^k)\big)$, and we wish to build a new estimate $\mathbf{x}^{k+1}$, based on the gradient at $\mathbf{x}^k$. We first explain how to calculate this gradient in a general manner. For simplicity, the current estimate, associated state and objective function value will be simply written here as $\mathbf{x}$, p and $e\big(\mathbf{x}, p\big)$.

3.3.2.1 Gradient calculation

Given the form of the objective function $e(\mathbf{x}, p)$, for any value $i \in [1 : N]$, the sensitivity of e with respect to x_i has two terms, one related to the explicit dependence on the parameters x_i, and one related to the implicit dependence of the state p on x_i, which can be formally written as:

$$\frac{\mathrm{d}e}{\mathrm{d}x_i} = \frac{\partial e}{\partial x_i} + \frac{\partial e}{\partial p} \cdot \frac{\mathrm{d}p}{\mathrm{d}x_i} \tag{3.4}$$

where $\partial e/\partial p$ should be understood as a differential form acting on pressure fields and $\mathrm{d}p/\mathrm{d}x_i$ is another field characterizing how much the pressure field depends on the parameter x_i.

The differential $\partial e/\partial p$ depends on the form of the objective function but will be rather simple for our application (see in section 4.1.2). In this section we will simply assume that this derivative is explicitly known. Now consider the remaining term $\mathrm{d}p/\mathrm{d}x_i$. As it has been pointed out in section 3.2.1, the function $p(\mathbf{x})$ is implicit since p is the solution of the state equation (3.1) in which the parameters $\mathbf{x}$ intervene. The derivative is therefore not as straightforward to express. We now present two possible approaches to calculate the derivative $\mathrm{d}e/\mathrm{d}x_i$, namely implicit differentiation and the adjoint state approach.

Implicit differentiation As the state is defined as the solution of an equation such as equation (2.12), one could attempt to define as well the field $\mathrm{d}p/\mathrm{d}x_i$ to be the solution of another equation.

This can be achieved by considering the derivative with respect to x_i of the state equation, which formally yields:

$$\frac{\mathrm{d}L}{\mathrm{d}x_i}(\mathbf{x})\,[p(\mathbf{x})] + L(\mathbf{x})\left[\frac{\mathrm{d}p}{\mathrm{d}x_i}(\mathbf{x})\right] = \frac{\mathrm{d}b}{\mathrm{d}x_i}(\mathbf{x})$$

This can be rearranged as follows:

$$L(\mathbf{x})\left[\frac{\mathrm{d}p}{\mathrm{d}x_i}(\mathbf{x})\right] = \tilde{b}(\mathbf{x}) \qquad \text{with} \quad \tilde{b}(\mathbf{x}) = \frac{\mathrm{d}b}{\mathrm{d}x_i}(\mathbf{x}) - \frac{\mathrm{d}L}{\mathrm{d}x_i}(\mathbf{x})\,[p(\mathbf{x})] \tag{3.5}$$

Assuming one can express the derivatives of the operator L and right-hand side b, since p is already known, the right-hand side of equation (3.5) is explicitly known as well, and therefore equation (3.5) has the same form as the state equation, with a different right-hand side $\tilde{b}$ and the unknown being the field $\mathrm{d}p/\mathrm{d}x_i$. This equation can be solved using the same method as the state equation, and therefore one can obtain the derivative field $\mathrm{d}p/\mathrm{d}x_i$, and recalling equation (3.4) the sensitivity of the objective function $\mathrm{d}e/\mathrm{d}x_i$. This method is referred to as *implicit differentiation*.

The main drawback of this approach is that for each parameter x_i, $i \in [1 : N]$, in order to obtain the term $\mathrm{d}p/\mathrm{d}x_i$, one needs to solve equation (3.5), which in our context means to solve a scattering problem, and can therefore be rather expensive regarding computation time. The whole gradient calculation therefore requires one to solve a diffraction problem N times (actually $N+1$ times since one problem had to be solved first to calculate the state p). If there are a large number of parameters, this approach would yield an excessive computation time.

Adjoint state approach Another approach consists of considering the state p as a different variable and treating the state equation as a constraint relating $\mathbf{x}$ and p. We here follow the development of Allaire [146], although the approach given here is essentially formal, without any mathematical details regarding the existence and the appropriate spaces of the different terms. A slightly more rigorous development specific to our application will be given in chapter 4.

Following a classical approach in constrained optimization, one can then introduce an associated Lagrangian, defined for arbitrary fields $\hat{p}$ and $\hat{q}$, which can be taken as:

$$\mathcal{L}(\mathbf{x}, \hat{p}, \hat{q}) = e(\mathbf{x}, \hat{p}) + c(\mathbf{x}, \hat{p}, \hat{q}) \qquad \text{with} \quad c(\mathbf{x}, \hat{p}, \hat{q}) = \langle L(\mathbf{x})[\hat{p}] - b(\mathbf{x}), \hat{q} \rangle$$

where $\langle ., . \rangle$ is a product defined between two pressure fields (it could be for instance a scalar product, but in the following derivation this is a not a requirement). The function c has been chosen to vanish when evaluated at the solution of the state equation $p(\mathbf{x})$, and this for any field $\hat{q}$:

$$(\forall \hat{q}) \qquad c\big(\mathbf{x}, p(\mathbf{x}), \hat{q}\big) = 0$$

This allows one to rewrite the objective function as:

$$(\forall \hat{q}) \qquad e\big(\mathbf{x}, p(\mathbf{x})\big) = \mathcal{L}\big(\mathbf{x}, p(\mathbf{x}), \hat{q}\big)$$

Now recalling equation (3.4), replacing the objective function with the Lagrangian yields:

$$(\forall \hat{q}) \qquad \frac{\mathrm{d}e}{\mathrm{d}x_i}\big(\mathbf{x}, p(\mathbf{x})\big) = \frac{\partial \mathcal{L}}{\partial x_i}\big(\mathbf{x}, p(\mathbf{x}), \hat{q}\big) + \frac{\partial \mathcal{L}}{\partial p}\big(\mathbf{x}, p(\mathbf{x}), \hat{q})\big) \cdot \frac{\mathrm{d}p}{\mathrm{d}x_i}(\mathbf{x}) \tag{3.6}$$

Now, since this equation (3.6) holds for any field $\hat{q}$, one can choose a constraint to be satisfied by this field to simplify the expression. Let us define the *adjoint state* $q(\mathbf{x})$ as the solution of the following equation:

$$\frac{\partial \mathcal{L}}{\partial p}\big(\mathbf{x}, p(\mathbf{x}), q(\mathbf{x})\big) = 0 \tag{3.7}$$

Substituting $\hat{q} = q(\mathbf{x})$ in equation (3.6) hence yields:

$$\frac{\mathrm{d}e}{\mathrm{d}x_i}\big(\mathbf{x}, p(\mathbf{x})\big) = \frac{\partial \mathcal{L}}{\partial x_i}\big(\mathbf{x}, p(\mathbf{x}), q(\mathbf{x})\big)$$

We therefore got rid of the implicit dependence term $\mathrm{d}p/\mathrm{d}x_i$ and expressed the total derivative as a partial derivative. Recalling the form of e and c, one can then write:

$$\begin{aligned}
\frac{\mathrm{d}e}{\mathrm{d}x_i}\big(\mathbf{x}, p(\mathbf{x})\big) =& \frac{\partial e}{\partial x_i}\big(\mathbf{x}, p(\mathbf{x})\big) + \frac{\partial c}{\partial x_i}\big(\mathbf{x}, p(\mathbf{x}), q(\mathbf{x})\big) \\
=& \frac{\partial e}{\partial x_i}\big(\mathbf{x}, p(\mathbf{x})\big) + \Big\langle \frac{\mathrm{d}L}{\mathrm{d}x_i}(\mathbf{x})\big[p(\mathbf{x})\big] - \frac{\mathrm{d}b}{\mathrm{d}x_i}(\mathbf{x})\,,\, q(\mathbf{x}) \Big\rangle \\
=& \frac{\partial e}{\partial x_i}\big(\mathbf{x}, p(\mathbf{x})\big) - \langle \tilde{b}(\mathbf{x})\,,\, q(\mathbf{x}) \rangle
\end{aligned} \tag{3.8}$$

with $\tilde{b}$ defined as in the previous paragraph. Again, all the terms appearing in this last equation are explicitly known, once the state and adjoint state are calculated.

Finally, the adjoint state equation (3.7) can be further written out. First one can define $L(\mathbf{x})^\dagger$ the pseudo-adjoint operator of $L(\mathbf{x})$, which by definition satisfies the property:

$$(\forall \hat{p}, \hat{q}) \;\; \langle L(\mathbf{x})[\hat{p}], \hat{q} \rangle = \langle L(\mathbf{x})^\dagger[\hat{q}], \hat{p} \rangle$$

This allows one to calculate explicitly the term $\partial c/\partial p$:

$$\frac{\partial c}{\partial p}\big(\mathbf{x}, \hat{p}, \hat{q}\big) = \frac{\partial}{\partial p}\langle L(\mathbf{x})[\hat{p}], \hat{q} \rangle = \frac{\partial}{\partial p}\langle L(\mathbf{x})^\dagger[\hat{q}], \hat{p} \rangle = L(\mathbf{x})^\dagger[\hat{q}]$$

The adjoint state equation hence becomes:

$$L(\mathbf{x})^\dagger[q(\mathbf{x})] = -\frac{\partial e}{\partial p}\big(\mathbf{x}, p(\mathbf{x})\big) \tag{3.9}$$

Basically the adjoint state satisfies an equation involving the pseudo-adjoint of the operator involved in the state equation and a different right-hand side, related to the form of the objective function. In case of acoustic scattering, it turns out that the operator L is symmetrical, which means $L^\dagger = L$, and therefore the adjoint state equation is another acoustic scattering problem to solve [149, 150].

Basically, to calculate the sensitivity of e with respect to each parameter x_i, one needs to

solve the state equation (3.1) and the adjoint state equation (3.9) to calculate the state and adjoint state $p(\mathbf{x})$ and $q(\mathbf{x})$, and then apply equation (3.8). The main advantage of the adjoint state approach, as opposed to the implicit differentiation method, is that once the state and the adjoint state are known, calculation of the sensitivity with respect to each parameter x_i is explicit, and usually represents a negligible computation time. This method is therefore well-suited to gradient-based optimization algorithms with a large number of variables.

3.3.2.2 Line search methods

We have described in section 3.3.2.1 two approaches to calculate the gradient of e for a given set of parameters $\mathbf{x}$. Recalling the iterative framework of gradient-based methods exposed in section 3.2.4, we are now able to specify how a new iterate $\mathbf{x}^{k+1}$ can be generated from the current estimate $\mathbf{x}^k$, based on the gradient. Following Nocedal [147], we define $e^k = e\big(\mathbf{x}^k, p(\mathbf{x}^k)\big)$ as the current objective function value and $\mathbf{g}^k = \nabla e\big(\mathbf{x}^k, p(\mathbf{x}^k)\big)$ the current gradient vector.

One first approach is to search the new iterate along a given direction - or *line* - from the current iterate, hence the name *line search* method. The general expression for the new iterate is in this case:

$$\mathbf{x}^{k+1} = \mathbf{x}^k + \alpha^k \, \mathbf{u}^k$$

where $\mathbf{u}^k$ is the search direction, which is a vector in $\mathbb{R}^N$, and α^k a positive step-size.

In the *steepest descent* method, the search direction is chosen to be the opposite of the gradient vector $\mathbf{u}^k = -\mathbf{g}^k$. Indeed, in this case one can theoretically ensure that for a small enough step-size, the value of e at the new iterate e^{k+1} will be smaller than e^k. The value of the step-size can be fixed a priori, or it can be found iteratively to ensure a sufficient decrease of the objective function (as specified for instance by the Armijo conditions [147]). A simple way to find an appropriate value of the step-size is the so-called backtracking line search approach [147], which consists of choosing a rather large step-size and decrease it iteratively until the condition is met.

In Newton's method, the search direction is given by $\mathbf{u}^k = -\left[H^k\right]^{-1} \mathbf{g}^k$, with H^k the Hessian matrix at the current estimate. This direction is referred to as the Newton direction. It comes from locally approximating the function by a quadratic model and minimizing it, and technically requires the Hessian to be positive definite to be properly defined. The convergence rate of Newton's method is much faster than that of the steepest descent method. However calculating the Hessian in this context can be rather cumbersome, even with an adjoint state approach. Besides, a unit step-size $\alpha_k = 1$ is usually assumed in Newton's method.

In quasi-Newton methods, one uses an approximation of the Hessian B^k instead of the true one, which is updated after each iteration based on the current and previous values of the gradients and iterates. The search direction is then $\mathbf{u}^k = -\left[B^k\right]^{-1} \mathbf{g}^k$. The update is chosen to be computationally effective, for instance by adding a low-rank matrix. A popular update is the so-called Broyden-Fletcher-Goldfarb-Shanno (BFGS) formula, which guarantees symmetry and positiveness of the approximate Hessian under some conditions [147]. One should point out that this method still requires a good approximation of the initial matrix B^0, which might not be easy to achieve. A possibility is to use finite differences, although this can be rather time

consuming (N evaluations of the gradient) and inaccurate.

Bounds constraints and projection The different approaches explained in this section are technically meant to be used in an unconstrained optimization context. However, they can be adapted rather easily in the case of bounds constraints, which is one type of constraints we have considered in problem (3.3). Indeed, even if the current iterate $\mathbf{x}^k$ satisfies the constraints, there is no guarantee the new iterate will. A possibility is to project the new iterate in the feasible domain, as done by Allaire [146]. Such a projection operator $\mathbb{P}$ is difficult to characterize in general, but has a simple expression in the case of bounds constraints:

$$\mathbb{P}(\mathbf{x}) = \min\big(\max(\mathbf{x}, \mathbf{l})\,,\, \mathbf{u}\big)$$

where the min and max values are taken element per element. The new iterate that satisfies the bounds constraints can then be written as:

$$\mathbf{x}^{k+1} = \mathbb{P}\big(\mathbf{x}^k + \alpha^k\,\mathbf{u}^k\big)$$

3.3.2.3 Examples of general methods: the Sequential Quadratic Programming (SQP) and the interior-point algorithm

The methods described in the previous sections have been mostly developed to solve unconstrained problems. They are hence not appropriate when dealing with complicated constrained problems, although they can be used as building blocks for more advanced methods. Two important methods which are able to handle most nonlinear constrained optimization problems are the Sequential Quadratic Programming (SQP) method and the interior point algorithm [147]. The SQP basically consists of locally approximating the objective function with a quadratic model and linearly approximating the constraints. This generates the so-called SQP subproblem, which can be solved for instance using a line search approach.

In the presence of inequality constraints only, the interior-point algorithm consists in a sequence of unconstrained minimizations of a perturbed function equal to the objective function plus a logarithmic barrier term related to the constraints and depending on a decreasing parameter. Although the first minimizer usually does not satisfy the constraints, the sequence usually converges to a solution that strictly satisfies them (it hence lies in the *interior* of the feasible domain).

Being among the most general gradient-based algorithms to solve nonlinear optimization problems, those methods have been widely used, although their implementation does rely on the different algorithms previously introduced in this section. They are for instance available as part of the Optimization Toolbox of the Matlab software [151].

3.3.3 Global search methods

We now briefly introduce the basic idea of a few global search methods, which are fundamentally different than sensitivity-based methods. First, evolutionary methods are presented. One can recall that those methods typically use a discrete search space, as stated in section 3.2.2, which

in the case of scattering surface admittance and shape optimization would require one to define a finite set of feasible values for each parameter. They however intrinsically allow a global search of the feasible set, as opposed to the local search provided by gradient-based methods.

Those methods are iterative, as the sensitivity-based methods are, but at each iteration a whole set - the *population* - of points - the *individuals* - in the search space are considered. Each iteration step is referred to as a *generation*. The process basically follows the principles of evolution introduced by Darwin at the end of the 19^{th} century: natural selection of individuals well-adapted to their environment and renewal of genetic information by probabilistic processes.

We now introduce the framework typically followed by an evolutionary method, as explained in [146]. The population is initialized, typically by uniform random selection in the feasible set. Each individual is then evaluated, which means the objective function is calculated for each individual. Based on their performance, a part of the population (the most "well-adapted") is selected. Mutation and crossover probabilistic operators are then applied to the selected individuals to generate new individuals - the *children* - which are evaluated as well. From the children and the parents, a new population is selected (this selection can be deterministic or probabilistic), both from the parents and the children. The algorithm is then repeated until convergence.

Different evolutionary methods exist - for instance genetic algorithms or evolutionary strategies -, which mostly differ in the way the mutation, crossover and selection operators are defined. We refer to the abundant literature on the topic, for instance the book by Eiben and Smith [152].

One can also mention the *simulated annealing* method, which is technically not evolutionary, but is however based on a random approach to efficiently explore the search space (controlled by a so-called temperature history), inspired from the physical process occurring during the cooling of a metal. At each iteration, a set of points is randomly generated in the neighborhood of the current iterate. Then the new iterate is chosen using a probabilistic selection, based on performance and a Boltzmann-type probability factor controlled by the temperature, which allows one to retain a point with worse performance as the new iterate. The idea of such a process is to prevent the algorithm from being "stuck" close to a local minimum, and therefore the chance to find a global solution is much higher.

3.3.4 General comments on the utility of global minimum finding

It is really the randomness introduced in both methods - either in the mutation/crossover/selection operators for evolutionary methods, and probabilistic acceptance of the new iterate in the simulated annealing - that allows them to globally search the feasible set. However, the possibility of reaching the actual global optimum may depend significantly on the problem under consideration as well as the choice of the parameters involved in the algorithm (number of selected individuals, population size, probability of mutation, convergence criterion, temperature history, etc...), and there is therefore no guarantee the global minimum will be found. Besides, one could add that, since the objective function - in our case for instance a weighted attenuation due to the low height noise barrier - is calculated under many simplifying assumptions due to the modeling of the physical problem, one could question the interest of finding "the" global solution of the

problem, which would truly be optimal in one specific context (for a noise barrier this could refer to source position, spectrum, receiver positions, surrounding geometrical features, etc...). One instead could seek an *optimized* solution - a solution with a *better* performance than the one we started with - as opposed to an *optimal* solution, which is precisely what local search methods achieve. Indeed it is likely that an optimized solution would stay optimized in a slightly different context (meaning with a *better* performance than obvious or simple solutions), whereas an optimal solution may not stay optimal (it might not be the *best* solution any more). This is another reason why using local gradient-based optimization methods seem quite appropriate for our application.

3.4 A review of shape and admittance optimization applications in acoustic scattering

The methodology introduced in this chapter has been extensively used in the past few decades for many different applications, mostly divided in two categories: design optimization of a given device (such as a cantilever beam, an airfoil, a noise barrier, an acoustic liner, etc) and identification of scatterers and acoustic properties of surface treatments based on measured data, which has been mostly referred to *inverse scattering* in the case of shape identification or *admittance eduction* in the case of admittance identification. However, due to its obvious industrial applications, one should recall that the field of optimal design has been developed and applied in many areas other than acoustic scattering. A few examples of those applications include reduction of heat conduction [153], sensitivity analysis [154] and optimized design and feature positioning of elastic solids [146, 155–158], wing drag optimization [159] or optimization of truss structures [160]. There is an extremely abundant literature on the topic, which is why we will mostly focus on applications related to acoustic scattering.

3.4.1 Admittance eduction

Admittance eduction refers to any application in which one wishes to identify *in situ* the acoustic characteristics - the admittance - of a treatment already implemented in a given context, from the knowledge of another quantity, such as the pressure value at a set of receivers. Such an identification can be achieved by minimizing the difference between predicted data - based on a trial set of parameter values - and measured data, and therefore the different methods introduced in the previous section can be used in this context.

Admittance eduction has been applied for instance to identify the impedance of the surface treatments in a room using the BEM and a SQP approach [161], mostly in the low frequency range (due to the computational load of the BEM). Besides, there has been several studies on duct liner admittance eduction, mostly in the presence of flow, with obvious application to aircraft engine noise control. Several researchers at NASA Langley [162–164] tackled this problem using a finite element method for prediction of the sound field in the duct, with or without flow. Of course, the frequency range in which one can educt the admittance is strongly dependent on the numerical method used to predict the sound field and the associated computational cost.

3.4.2 Optimized design of admittance

The other natural application of admittance optimization is the improved design of noise control devices. For instance, Chang et al. used both a genetic algorithm [165] and a simulated annealing approach [166] to design an optimized sound absorber (micro-perforated plate, porous layer and back cavity) at a given frequency. Simulated annealing was also applied by Ruiz et al. [167] to design multilayer micro-perforated panels with good absorption properties on a wide frequency band (1-6 kHz).

The acoustic liner community also used admittance optimization methods to design new efficient liners. Approaches mostly differ in the used numerical model and the assumed geometry, for instance semi-analytical modal representation in annular nozzles [168] or finite element calculation applied to aircraft engine nacelles [169]. One can also refer to the work of Reimann [170] who compared several optimization methods (both gradient-based and evolutionary) to design liners in aircraft engine nacelles, mostly using the Equivalent Source Method (ESM) to predict the sound field. Such optimized liners can induce a significant attenuation of the radiated noise.

Finally, a few studies also considered noise barriers. Other than the already mentioned studies by Baulac et al. [4, 6, 128], one can mention Thorsson's work [9, 10], who specifically studied the effect of the admittance for low-height barriers, either using an ESM method [9] or the BEM coupled with a SQP algorithm [10]. Particularly, the author showed that a soft admittance can strongly enhance the insertion loss of the barrier, although the results were derived only at two selected frequencies only (200 and 400 Hz). Similar conclusions were drawn from other studies [132–134].

3.4.3 Scatterer shape optimization and reconstruction

Several studies following optimization approaches in order to design or reconstruct the shape of acoustic scatterers - including but not limited to noise barriers - have been published. The two main types of optimization outlined in this chapter, namely evolutionary and sensitivity-based methods, have both been used in this context.

Evolutionary methods, especially genetic algorithms, have been used extensively to design highway noise barriers [101, 128, 171–173] and specific sonic crystals used as low-height noise barriers [11, 174]. One should also point out that the simulated annealing algorithm has been applied as well in a more engineering-type configuration [175]. Depending on the context, the improvement of the optimized shape barriers can be an additional 5 dB of attenuation compared to a simpler shape. One should point out however that in the given references, evolutionary optimization methods were applied for barriers represented in a very specific way - succession of wells in [101], binary (filled/empty rectangles) representation in [171], multiple-edge geometry in [128] or parallel arrangement of cylinders in the sonic crystal case [11].

Sensitivity-based methods have been used as well, for instance using the boundary element method [176–178] applied to 2D and 3D shape sensitivity analysis, or the finite element method to design a muffler along a duct [179]. It has been applied as well for noise barrier design using an engineering calculation method, a pre-calculated table of values and a linear interpolation [180].

Those methods have also been applied in the context of inverse (or shape reconstruction) problems, for instance to identify the locations and shape of unknown scatterers based on a measured diffraction pattern using shape sensitivity [149, 181]. This has been extended to the identification of both the shape and the admittance of a scatterer using a level-set method [150].

3.4.3.1 Topological approaches

We briefly mention another approach, radically different from what has been presented above, which is the so-called topology optimization. The idea is to represent the scattering object not as a boundary but as a distributed function quantifying the presence or not of the scatterer, coupled to a level set method. This allows the topology of the scatterer - that is the number of disconnected obstacles - to vary as well, for instance by adding extra scattering bodies, based on the so-called topological derivative (or sensitivity). Those methods have been applied in the context of noise barriers [182–184], although these studies mostly focused on low frequencies (below 200 Hz). Topological sensitivity has been applied successfully as well in inverse scattering applications [185, 186].

3.4.4 Conclusion of the review

Comparing the results obtained by these different approaches to optimally design acoustic scatterers such as noise barriers, one can notice that the obtained designs have very different characters if an evolutionary method is used as opposed to a sensitivity-based method. This suggests that both approaches, with their pros and cons, can be successfully used but in somewhat different applications: a shape optimization problem assuming a discrete representation of the shape may be more conveniently tackled using an evolutionary method, whereas if one is more interested in continuous representations, sensitivity-based methods (including topological methods) may be more appropriate. The question of computational load is also important since it greatly influences the choice of the calculation method: complicated environments typically require simple calculation methods whereas more accurate methods such as the BEM have been limited mostly to low frequency applications. Simplifying the considered model with appropriate assumptions seems therefore paramount to apply optimization methods to low-height noise barriers over a wide frequency range, which is the purpose of this work.

3.5 Details of the chosen optimization algorithm

We finally present more details about the chosen optimization method that has been applied to our application: full design optimization of a low-height noise barrier (including surface treatments and shape) in the most general fashion possible. As stated previously, the choice of a continuous search space to describe the parameters seemed like a more appropriate choice, and since the sensitivity information can be obtained conveniently following for instance the adjoint state approach (this will be detailed in chapter 4), it has been decided to use a line-search sensitivity-based method. Using the adjoint state method also allows to use a large number of variables, and therefore it has been decided to describe the shape in a general manner, using

an arbitrary set of control nodes (which is the way a shape is defined in the BEM software MICADO introduced in chapter 2). Admittance parameters optimization, which has been studied extensively in [1], can be achieved as well with this approach.

One could first try to use the same minimization method to find optimized values of admittance parameters and shape parameters. However, it has been chosen in this work to differentiate the optimization method between the two types of variables. The reason is essentially related to the fact that the two types of variables are subject to different constraints. Indeed, if one refers to the vector of admittance parameters $\mathbf{x}_\beta$ and the vector of shape parameters $\mathbf{x}_\Gamma$, the optimization problem (3.3) can be written as:

$$\min_{\mathbf{x}_\beta, \mathbf{x}_\Gamma} e\big(\mathbf{x}_\beta, \mathbf{x}_\Gamma, p(\mathbf{x}_\beta, \mathbf{x}_\Gamma)\big) \qquad \text{s.t.} \quad \begin{cases} \mathbf{l}_\beta \leqslant \mathbf{x}_\beta \leqslant \mathbf{u}_\beta \\ \mathbf{l}_\Gamma \leqslant \mathbf{x}_\Gamma \leqslant \mathbf{u}_\Gamma \\ \Gamma(\mathbf{x}_\Gamma) \text{ is injective} \end{cases}$$

with $\mathbf{l}_\beta, \mathbf{u}_\beta, \mathbf{l}_\Gamma, \mathbf{u}_\Gamma$ referring to lower and upper bounds corresponding either to the parameters $\mathbf{x}_\beta$ or $\mathbf{x}_\Gamma$. Under this form, it is clear that the admittance parameters are minimized under bound constrains only, whereas the shape parameters are minimized under bound constraints and the much more restrictive shape injectivity constraint.

Now it would make sense to take advantage of the convergence speed provided by quasi-Newton methods to perform the minimization, using for instance the SQP minimization routine available in the software Matlab. However, as pointed out in section 3.3.2.2, quasi-Newton methods naturally use a unit step size, which means there is little control on how much the shape is modified from one step to the next. In particular, it would be more difficult to ensure that the shape injectivity constraint is satisfied, which is a rather cumbersome test (see the details of this test in appendix D.1). On the other hand, the feasible set of admittance parameters is essentially a hypercube - which is the type of set corresponding to bound constraints only - and therefore using an SQP routine raises no issues.

A simple steepest descent method, however, leaves more freedom in the choice of the step size (through the backtracking algorithm), which makes it possible to ensure the injectivity constraint in a more convenient way. This method has the main disadvantage to be slower than quasi-Newton methods.

To ensure the shape injectivity constraint but to keep convergence speed as fast as possible, it has therefore been decided to differentiate the minimization with respect to admittance parameters, which will be done using a SQP method (implemented in Matlab), and the minimization with respect to shape parameters, which will be done with an adapted steepest descent method. Both types of variables will therefore be optimized alternatively, until convergence. The main framework of the admittance and shape optimization algorithm is outlined in figure 3.1. Typically the convergence tolerance can be taken as $\epsilon_0 = 10^{-4}$. Details of the adapted steepest descent method as well as the loop detection test are given in appendix D.

Given ϵ_0 (convergence tolerance)
Given $\mathbf{x}_\beta^0$ (initial admittance parameters), $\mathbf{x}_\Gamma^0$ (initial shape parameters)
Evaluate initial objective function value and gradient: $e^0 = e\big(\mathbf{x}_\beta^0, \mathbf{x}_\Gamma^0\big)$, $\mathbf{g}^0 = \nabla e\big(\mathbf{x}_\beta^0, \mathbf{x}_\Gamma^0\big)$
$i = 0$, $\mathbf{x}_\beta^i = \mathbf{x}_\beta^0$, $\mathbf{x}_\Gamma^i = \mathbf{x}_\Gamma^0$, $e_\Gamma^i = e_\beta^i = e^0$, $\mathbf{g}^i = \mathbf{g}^0$

while $\Big(|e_\beta^i - e_\Gamma^i| > \epsilon_0$ or $i = 0\Big)$
  Perform the admittance optimization (SQP): find $\mathbf{x}_\beta^{i+1}$
  Update objective function value and gradient: $e_\beta^{i+1} = e\big(\mathbf{x}_\beta^{i+1}, \mathbf{x}_\Gamma^i\big)$, $\mathbf{g}_\beta^{i+1} = \nabla e\big(\mathbf{x}_\beta^{i+1}, \mathbf{x}_\Gamma^i\big)$

  Perform the shape optimization (steepest descent): find $\mathbf{x}_\Gamma^{i+1}$
  Update objective function value and gradient: $e_\Gamma^{i+1} = e\big(\mathbf{x}_\beta^{i+1}, \mathbf{x}_\Gamma^{i+1}\big)$, $\mathbf{g}_\Gamma^{i+1} = \nabla e\big(\mathbf{x}_\beta^{i+1}, \mathbf{x}_\Gamma^{i+1}\big)$
  $i \leftarrow i + 1$
end

Figure 3.1: Main outline of the shape and admittance optimization algorithm.

3.6 Conclusion

Optimization methods have been widely studied and applied to many different applications, which explains why numerous numerical methods are available to tackle optimization problems. We here reviewed some of the most common methods, among which one can define two main categories: sensitivity-based methods and evolutionary methods. Evolutionary methods do not require the knowledge of the gradient and allow a rather global search, typically on a discrete space, at the cost of a large number of objective function evaluations. On the other hand, sensitivity-based methods require a continuous feasible set, a sufficiently smooth objective function and the knowledge of the gradient, and therefore are fundamentally less general than evolutionary methods, although they have been applied to a large range of problems including acoustic scatterer optimization. They are however faster than evolutionary methods but are only able to find local solutions to the optimization problem.

Sensitivities (the gradient) may be computed either by implicit differentiation, which requires one to solve one extra diffraction problem for each parameter, or by the adjoint state approach, which only requires one to solve one extra diffraction problem regardless of the number of parameters, which makes this adjoint state method much more efficient computationally.

For the different reasons pointed out across this chapter (more natural continuous representation of the admittance and shape parameters, speed of sensitivity-based methods, possibility to calculate the gradient without too much increase of the computation time), we therefore chose to use a sensitivity-based method to optimize the surface treatment and the cross-sectional shape of the considered noise barrier. Besides, the adjoint state approach makes it possible to describe the shape of the barrier in a general manner by a potentially large set of control nodes.

An algorithm coupling two different methods to perform the optimization with respect to admittance parameters and shape parameters is hence proposed. This algorithm uses a classical SQP approach and an adapted steepest descent, which provides a good compromise between achieving good convergence speed and satisfying constraints at every iteration.

Chapter 4

Shape and admittance sensitivity expressions

In this chapter we derive the expressions of the sensitivity with respect to the parameters describing the admittance and the shape of the noise barrier, which can then be used in a sensitivity-based optimization algorithm as exposed in chapter 3. Numerical implementation of these theoretical expressions is discussed and validated against finite difference calculations.

4.1 Barrier implementation and modeling assumptions

4.1.1 Physical assumptions and geometry

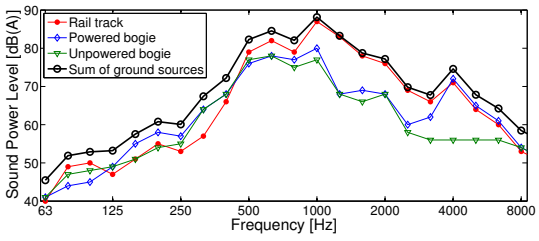

Figure 4.1: Comparison of third octave spectra of the different sources identified by Pallas et al. [26] and their incoherent summation.

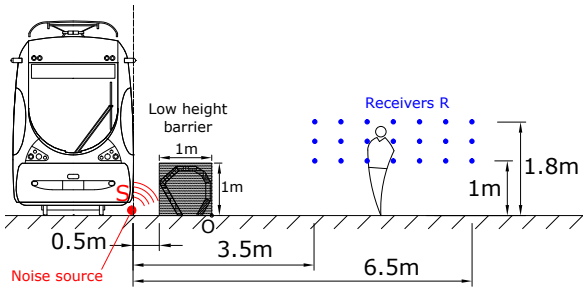

Figure 4.2: Geometrical configuration for the implementation of the low-height tramway noise barrier. Dotted line: idealization of the tramway side as a vertical baffle.

First we review the modeling assumptions of the problem under consideration: the optimization of the performance of a tramway low height noise barrier. Using simplifying assumptions is indeed convenient in an optimization application since the objective function will be evaluated many times, and therefore decreasing the computation time of each evaluation is worth it, even if this induces a slight decrease of accuracy.

The atmosphere is assumed homogeneous with a speed of sound of $c_0 = 343\,\mathrm{m/s}$. The source is idealized as an infinite line source located on the ground with a spectral content given by the incoherent sum of the rail track and bogie contributions in [26] (see in figure 4.1). One can infer

that most of the A-weighted acoustic energy is contained in the frequency range 100-2500 Hz, which will be the frequency range of study. It is also assumed that the geometry is invariant along the axis of the track, which makes the problem purely two dimensional. This assumption has been shown [28] to be correct when predicting excess attenuation at single frequencies due to point sources, which is what we will use in the calculation of the broadband attenuation.

The presence of the tramway will cause the sound to bounce on its surface and diffract at the roof edge and at the gap between the carriage and the ground. Those geometrical details could be modeled with the BEM, but one can also idealize the tramway side as an infinite rigid vertical baffle (see in figure 4.2). This is mathematically equivalent to introducing an *image* barrier, symmetrical to the original one with respect to the tramway side surface, which greatly reduces the mesh surface and therefore the computation time. The barrier and its image with respect to the vertical baffle are represented by the boundary Γ, which separates the 2D plane as an interior domain Ω^i and an exterior domain Ω^e. Finally, the ground is modeled as rigid, which represents correctly many urban-like surfaces.

The barrier cross section is assumed to lie in a one meter wide square, half a meter away from the tramway (see in figure 4.2). The surface of the barrier is assumed locally reacting and its acoustical behavior described in terms of a normalized acoustic admittance β.

The receiver locations (R_m) have been chosen to represent a range of possible locations of pedestrian ears: horizontal distance from the bottom-right corner of the barrier between 2 m and 5 m, and height between 1 m and 1.8 m (see again in figure 4.2).

4.1.2 Objective function

The purpose of this work is to maximize the insertion loss calculated at the receivers by changing the shape of the barrier. The 2D BEM, implemented in the software MICADO developed at the CSTB by Jean [120], has been used for this purpose. The BEM provides a way to calculate the complex pressure amplitude $p(R, f)$ at each frequency and at each receiver point for an arbitrary geometry. One can then define an average attenuation across all receivers at the frequency f_n:

$$A_n = \frac{P(f_n)}{P^{\mathrm{in}}(f_n)} \qquad \text{with} \quad \begin{cases} P(f_n) = \left[\sum_m |p(R_m, f_n)|^2\right]^{\frac{1}{2}} \\ P^{\mathrm{in}}(f_n) = \left[\sum_m |p^{\mathrm{in}}(R_m, f_n)|^2\right]^{\frac{1}{2}} \end{cases} \tag{4.1}$$

where $p = p^{\mathrm{in}} + p^{\mathrm{sc}}$ is the total pressure field, p^{in} is the incident field (field without the barrier) and p^{sc} the scattered field. P is an average pressure across the receivers and P^{in} the incident pressure which is a normalizing constant independent of the barrier geometry. Then, a broadband attenuation based on the sound power levels L_w shown in figure 4.1 and the attenuations at each frequency is considered. In order to have a somewhat faster evaluation of the objective function (which will be called many times in the optimization) but a good evaluation of the third octave insertion losses, we consider a few frequencies per third-octave between 100 and 2500 Hz (typically 4 or 10, depending on the context). For each third-octave band, we define an

amplitude-like quantity $S = 10^{L_w/10}$, which is assigned to all the frequencies in this third-octave band. Recalling equation (1.1), the broadband attenuation is then given by:

$$e = \frac{\sum_n S_n A_n^2}{\sum_n S_n} \tag{4.2}$$

which is similar to the objective function considered by other authors [4, 11]. We would like to minimize the function e, which only depends on the properties of the barrier, that is its geometry and its admittance. One can also calculate from the objective function a broadband insertion loss for the considered source spectrum in dB(A) defined by $\mathrm{IL} = -10 \log e$.

The purpose of this chapter is to derive explicit expressions of the sensitivity of the objective function with respect to the different parameters describing the low-height barrier, namely its shape and the parameters describing the surface admittance. This will allow us to use this information in a sensitivity-based optimization method, as described in chapter 3.

4.2 Formal definitions of the gradient with respect to the admittance and the shape

First we quickly introduce the mathematical concepts used in the calculation of the derivative of the objective function with respect to changes in the admittance and/or the shape of the barrier. This section is not meant to be completely rigorous from a mathematical standpoint, especially concerning the spaces which the different variables belong to and concerning the behavior at infinity which requires specific attention as mentioned in chapter 2, but simply to give the reader an idea of the concepts needed. For a more rigorous analysis, one can refer to other works [146, 150].

4.2.1 Field derivative

First, we need to define the gradient with respect to the pressure field, and therefore we now introduce the concept of field derivative. Let D be the set of piecewise sufficiently smooth complex functions defined on Ω^e (D can be for instance $H^1(\Omega^e)$). The dot notation $u \cdot v$ refers to the integral of the product of two functions in D (which is similar to a duality product):

$$u \cdot v = \int_{\Omega^e} uv \, \mathrm{d}\Omega$$

This product is technically not a scalar product (since $u \cdot u$ is not a positive real number), but this definition is sufficient for the purpose of this work.

Let F be a complex functional defined on D. F is said to be differentiable in $f \in D$ if there exists a linear form L_f such that:

$$(\forall g \in D) \quad F(f+g) = F(f) + L_f(g) + o\big(\,||g||\,\big) \tag{4.3}$$

where $||.||$ is an appropriate norm for the space D (it could be for instance the H^1-norm). In

this context, one can then identify the linear form L_f to a complex function $\mathrm{d}F/\mathrm{d}f$ (called the "gradient" or the "field derivative" of F) such that:

$$(\forall g \in D) \quad L_f(g) = \frac{\mathrm{d}F}{\mathrm{d}f} \cdot g \tag{4.4}$$

Actually the function $\mathrm{d}F/\mathrm{d}f$ could be a generalized function, and in this case the definition is to be taken in a distribution sense. Also, if a complex functional F is linear and has the form $F(f) = f_0 \cdot f$ then the derivative is simply given by $\mathrm{d}F/\mathrm{d}f = f_0$. When the functional has several arguments, one can naturally use the notion of partial functional derivatives, written as $\partial F/\partial f$.

In the particular case when F takes real values, the gradient term $L_f(g)$ has to be real as well, and therefore it could be replaced by its real part in the definition (4.3). So, if F takes real values, it is equivalent to state that F is differentiable in f if there exists a complex function $\mathrm{d}F/\mathrm{d}f$ such that:

$$(\forall g \in D) \quad F(f+g) = F(f) + \mathrm{Re}\left(\frac{\mathrm{d}F}{\mathrm{d}f} \cdot g\right) + o\big(\,||g||\,\big) \tag{4.5}$$

Several properties of usual derivatives can be extended to the case of field derivatives. For instance, for F a complex differentiable functional on D, one can also show that:

$$\frac{\mathrm{d}|F|^2}{\mathrm{d}f} \cdot g = F^* \left(\frac{\mathrm{d}F}{\mathrm{d}f} \cdot g\right) + F \left(\frac{\mathrm{d}F}{\mathrm{d}f} \cdot g\right)^* = \mathrm{Re}\left(2\,F^* \frac{\mathrm{d}F}{\mathrm{d}f} \cdot g\right) \tag{4.6}$$

with * denoting complex conjugation. From this follows:

$$\frac{\mathrm{d}|F|^2}{\mathrm{d}f} = 2\,F^* \frac{\mathrm{d}F}{\mathrm{d}f} \quad \text{and} \quad \frac{\mathrm{d}|F|}{\mathrm{d}f} = \frac{F^*}{|F|} \frac{\mathrm{d}F}{\mathrm{d}f} \tag{4.7}$$

4.2.2 Boundary field derivative

Similarly, one can define the derivative of a functional defined on D_Γ, the set of piecewise sufficiently smooth complex functions defined on Γ. The pressure field evaluated on the scatterer boundary Γ as well as the admittance β are typical functions belonging to D_Γ. For simplicity, we keep the dot notation to refer to the duality product, even though for the functions u_Γ and v_Γ in D_Γ, the product is defined as:

$$u_\Gamma \cdot v_\Gamma = \int_\Gamma u_\Gamma v_\Gamma \,\mathrm{d}\Gamma$$

Let F_Γ be a complex functional defined on D_Γ. F_Γ is said to be differentiable in $f_\Gamma \in D_\Gamma$ if there exists a linear form L_f such that:

$$(\forall g_\Gamma \in D) \quad F(f_\Gamma + g_\Gamma) = F(f_\Gamma) + L_f(g_\Gamma) + o\big(\,||g_\Gamma||\,\big) \tag{4.8}$$

where again $||.||$ is a suitable norm. Again one can then identify the linear form L_f to a complex function $\mathrm{d}F/\mathrm{d}f_\Gamma$ such that:

$$(\forall g_\Gamma \in D_\Gamma) \quad L_f(g_\Gamma) = \frac{\mathrm{d}F}{\mathrm{d}f_\Gamma} \cdot g_\Gamma \tag{4.9}$$

The properties recalled in equation (4.7) valid for field derivatives also hold for boundary field derivatives.

4.2.3 Shape derivative

Similarly, the concept of shape derivative can be understood as a linear form acting on the set of displacements fields, which we will refer to as *velocity* fields. A velocity field $\boldsymbol{\theta}$ is simply a mapping $\mathbf{x} \mapsto \boldsymbol{\theta}(\mathbf{x})$ in the 2D plane. Let D_θ be the set of sufficiently smooth (typically bounded and with compact support) velocity fields in the 2D plane. Such a velocity field can therefore transform the initial boundary Γ to a new boundary $\Gamma(\boldsymbol{\theta})$ defined as $\Gamma(\boldsymbol{\theta}) = \Gamma + \boldsymbol{\theta}$, which can also be written as $\Gamma(\boldsymbol{\theta}) = \{\ \mathbf{x}+\boldsymbol{\theta}(\mathbf{x})\ :\ \mathbf{x} \in \Gamma\ \}$. Now, consider a complex functional J depending on the boundary Γ. J is said to be differentiable with respect to the shape Γ if there exists a linear form that we will write $\mathrm{d}J/\mathrm{d}\Gamma$ acting on D_θ such that:

$$(\forall \boldsymbol{\theta} \in D_\theta) \quad J\big(\Gamma(\boldsymbol{\theta})\big) = J\big(\Gamma\big) + \frac{\mathrm{d}J}{\mathrm{d}\Gamma} \cdot \boldsymbol{\theta} + o\big(\,||\boldsymbol{\theta}||\,\big) \tag{4.10}$$

where again we keep the dot notation to refer to the duality product between D_θ and its dual for consistency, and $||.||$ refers to an appropriate norm. For instance, let us consider a functional F defined as:

$$F(\Gamma) = \int_{\Omega^e} f \,\mathrm{d}\Omega$$

with f a piecewise smooth function (or generalized function) defined on Ω^e. F depends indeed on Γ since there is a unique correspondence between Γ and its exterior domain Ω^e. One can show that the shape derivative in this case is given by [149, 150, 187]:

$$\frac{\mathrm{d}F}{\mathrm{d}\Gamma} \cdot \boldsymbol{\theta} = \int_{\Omega^e} \boldsymbol{\nabla} \cdot (f\boldsymbol{\theta}) \,\mathrm{d}\Omega$$

Applying the divergence theorem and defining $\theta_n = \boldsymbol{\theta} \cdot \mathbf{n}$ the normal component of the velocity field on Γ, one has:

$$\frac{\mathrm{d}F}{\mathrm{d}\Gamma} \cdot \boldsymbol{\theta} = -\int_{\Gamma} f\theta_n \,\mathrm{d}\Gamma \tag{4.11}$$

One should point out that the minus sign is due to the fact that the normal $\mathbf{n}$ has been defined as exterior to Γ and therefore interior to Ω^e, and that there is no contribution from infinity since $\boldsymbol{\theta}$ is typically assumed to have a compact support. Now consider a functional G of the form:

$$G(\Gamma) = \int_{\Gamma} f \,\mathrm{d}\Gamma$$

The formula for the shape derivative of this functional, one can most easily find in the literature, holds for a closed smooth surface [149, 150]. However, in a numerical discretized context with

linear shape functions, the shape will be represented by a set of segments with possible abrupt changes of directions from one segment to another, which cannot be modeled well as a smooth curve. This is why here we consider that the boundary Γ and the function f are only piecewise smooth. Let $\Gamma_i = [\mathbf{x}^{(i-1)}, \mathbf{x}^{(i)}], i \in [1:N]$ the smooth portions of the curve Γ. $\mathbf{x}^{(0)}$ and $\mathbf{x}^{(N)}$ are the start and end points of Γ, and $\mathbf{x}^{(i)}$ are the points where the curve is not smooth. The parts Γ_i are such that they do not overlap, except at both their ends, but their union recovers the entire curve Γ. Also, the function f is assumed to be smooth on each Γ_i separately, but are not necessarily smooth at the edges of each part so that f or its gradient may have jumps at the edges of each part. Also, the velocity field on Γ is broken down in tangential and normal components: $\boldsymbol{\theta} = \theta_n \, \mathbf{n} + \theta_t \, \mathbf{t}$. One can show (see appendix E) that in this case the shape derivative is:

$$\frac{\partial G}{\partial \Gamma} \cdot \boldsymbol{\theta} = \int_\Gamma \Big(\frac{\partial f}{\partial n} + H f \Big) \theta_n \, \mathrm{d}\Gamma - \sum_{i=1}^{N-1} [\![f\theta_t]\!]^{(i)} + (f\theta_t)(\mathbf{x}^{(N)}) - (f\theta_t)(\mathbf{x}^{(0)}) \tag{4.12}$$

where $[\![.]\!]^{(i)}$ is the jump of a function at the point $\mathbf{x}^{(i)}$, defined as the limiting value after the jump minus the limiting value before the jump, and H the mean curvature. Equation (4.12) is a particular case of the general expressions derived by Petryk and Mroz [187]. Besides, when the boundary Γ is piecewise linear (as it will be the case in the considered BEM discretized context), the curvature is locally zero, and therefore has no contribution to the integral. In a way, one could say that the curvature contribution to the shape derivative is best described here by the jump terms at the end of each segment. In this case the expression simplifies to:

$$\frac{\partial G}{\partial \Gamma} \cdot \boldsymbol{\theta} = \int_\Gamma \frac{\partial f}{\partial n} \theta_n \, \mathrm{d}\Gamma - \sum_{i=1}^{N-1} [\![f\theta_t]\!]^{(i)} + (f\theta_t)(\mathbf{x}^{(N)}) - (f\theta_t)(\mathbf{x}^{(0)}) \tag{4.13}$$

4.3 Derivation of the sensitivity expressions

To carry on the optimization of the objective function, an iterative method based on the gradient has been chosen. Accurate calculation of the sensitivities (derivatives or gradients) with respect to the admittance and shape are therefore necessary. We derive here simple expressions based on the adjoint state approach.

4.3.1 General expressions

First, we derive the expression of the shape and admittance sensitivity of the RMS pressure P at a given frequency, as recalled in section 4.1. Let us recall that the total pressure field p satisfies the scattering problem (2.1). Let us now consider the weak formulation of this problem, as done by Bonnet [149], which will allow an easier derivation of the sensitivity expressions. Again, the mathematical treatment given here is not extremely rigorous, since special care should be given to express the weak formulation in a bounded domain and to bring down the radiation condition at a finite distance (as exposed in section 2.2). However, the results given here would not be changed if these precautions were taken, which is why a simpler approach is followed. Again, we refer to the work by He et al. [150] and Terrasse [136] for a more rigorous treatment, as well

as to section 2.2.

We consider the 2D scattering problem exposed in section 2.1, in which Γ refers to the noise barrier and its image with respect to the vertical baffle which approximates the effect of the tramway side, and Ω^e is the exterior domain. Given any sufficiently smooth and locally integrable function $\hat{q}$ in Ω^e (typically belonging to $H^1(\Omega^e)$) which satisfies the radiation condition, recalling equation (2.6) - but ignoring the term on the surrounding half-sphere S_R - the problem (2.1) is equivalent to:

$$\forall \hat{q} \qquad Q(\Gamma, \beta, p, \hat{q}) = 0$$

with Q defined for arbitrary regular functions $\hat{p}$ and $\hat{q}$ as:

$$Q(\Gamma, \beta, \hat{p}, \hat{q}) = \mathrm{Re}\left[- \int_{\Omega^e} \boldsymbol{\nabla} \hat{p} \cdot \boldsymbol{\nabla} \hat{q} \, \mathrm{d}\Omega^e + k^2 \int_{\Omega^e} \hat{p}\, \hat{q} \, \mathrm{d}\Omega^e + \mathrm{i}k \int_{\Gamma} \beta \, \hat{p}\, \hat{q} \, \mathrm{d}\Gamma + \hat{q}(S) \right] \tag{4.14}$$

We now define the Lagrangian:

$$\mathcal{L}(\Gamma, \beta, \hat{p}, \hat{q}) = P(\Gamma, \beta, \hat{p}) + Q(\Gamma, \beta, \hat{p}, \hat{q})$$

By definition, we have $Q(\Gamma, \beta, p, \hat{q}) = 0$ for all functions $\hat{q}$, therefore:

$$(\forall \hat{q}) \qquad P(\Gamma, \beta, p) = \mathcal{L}(\Gamma, \beta, p, \hat{q}) \tag{4.15}$$

Since p implicitly depends on Γ and β as the solution of the scattering problem (2.1), taking the derivative of equation (4.15) with respect to Γ and β, in the sense explained in section 4.2, yields:

$$(\forall \hat{q}) \quad \begin{cases} \dfrac{\mathrm{d}P}{\mathrm{d}\Gamma}(\Gamma, \beta, p) = \dfrac{\partial \mathcal{L}}{\partial \Gamma}(\Gamma, \beta, p, \hat{q}) + \dfrac{\partial \mathcal{L}}{\partial p}(\Gamma, \beta, p, \hat{q}) \cdot \dfrac{\mathrm{d}p}{\mathrm{d}\Gamma} \\ \dfrac{\mathrm{d}P}{\mathrm{d}\beta}(\Gamma, \beta, p) = \dfrac{\partial \mathcal{L}}{\partial \beta}(\Gamma, \beta, p, \hat{q}) + \dfrac{\partial \mathcal{L}}{\partial p}(\Gamma, \beta, p, \hat{q}) \cdot \dfrac{\mathrm{d}p}{\mathrm{d}\beta} \end{cases} \tag{4.16}$$

Now, let us define the *adjoint state* q as the solution of the following variational problem:

$$(\forall \hat{w}) \quad \frac{\partial \mathcal{L}}{\partial p}(\Gamma, \beta, p, q) \cdot \hat{w} = 0 \tag{4.17}$$

Since equation (4.16) is valid for any function $\hat{q}$, especially for $\hat{q} = q$, and using equation (4.17), we have:

$$\begin{cases} \dfrac{\mathrm{d}P}{\mathrm{d}\Gamma}(\Gamma, \beta, p) = \dfrac{\partial \mathcal{L}}{\partial \Gamma}(\Gamma, \beta, p, q) \\ \dfrac{\mathrm{d}P}{\mathrm{d}\beta}(\Gamma, \beta, p) = \dfrac{\partial \mathcal{L}}{\partial \beta}(\Gamma, \beta, p, q) \end{cases} \tag{4.18}$$

which are explicit functions of the shape Γ, the admittance β, the state p and the adjoint state q.

4.3.1.1 Adjoint state equation

In this section we derive the explicit form of the problem the adjoint state q must satisfy. Recalling equation (4.14), one can see Q is a linear function of p plus a source term which is

independent of p, and therefore:

$$\frac{\partial Q}{\partial p}(\Gamma, \beta, \hat{p}, \hat{q}) \cdot \hat{w} = \mathrm{Re}\left[- \int_{\Omega^e} \boldsymbol{\nabla} \hat{q} \cdot \boldsymbol{\nabla} \hat{w} \, \mathrm{d}\Omega^e + k^2 \int_{\Omega^e} \hat{q}\, \hat{w} \, \mathrm{d}\Omega^e + \mathrm{i}k \int_{\Gamma} \beta\, \hat{q}\, \hat{w} \, \mathrm{d}\Gamma \right]$$

Recalling equation (4.7) and the definition of P given in equation (4.1), the partial derivative of P with respect to p is given by:

$$\frac{\partial P}{\partial p}(\Gamma, \beta, \hat{p}) \cdot \hat{w} = \mathrm{Re}\left[\sum_m \frac{\hat{p}(R_m)^*}{P}\, \hat{w}(R_m) \right]$$

Therefore the adjoint state equation (4.17) becomes:

$$(\forall \hat{w}) \quad \mathrm{Re}\left[- \int_{\Omega^e} \boldsymbol{\nabla} q \cdot \boldsymbol{\nabla} \hat{w} \, \mathrm{d}\Omega + k^2 \int_{\Omega^e} q\, \hat{w} \, \mathrm{d}\Omega + \mathrm{i}k \int_{\Gamma} \beta\, q\, \hat{w} \, \mathrm{d}\Gamma + \sum_m \frac{p(R_m)^*}{P}\, \hat{w}(R_m) \right] = 0$$

The similarity with the weak formulation of the initial scattering problem (2.1) allows us to recognize that this equation is the weak formulation of the following scattering problem :

$$\begin{cases} -(\nabla^2 + k^2)\, q = \displaystyle\sum_m \frac{p(R_m)^*}{P}\, \delta(R_m, .) \quad \text{in } \Omega^e \\ \dfrac{\partial q}{\partial n} + \mathrm{i}k\, \beta\, q = 0 \quad \text{on } \Gamma \\ \dfrac{\partial q}{\partial n} = 0 \quad \text{on } \Gamma_g \\ + \quad \text{radiation condition} \end{cases} \tag{4.19}$$

where $\delta(R_m, .)$ is the Dirac delta function located at the point (R_m). The solution q of this problem is therefore the field due to the radiation of weighted point sources located at the receivers (see figure 4.3), which had already been pointed out by Bonnet [149]. The problem (4.19) will be referred to as the *dual* or *adjoint* scattering problem, whereas the initial problem (2.1) will be referred to as the *primal* or *direct* scattering problem.

One can point out that if the term involving the Dirichlet-Neumann operator on a surrounding half-sphere (see in section 2.2) had been kept, the scattering problem satisfied by the adjoint state would have been the same, due to the fact that the operator T is itself symmetrical. One could state that considering the weak formulation of the problem in the unbounded domain but implicitly assuming the radiation condition is essentially equivalent to considering the weak formulation in the bounded domain with the extra term involving the Dirichlet-Neumann operator.

In order to solve the adjoint problem, one can use once again the BEM, which would yield the boundary field q_Γ. To do so, one only needs to solve the equivalent of the integral equation (2.12) for the adjoint problem, which is given by:

$$N q_\Gamma + D^*(\mathrm{i}k\beta q_\Gamma) + \mathrm{i}k\beta\, D q_\Gamma + \mathrm{i}k\beta\, S(\mathrm{i}k\beta q_\Gamma) = h_2^{\mathrm{in}}(\beta, p) \tag{4.20}$$

with $h_2^{\text{in}}(\beta, p) = -\dfrac{\partial q^{\text{in}}}{\partial n}\Big|_\Gamma - \mathrm{i}k\beta\, q^{\text{in}}|_\Gamma$ and $q^{\text{in}}(\mathbf{x}) = \displaystyle\sum_m \frac{p(R_m)^*}{P}\, G(R_m, \mathbf{x})$. Equation (4.20) will be referred to as the *adjoint state* equation, as opposed to equation (2.12) which is referred to as the *state* equation.

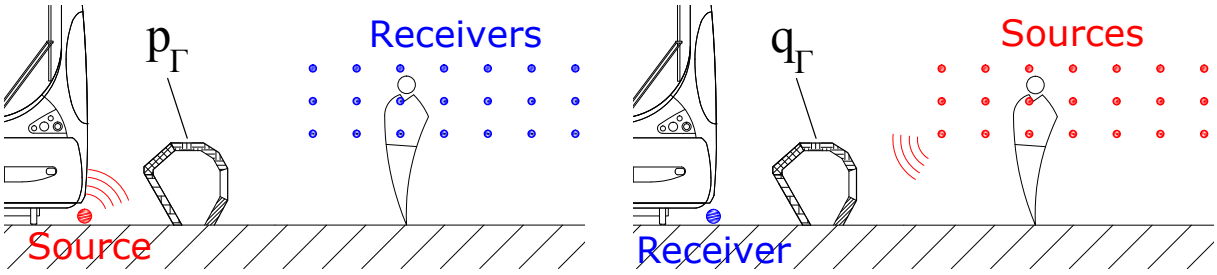

Figure 4.3: Source-receiver configuration for calculation of the state p_Γ (left) and that of the adjoint state q_Γ (right). The source has a unit amplitude in the primal problem, but in the dual problem each source is weighted by the coefficient $p(R_m)^*/P$ (P being the average pressure amplitude across the receivers, as defined in equation (4.1)).

4.3.1.2 Shape derivative expression

In this section, we give the explicit expression of the shape derivative expression given in the first line of equation (4.18). We therefore consider a velocity field $\boldsymbol{\theta}$ acting in a neighborhood of the shape Γ, and therefore of zero value at the source location (S) and receivers locations (R_m). This assumption is essentially related to the fact that the source and receivers locations are fixed in our problem, even when the shape Γ is modified. Let $\theta_n = \boldsymbol{\theta}\cdot\mathbf{n}$ and $\theta_t = \boldsymbol{\theta}\cdot\mathbf{t}$ be the normal and tangent trace of the velocity field on Γ.

Assuming that the boundary Γ is piecewise smooth and keeping the same notations as in section (4.22), we can now apply equations (4.11) and (4.12) to the expression of Q recalled in equation (4.14), which yields:

$$\begin{aligned}
\frac{\partial Q}{\partial \Gamma}(\Gamma,\beta,p,q)\cdot\boldsymbol{\theta} =& \mathrm{Re}\Big[\int_\Gamma \boldsymbol{\nabla} p\cdot\boldsymbol{\nabla} q\,\theta_n\,\mathrm{d}\Gamma - k^2\int_\Gamma pq\,\theta_n\,\mathrm{d}\Gamma + \mathrm{i}k\int_\Gamma \beta\left(\frac{\partial(pq)}{\partial n} + H\,pq\right)\theta_n\,\mathrm{d}\Gamma \\
& -\mathrm{i}k\sum_i [\![\beta pq\theta_t]\!]^{(i)} + \mathrm{i}k\big[(\beta pq\theta_t)(\mathbf{x}^{(N)}) - (\beta pq\theta_t)(\mathbf{x}^{(0)})\big] \\
=& \mathrm{Re}\Big[\int_\Gamma \theta_n\Big(\boldsymbol{\nabla} p\cdot\boldsymbol{\nabla} q + \mathrm{i}k\beta\frac{\partial(pq)}{\partial n} + (-k^2 + \mathrm{i}k\beta H)\,pq\Big)\,\mathrm{d}\Gamma \\
& -\mathrm{i}k\sum_i [\![\beta pq\theta_t]\!]^{(i)} + \mathrm{i}k\big[(\beta pq\theta_t)(\mathbf{x}^{(N)}) - (\beta pq\theta_t)(\mathbf{x}^{(0)})\big]\Big]
\end{aligned}$$

with H is the curvature of the curve Γ and $[\![.]\!]^{(i)}$ is the jump at the point $\mathbf{x}^{(i)}$. Now, recalling the boundary condition satisfied by p and q and the fact that the gradient can be broken up in tangential and normal components, we have:

$$\boldsymbol{\nabla} p\cdot\boldsymbol{\nabla} q + \mathrm{i}k\beta\frac{\partial(pq)}{\partial n} = \frac{\partial p}{\partial t}\frac{\partial q}{\partial t} + \frac{\partial p}{\partial n}\frac{\partial q}{\partial n} + \underbrace{\mathrm{i}k\beta p}_{=-\partial p/\partial n}\frac{\partial q}{\partial n} + \mathrm{i}k\beta q\underbrace{\frac{\partial p}{\partial n}}_{=-\mathrm{i}k\beta q} = \frac{\partial p}{\partial t}\frac{\partial q}{\partial t} + k^2\beta^2\,pq$$

Therefore one has:

$$\begin{aligned}\frac{\partial Q}{\partial \Gamma}(\Gamma,\beta,p,q)\cdot\boldsymbol{\theta} =& \mathrm{Re}\bigg[\int_\Gamma \theta_n\Big(\frac{\partial p}{\partial t}\frac{\partial q}{\partial t}+\big(k^2(\beta^2-1)+\mathrm{i}k\beta H\big)\,pq\Big)\,\mathrm{d}\Gamma \\ &-\mathrm{i}k\sum_i [\![\beta pq\theta_t]\!]^{(i)}+\mathrm{i}k\big[(\beta pq\theta_t)(\mathbf{x}^{(N)})-(\beta pq\theta_t)(\mathbf{x}^{(0)})\big]\bigg]\end{aligned} \tag{4.21}$$

Now, recalling that the function P explicitly depends only on the field p at the receiver points (R_m) which are not moved by the velocity field $\boldsymbol{\theta}$, we can conclude that the function P does not explicitly depend on the shape Γ when it is transported by $\boldsymbol{\theta}$, and therefore $(\partial P/\partial\Gamma)\cdot\boldsymbol{\theta}=0$. Since $\mathcal{L}=P+Q$, we have:

$$\begin{aligned}\frac{\mathrm{d}P}{\mathrm{d}\Gamma}(\Gamma,\beta,p)\cdot\boldsymbol{\theta} =& \frac{\partial Q}{\partial \Gamma}(\Gamma,\beta,p,q)\cdot\boldsymbol{\theta} \\ =& \mathrm{Re}\bigg[\int_\Gamma \theta_n\Big(\frac{\partial p}{\partial t}\frac{\partial q}{\partial t}+\big(k^2(\beta^2-1)+\mathrm{i}k\beta H\big)\,pq\Big)\,\mathrm{d}\Gamma \\ &-\mathrm{i}k\sum_i [\![\beta pq\theta_t]\!]^{(i)}+\mathrm{i}k\big[(\beta pq\theta_t)(\mathbf{x}^{(N)})-(\beta pq\theta_t)(\mathbf{x}^{(0)})\big]\bigg]\end{aligned} \tag{4.22}$$

Equation (4.22) is similar to the expression derived by He et al. [150] , which generalizes the one found by Bonnet [149] in case of a finite admittance boundary condition. Besides, if the curve is piecewise linear (which will be the case in the numerical implementation), the curvature H is zero except maybe on a zero-measure set (the points $\mathbf{x}^{(i)}$), and therefore has no contribution to the integral term. In this case the shape derivative is:

$$\begin{aligned}\frac{\mathrm{d}P}{\mathrm{d}\Gamma}(\Gamma,\beta,p)\cdot\boldsymbol{\theta} =& \mathrm{Re}\bigg[\int_\Gamma \theta_n\Big(\frac{\partial p}{\partial t}\frac{\partial q}{\partial t}+k^2\,(\beta^2-1)\,pq\Big)\,\mathrm{d}\Gamma \\ &-\mathrm{i}k\sum_i [\![\beta pq\theta_t]\!]^{(i)}+\mathrm{i}k\big[(\beta pq\theta_t)(\mathbf{x}^{(N)})-(\beta pq\theta_t)(\mathbf{x}^{(0)})\big]\bigg]\end{aligned} \tag{4.23}$$

4.3.1.3 Admittance derivative expression

Similarly, one can explicitly give the expression for the derivative with respect to the admittance given in the second line of equation (4.18). Again, there is no explicit dependence of P on β since the admittance function exists only at the boundary Γ, which is far from the receiver points, and therefore $\partial P/\partial\beta=0$. Finally, recalling equation (4.14), one can see that Q is a linear function of β plus a term independent of β, and therefore the derivative with respect to β applied to a perturbation γ is simply given by:

$$\frac{\mathrm{d}P}{\mathrm{d}\beta}(\Gamma,\beta,p)\cdot\gamma=\mathrm{Re}\bigg[\mathrm{i}k\int_\Gamma \gamma\,pq\,\mathrm{d}\Gamma\bigg] \tag{4.24}$$

Again, equation (4.24) is similar to the one obtained by He et al. [150] and by the author in [1] (although in this case the derivation was based on integral equations only). We can also directly

write the boundary field derivative function:

$$\frac{\mathrm{d}P}{\mathrm{d}\beta}(\Gamma, \beta, p) = \mathrm{i}k\, pq \tag{4.25}$$

4.3.2 Derivatives with respect to shape and admittance parameters

From the general results derived in section (4.3.1), one can easily write the derivative of P with respect to particular parameters used to describe the admittance distribution as well as the shape. The idea is to find a perturbation (either on the admittance or the shape) that induces a change in one parameter only, and apply the general expression. We here give a few examples of this process.

4.3.2.1 Derivative with respect to an admittance parameter

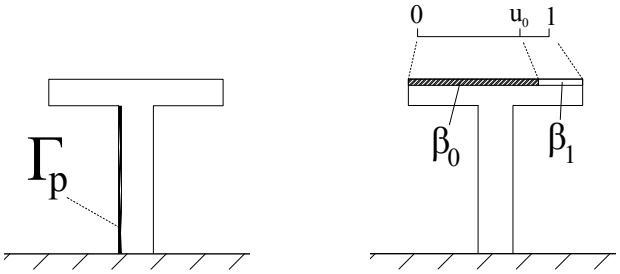

Figure 4.4: Schematic for calculation of the objective function sensitivity with respect to admittance parameters. Left: case of a segment Γ_p covered with an uniform admittance β_p. Right: case of a parameter u_0 defining the location of an admittance discontinuity.

Let us assume that the admittance β is described by a small number of parameters b_j, for instance if the barrier is covered with a finite number of segments of uniform admittance, and if each admittance value is described by a few parameters (which is the case for most admittance models), then the derivative of the RMS pressure at the receivers with respect to the parameter b_j is given by:

$$\frac{\mathrm{d}P}{\mathrm{d}b_j} = \mathrm{Re}\left(\frac{\mathrm{d}P}{\mathrm{d}\beta} \cdot \frac{\mathrm{d}\beta}{\mathrm{d}b_j}\right) = \mathrm{Re}\left(\mathrm{i}k\, pq \cdot \frac{\mathrm{d}\beta}{\mathrm{d}b_j}\right)$$

Here the dot notation refers to the duality product on the boundary (integral on Γ of the product of two functions). For instance, if a panel covering the part Γ_p of the barrier (see figure 4.4, left part) is made of a Delany and Bazley porous layer with an admittance β_p depending on the parameters σ and d, the gradient of P for instance with respect to σ is:

$$\frac{\mathrm{d}P}{\mathrm{d}\sigma} = \mathrm{Re}\left[\mathrm{i}k\, \frac{\mathrm{d}\beta_p}{\mathrm{d}\sigma} \int_{\Gamma_p} pq\right] \tag{4.26}$$

This requires the knowledge of the expression of the derivative of the admittance model with respect to each parameter (the term $\mathrm{d}\beta_p/\mathrm{d}\sigma$), which can be done easily for most models (see appendix F for the values of those derivatives for the two admittance models we will be using in this work).

It is also possible to calculate the gradient with respect to a change in width of a certain panel. For instance, let us assume that the curve Γ is parametrized by $u \in [0,1]$, and that a panel covers the part of the curve corresponding to $[0, u_0]$ with $u_0 \leqslant 1$ (see figure 4.4, right part). We assume that the panel has an admittance β_0 and the rest of the barrier is covered with an admittance β_1. The admittance function as a function of the parameter u can be written as:

$$\beta(u) = \beta_0\, H(u_0 - u) + \beta_1\, H(u - u_0)$$

The derivative of this function considered as a distribution with respect to u_0 can be directly written as:

$$\frac{\mathrm{d}\beta}{\mathrm{d}u_0}(u) = \beta_0\, \delta(u - u_0) - \beta_1\, \delta(u - u_0) = (\beta_0 - \beta_1)\, \delta(u - u_0)$$

So that the derivative of P with respect to u_0 is:

$$\begin{aligned} \frac{\mathrm{d}P}{\mathrm{d}u_0} =& \mathrm{Re}\left[\mathrm{i}k \int_0^1 p(u)\, q(u)\, J_\Gamma(u)\, (\beta_0 - \beta_1)\, \delta(u - u_0)\, \mathrm{d}u\right] \\ =& \mathrm{Re}\left[\mathrm{i}k\, (\beta_0 - \beta_1)\, p(u_0)\, q(u_0)\, J_\Gamma(u_0)\right] \end{aligned} \tag{4.27}$$

with J_Γ is the Jacobian of the transformation from the parameter space to the geometrical space. For instance, on a straight segment of physical length L parametrized by $u \in [0,1]$, the Jacobian is constant of value L.

It is interesting to notice that one can find the expression given in equation (4.27) with the given general expression for the shape derivative given in equation (4.22). Indeed, in order to make the parameter u_0 vary, one can also apply a local tangential velocity field $\boldsymbol{\theta}_{u_0}$ defined as: $\boldsymbol{\theta}_{u_0} = J_\Gamma(u_0)\, \mathbf{t}(u_0)$ in a neighborhood of $\mathbf{x}(u_0)$ and zero everywhere else. Then, applying equation (4.22), since the point $\mathbf{x}(u_0)$ is precisely a point where there is an admittance jump and since the velocity field is purely tangential, the derivative with respect to u_0 can be written as:

$$\frac{\mathrm{d}P}{\mathrm{d}u_0} = \mathrm{Re}\left[-\mathrm{i}k [\![\beta\, pq\, J_\Gamma(u_0)]\!]\big(\mathbf{x}(u_0)\big)\right] = \mathrm{Re}\left[\mathrm{i}k\, (\beta_0 - \beta_1)\, p(u_0)\, q(u_0)\, J_\Gamma(u_0)\right]$$

since here the admittance jump (defined as the value after minus the value before the discontinuity) at $\mathbf{x}(u_0)$ is: $[\![\beta]\!] = (\beta_1 - \beta_0) = -(\beta_0 - \beta_1)$. One can point out that this expression could not have been found with the classical shape derivative expression of a smooth line integral.

4.3.2.2 Derivative with respect to a node coordinate

We can also use the general shape derivative expression given in equation (4.22) in order to calculate the derivative of the P with respect to parameters describing the shape of the barrier. In order to be as general as possible, we will here consider the derivative with respect to a node coordinate of a "control mesh". Here we assume the BEM discretized context implemented in the software MICADO, which is that the boundary Γ is represented by a set of straight segments. Following the notations introduced in section 4.3.1.2, let $\mathbf{x}^{(i)}$ ($i \in [0:N]$) be the set of control nodes and $\Gamma_i = [\mathbf{x}^{(i-1)}, \mathbf{x}^{(i)}]$ ($i \in [1:N]$) be each straight segment defining the curve Γ (see figure 4.5). One can point out that here the barrier is oriented clockwise. The coordinates of

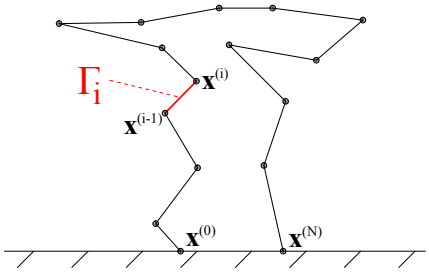

Figure 4.5: Representation of a generic barrier in the software MICADO, based on the control nodes $\mathbf{x}^{(i)}$ and assuming linear interpolation.

the control nodes are the parameters needed to define the geometry in the software MICADO. From this set of control nodes, MICADO generates the calculation mesh based on two criteria: a minimum number of elements per segment, and a minimum number of elements per wavelength. The calculation mesh is therefore usually much finer than the mesh defined by the control nodes. This differentiation between the control mesh and the calculation mesh is necessary since the calculation mesh should be frequency dependent, whereas the control mesh should not, since its variation is controlled by a broadband objective function.

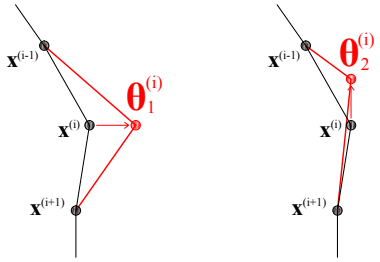

Figure 4.6: Definition of the node specific velocity field $\boldsymbol{\theta}_j^{(i)}$, which moves the control node $\mathbf{x}^{(i)}$ along the j^{th} component.

Now, the derivative of P with respect to a change of coordinate of the control node $\mathbf{x}^{(i)} = (x_1^{(i)}, x_2^{(i)})$ can be defined by applying a specific velocity field which moves only this control node along one direction $j = 1, 2$. We therefore define the velocity field $\boldsymbol{\theta}_j^{(i)}$ on the control nodes by:

$$(\forall k \in [0:N]) \quad \boldsymbol{\theta}_j^{(i)}\left(\mathbf{x}^{(k)}\right) = \delta_{ik}\,\mathbf{e}_j$$

with δ_{ik} being the Kronecker delta function and $\mathbf{e}_j$ the unit vector in the j^{th} coordinate. Then, on the two segments Γ_i and Γ_{i+1} adjacent to $\mathbf{x}^{(i)}$, the velocity field is linearly interpolated (see figure 4.6). This allows one to define the derivative of P with respect to $x_j^{(i)}$ as:

$$\frac{\mathrm{d}P}{\mathrm{d}x_j^{(i)}} = \frac{\mathrm{d}P}{\mathrm{d}\Gamma} \cdot \boldsymbol{\theta}_j^{(i)} \tag{4.28}$$

One should point out that a symmetrical velocity field is applied on the corresponding part of the image barrier, which means that when a node on the actual barrier is moved, its image is

moved as well in a symmetrical fashion.

4.3.3 Derivatives of the broadband objective function

Finally, one can write the expression of the derivative of the broadband objective function defined in section 4.1.2 with respect to a generic admittance or shape parameter x. Recalling equation (4.2) the derivative of e with respect to a parameter x is simply given by:

$$\frac{\mathrm{d}e}{\mathrm{d}x} = \frac{1}{\sum_n S_n} \sum_n S_n \frac{2\,P(f_n)}{P^{\mathrm{in}}(f_n)^2} \frac{\mathrm{d}P(f_n)}{\mathrm{d}x} \tag{4.29}$$

with $\mathrm{d}P(f_n)/\mathrm{d}x$ calculated as explained in section 4.3.2.

We are now able to calculate the gradient of the objective function with respect to the parameters describing the admittance and the shape. For each frequency, one only needs to know the state and the adjoint state, which is achieved by solving two classical BEM integral equations per frequency. This increases the computation time compared to the evaluation of the evaluation of the objective function only, but only by a small amount. Indeed, since the difference between the state and adjoint state equations only comes from source locations, the equations to solve both boundary fields use the same matrix but different right-hand sides, which does not severely increase the computation time.

Furthermore, the main advantage of using the adjoint state approach is, once the state and the adjoint state are known, the calculation of the gradient with respect to a parameter is fast (it is an explicit integral), and therefore a great number of parameters can be used without significant increase of computation time. Also, the expression of the gradient is simply a post-treatment of the BEM calculations, and therefore its calculation does not require coding a new integral equation solver, and can therefore be achieved using the results of any commercial BEM solver. For instance, in this work, the calculation of the states and adjoint states have been achieved using the software MICADO, whereas the calculation of the gradient have been performed in Matlab.

4.4 Numerical implementation

4.4.1 Numerical evaluation of the sensitivity expressions from BEM solutions

In order to evaluate numerically the sensitivity expressions derived in section 4.3.1, one only needs to know the values of the state p_Γ and adjoint state q_Γ at the boundary Γ and the value of the RMS pressure P which can be calculated from the boundary values of p thanks to the integral representation explained in chapter 2. The values of p_Γ and q_Γ are found by solving the two integral equations (2.12) and (4.20). In practice, one can set point sources at the actual source location (S) and at each receiver point (R_m), solve for the boundary fields p_Γ - corresponding to (S) - and q_{Γ,R_m} - corresponding to (R_m). From p_Γ one can calculate $p(R_m)$ and P, and since

the adjoint state equation is linear, finally calculate the adjoint state boundary values by:

$$q_\Gamma = \sum_m \frac{p(R_m)^*}{P}\, q_{\Gamma,R_m}$$

In a BEM discretized context, the solutions of the integral equations are typically a set of nodal values $\{p_\Gamma\}$ and $\{q_\Gamma\}$, corresponding to the values of the state and adjoint state at the BEM calculation mesh, which is finer than the control mesh. Typically, calculations were performed with a requirement of 10 elements per wavelength and at least 3 elements per straight segment (joining two following control nodes). MICADO assumes linear shape function and therefore for consistency we will assume linear shape functions as well to represent the two fields on the boundary. Therefore, defining $\{\mathrm{N}(a)\}^t = \{1-a, a\}$ and $\{f\}_i^t = \{f(\mathbf{x}^{(i-1)}), f(\mathbf{x}^{(i)})\}$ the two nodal values of a field f on the element Γ_i, we therefore have:

$$f_{|\Gamma_i}(a) = \{\mathrm{N}(a)\}^t \{f\}_i \qquad \text{with} \quad a \in [0,1]$$

Also, the tangential derivative of f is constant and is simply given by:

$$\left.\frac{\partial f}{\partial t}\right|_{\Gamma_i} = \frac{f(\mathbf{x}^{(i)}) - f(\mathbf{x}^{(i-1)})}{l_i} = \frac{1}{l_i}\{\mathrm{DN}\}^t \{f\}_i$$

where the vector DN is given by $\mathrm{DN} = \{-1, 1\}^t$ and $l_i = ||\mathbf{x}^{(i)} - \mathbf{x}^{(i-1)}||$ is the length of the element, which is also the value of the Jacobian of the transformation from the reference to the geometrical element.

4.4.1.1 Sensitivity with respect to a node coordinate

Now, consider the calculation of the derivative of P with respect to a $x_j^{(i)}$, with $0 < i < N$. Recalling equation (4.28), since the velocity field $\boldsymbol{\theta}_j^{(i)}$ is non zero only on the two segments Γ_i and Γ_{i+1}, one can write:

$$\begin{aligned}\frac{\mathrm{d}P}{\mathrm{d}x_j^{(i)}} =& \frac{\mathrm{d}P}{\mathrm{d}\Gamma}\cdot\boldsymbol{\theta}_j^{(i)} = \mathrm{Re}\left[\int_{\Gamma_i\cup\Gamma_{i+1}} \theta_j^{(i)}\, n_j \left(\frac{\partial p}{\partial t}\frac{\partial q}{\partial t} + k^2\left(\beta^2-1\right)pq\right)\mathrm{d}\Gamma - \mathrm{i}k[\![\beta pq\theta_j^{(i)}\, t_j]\!]^{(i)}\right] \\ =& \mathrm{Re}\Big[B_{i-}\, n_j^i + B_{i+}\, n_j^{i+1} + k^2\left(\beta_i^2-1\right)C_{i-}\, n_j^i + k^2\left(\beta_{i+1}^2-1\right)C_{i+}\, n_j^{i+1} \\ & - \mathrm{i}k\, p(\mathbf{x}^{(i)})q(\mathbf{x}^{(i)})(\beta_{i+1}t_j^{i+1} - \beta_i t_j^i)\Big]\end{aligned} \tag{4.30}$$

where β_i is the assumed constant value of the admittance on the segment Γ_i, $\mathbf{n}^i = (n_1^i, n_2^i)$ and $\mathbf{t}^i = (t_1^i, t_2^i)$ are respectively the normal and tangent vectors on the segment Γ_i, and the integrals B_{i-}, B_{i+}, C_{i-} and C_{i+} are defined as follows:

$$B_{i-} = \int_{\Gamma_i} \frac{\partial p}{\partial t}\frac{\partial q}{\partial t}\,\theta_j^{(i)}\,\mathrm{d}\Gamma \qquad B_{i+} = \int_{\Gamma_{i+1}} \frac{\partial p}{\partial t}\frac{\partial q}{\partial t}\,\theta_j^{(i)}\,\mathrm{d}\Gamma$$

$$C_{i-} = \int_{\Gamma_i} pq\,\theta_j^{(i)}\,\mathrm{d}\Gamma \qquad C_{i+} = \int_{\Gamma_{i+1}} pq\,\theta_j^{(i)}\,\mathrm{d}\Gamma$$

Due to the definition of the node-specific velocity field $\theta_j^{(i)}$ given in section 4.3.2.2, one has: $\{\theta_j^{(i)}\}_i = \{0,1\}$ and $\{\theta_j^{(i)}\}_{i+1} = \{1,0\}$. Using the linear shape function representation for the other fields yields:

$$\begin{aligned}
B_{i-} =& \frac{1}{l_i}\,\{q\}_i^t\{\mathrm{DN}\}\,\{\mathrm{DN}\}^t\{p\}_i \int_0^1 a\,\mathrm{d}a = \frac{1}{2\,l_i}\,\{q\}_i^t \begin{bmatrix} 1 & -1 \\ -1 & 1 \end{bmatrix} \{p\}_i \\
B_{i+} =& \frac{1}{l_{i+1}}\,\{q\}_{i+1}^t\{\mathrm{DN}\}\,\{\mathrm{DN}\}^t\{p\}_{i+1} \int_0^1 (1-a)\,\mathrm{d}a = \frac{1}{2\,l_{i+1}}\,\{q\}_{i+1}^t \begin{bmatrix} 1 & -1 \\ -1 & 1 \end{bmatrix} \{p\}_{i+1} \\
C_{i-} =& l_i \int_0^1 \{p\}_i^t\{\mathrm{N}(a)\}\,\{\mathrm{N}(a)\}^t\{q\}_i\,a\,\mathrm{d}a = l_i\,\{q\}_i^t \begin{bmatrix} 1/4 & 1/12 \\ 1/12 & 1/12 \end{bmatrix} \{p\}_i \\
C_{i+} =& l_{i+1} \int_0^1 \{p\}_{i+1}^t\{\mathrm{N}(a)\}\,\{\mathrm{N}(a)\}^t\{q\}_{i+1}\,(1-a)\,\mathrm{d}a = l_{i+1}\,\{q\}_{i+1}^t \begin{bmatrix} 1/12 & 1/12 \\ 1/12 & 1/4 \end{bmatrix} \{p\}_{i+1}
\end{aligned}$$

One can finally point out that these expressions correspond to integration over the actual barrier only, and therefore one should add the contribution due to the image barrier, which is calculated in a similar fashion.

Sensitivity with respect to nodes on the ground The sensitivities with respect to the nodes $\mathbf{x}^{(0)}$ and $\mathbf{x}^{(N)}$ are calculated in a similar way, except that the corresponding velocity fields are non zero on one element only. Besides, these nodes cannot be moved along the x_2 direction in order to keep the curve Γ connected to the ground. Therefore, one has:

$$\begin{aligned}
\frac{\mathrm{d}P}{\mathrm{d}x_1^{(0)}} =& \mathrm{Re}\left[B_{1+}\,n_1^1 + k^2\,(\beta_1^2-1)\,C_{1+}\,n_1^1 - \mathrm{i}k\,p(\mathbf{x}^{(0)})q(\mathbf{x}^{(0)})\beta_1 t_1^1\right] \\
\frac{\mathrm{d}P}{\mathrm{d}x_1^{(N)}} =& \mathrm{Re}\left[B_{N-}\,n_1^N + k^2\,(\beta_N^2-1)\,C_{N-}\,n_1^N + \mathrm{i}k\,p(\mathbf{x}^{(N)})q(\mathbf{x}^{(N)})\beta_N t_1^N\right] \\
\frac{\mathrm{d}P}{\mathrm{d}x_2^{(0)}} =& 0 \qquad , \qquad \frac{\mathrm{d}P}{\mathrm{d}x_2^{(N)}} = 0
\end{aligned}$$

4.4.1.2 Sensitivity with respect to an admittance parameter

Similarly, one can evaluate the derivative with respect to an admittance parameter from the nodal values of the state and the adjoint state. Say the segment Γ_i is covered by an admittance β_i function of several parameters $(b_1, b_2, ...)$. Recalling equation (4.26), one has:

$$\frac{\mathrm{d}P}{\mathrm{d}b_q} = \mathrm{Re}\left[\mathrm{i}k\,\frac{\mathrm{d}\beta_i}{\mathrm{d}b_q}\int_{\Gamma_i} pq\,\mathrm{d}\Gamma_i\right] = \mathrm{Re}\left[\mathrm{i}k\,\frac{\mathrm{d}\beta_i}{\mathrm{d}b_q}\,l_i\,\{q\}_i^t \begin{bmatrix} 1/3 & 1/6 \\ 1/6 & 1/3 \end{bmatrix} \{p\}_i\right]$$

4.4.2 Mesh refinement close to corners

As we have seen in section 2.4, the presence of a corner with an exterior angle greater than π induces a local singularity in the pressure gradient, which becomes unbounded although integrable in the vicinity of the corner. It has also been pointed out this phenomenon causes inaccuracy in numerical calculations involving the tangential derivative. Since the shape derivative expres-

sion given in equation (4.22) does require integration of the product of the state and adjoint state tangential derivative, it is expected that the evaluation of the sensitivity with respect to a control node coordinate will not be accurate close to corners.

One approach to somewhat limit this effect is to force a finer mesh in the vicinity of corners. In the BEM software MICADO, two meshing criteria have to be provided by the user on each segment defining the geometry: c_1 the minimum number of elements per wavelength, and c_2 the minimum number of elements per segment. From the knowledge of the geometry, one can evaluate the exterior angle at the beginning and at the end of the segment Γ_i. We will call the maximum of those two angles ϕ_i. In the rest of this work, given two generic values of the criteria c_1 and c_2 (typically those two values will be taken as $c_1 = 10$ and $c_2 = 3$ when the shape derivative will be evaluated, and $c_1 = 6$ and $c_2 = 1$ otherwise), the following values for the meshing criteria on each segment are proposed:

$$\begin{cases} c_1^i = c_1 \left[1 + \max\left(\dfrac{\phi_i}{\pi} - 1, 0\right)\right] \\ c_2^i = c_2 \left[1 + 4\ \max\left(\dfrac{\phi_i}{\pi} - 1, 0\right)\right] \end{cases}$$

These expressions are heuristic and were found to be a good compromise in limiting both the inaccuracy in the shape derivative numerical evaluation and the computation time. Nevertheless, as it has been shown in section 2.4, some inaccuracy will remain even with an extremely fine mesh since usual shape functions cannot resolve the singular behavior of the pressure gradient. The purpose of this refined meshing strategy is essentially to make sure that the error in the evaluation of the shape derivative is not excessively large.

4.4.3 Validation

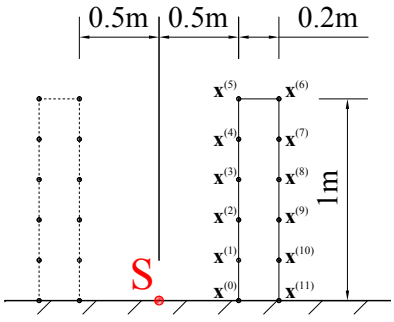

Figure 4.7: Schematic of the barrier (solid line) and its image (dashed line) used for the validation of the shape sensitivity calculations. The control nodes are numbered from 0 to 11 as shown.

To validate the calculation of the sensitivity with respect to control nodes coordinates and admittance parameters, we consider a simple wall barrier geometry (1 m high, 0.2 m wide). Control nodes are placed every 20 cm, so there are $N = 12$ nodes on the true barrier (see figure 4.7), and therefore 22 shape independent variables (corresponding to the two coordinates of each node except the nodes on the ground which only have one shape variable, their first coordinate). The node coordinates of the image barrier are not considered as variables since

their displacement is not independent of that of their corresponding nodes on the actual barrier. In addition, the barrier is covered by a fictitious admittance distribution which we set to be:

$$\beta_i = \frac{1+\mathrm{i}}{2}\left(1 - \frac{i-1}{N-1}\right) \qquad i \in [1 : N-1]$$

There are therefore 11 complex admittance parameters, hence 22 real admittance parameters (each corresponding to either the real and imaginary part of the segment admittance). We calculate the derivative of the broadband objective functions (with four frequencies per third-octave between 100 and 2500 Hz) with respect to every node coordinate and every admittance variable using equation (4.29) and the approach exposed in section 4.4.1. The state and the adjoint state are solved with the two MICADO meshing criteria set as: $c_1 = 10$ and $c_2 = 3$.

The sensitivity can also be estimated by a finite difference approach. Considering for instance the variation of a generic parameter x, one can consider e as a function of this parameter, and given a small parameter ϵ, one can estimate the sensitivity as:

$$\frac{\mathrm{d}e}{\mathrm{d}x} \approx \frac{e(x+\epsilon) - e(x)}{\epsilon}$$

However, it is not easy to choose the parameter ϵ a priori, since by setting it too small we would run into numerical errors, and by setting too large the variation of e might be no longer well described by a linear curve. If one assumes that the numerical evaluation of the sensitivity based on the adjoint state yields at least the correct order of magnitude, one can choose the parameter ϵ to ensure that the function approximately varies by a relative amount δ. Calling $\mathrm{d}e/\mathrm{d}x|_{\mathrm{AS}}$ the evaluation of the gradient using the adjoint state approach, one could then write:

$$e(x+\epsilon) \approx e(x) + \epsilon \left.\frac{\mathrm{d}e}{\mathrm{d}x}\right|_{\mathrm{AS}}$$

Now say that we would like the function to vary by about 0.1%, we set $\delta = 10^{-3}$ and we can write: $e(x+\epsilon) = (1+\delta)\, e(x)$. This yields;

$$\delta\, e(x) \approx \epsilon \left.\frac{\mathrm{d}e}{\mathrm{d}x}\right|_{\mathrm{AS}} \quad \Leftrightarrow \quad \epsilon \approx \tilde{\epsilon}(x) \qquad \text{with} \quad \tilde{\epsilon}(x) = \delta \left|\frac{e(x)}{\mathrm{d}e/\mathrm{d}x|_{\mathrm{AS}}}\right|$$

One can then set a range of possible values for ϵ in the vicinity of $\tilde{\epsilon}(x)$ - for instance in the range $[0.1\,\tilde{\epsilon}(x), 10\,\tilde{\epsilon}(x)]$ - and then do a polynomial fit. The sensitivity is then the coefficient of the linear term of this polynomial.

Even though this process is relatively tedious, it is clear that errors may remain in the evaluation of the sensitivity using finite differences. This is one of the reasons why sensitivities are usually not calculated with this approach. Here this calculation is done for the purpose of validating the expressions derived in section 4.3.1.

4.4.3.1 Shape parameters

Results for the sensitivities with respect to shape parameters are presented table 4.1. Writing $\nabla e|_{\mathrm{AS}}$ the gradient vector obtained by the adjoint state calculation of the sensitivities and $\nabla e|_{\mathrm{FD}}$

that obtained using finite differences, one can define the error based on the infinity-norm of the gradient vector, defined as:

$$E_\infty = \frac{||\nabla e|_{\text{FD}} - \nabla e|_{\text{AS}}||_\infty}{||\nabla e|_{\text{FD}}||_\infty}$$

which gives an estimate on how accurate the whole gradient vector is, since this is really what is used in the optimization algorithm.

Relative errors for each node and each component between the sensitivity value derived from finite differences (FD) and that derived from the adjoint state approach (AS) are shown, as well as the error E_∞ based on the infinity norm for all nodes and each component. First of all, one can notice that the displacements of nodes located close to the source (nodes 0 to 5) induce a much bigger change in the objective function than nodes on the opposite side (nodes 6 to 11). The relative error is also significantly larger for the opposite nodes, but because the sensitivity is much smaller on this side, this should not influence the optimization process too much. Also, one should realize that without the added jump terms in the shape derivative formula given in equation (4.22), one would have obtained zero for the calculation of the second component of most nodes sensitivities (except the nodes 5 and 6), since their variations correspond to tangential velocity fields.

Even though the error is rather small for most nodes with a significant sensitivity, it is large for nodes 5 and 6, that is at the nodes making the corners of the wall. Indeed, there is a large difference in the error based on the infinity norm when the two corner nodes are taken into account or not: 35% and 43% with, 1.3 and 2.8% without. Such a large error when evaluating the sensitivity with respect to corner node coordinates was expected, as mentioned in section 4.4.2, due to the singularity in the pressure gradient which cannot be resolved numerically. It is however noticed that sensitivities at the corner have at least the correct sign, which means that an actual decrease (respectively increase) in the objective function by increasing a node coordinate is predicted by the adjoint state sensitivity calculation to be a decrease (respectively an increase) as well, even though the predicted change might be significantly over- or under-estimated. Because of this fact, it is likely that this source of error will not cause too big an issue in the optimization process.

Node #	Shape sensitivity values					
	First component			Second component		
	FD	AS	Err.[%]	FD	AS	Err.[%]
0	-8.59e-2	-8.57e-2	0.1	-	-	-
1	2.39e-2	2.39e-2	<0.1	-1.92e-3	-1.92e-3	0.3
2	8.69e-2	8.75e-2	0.8	-4.85e-3	-4.97e-3	2.6
3	-5.70e-2	-5.59e-2	1.9	-1.42e-3	-1.41e-3	<0.1
4	-3.35e-2	-3.37e-2	0.6	-4.28e-4	-4.41e-4	3.1
5	-3.93e-2	-8.84e-3	77.5	3.10e-2	5.14e-3	83.4
6	-4.09e-2	-4.47e-2	9.2	-5.88e-2	-5.61e-2	4.5
7	1.29e-2	1.30e-2	0.3	-5.68e-4	-4.30e-4	24.2
8	-1.53e-3	-1.78e-3	16.2	-2.48e-4	-2.03e-4	18.1
9	3.02e-3	3.06e-3	1.2	-2.07e-5	-5.25e-5	154.1
10	3.41e-3	3.45-3	0.9	-2.39e-4	-1.97e-4	17.8
11	-5.83e-3	-5.84e-3	0.2	-	-	-
Error E_∞	-	-	35	-	-	43

Table 4.1: Comparison of the broadband objective function sensitivity with respect to control nodes coordinates for the geometry given in figure 4.7, calculated with finite differences (FD) and the adjoint state approach (AS) (with four frequencies per third-octave between 100 and 2500 Hz).

4.4.3.2 Admittance parameters

A similar comparison can be made for admittance parameter sensitivities. Here it has been assumed that the fictitious admittance distribution is constant over frequency and that the parameters describing the admittance are the admittance values themselves. Results are presented in table 4.2. The error is small for most segments, although slightly larger close to corners (segments 5, 6 and 7). The error is however smaller than in the node coordinate case, since the admittance sensitivity depends on the state and adjoint state values only, which are solved with a much better accuracy than for the tangential derivatives.

Segment #	Shape sensitivity values					
	Real part			Imaginary part		
	FD	AS	Err.[%]	FD	AS	Err.[%]
1	-8.55e-2	-8.56e-2	0.1	1.24e-2	1.24e-2	<0.1
2	-1.73e-2	-1.73e-2	<0.1	2.25e-3	2.26e-3	0.4
3	-2.17e-2	-2.17e-2	<0.1	7.64e-3	7.65e-3	0.2
4	-1.14e-2	-1.14e-2	0.1	1.13e-2	1.13e-2	0.1
5	-1.02e-2	-1.03e-2	0.4	-4.23e-3	-4.27e-3	1.0
6	-4.95e-3	-4.98e-3	0.6	-2.02e-2	-2.02e-2	0.2
7	-4.18e-3	-4.21e-3	0.6	-2.87e-4	-2.71e-4	5.5
8	5.26e-4	5.27e-4	0.2	9.93e-4	9.89e-4	0.4
9	-8.22e-3	-8.88e-3	8.0	-2.08e-4	-2.08e-4	<0.1
10	1.82e-4	1.74e-3	4.3	9.47e-4	9.48e-4	0.1
11	2.74e-5	3.52e-5	28.2	-1.00e-3	-9.99e-4	0.1
Error E_∞	-	-	0.2	-	-	0.2

Table 4.2: Comparison of the broadband objective function sensitivity with respect to admittance parameters for the geometry given in figure 4.7, calculated with finite differences (FD) and the adjoint state approach (AS) (with four frequencies per third-octave between 100 and 2500 Hz).

4.5 Conclusion

The goal of this chapter was essentially to show that it is possible to calculate efficiently and accurately the sensitivity of the chosen objective function (the weighted broadband attenuation of the low-height noise barrier) with respect to parameters describing the shape and the admittance distribution of the barrier. Convenient derivation of the sensitivity expressions can be made by expressing the scattering problem under a weak formulation and by consideration of the adjoint state, which is found to be the pressure field solution of another scattering problem. Although this approach has been followed by many authors including Allaire [146] and Bonnet [149], we have focused more specifically on the context of the MICADO software (BEM resolution with linear shape functions) and in the assumed modeling context (2D modeling, image barrier approximation, rigid ground). The given expressions however include extra terms to take into account discontinuities of the different fields.

It is also found that shape sensitivity calculation is not accurate close to geometrical singularities, namely corners, as soon as the exterior angle exceeds π. This is due to a singularity in the pressure gradient close to corners, which cannot be resolved properly by classical finite element discretization techniques. A refinement strategy specifically close to corners is proposed to limit the error, which nevertheless stays important. Is is however believed that this inaccuracy will not cause severe issues in the optimization process.

Chapter 5

Application to the shape optimization of rigid barriers

5.1 Introduction

The optimization algorithm is first applied to the case of entirely rigid barriers. Acoustical treatments which can typically provide absorption can indeed help in increasing the performance of the low-height noise barrier, however such treatments can be costly and require proper packaging to avoid any health hazard issues. Sustainability of an absorbing treatment acoustical performance is also an issue especially in outdoor environments. Therefore in this chapter we focus on purely rigid barriers, which could be made out of concrete for instance, but we allow the shape of the barrier cross-section to be optimized. This implies that the admittance β is set to zero over the whole boundary Γ.

Several "starting" geometries are considered, which we will referred to as: small wall, medium wall, quarter cylinder, T-shape and Gamma-shape (see figure 5.1). The medium wall seems like the most natural choice for a low-height barrier. The small wall geometry (which is essentially a simple wall but only 0.5 m high) has been chosen to see if the shape optimization process would tend to increase the height or not. The quarter-cylinder was chosen because a round geometry diffracts sound in a radically different way compared to more usual straight geometries. The T-shape geometry also seemed like a natural choice as it is considered in general as one of the best geometry for a noise barrier (especially in the highway case). Finally, the Gamma-shape geometry is essentially a more compact version of the T-shape, and therefore it seemed interesting to study how much the far end of the "T" would influence the result of the optimization.

The control mesh of each initial geometry is first generated with a maximum distance between two adjacent nodes of 2 cm. Depending on the geometry, this yields 62 to 183 control nodes, therefore 112 to 364 optimization variables (details are given in the caption of figure 5.1). The optimization algorithm is the steepest descent method with backtracking and box projection (as explained in section 3.5 and appendix D).

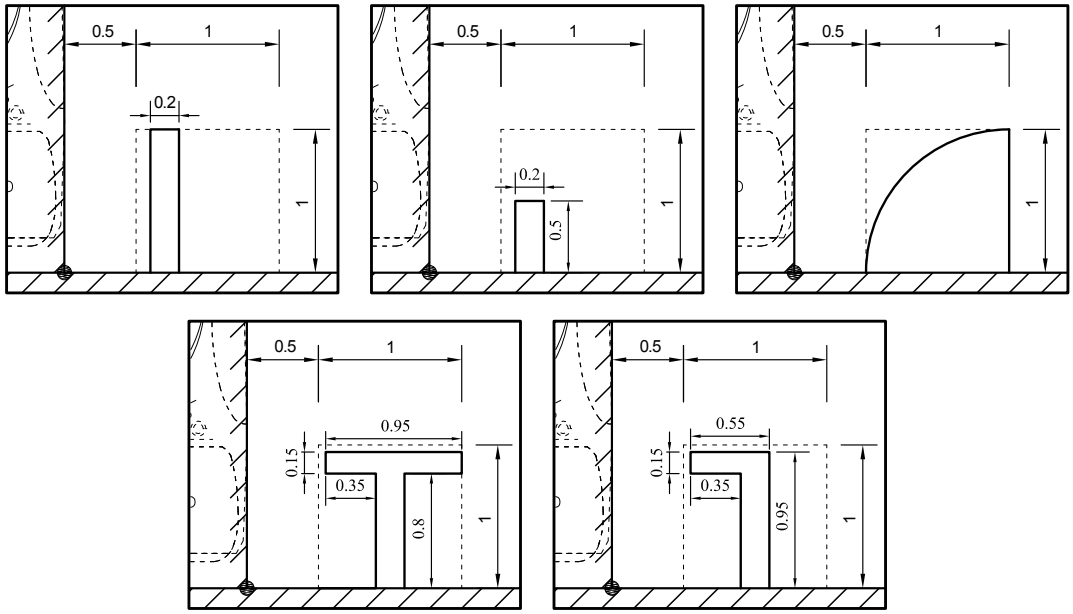

Figure 5.1: Definition of the five initial geometries for the rigid low-height barrier shape optimization. Dimensions are given in meters. The dotted line represents the one meter wide constraint box. The number of nodes representing each geometry is indicated as well in parenthesis. Top left: medium wall (112 nodes) ; top middle: small wall (62 nodes) ; top right: quarter cylinder (131 nodes) ; bottom left: T-shape (183 nodes) ; bottom right: Gamma-shape (143 nodes).

5.2 Results

First, geometries at the initial and final step of the optimization algorithm for the considered cases are shown in figure 5.2. Corresponding broadband insertion losses in the considered frequency range are shown in table 5.1, as well as third-octave insertion losses in figure 5.3. First of all, one can notice that the shape optimization increased the efficiency significantly in all cases (of about 6 dB(A) in general and of 11 dB(A) for the medium wall geometry) except for the quarter cylinder case (+ 3 dB(A)). However, the initial performance of the quarter cylinder barrier was much higher than those of the other cases, and therefore one could have expected a smaller improvement due to the optimization.

Table 5.1: Comparison of broadband insertion losses in dB(A) in the 100-2500 Hz range for the considered starting geometries and corresponding optimized geometries.

	Medium wall	Small wall	Quarter cylinder	T-shape	Gamma-shape
Initial	4.2	1.8	10.3	5.3	5.9
Optimized	15.2	8.2	13.3	11.3	11.1

For all geometries, the part of the barrier opposite to the source (the “back” side) does not undergo strong alterations. Indeed, since the displacement of the geometry is based on the sensitivity, which is small for nodes located on this part of this barrier as shown in section 4.4.3, the algorithm had no reasons to alter the back side significantly. Furthermore, this also implies that any type of treatment could be applied on the back side of the barrier, due to its limited influence on the acoustic performance. For instance, one could think of covering it with vegetation or any material that could meet aesthetic or environmental requirements.

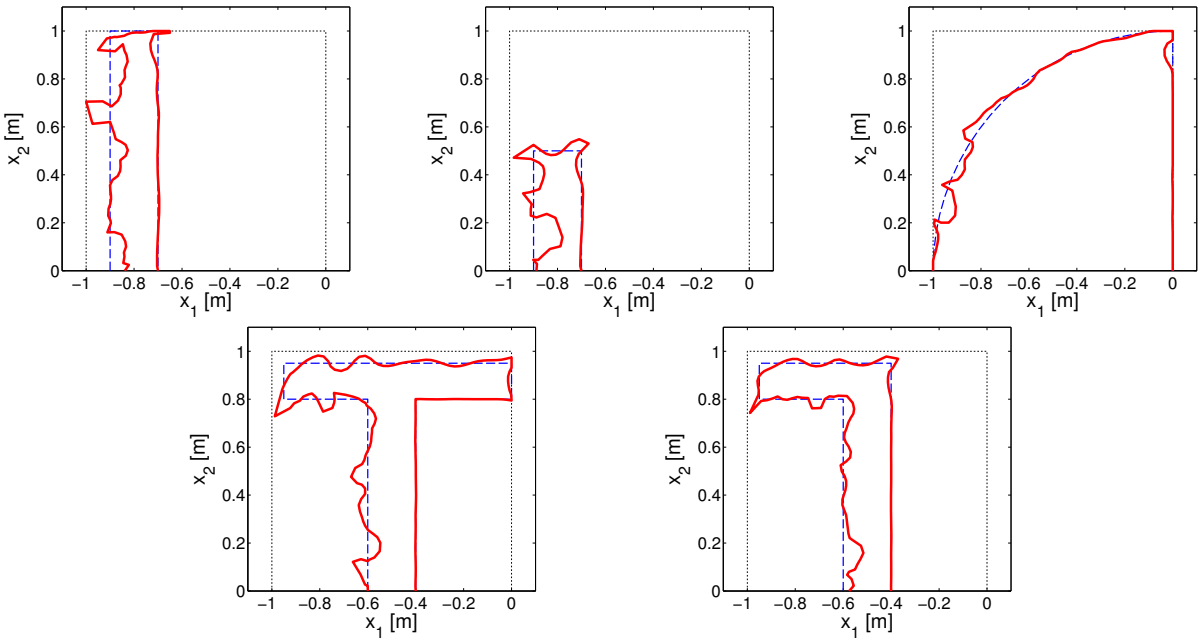

Figure 5.2: Initial and optimized geometries for the considered starting geometries and assuming rigid admittance coverage. Top left: medium wall - top center: small wall - top right: quarter cylinder - bottom left: T-shape - bottom right: Gamma-shape. Solid line: optimized geometry - dotted line: initial geometry. The one meter wide constraint box is shown as well.

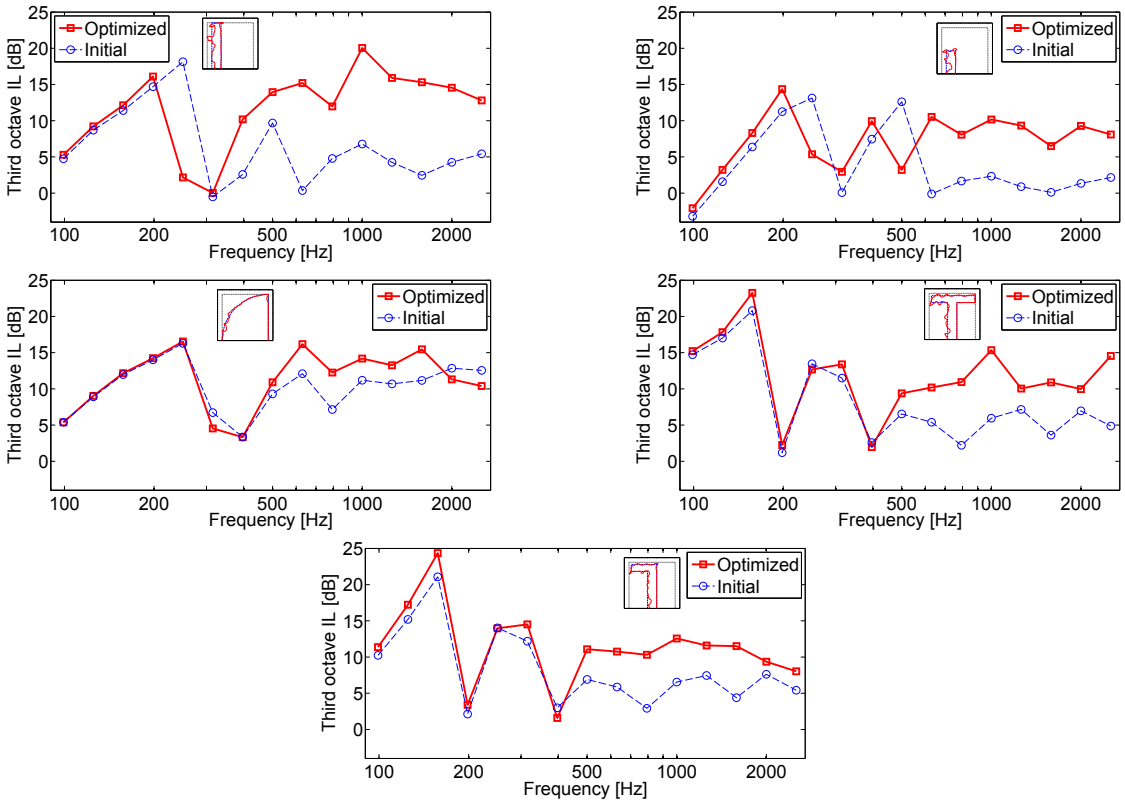

Figure 5.3: Comparison of third-octave insertion losses in dB between initial and optimized geometry, and for the five considered starting geometries. Solid line: optimized geometry - dotted line: initial geometry. Top left: medium wall - top right: small wall - middle left: quarter cylinder - middle right: T-shape - bottom: Gamma-shape.

However, there seems to be a general trend in the way the shape optimization altered the different geometries: the part of the barrier most exposed to the radiation of the source - the "source" side - tends to become more irregular. Especially in the small wall case, instead of significantly increasing the height, the optimization rather made the barrier cross section more irregular, and indeed the broadband efficiency of the optimized small wall is higher than that of the initial straight medium wall. From the third-octave insertion losses (see in figure 5.3), one can see that all optimized geometries attenuate higher frequencies (typically above 600 Hz) more efficiently. We believe that the insertion losses of the optimized geometries are higher because multiple reflections phenomena between the barrier and the baffle (tramway side) are somewhat prevented due to the irregularities. However, since the barriers have been assumed rigid, there is no absorption of acoustic energy, which implies the increase of attenuation at higher frequencies is related to the redirection of the acoustic energy, away from the shadow zone. To have a closer look at this effect, one can compare the intensity map between the initial and optimized geometry, calculated at a frequency where the attenuation is increased. The time-averaged intensity vector $\mathbf{I}$ is calculated at one frequency as:

$$\mathbf{I} = \frac{1}{2}\,\mathrm{Re}(p^*\mathbf{v}) = \frac{1}{2}\,\mathrm{Re}\Big(\frac{p^*\nabla p}{\mathrm{i}k\,\rho_0 c_0}\Big)$$

with $\mathbf{v}$ the particle velocity which has rewritten in terms of the pressure gradient using Euler's equation. The pressure gradient is calculated via its integral representation, as explained in chapter 2. Examples of intensity maps calculated at 1000 Hz in the medium wall case and the small wall cases are shown in figure 5.5. One can indeed notice that for the optimized geometry, the energy tends to propagate mostly in the x_2 direction, parallel to the vertical baffle, whereas in the initial geometry a significant part of the energy is directed towards the shadow zone. One can also notice the presence of recirculating regions of sound energy with the optimized irregular shapes, which would also cause less energy to reach the shadow zone. Those two effects could explain why there is an increase of attenuation behind the barrier with the optimized shapes compared to the case of simple straight barriers.

Finally, the evolution of the objective function for all geometries is shown in figure 5.4. One can notice the convergence was rather fast (at most a few dozens iterations). This is consistent with the fact that, as pointed out in chapter 3, sensitivity-based methods are inherently faster than evolutionary methods (convergence is achieved in a small number of iterations).

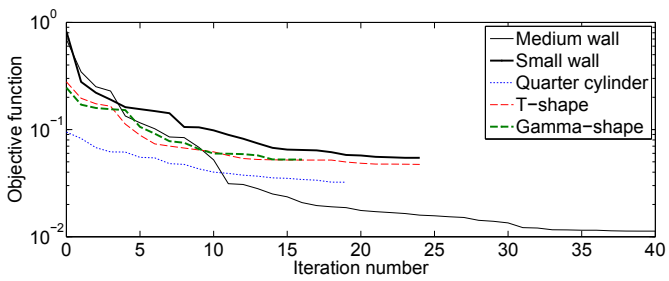

Figure 5.4: Evolution of the objective function during the optimization for the five geometries given in figure 5.1, with either 4 or 10 frequencies per third octave. Thin solid line: medium wall - thick solid line: small wall - dotted line: quarter cylinder - thin dashed line: T-shape - thick dashed line: Gamma-shape.

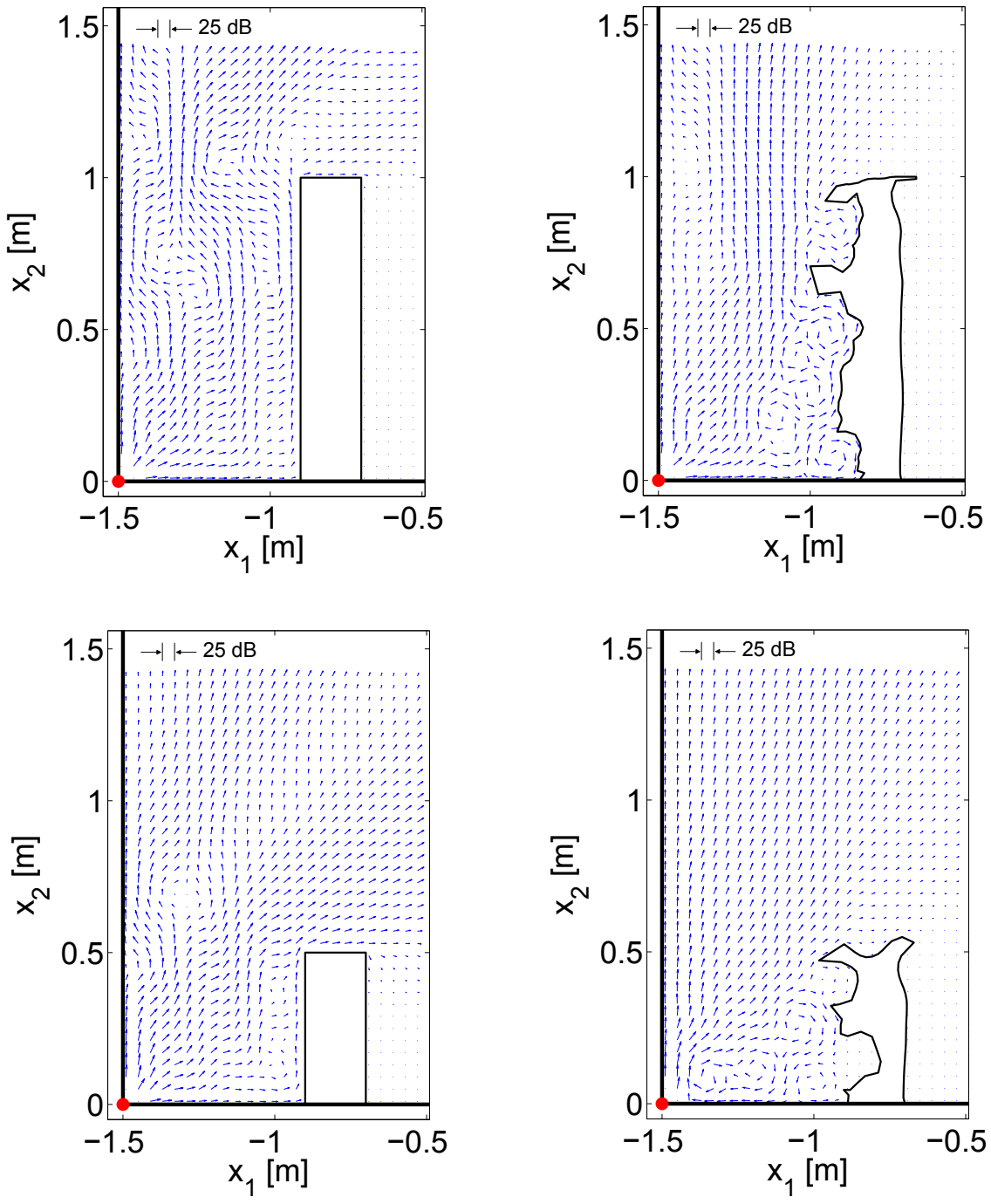

Figure 5.5: Comparison of intensity maps at 1000 Hz between the initial and optimized geometries calculated on a grid of step $h = 4\,\text{cm}$. The intensity vector is calculated as $\mathbf{I} = \text{Re}\,(p^* \mathbf{v})/2$ with $\mathbf{v}$ the particle velocity. Each vector is scaled so that its norm is the norm of the intensity vector $\mathbf{I}$ in dB (length h: reference value (maximum intensity) - length zero: reference minus 25 dB). Top left: initial medium wall - top right: optimized medium wall - bottom left: initial small wall - bottom right: optimized small wall.

5.3 Efficiency of smoothed and randomly perturbed shapes

In order to make sure that the irregularities generated by the shape optimization physically explain the increase of efficiency and are not simply due to numerical artifacts, one can consider smoothed versions of the optimized generated shapes and compare the efficiency of this smoothed shape compared to the original one. The smoothing is simply based on a low-pass filtering of the nodes coordinates, as explained in appendix G, with a characteristic length $l = 0.2\,\mathrm{m}$. The smoothing process essentially removes the sharp angles in the geometry but keeps the general features of the shape the same. Third-octave insertion losses for the optimized medium wall and small wall geometries and their smoothed versions are given in figure 5.6. One can indeed notice that the efficiency is significantly lowered above a few hundred hertz when the shape is smoothed, and that is precisely the range where the attenuation was increased between the initial straight geometry and the optimized irregular geometry. This seems to suggest that the presence of the irregularities, especially the sharp features, physically alter the sound field in such a way that the attenuation in the shadow zone is increased, by an energy redirection or scattering effect, as explained in the previous section.

Nevertheless, one could also wish to know the influence on the performance of a small perturbation of the optimized shape, for instance due to some inaccuracy in the barrier manufacture process. For this purpose, several calculations were done by randomly perturbing each node coordinate of the optimized medium wall, following normal distributions of a given standard deviation, taken here as 5 mm. It has been found that the variability on the insertion losses is more important at higher frequencies (see in figure 5.7), which however causes a decrease smaller than 1.5 dB(A) on the broadband efficiency (with 90% confidence). This suggests once again that the features of the optimized geometry are important for the noise barrier good performance, although small perturbations will not completely annihilate the benefit of the optimized geometry.

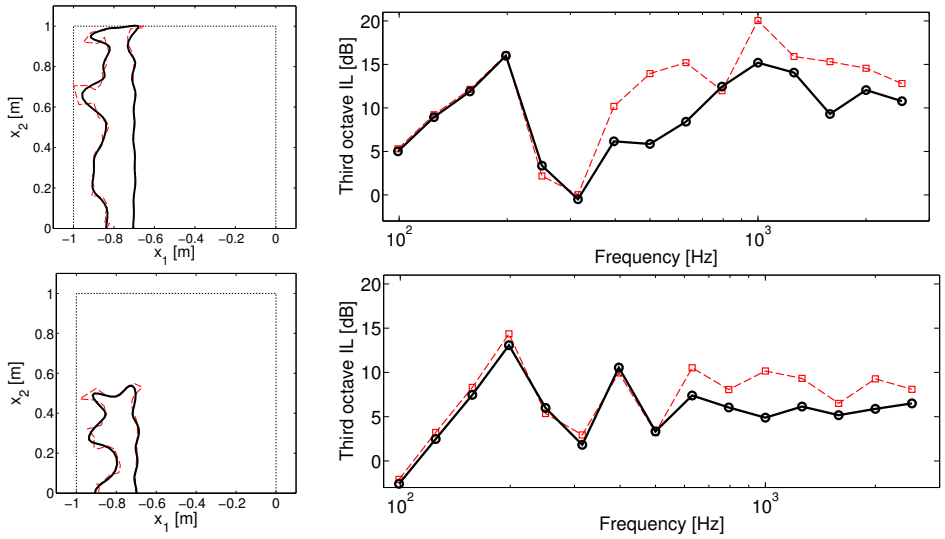

Figure 5.6: Comparison of optimized geometries and smoothed optimized geometries and comparison of third-octave insertion losses in dB. The low-pass characteristic length is here $l = 0.2\,\mathrm{m}$. Left: geometry comparison - right: third-octave insertion losses in dB. In both plots, the thin dotted line corresponds to the original optimized geometry and the thick solid line to the smoothed geometry. Top: medium wall - bottom: small wall.

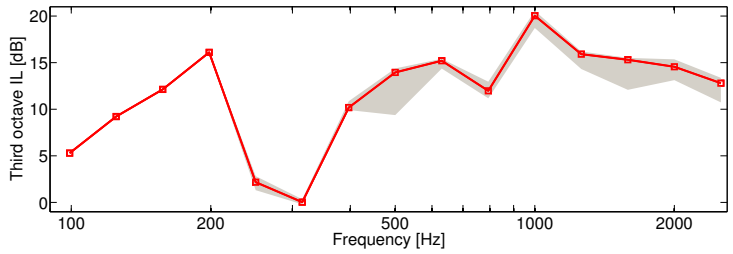

Figure 5.7: Third octave insertion loss variability for the medium wall optimized geometry (in dB). The shaded area corresponds to the 90% confidence interval of each third-octave insertion loss value under normally distributed random perturbations of the optimized geometry node coordinates (with a standard deviation of 5 mm). Third-octave insertion losses of the unperturbed optimized geometry are shown as well (thick red line).

5.4 Influence of the modeling approximations

The shape of the barrier has been optimized under several important assumptions in order to keep the computation time sufficiently small to allow a convenient optimization process: 2D modeling, rigid ground and modeling of the tramway as a vertical infinite baffle. However, after the optimization has been performed and some optimized designs have been found, the issue of reducing computation time is not as critical since numerical simulations will be performed for a few designs only. We therefore end this chapter by considering more complex (meaning also a lot more computationally expensive) modeling situations in order to predict the performance of the shape-optimized barriers for some of the considered starting geometries.

5.4.1 Effect of the tramway cross-section and of the ground impedance in 2D

A finer description of the tramway geometry might indeed influence the performance of the noise barrier for several reasons. For instance, at low frequencies, we expect that the tramway will not act as an infinite reflector because of its finite height. Also, at high frequencies, fine details of the tramway cross section such as the curvature of the side and the presence of the gap underneath the tramway might also have a significant effect on the sound field.

Furthermore, the assumption of rigid ground is clearly not valid in all circumstances since the measurements of Pallas et al. were also done in grassy-like environments, and showed that a soft ground close to the source can significantly reduce the noise emission of the tramway [26], although this is also influenced by the stiffness of the rail pads. Indeed, the question of the relative importance of the barrier design (shape and surface treatment) to the ground effect in assessing the performance of noise barriers is crucial and has been discussed by several authors. Hothersall et al. [118] claimed that most the time going from hard to soft (grass-covered) ground has a similar effect regardless of the configuration of the barrier, which is to increase the broadband insertion loss by 5 dB(A). However, Hutchins et al. [59] showed that a change in barrier shape in a highway context has a greater effect when the ground is rigid, and therefore the predicted benefit of a barrier would be decreased when the finite impedance of the ground is considered. Furthermore, Thorsson [10] showed that optimizing the impedance of the ground close to the source can yield a significant improvement on the insertion loss at selected

frequencies of about 15 dB, but also showed that optimizing the impedance on a low-height barrier, even with an optimized ground, can yield another gain of 10 to 15 dB. This means that even in the presence of a soft ground, at least in the context of urban low height barriers, the barrier design can have a significant effect on the attenuation. The author makes the suggestion that a soft ground surface close to the source basically acts as a reduction of the source power level, which is consistent with the results observed by Hothersall et al. [118].

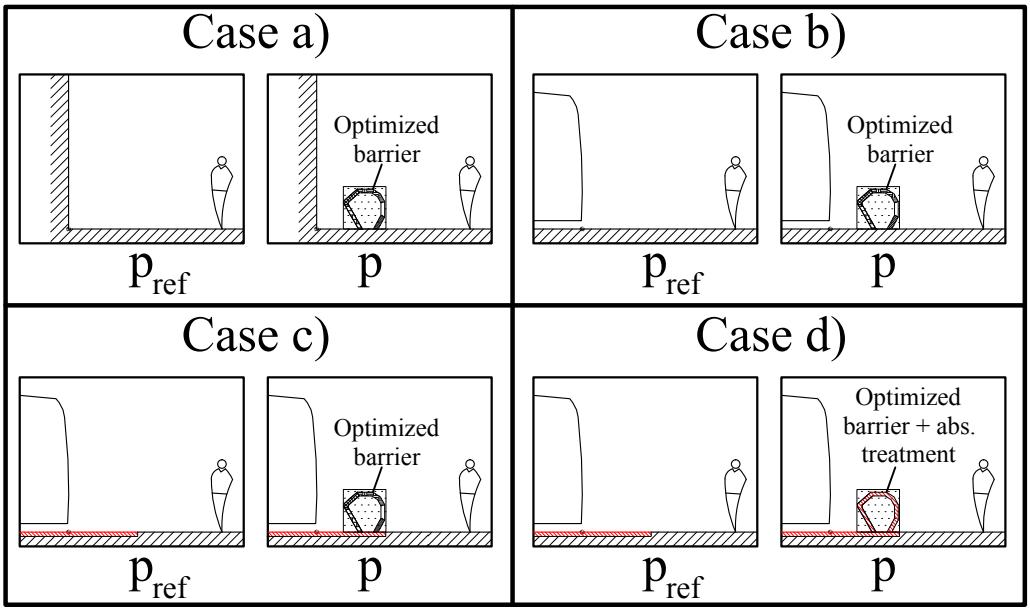

Figure 5.8: Description of the four cases to assess the effect of an absorbing ground (Delany & Bazley layer with $\sigma = 50\,\mathrm{kPa\,m\,s^{-2}}$ and $d = 5\,\mathrm{cm}$) and of a more realistic tramway geometry. In each case, p is the field at the receiver with the barrier present and p_{ref} is the field without the barrier. The attenuation is given by the ratio $|p_{\mathrm{ref}}/p|$ in dB. a) Rigid ground, infinite baffle and optimized barrier treatment - b) rigid ground, realistic tram and optimized barrier treatment - c) absorbing ground, realistic tram and optimized barrier treatment - d) absorbing ground, realistic tram and uniform absorbing barrier treatment

Hence, we have to assess how much the rigid ground and vertical baffle approximations influence the predicted benefit of the optimized barrier shapes. In this context, the description of the reference field used in the calculation of the attenuation is critical, and should be chosen to evaluate the benefit of the barrier only. To do so, we will compare BEM calculations of insertion losses using four different cases detailed in figure 5.8. In every case, the attenuation is given by the ratio $|p/p_{\mathrm{ref}}|$ in dB. Third-octave insertion losses results are shown in figure 5.9 and broadband efficiencies based on the tramway spectrum in the 100-2500 Hz range are shown in table 5.2. The absorbent treatment on the ground and on the barrier in case d) is modeled with a Delany & Bazley layer with $\sigma = 50\,\mathrm{kPa.s/m^2}$ and $d = 5\,\mathrm{cm}$, which corresponds to a strongly absorptive porous material and therefore should be considered as a limiting case.

Comparing the results obtained for cases a) and b) in figure 5.9, one can conclude that the infinite baffle approximation for the tram is relatively accurate to predict the insertion loss of the optimized barriers, although some of the interference dips and peaks are shifted in frequency and not as marked when the more realistic geometry is considered. The differences are typically more important in the low-frequency range (below 300 Hz) although some difference can be observed as well at higher frequencies. Those differences yield an over-prediction in the

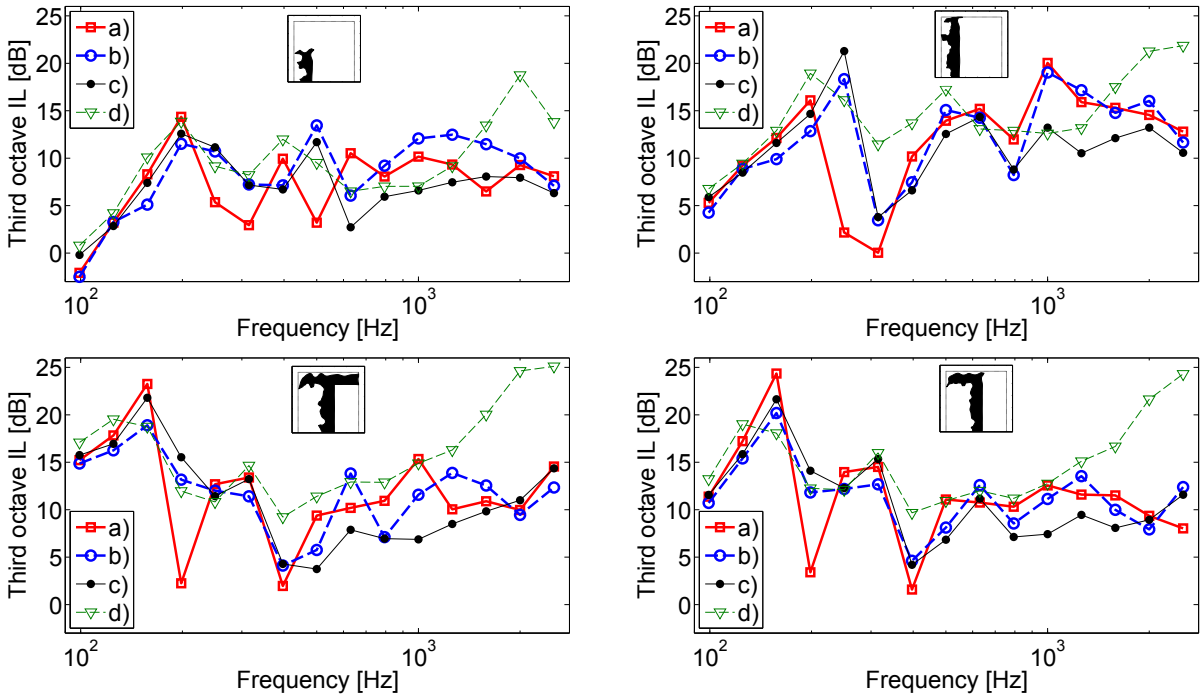

Figure 5.9: Comparison of third-octave insertion losses for four considered optimized geometries and for the four cases detailed in figure 5.8. Top left: small wall - top right: medium wall - bottom left: T-shape - bottom right: Gamma-shape.

Table 5.2: Comparison of broadband insertion losses in dB(A) in the 100-2500 Hz range for the four cases described in figure 5.8 and for the considered initial geometries.

Cases	Barrier initial geometry			
	Small wall	Medium wall	T-shape	Gamma-shape
a)	8.2	15.2	11.3	11.1
b)	9.9	14.2	10.1	10.5
c)	6.0	11.9	6.9	8.1
d)	7.7	13.4	14.1	12.7

broadband efficiency of about 1 dB(A) for all geometries except the small wall geometry, for which idealizing the tramway as an infinite baffle actually under-predicts the performance of the optimized barrier by almost 2 dB(A).

Comparison between the results of cases b) and c) shows that, in agreement with Hutchins et al. [59], the benefit due to the barrier only (measured by the insertion loss) is reduced when the ground is treated. This effect mostly happens above 400 Hz, inducing a decrease of the broadband insertion loss of 3-4 dB(A). This decrease can be explained by the fact that the pressure level with the barrier, with and without absorbing ground, is not changed much, whereas the level without the barrier (incident level) is significantly decreased when the ground is absorbing. Further, one should recall that the ground treatment chosen in case c) corresponds to a strongly absorbing material, and therefore it is believed that more usual ground treatments, such as grass, would induce a smaller decrease of performance compared to the case of a rigid ground. Furthermore, treating the ground might not be a feasible solution as opposed to building an optimized barrier. In this case, the benefit of the barrier might be much closer to what has been predicted in case b). It also seems clear that in the case of an already existing rigid ground,

treating the ground with absorbing material will act concurrently with the barrier in decreasing the noise levels in the shadow zone, as pointed out by Thorsson [10]. The point of considering case c) was to make sure that the benefit in noise reduction due to the optimized barrier was not too severely diminished in case of an already existing absorbing ground as opposed to a rigid ground.

Finally, the results obtained in case d) shows how much increase can be gained by treating the optimized barriers with an absorbing material instead of considering them rigid, keeping the ground absorbing as well. The benefit is not that important - about 1.5 dB(A) - for the small wall and medium wall optimized geometries, but is more important for the T-shape and for Gamma-shape geometries - with gains of 7 and 4.5 dB(A) respectively. This enhanced benefit of covering the barrier with absorbing material can be explained from the fact that with the Gamma and T geometries, the environment between the tramway and the barrier is more confined, which would enhance the multiple reflections phenomenon. When the barrier is rigid, those reflections could at most be scattered by the irregularities of the optimized geometry but not absorbed. Replacing the rigid coverage by an absorbing treatment would have a great impact on the multiple reflections and therefore would increase the insertion loss significantly, which is what is observed here.

Nevertheless, the optimized shape does induce an increase of performance by a few dB(A), even in the case of an absorbing treatment. For instance, for the T-shape geometry, going from the straight absorbing barrier to the optimized absorbing barrier increases the performance by 2.2 dB(A) (see in table 5.3). This gain reaches 3.2 dB(A) for the wall geometry. Besides, one can point out that here the shape has been optimized assuming a rigid coverage, and therefore one can expect a more significant effect of the shape optimization if the barrier had been assumed absorbing at first (which is what will be done in the next chapter).

Table 5.3: Comparison of broadband insertion losses in dB(A) in the 100-2500 Hz range for the initial and optimized T-shape and medium wall geometries, with and without absorbing treatment (Delany and Bazley layer of parameter $\sigma = 50\,\mathrm{kPa.s/m^2}$ and $d = 5\,\mathrm{cm}$), assuming the case c) configuration of figure 5.8 (absorbing ground and more realistic tramway geometry).

Geometry	Straight rigid	Straight abs.	Optimized rigid	Optimized abs.
T-shape	4.2	11.9	6.9	14.1
Medium wall	3.2	10.2	11.9	13.4

5.4.2 Effect of the source modeling

In the previous section, we looked at the effects of a more accurate modeling of the tramway cross section and the effect of an absorbing ground, but all the predictions were still assuming 2D propagation, that is an infinitely long tramway and barrier as well as an infinite coherent line source. Finally, in this section, we assess the importance of the modeling of the source, since it has been shown that the predicted benefit of a noise barrier can depend largely on it [144]. The 2D approximation indeed implicitly assumes that the source is an infinite coherent line, but as it has been pointed out earlier, it has been shown that this assumption can be used to approximately calculate excess attenuations in narrow frequency bands due to a 3D point source in many situations [28]. However, using the approach described by Duhamel [28], it is possible

to post-treat a set of 2D calculations to calculate the attenuation in the case of an incoherent line source or a set of incoherent point sources placed along the line of sources (perpendicular to the plane of the 2D calculations), which is referred to as 2.5D modeling. This post-treatment has been implemented in the MICADO software and tested by Jean et al. [144]. The direction perpendicular to the plane of 2D calculations will be referred to as the x_3-direction (see in figure 5.10), with $x_3 = 0$ corresponding to the 2D plane where the receiver is. Notice that, due to the increased complexity of the modeling, calculations will be made only up to the third-octave band centered at 1600 Hz.

We consider again the four cases described in figure 5.8. When non rigid surfaces are present, the extension of the 2.5D modeling in the presence of absorbing surfaces [143] is used. Besides, in order to compute third-octave insertion losses which requires calculation of the attenuation at several frequencies per third-octave, the approximation that the admittance is constant over each third-octave band is made, so that one set of 2D results per third-octave can be used in the 2D to 3D transformation. This approximation is not necessarily accurate for reactive treatments close to resonance for instance, but Jean [144] has shown that this approximation is usually sufficient to predict third octave or broadband insertion losses, which is what we are mostly interested in. Also, the so-called "imaginary" frequencies are not taken into account in our calculation since this increases the computation time significantly, but again this has been shown to have a negligible influence in the considered frequency range [28, 144].

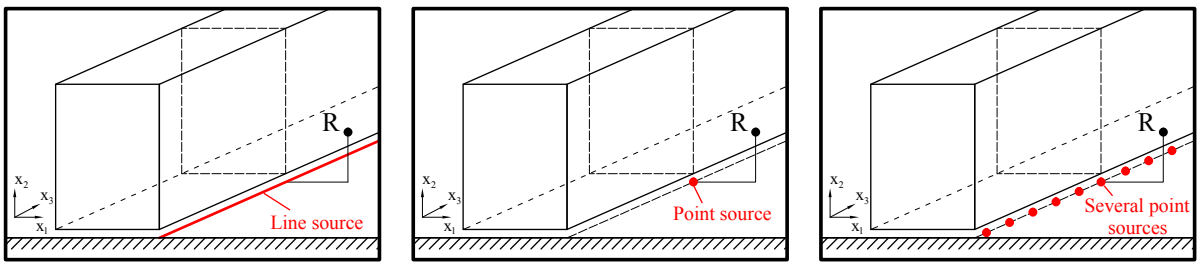

Figure 5.10: Source configurations assumed in the 2.5D modeling. Left: infinite line source (coherent or incoherent) - middle: one 3D point source in the same vertical plane as the receivers - right: several incoherent 3D point sources (placed every 0.5 m and covering a length of 42 m, which is a typical tramway length).

Four types of modeling for the tramway noise source are considered: infinite coherent line source (2D), one 3D point source located at $x_3 = 0$, several incoherent point source located along the tramway line from $x_3 = -21$ m to $x_3 = +21$ m every 0.5 m, and finally an infinite incoherent line source (see in figure 5.10). The finite extension of the several incoherent point sources has been chosen according to a typical length of a modern tramway, such as the one presented in [26] (about 40 m).

We first present the broadband insertion losses in dB(A) in the frequency band 100-1800 Hz, for the four cases presented in figure 5.8, for the four types of source models and for the four geometries (see table 5.4). Then, comparisons of third-octave insertion losses corresponding to the four source models in each ground/tramway configuration are presented in figures 5.12 to 5.15.

First of all, one can notice that the insertion losses in the case of a coherent line source are actually slightly under-predicted, by about 0.5 to 2 dB(A), compared to the case of one

Table 5.4: Comparison of the broadband insertion losses in dB(A) in the 100-1800 Hz band assuming the different cases of figure 5.8 and the four types of source models, for the four considered optimized geometries.

Barrier type	Cases	Source model			
		Coherent line	One point source	Incoherent point sources	Incoherent line
Small wall	a)	8.2	10.2	7.9	4.5
	b)	9.9	10.5	9.4	3.2
	c)	5.9	6.4	4.7	4.2
	d)	7.6	8.0	7.0	6.4
Medium wall	a)	15.2	17.6	11.3	4.8
	b)	14.2	16.3	11.5	2.7
	c)	11.9	13.3	8.2	7.2
	d)	13.3	13.9	12.3	10.8
T-shape	a)	11.3	14.1	9.9	5.8
	b)	10.1	11.7	9.2	3.1
	c)	6.8	8.2	5.4	5.1
	d)	13.9	14.7	12.3	11.6
Gamma-shape	a)	11.2	13.3	10.1	5.7
	b)	10.6	12.4	9.9	3.2
	c)	8.0	9.1	6.6	6.3
	d)	12.5	13.1	11.2	10.5

point source, and this regardless of the tramway/ground configuration. However, overall third-octave insertion losses assuming a coherent line source or a 3D point source follow similar trends. Extrapolating the insertion losses calculations in 2D to the case of one 3D point source therefore seems relatively accurate.

Furthermore, when the source is modeled as several incoherent point sources, which seems like a more realistic model, the following trends can be observed: 1) going from an idealized to a more realistic tramway cross section slightly decreases the efficiency by less than 1 dB(A), except for the small wall geometry for which the efficiency is actually increased by 1.5 dB(A), without changing dramatically the shape of the third-octave insertion loss curve; 2) adding absorption to the ground further decreases the efficiency of the noise barrier itself (by 3-4 dB(A)). However, comparing the third octave insertion losses in the case of one or several point sources (see in figures 5.12 to 5.14, top right and bottom left graphs), one can see that, for all geometries, the presence of several incoherent sources greatly decreases the low frequency performance and smooths the dips and peaks of the third-octave insertion loss curves. Those dips and peaks are probably related to interference effects happening between the tramway and the barrier, which are typically more marked in the case of a coherent source (such as a 2D line source or a 3D point source), and therefore it makes sense that they would be somewhat diminished when the source is spatially incoherent.

Still considering the case of incoherent point sources, adding absorbing treatment on the barrier increases the performance, but again the gain is smaller for the wall-like geometries (2-4 dB(A)) than for the T and Gamma shape geometries (4.5-7 dB(A)). It is interesting to notice however that the optimized medium wall has a similar or better performance than the optimized T-shape (regardless of the barrier being rigid or absorptive).

But, the biggest difference in the results due to the source model corresponds to the case of an infinite incoherent line source with a rigid ground - cases a) and b). Indeed, the broadband efficiency dramatically drops compared to the case of incoherent point sources for all geometries.

One can also notice that the decrease in attenuation is significant across the whole frequency range (see in figures 5.12 to 5.15, bottom left and bottom right graphs, thick solid and thick dashed lines). However when the ground is absorbing - cases c) and d) - the decrease is a lot smaller (see in the same figures, same graphs, thin solid and thin dashed lines).

However, it has been shown that the difference in predicted levels between the infinite incoherent line source model and a finite set of incoherent point sources model is mostly due to the finite extent of the point sources along the x_3-axis [144]. This difference is not visible when the ground is absorbing because contributions from distant sources are highly attenuated while propagating above the ground. In the case of a tramway, it is clearly more realistic to consider a finite extent of sources, and therefore we believe that the predicted results assuming a set of incoherent point sources are more likely to be realistic than those obtained assuming an infinite incoherent line source.

Finally, in order to evaluate the benefit of the optimization even in a more advanced modeling situation, one can compare the performance in terms of third-octave insertion losses of the two best obtained rigid solutions (optimized medium wall and optimized T-shape) with that of their corresponding "starting" geometry, for what we consider the most realistic model: realistic tramway cross-section, several incoherent point sources, rigid or absorbing ground (see figure 5.11). Even in a more complicated modeling situation, one can notice that the gain in performance due to the optimization is significant (+ 6 dB(A) for the medium wall, + 2-3 dB(A) for the T-shape), and that optimized geometries perform significantly better than straight geometries at mid and high frequencies (above 400 Hz for the medium wall, and above 600 Hz for the T-shape), as noticed in the 2D calculations.

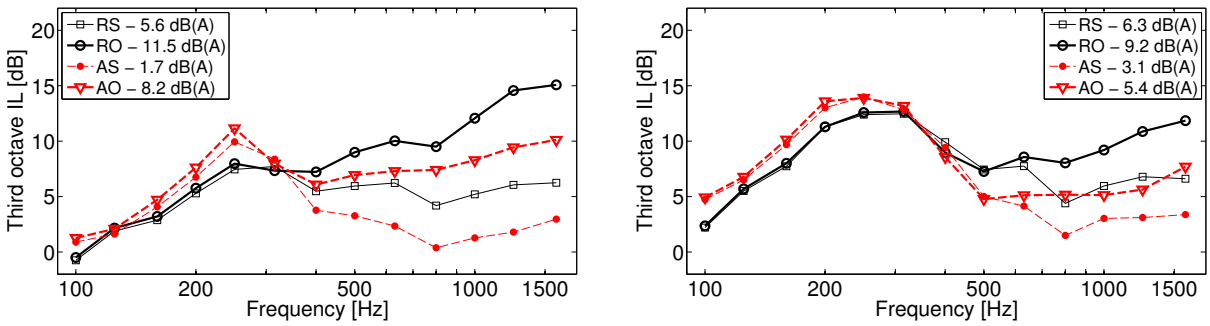

Figure 5.11: Comparison of third octave insertion losses in dB between rigid straight (initial) and rigid optimized geometries, assuming incoherent point sources, more realistic tramway geometry and either rigid or absorbing ground, for two starting geometries. Broadband insertion losses in dB(A) calculated in the range 100-1800 Hz are shown as well. Left: medium wall - right: T-shape. Thin solid line: Rigid ground and Straight geometry (RS) - thick solid line: Rigid ground and Optimized geometry (RO) - thin dashed line: Absorbing ground and Straight geometry (AS) - thick dashed line: Absorbing ground and Optimized geometry (AO).

5.5 Conclusion

In this chapter, the sensitivity-based shape optimization algorithm developed in the previous parts of this work has been applied to the cases of rigid tramway low-height barriers. Several starting geometries were chosen (small and medium wall, quarter cylinder, T and Gamma shape)

and convergence to a solution was achieved in each case rather rapidly (within a few dozens iterations). Several dB(A) of improvement were observed, from 3 dB(A) for the quarter cylinder to 11 dB(A) in the medium wall case, although since the barrier is assumed rigid no energy absorption happens in the considered model.

The generated optimized shapes tend to present sharp irregularities on the side of the barrier directly exposed to the source radiation and to the reflections on the tramway side. On the other hand the opposite side (facing the receivers) is almost not changed for most geometries. Intensity calculations suggest that the presence of the irregularities of the optimized shapes cause the multiple reflections happening between the tramway and the barrier to scatter, therefore redirecting part of the acoustic energy upwards and away from the shadow zone, and cause recirculating regions of sound energy to appear. Those two effects seem to explain the increase of performance happening even without any absorption phenomena.

Extra calculations show that smoothing the irregularities provokes a decrease in performance, which suggests that the sharp irregularities are not numerical artifacts but do physically alter the sound field in order to increase the noise reduction in the shadow zone, by the energy redirection effect. However, small perturbation of the optimized shape - which might be due to manufacturing inaccuracies for instance - does not completely annihilate the benefit of the shape optimized barrier.

More advanced numerical calculations were performed on the optimized designs in order to assess how much the assumed approximations in the optimization model influence the performance. To achieve this, a more realistic tramway geometry is considered, as well as an absorbing ground and different source models using 2.5D calculations. The following trends are observed:

- the vertical baffle approximation is rather accurate for most optimized geometries, within about 1 dB(A).
- the insertion loss of the barrier is decreased when the ground is strongly absorbing, by 3-4 dB(A).
- the 2D source model (coherent line source) represents quite accurately the case of a single 3D point source in the considered cases.
- considering a finite set of incoherent sources instead of one point source smooths out interference peaks and dips and decreases third-octave insertion losses (mostly at low frequencies), although the performance of the optimized barriers remains significant (above 9 dB(A) in case of a rigid ground).
- covering the barrier with absorbing material provides several dB(A) of extra attenuation, this effect being more important for the T and Gamma-shape barriers since the space between the barrier and the tramway is more confined with this kind of geometry.

Furthermore, extra effects that have not been taken into account in the modeling are susceptible of having an influence on the performance of the barrier, such as the directivity of the source and the finite length of the barrier. One can however state that considering omnidirectional point sources - therefore sources that radiate equally in all directions, especially in

the horizontal plane - is likely to yield a conservative estimate of the performance of the noise barrier, since with more realistic directivity patterns distant sources would contribute less to the pressure level that has been calculated here and therefore the performance would be closer to what has been predicted in the one point source case.

On the other hand, considering the barrier infinite obviously over-predicts the performance compared to a barrier of similar shape but of finite length. Quantifying this difference would require however full 3D calculations which are beyond the scope of this study.

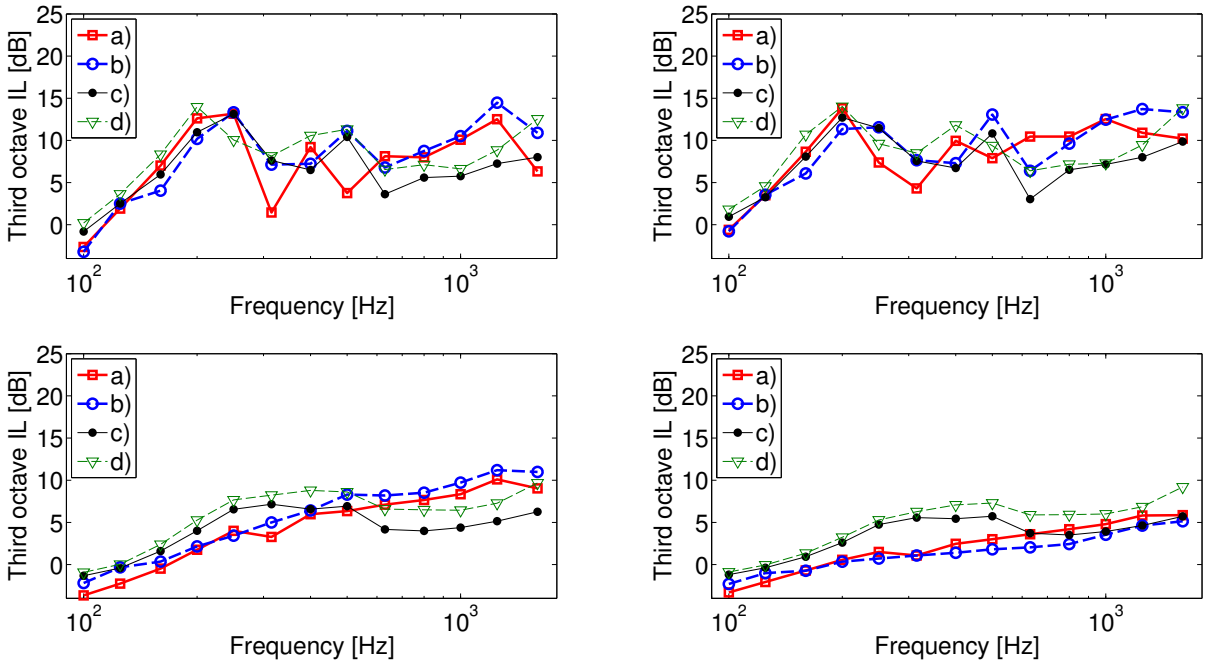

Figure 5.12: Comparison of the third octave insertion losses in dB assuming the different cases of figure 5.8 and the four types of source models, for the optimized small wall barrier. Top left: coherent line source - top right: one point source - bottom left: incoherent point sources - bottom right: incoherent line source.

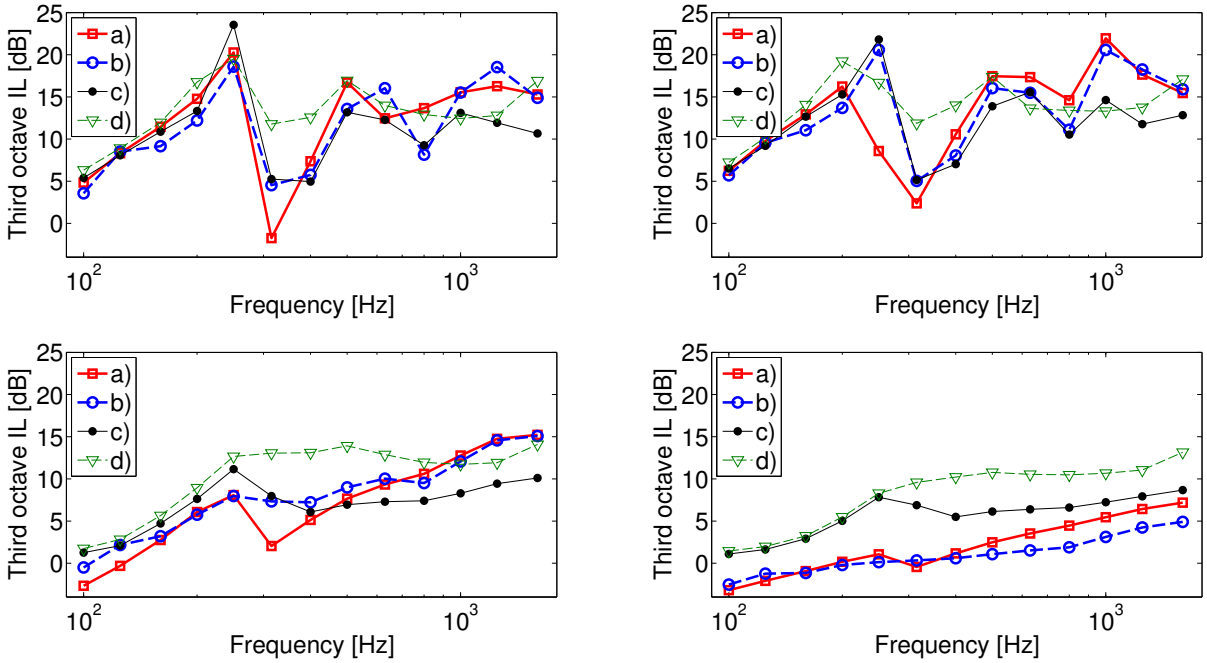

Figure 5.13: Comparison of the third octave insertion losses in dB assuming the different cases of figure 5.8 and the four types of source models, for the optimized medium wall barrier. Top left: coherent line source - top right: one point source - bottom left: incoherent point sources - bottom right: incoherent line source.

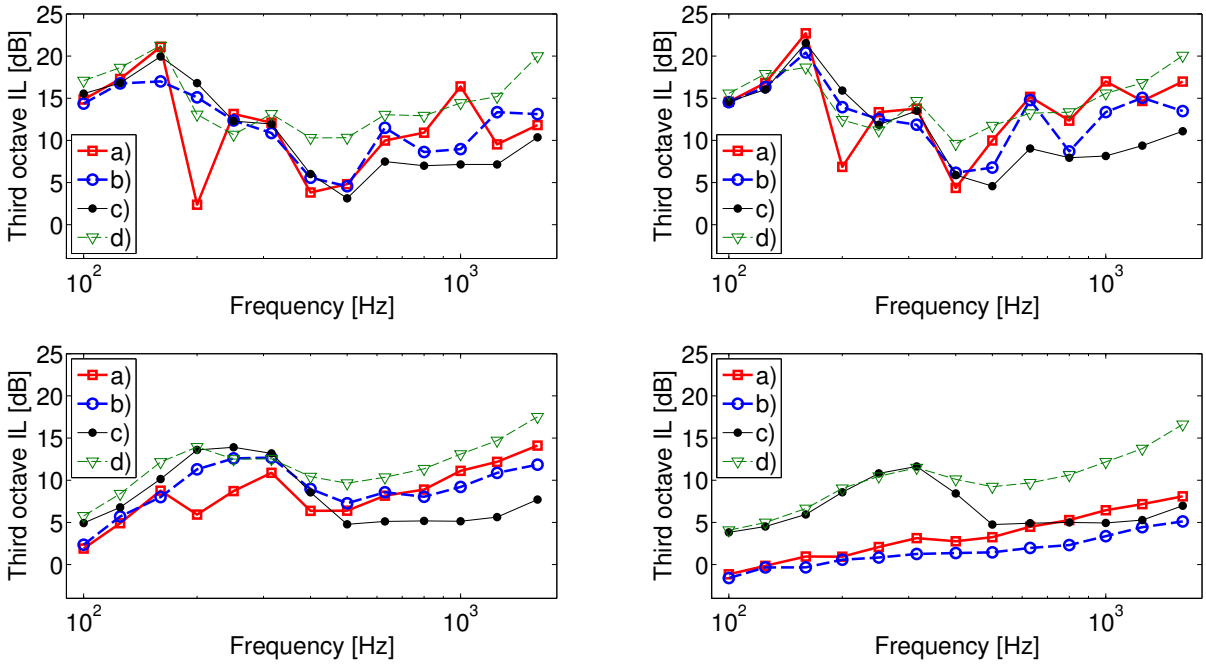

Figure 5.14: Comparison of the third octave insertion losses in dB assuming the different cases of figure 5.8 and the four types of source models, for the optimized T-shape barrier. Top left: coherent line source - top right: one point source - bottom left: incoherent point sources - bottom right: incoherent line source.

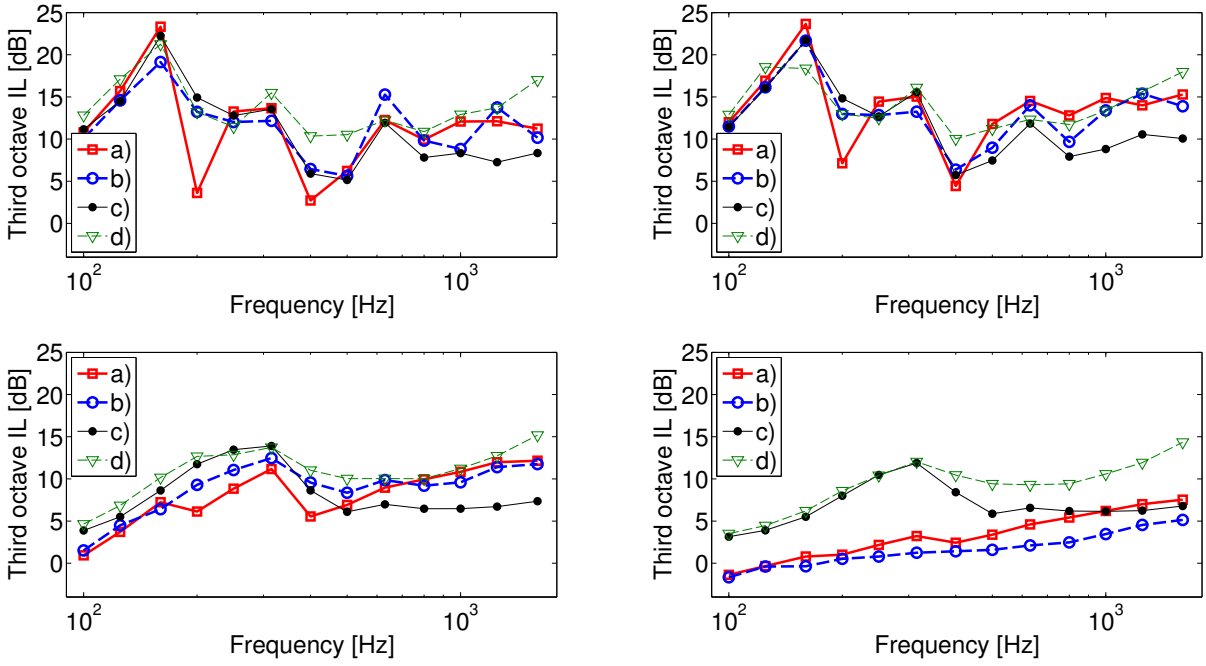

Figure 5.15: Comparison of the third octave insertion losses in dB assuming the different cases of figure 5.8 and the four types of source models, for the optimized Gamma-shape barrier. Top left: coherent line source - top right: one point source - bottom left: incoherent point sources - bottom right: incoherent line source.

Chapter 6

Application to coupled admittance and shape optimization of barriers with acoustic treatments

In the previous chapter, the shape optimization algorithm has been applied to the case of rigid low height barriers since we were interested in finding how much improvement can be obtained due to an optimized shape design only, assuming it would be built with an acoustically rigid material such as concrete. However, using acoustic surface treatments is also a natural choice if one seeks to improve the performance of a low height noise barrier, especially since this would help in attenuating the multiple reflections phenomenon happening between the barrier and the tramway. We present in this chapter some optimized designs found either by optimizing the shape in the case of an assumed surface admittance, or by optimizing both the shape and a part of the surface admittance.

6.1 Considered acoustic treatments

As pointed out in section 1.6 there are mostly two main types of acoustic treatments: porous treatments and reactive treatments. We will assume two kinds of porous treatments, a layer of fibrous material such as fiberglass, modeled with the Delany and Bazley empirical model (see in figure 1.6.1), and a hemp concrete layer, modeled with the hybrid model explained in section 1.6.2. The considered reactive treatment is the micro-perforated panel resonator (MPPR) resonator, modeled by the Crandall-Sivian-Fok model, as explained in section 1.6.3. We will therefore consider several configurations, in which some part of the barrier can be shape-optimized, and some part of it can be admittance-optimized. Generally speaking those parts can overlap, however feasibility constraints should be taken into account if the optimized barrier was to be built. For instance, we will not allow the shape of a MPPR to be optimized (it will remain flat).

To completely define the optimization problem, we need to choose a range of possible values for the admittance parameters, which depends on the type of parameter:

- **MPPR**. Porosity: $s \in [0.01, 0.4]$; hole radius: $a_0 \in [0.5, 5]\,\text{mm}$; panel thickness: $l_0 \in [0.2, 1]\,\text{cm}$; cavity depth $D \in [1, 10]\,\text{cm}$
- **Porous fibrous layer**. Flow resistivity: $\sigma \in [50, 200]\,\text{kPa}\,\text{s}\,\text{m}^{-2}$; layer depth: $d \in [1, 10]\,\text{cm}$

The parameters describing the hemp concrete will however not be optimized. The choice of those ranges is based on physically feasible values. Regarding shape optimization, the 1 m wide box constraint considered in chapter 5 is kept here as well.

6.2 Shape optimization of a barrier covered entirely with a fibrous absorbing treatment

First, a shape optimization is conducted on simple geometries, assuming a fibrous fiberglass-like porous treatment covering the whole surface of the barrier. Indeed, it has been noticed in chapter 5 that an absorbing treatment can act concurrently with the scattering effect provided by an irregular shape-optimized barrier, however it is not clear how much improvement a shape optimization can provide in terms of extra attenuation in the shadow zone when the barrier is already assumed absorbing.

For this purpose, the medium wall and Gamma-shape initial geometries are considered (see in figure 6.1, top plots), with a fixed - meaning not allowed to be optimized - surface treatment modeled as a Delany and Bazley porous layer (flow resistivity $\sigma = 50\,\text{kPa.s/m}^2$ and thickness $d = 5\,\text{cm}$). The initial control mesh is generated with a maximum distance between two following nodes of 2 cm, yielding 112 and 143 nodes respectively for the medium wall and Gamma-shape geometries. The obtained optimized shapes are presented as well in figure 6.1, bottom plots. The broadband insertion losses are given in table 6.1 and third-octave insertion losses in figure 6.2. Finally, convergence was obtained respectively in 12 and 14 iterations.

Table 6.1: Comparison of broadband insertion losses in dB(A) in the 100-2500 Hz range for the two starting geometries and corresponding optimized geometries, in the case of a barrier fully covered with a fibrous layer as shown in figure 6.1.

	Medium wall	Gamma-shape
Initial	15.1	15.4
Optimized	20.7	23.6

First of all, one can notice that a noticeable improvement of the barrier performance has been obtained in both cases: +5 dB(A) for the medium wall and almost +10 dB(A) for the Gamma-shape wall. As in the rigid barrier case (see in chapter 5), some irregularities are generated by the shape optimization, and the back side of the barrier is almost not modified.

However, it is interesting to notice that the way the shape has been deformed is somewhat different from what was observed in the case of rigid barrier shape optimization (see in figure 6.3 for a comparison of shape-optimized barriers assuming either rigid or absorbing surface treatment). Indeed, when the barrier was assumed rigid, it has been noticed that the source side underwent rather important deformation and became quite irregular (see in chapter 5), which

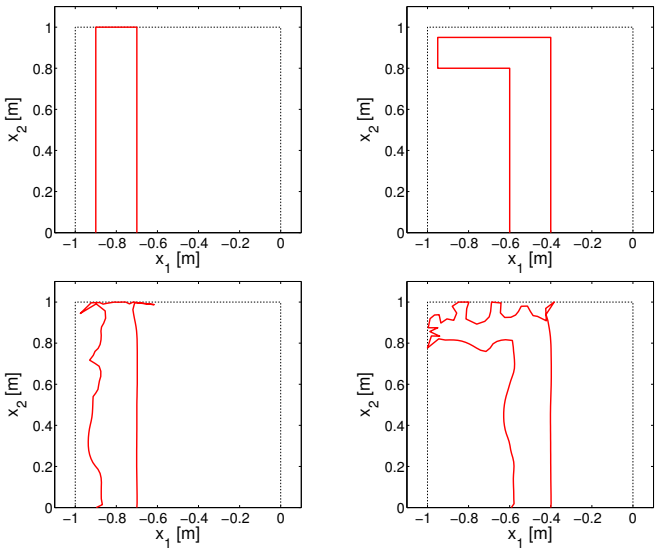

Figure 6.1: Initial and optimized barrier designs considered in the shape-optimized fully absorbing barrier configuration (fibrous layer modeled with the Delany and Bazley's model with parameters $\sigma = 50\,\mathrm{kPa.s/m^2}$ and $d = 5\,\mathrm{cm}$). Left: medium wall - right: Gamma-shape. Top: initial geometry - bottom: optimized geometry. The one meter wide constraint box is shown as well (thin dotted line).

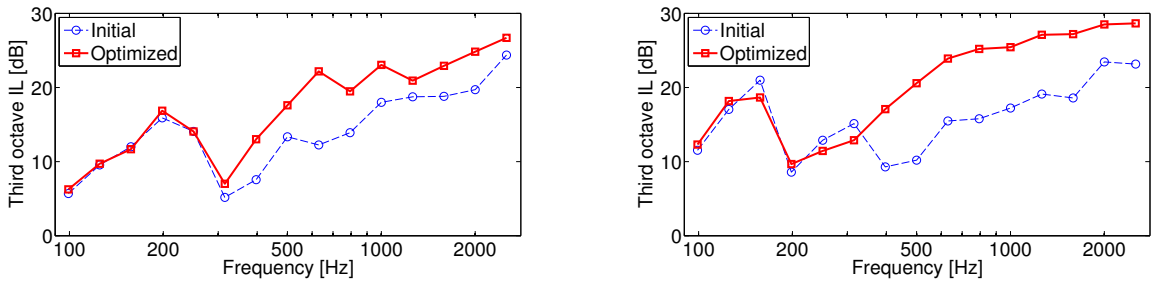

Figure 6.2: Comparison of third-octave insertion losses in dB between initial and optimized geometry in the case of shape optimization of a fully absorbing barrier (fibrous Delany and Bazley layer), as shown in figure 6.1. Solid line: optimized geometry - dashed line: initial geometry. Left: medium wall - right: Gamma-shape.

would induce some energy scattering of the multiple reflections. However, when the barrier was assumed absorbing, it seems like the deformation on the source side was not as important, but on the other hand was more important in the top region of the barrier. This could be explained from the fact that, when the barrier is rigid, the performance is mostly influenced by the multiple reflection phenomenon happening between the source side of the barrier and the tramway, and therefore the shape optimization tends to act against this effect by mostly modifying the source side geometry, which is where the multiple reflections happen. However, when the barrier is absorbing, the multiple reflections are greatly attenuated, and therefore this time the performance of the barrier may be influenced as well by diffraction effects, which happen essentially in the top region, and it would consequently make sense that the shape optimization tends to modify the geometry to enhance those effects. This is suggested by the comparison of the generated optimized geometries in both cases (see in figure 6.3), especially for the Gamma-shape starting geometry. Indeed it seems like the top of the medium wall geometry has not been modified too significantly since the nodes of this area were already rather close to the constraint box, which somewhat limited the deformation.

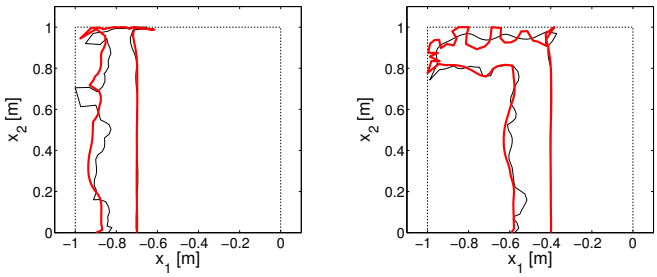

Figure 6.3: Comparison of shape-optimized barrier geometries in the case of either rigid or absorbing surface treatment, with the same initial starting geometry. Left: medium wall - right: Gamma-shape. Thin black line: rigid barrier - thick red line: absorbing barrier.

6.3 Shape optimization of absorbing source side and reactive treatment optimization on top

In this section a design coupling the benefit of a shape optimized source side and a reactive treatment on top of the device is studied. As in the previous section, an absorbing treatment (the same fibrous layer than in the previous case) is added on the source side to act against the multiple reflections happening between the barrier and the tramway, but the shape is also allowed to be optimized for further enhancement. Besides, it seemed interesting to study if a reactive treatment on top of the barrier may enhance the performance in a suitable frequency band. As pointed out before, the attenuation is not influenced significantly by the part of the barrier facing the receivers (the back side), and therefore it is assumed rigid and fixed in the optimization for simplicity (although as pointed out in chapter 5, one could use any type of treatment on this side, for instance for purely aesthetic reasons).

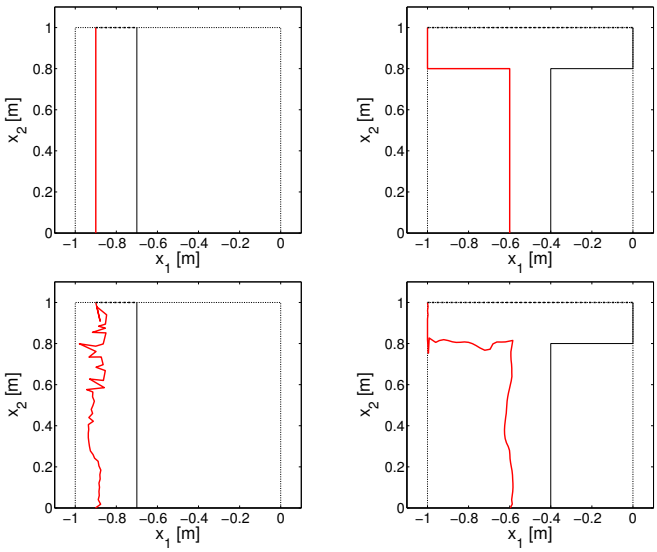

Figure 6.4: Initial and optimized barrier designs considered in the shape-optimized porous source side and MPPR top side configuration. Left: medium wall - right: T-shape. Top: initial geometry - bottom: optimized geometry. The one meter wide constraint box is shown as well (thin dotted line). Surface treatment color coding: rigid (thin black solid line); fibrous layer (thick red solid line); MPPR (thick black dotted line).

Table 6.2: Type of treatment, optimized parameter values and broadband insertion losses in the 100-2500 Hz range in dB(A) for the optimized designs given in figure 6.4.

Initial geometry	Type of treatment and parameters			Broadband IL [dB(A)]
	Source side	Top side	Back side	
Medium wall	Fibrous layer $\sigma = 50\,\text{kPa.s/m}^2$ $d = 4.3\,\text{cm}$	MPPR $s = 0.186$ $a_0 = 0.5\,\text{mm}$ $l_0 = 5.4\,\text{mm}$ $D = 8\,\text{cm}$	Rigid	23.0
T-shape	Fibrous layer $\sigma = 50\,\text{kPa.s/m}^2$ $d = 5\,\text{cm}$	MPPR $s = 0.122$ $a_0 = 2.8\,\text{mm}$ $l_0 = 6.6\,\text{mm}$ $D = 10\,\text{cm}$	Rigid	23.3

Two starting geometries are considered: the medium wall and the T-shape (see figure 6.4, top plots). Again the control nodes on the source side are initially separated by 2 cm. The initial admittance parameters are chosen randomly in the feasible range given above. Generated optimized designs are shown in the figure 6.4 bottom plots, whereas optimized admittance parameter values as well as broadband insertion losses are given in table 6.2. Again convergence was achieved rapidly, within 20 iterations.

The same trend that has been observed in chapter 5 is observed here as well, which is that the shape optimization alters the source side mostly by making it more irregular. One can notice however that the irregularities are more pronounced in the medium wall case compared to the T-shape case. This might be due to the fact that most of the nodes of the initial T-shape geometry were located on the constraint box, and therefore could not be displaced much. This suggests that using a geometry not in contact with the constraint box might be a better choice for the starting point of the shape optimization algorithm.

The relative benefit of optimizing the shape as opposed to optimizing the admittance can furthermore be studied a posteriori by comparing the insertion losses in the case of a fully optimized design (shape and admittance, referred to afterwards as the OS-OT case), as opposed to the case of an optimized shape covered with absorbing treatment only (referred to as the OS-AT case) and the case of the initial straight geometry covered with the found optimized admittance (referred to as the IS-OT case). Third-octave and broadband insertion losses in these three different cases for the medium wall and T-shape geometries are presented in figure 6.5.

Comparing cases OS-OT and OS-AT, one can notice that the benefit of the optimized admittance - which is essentially related to the presence of the optimized MPPR on top - mostly improves the performance in the mid-frequency range, between 600 and 1500 Hz for the medium wall geometry and between 400 and 1000 Hz for the T-shape geometry, inducing an increase of performance respectively of 2 and 4 dB(A). Those frequency ranges roughly correspond to the first resonance of the MPPRs, as can be seen in their admittance functions given in figure 6.6. On the other hand, comparing cases OS-OT and IS-OT suggests that for the T-shape geometry optimizing the shape of the source side has a little influence (increase of 1.7 dB(A) in the performance), but is much more significant in the medium wall case (increase of more than 6 dB(A)). This is in agreement with the fact that the geometry has been modified more significantly in the medium wall case, and it would therefore make sense that the shape optimization would provide more improvement of the broadband performance.

In summary, in the two considered cases, both optimizing the shape on the source side and optimizing the surface treatment on the top (here assumed to be a reactive treatment) seem to have an influence, although the influence of the MPPR seems more important for the T-shape geometry, whereas the influence of the shape seems more important for the medium wall.

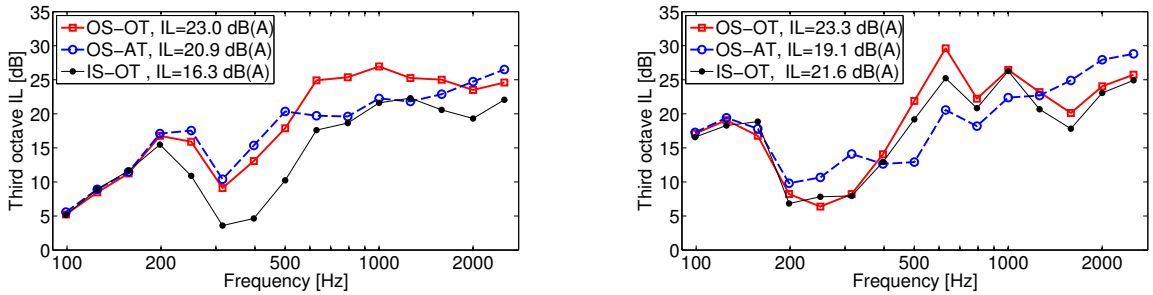

Figure 6.5: Comparison of third-octave insertion losses in dB for different configurations of barrier shape and surface treatment related to the optimization case considered in figure 6.4. Broadband insertion losses in dB(A) are given in the legend as well. Thick solid line (OS-OT): Optimized Shape (see in figure 6.4 bottom plot) and Optimized surface Treatment (parameters given in table 6.2) ; thick dashed line (OS-AT): Optimized Shape (see in figure 6.4 bottom plot) and Absorbing surface Treatment (Delany-Bazley porous layer with $\sigma = 50\,\mathrm{kPa.s/m^2}$ and $d = 5\,\mathrm{cm}$) covering the whole barrier ; thin solid line (IS-OT): Initial straight Shape (see in figure 6.4 top plot) and Optimized surface Treatment (parameters given in table 6.2). Left: medium wall - right: T-shape.

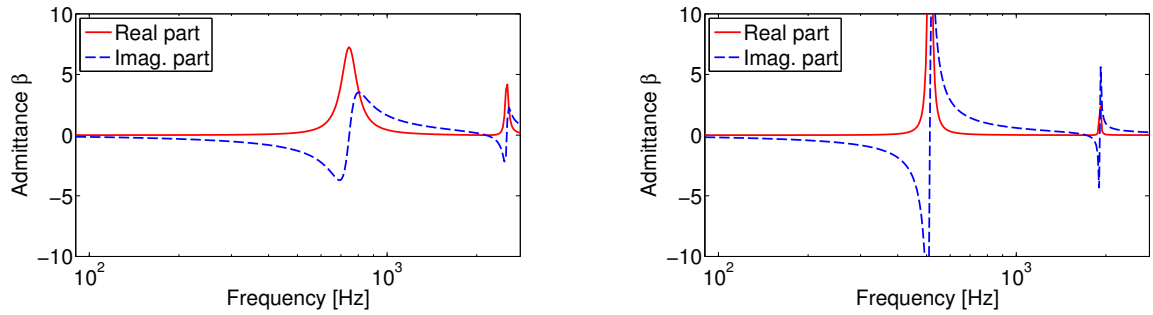

Figure 6.6: Normalized admittance β of the MPPR on top of the barrier for the two optimized designs given in figure 6.4. Parameters of the MPPRs are given in table 6.2. Real part: solid line ; imaginary part: dashed line.

6.4 Results with hemp concrete as the absorbing treatment

The porous absorbing treatment assumed in the previous sections has been modeled by a Delany and Bazley layer of low flow resistivity ($\sigma = 50\,\mathrm{kPa.s/m^2}$), which would typically correspond to a layer of sound insulating fibrous material such as fiberglass. Such a strongly absorbing material would require proper packaging in order to be used in an outdoor environment and also has a rather strong environmental footprint. One may wish to use instead a more sustainable material, but with good acoustic absorption properties. An example of such material is hemp concrete, which has been introduced in section 1.6.2. This material has slightly different acoustic properties compared to a Delany and Bazley fiberglass-type material, as one can see from their normalized admittance functions and absorption coefficients, given in figure 6.7. Hemp concrete is not as absorptive at high frequencies, but does provide more absorption at low frequencies.

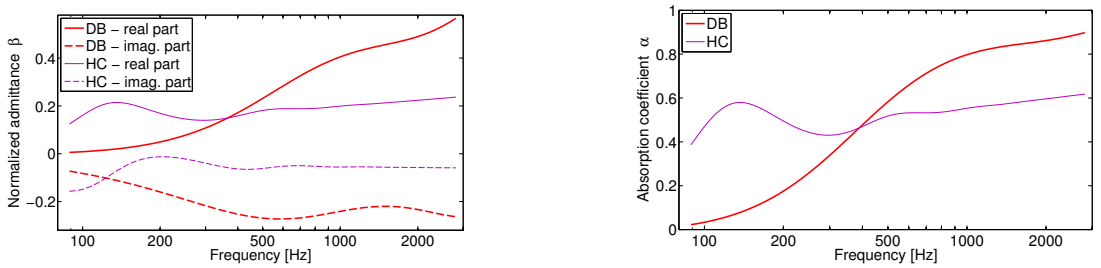

Figure 6.7: Comparison of normalized admittance β (left plot) and absorption coefficient α (right plot) of a fibrous material, modeled as a Delany and Bazley layer of parameters $\sigma = 50\,\text{kPa.s/m}^2$ and $d = 5\,\text{cm}$, and of a hemp concrete layer (the used model and the parameters are given in section 1.6.2). Thick red line (DB): Delany and Bazley layer; thin purple line (HC): Hemp Concrete layer. (Left plot - real part: solid line; imaginary part: dashed line.)

We now briefly present some optimized designs when hemp concrete is used as the absorbing treatment instead of a layer of fibrous porous material.

6.4.1 Uniform porous treatment

We first assume, as in section 6.2, that the barrier is uniformly covered with absorbing treatment (again here, it is assumed to be hemp concrete), and the shape is optimized. The two same starting geometries are considered: medium wall and Gamma-shape (see figure 6.8, top plots). The optimized barrier shapes are shown in figure 6.8, bottom plots. The comparisons of broadband and third-octave insertion losses between the initial shapes and optimized shapes are shown in table 6.3 and figure 6.9. The improvement due to the shape optimization is similar to what has been obtained for the fibrous absorbing material (+7 dB(A) for the medium wall, +9.5 dB(A) for the Gamma-shape) and the shape has been modified in a similar fashion. Broadband attenuations however are slightly smaller than what had been found in section 6.2 for the barrier covered with fibrous material (by about 1.5 dB(A)), due to smaller insertion loss values at high frequencies. This difference was expected since, as pointed out above, hemp concrete is not as absorptive at high frequencies. Nevertheless, the obtained performances are similar for the two absorbing treatments, and therefore using hemp concrete as opposed to a more typical sound absorbing fibrous material seems like a suitable option regarding acoustic performance.

Besides, the performance of the optimized absorbing barrier is somewhat stable, in the sense that small perturbations of the shape do not induce too much of a decrease of the broadband insertion loss. Doing a similar calculation as in section 5.3, it has been found indeed that randomly perturbing the absorbing medium wall optimized geometry - again with normally distributed perturbations of standard deviation 5 mm - induced on average a decrease smaller than 0.1 dB(A).

Table 6.3: Comparison of broadband insertion losses in dB(A) in the 100-2500 Hz range for the two starting geometries and corresponding optimized geometries, in the case of a barrier fully covered with hemp concrete.

	Medium wall	Gamma-shape
Initial	12.3	13.1
Optimized	19.2	22.6

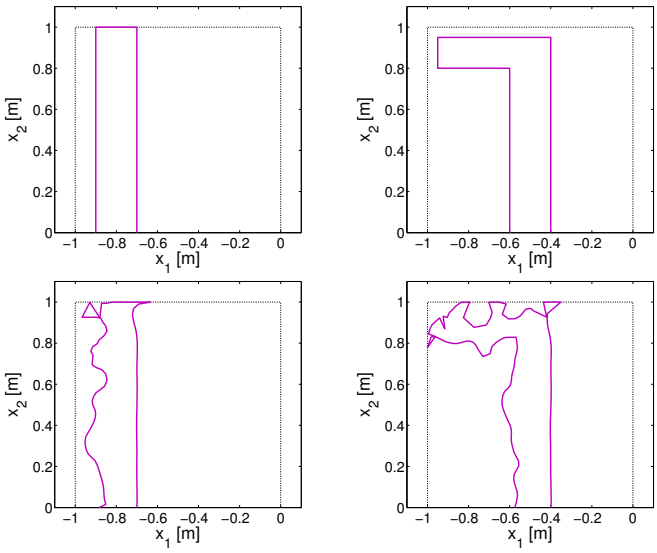

Figure 6.8: Initial and optimized barrier designs considered in the shape-optimized fully absorbing barrier configuration (hemp concrete layer). Left: medium wall - right: Gamma-shape. Top: initial geometry - bottom: optimized geometry. The one meter wide constraint box is shown as well.

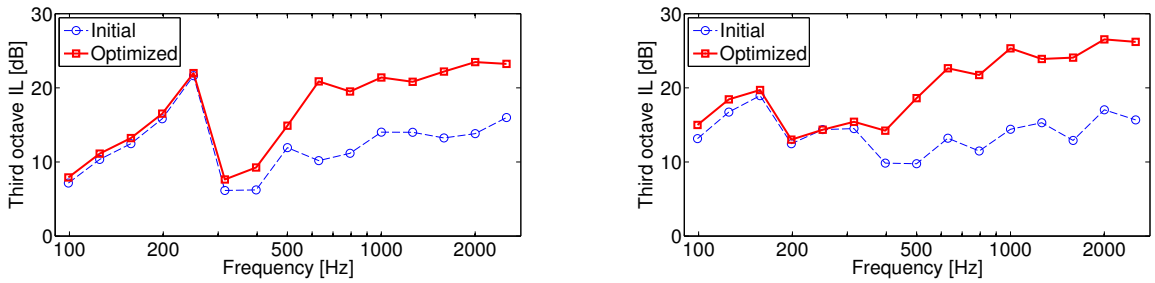

Figure 6.9: Comparison of third-octave insertion losses in dB between initial and optimized geometry in the case of the shape optimization of a barrier fully covered by hemp concrete. Solid line: optimized geometry - dashed line: initial geometry. Left: medium wall - right: Gamma-shape.

6.4.2 Porous and reactive treatment

Similar to what has been looked at in section 6.3, we now consider barrier designs with the source side covered with hemp concrete, a MPPR on the top side and a rigid back. The two considered starting geometries are the medium wall geometry and the T-shape geometry (see the figure 6.10 top plots). Optimization is applied to the shape of the source side, again with initial control nodes distant of 2 cm, and to the parameters describing the MPPR. Resulting designs are shown in the figure 6.10 bottom plots. Optimized MPP parameters and broadband insertion losses are given in table 6.4.

The resulting optimized shapes are slightly different than what had been found in section 6.3. First, one should point out that the starting geometries were not exactly the same in the two cases (see in the figures 6.4 and 6.10 top plots): when hemp concrete was used, the initial medium wall was slightly offset closer to the source and the top of the T further away from the source. This was done to loosen the shape bound constraints, which would hopefully allow more improvement thanks to the shape optimization.

For the medium wall case (comparing figure 6.4 and figure 6.10, bottom left plots), irreg-

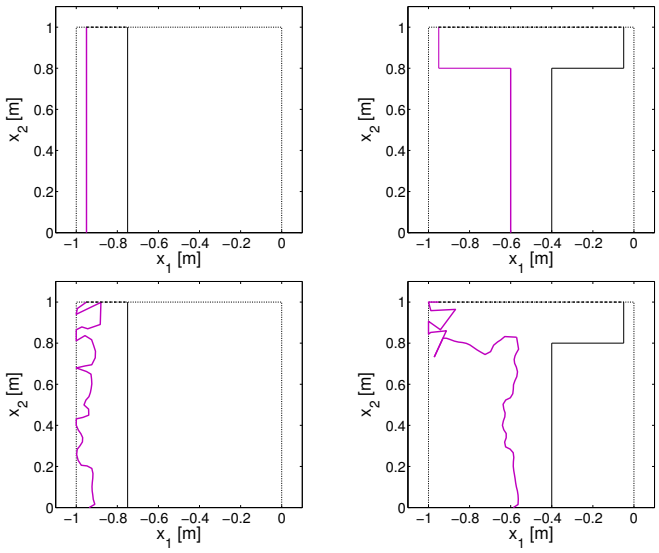

Figure 6.10: Initial and optimized barrier designs considered in the shape-optimized hemp concrete source side and MPPR top side configuration. Left: medium wall - right: T-shape. Top: initial geometry - bottom: optimized geometry. The one meter wide constraint box is shown as well. Surface treatment color coding: rigid (thin black solid line); hemp concrete layer (thick purple solid line); MPPR (thick black dotted line).

Table 6.4: Type of treatment, optimized parameters values and broadband insertion losses in the 100-2500 Hz range in dB(A) for the optimized designs given in figure 6.10.

Initial geometry	Type of treatment and parameters			Broadband IL [dB(A)]
	Source side	Top side	Back side	
Medium wall	Hemp concrete	MPPR $s = 0.162$ $a_0 = 3.6\,\text{mm}$ $l_0 = 9.5\,\text{mm}$ $D = 9.8\,\text{cm}$	Rigid	22.4
T-shape	Hemp concrete	MPPR $s = 0.173$ $a_0 = 0.5\,\text{mm}$ $l_0 = 5.8\,\text{mm}$ $D = 8.6\,\text{cm}$	Rigid	24.4

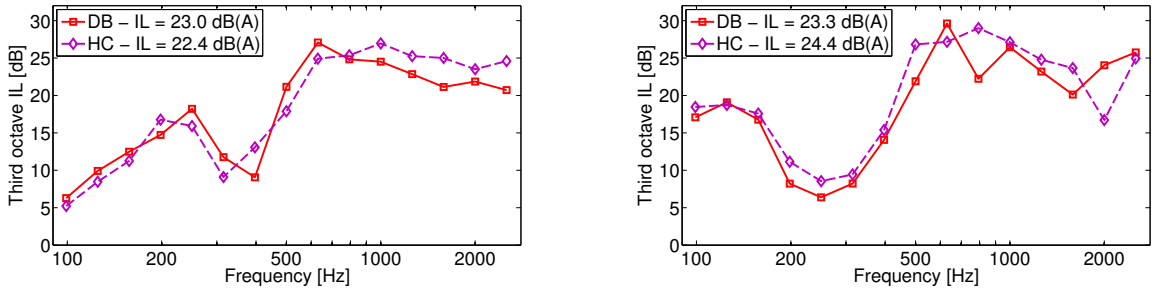

Figure 6.11: Comparison of third-octave insertion losses in dB in the case of an absorbing shape-optimized source side and optimized MPPR on top side (parameters are given in table 6.2 and 6.4). The absorbing treatment is either a layer of fibrous material (modeled with the Delany and Bazley model with parameters $\sigma = 50\,\text{kPa.s/m}^2$ and $d = 5\,\text{cm}$) or a layer of hemp concrete (see in section 1.6.2 for the corresponding model and parameters values). Broadband insertion losses in dB(A) are given in the legend as well. Thick solid line (DB): Delany and Bazley layer; thick dashed line (HC): Hemp Concrete layer. Left: medium wall - right: T-shape.

ularities were more strongly marked and more concentrated close to the top with the fibrous treatment. Regarding the T-shape geometry, as expected the top region of the source side has undergone more deformation during the optimization, which in turn yielded a slightly better broadband performance (24.4 dB(A) with hemp concrete and 23.3 dB(A) with fibrous absorbing

material).

Finally, comparison of third-octave insertion losses for both starting geometries and for both porous treatments, given in figure 6.11, show that a similar performance can be obtained using both types of porous treatments, even though hemp concrete is not as absorptive at high frequencies.

6.5 Performance of some optimized designs using more advanced modeling

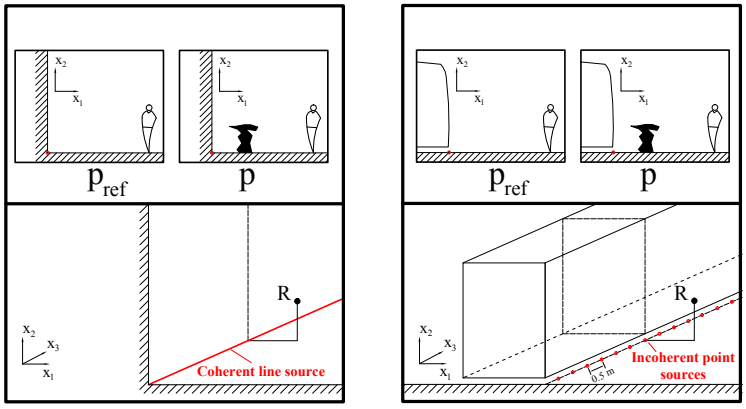

Figure 6.12: Schematics representing the so-called *simplified model* (used during the optimization process) and *advanced model*. Left: simplified model (tramway body modeled by a vertical baffle, coherent line source, rigid ground) - right: advanced model (more realistic tramway body geometry, set of incoherent point sources covering a length of 42 m and placed every 0.5 m, rigid ground).

As stated in section 5.4, once some optimized noise barrier designs are found, it is not as critical to keep the computation time as small as possible because the evaluation of the attenuation is performed only once per found design. We therefore end this chapter by presenting predicted insertion losses using a more advanced model: instead of modeling the tramway body as a rigid baffle, we consider a more accurate geometry (including a gap under the body), and the noise source is modeled as a set of incoherent point sources located on the ground. This will be referred to as the *advanced model*, whereas the model assumed during the optimization process will be referred to as the *simplified model* (see in figure 6.12). Although it has been found in section 5.4 that the absorption of the ground influences the intrinsic performance of the noise barrier (it typically decreases the insertion loss by a few dB(A)), we will assume a rigid ground in both models for simplicity.

The four optimized designs for which we will perform the calculation of the attenuation using the advanced model are presented in figure 6.13. These solutions all use hemp concrete as the absorptive treatment, since it has been shown that similar noise reduction performance can be obtained with this material compared to using a more classical fibrous sound insulating material, but at the same time hemp concrete is a more sustainable material.

Predicted broadband and third-octave insertion losses for the four designs and the two models are presented in table 6.5 and in figure 6.14. Again due to the increased complexity of the

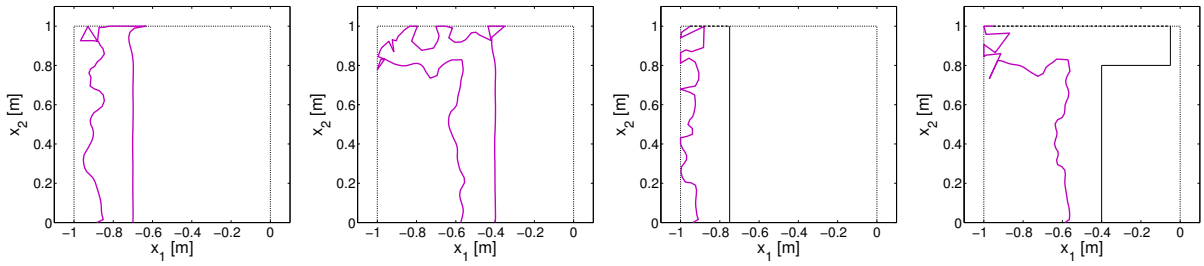

Design a) Design b) Design c) Design d)

Figure 6.13: Considered optimized designs for the comparison of predicted performance using the simplified and advanced models (see in figure 6.12). Hemp concrete is used as the absorbing treatment in this case. Design a): shape optimized fully absorbing barrier, medium wall starting geometry. Design b): shape optimized fully absorbing barrier, Gamma-shape starting geometry. Design c): shape optimized absorbing source side, optimized MPPR on top and rigid back, medium wall starting geometry. Design d): shape optimized absorbing source side, optimized MPPR on top and rigid back, T-shape starting geometry. Optimized admittance parameters are given in table 6.4.

advanced model, the calculations are made up to 1800 Hz only. One can essentially notice a similar behavior compared to the entirely rigid barrier case (see in section 5.4), which is that insertion losses are lowered when the more advanced model is used, especially in the low frequency range, and that interference dips are smoothed out. Broadband noise reductions remain however important, reaching 19 dB(A), whereas the performance of the shape optimized rigid barriers found in chapter 5 predicted using the same model were closer to 10 dB(A). This suggests that using acoustic surface treatment - especially absorbing treatment - provides a significant advantage in terms of acoustic performance even when the shape of the barrier is optimized.

Table 6.5: Comparison of broadband insertion losses in dB(A) in the 100-1800 Hz range for the four optimized designs given in figure 6.13 predicted either using the simplified model (coherent line source, infinite vertical baffle, rigid ground) or the advanced model (set of incoherent point sources, more realistic tramway geometry, rigid ground).

Design	a)	b)	c)	d)
Simplified model	19.1	22.5	22.5	25.2
Advanced model	16.1	19.1	18.6	18.6

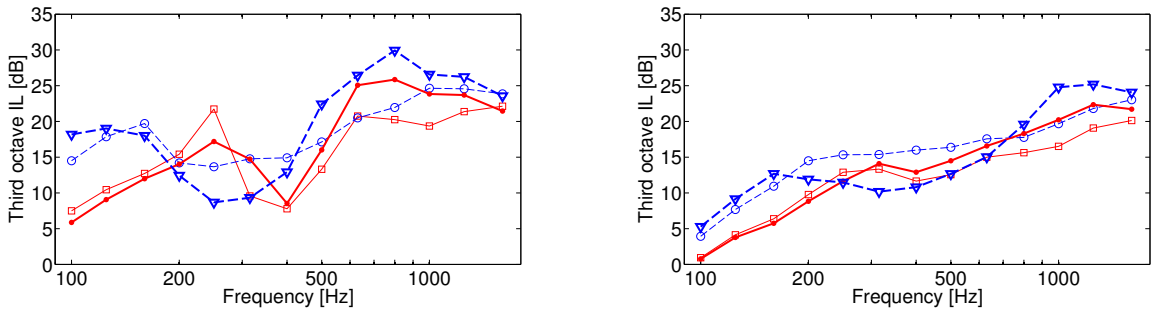

Figure 6.14: Comparison of third-octave insertion losses in dB in the 100-1800 Hz range for the four optimized designs given in figure 6.13 predicted either with the simplified model (coherent line source, infinite vertical baffle, rigid ground) or the more advanced model (set of incoherent point sources, more realistic tramway geometry, rigid ground). Thin solid red line: design a) - thin dashed blue line: design b) - thick solid red line: design c) - thick dashed blue line: design d). Left: simplified model - right: advanced model.

6.6 Conclusion

In this chapter, the general method presented in chapter 3 for coupling a shape optimization and an admittance optimization strategy is used to design optimized low height tramway noise barriers. Two types of treatments are considered, layers of porous materials (either fibrous or made out of hemp concrete) and a micro-perforated panel resonator. The optimization method has been run in different configurations of surface treatments, with different starting geometries.

The results show that even in the presence of an absorbing treatment, shape optimization tends to generate irregularities, which help redirect the acoustic energy and therefore can increase the noise reduction in the shadow zone of the barrier, similarly to what has been found when the barrier was assumed entirely rigid (see in chapter 5). However, it seems that the presence of acoustic absorbing treatment, irregularities on the top region of the barrier can also increase the attenuation, and that depending on the initial shape, the source side does not need to be very irregular. Besides, reactive treatments with tuned resonances also seem to potentially increase the performance of the barrier. It is also found that similar performances can be obtained with highly absorptive fibrous material or with hemp concrete as the porous absorbing treatment.

The predicted acoustic performance of fully optimized barriers can reach more than 24 dB(A) of tramway noise reduction, under several simplifying assumptions that were made to decrease computation time. Besides, extra calculations performed with what seems to be a more accurate model (more accurate tramway geometry and finite set of incoherent point sources) show that the found optimized designs can provide up to 19 dB(A) of attenuation. However, one should point out that those more advanced calculations were made still assuming that the barrier was infinitely extended in one dimension, that all surface treatments were locally reacting and neglecting any directivity effects.

In addition, feasibility issues should be considered if one would want to build such an optimized noise barrier. Indeed, the generated optimized shapes can be rather complicated and therefore one should check that such irregular shapes could be built, especially when covered with acoustic treatment. Nevertheless, let us recall that, based on BEM calculations, a significant improvement in tramway noise reduction can be obtained with such optimized designs compared to more simple ones (more than 6 dB(A) in most cases), and therefore it is probably worth it to explore ways to actually build those devices.

Chapter 7

Scale model measurements of tramway low-height noise barriers performances

7.1 Introduction

Numerical modeling is useful to predict the efficiency of a noise abatement device such as a noise barrier. However, as it has already been pointed out, calculations are made under many physical assumptions which might not be completely true in an actual implementation situation. It is of course desirable to test a new noise barrier design *in situ* (an example will be shown in chapter 8), but due to the complexity of such an implementation, one or few designs are usually tested (one can also refer to other studies [41, 67, 102, 124, 127]). A useful alternative that has been used for many decades in order to consider somewhat more realistic situations than typical numerical mathematically idealized situations, is to test a design in a controlled laboratory environment with a scale model. This typically allows more exhaustive studies since it is much cheaper to build many different designs at the model scale. This has been applied to test different shapes for highway noise barriers [122], quarter-resonator reactive noise barriers [103], inclined noise barriers [188], railway noise barriers [123], jagged-edge noise barriers [81, 129] as well as physical effects that can affect a noise barrier's efficiency, such as atmospheric refraction [42, 43]. Scale model measurements have also been extensively used by Baulac et al. to study traffic low-height noise barriers [4–6] and by Koussa to study gabions noise barriers [11, 13]. Those studies showed that numerical predictions usually agree well with the measurements (depending on the complexity of the considered situation).

In the context of low-height noise barriers, which are typically less than one meter high and one meter wide, a scale reduction factor of 10 is usually chosen since this makes the models sufficiently small to be built easily and sufficiently large to be able to render some small geometrical details (say of the order of 1 cm at full scale). As we will see, the frequency range needed in the scale model measurements to represent a typical transportation noise emission spectrum is also relatively easy to achieve at a 1/10th scale.

Even though scale measurements have been used extensively to study noise barriers efficiency, to the best of the author's knowledge, they have not been applied yet to study tramway

noise barriers other than in [1]. Especially, scale measurements would be helpful to assess the importance of the multi-reflections phenomenon, which has been mentioned several times in this work to explain the rather poor performance of simple rigid barriers, as well as the feasibility of the designs.

Although it seems possible to study some of the shape optimized designs that have been presented in chapter 5 and 6, using for instance laser cutting technology, this chapter is essentially concerned with the development of a methodology to perform scale model measurements of a low height barrier close to a tramway. Some applications will be considered as well, mostly considering the effect of the absorbing treatment on simple shapes such as the T-shape. Finally, it should be pointed out that most of the results of this chapter can also be found in [1].

7.2 Theoretical issues related to scale change

7.2.1 Physical quantities similarities

In order to represent the same diffraction phenomena - and therefore the same effect of the barrier - happening at the actual scale with a reduced scale geometry, one has to satisfy some similarity conditions. In the following, we will be referring to quantities at the reduced scale (as opposed to the full scale) with a superscript ^{s}.

First of all, it is well known that when geometrical dimensions are reduced by a factor N ($N = 10$ in our case), the wavelength has to be reduced by the same factor: $\lambda^s = \lambda/N$. Since the propagation will occur in the same medium at both scales (air), the speed of sound remains the same. Using the relationship $\lambda = c/f$ yields that frequencies at the reduced scale satisfy:

$$f^s = Nf$$

This also corresponds to keeping the value of the kr number constant, with r a generic distance between two relevant points in the problem (source, scatterer or receiver), which is the most important parameter in diffraction problems. In the case of a tramway low-height noise barrier, the frequency range of interest is roughly from 100 Hz to 2000 Hz at full scale, and therefore from 1 kHz to 20 kHz at reduced scale.

Also, in order to keep the similarity of the boundary condition, one has to require that the normalized specific acoustic admittance at the boundary, evaluated at the corresponding frequencies, should remain constant. In other terms, one should impose:

$$\beta^s(f^s) = \beta(f) \tag{7.1}$$

This imposes relationships on the admittance parameters between the two scales. For instance, this condition can be applied to the Delany and Bazley model which is going to be used to characterize the properties of absorbing materials.

From the expression of the normalized impedance and wavenumber of this model (see in section 1.6.1), one can see that only one characteristic number matters for this model: σ/f. Therefore, admittance similarity as given by equation (7.1) is ensured if the flow resistivity at

the reduced scale σ^s satisfies:

$$\frac{\sigma^s}{f^s} = \frac{\sigma}{f} \quad \Leftrightarrow \quad \sigma^s = \frac{f^s}{f}\,\sigma = N\sigma$$

For instance, with a reduction factor of 10, to represent a material which would have a flow resistivity of $\sigma = 50\,\text{kPa.s/m}^2$ at full scale, one needs a material with a flow resistivity of $\sigma^s = 500\,\text{kPa.s/m}^2$. Typically layers of felt have been used to represent typical absorbing porous materials [5], which is what we will use in our measurements (see in section 7.5).

7.2.2 Air absorption

As it has just been mentioned, reduced scale model measurements require rather high frequency studies (typically in our case from 1 kHz to about 20 kHz). However, at these high frequencies, atmospheric air absorption might not be negligible any more, which could bias the measurements. This attenuation, which is related to visco-thermal dissipation effects in air itself as well as molecular relaxation effects, can be calculated using standard procedures [189, 190], and depends on ambient temperature, relative humidity and ambient pressure. For a typical ambient pressure of one atmosphere and a typical range of values for the two other parameters (temperature from 10 to 30°C and relative humidity from 20 to 70%), in the considered frequency range (1 kHz to 25 kHz), air absorption is always smaller than 1 dB/m (see figure 7.1). Propagation distances we will consider typically are of the order of one meter at the reduced scale, and therefore air absorption will never cause more than 1 dB of difference in level, which can be neglected in our context.

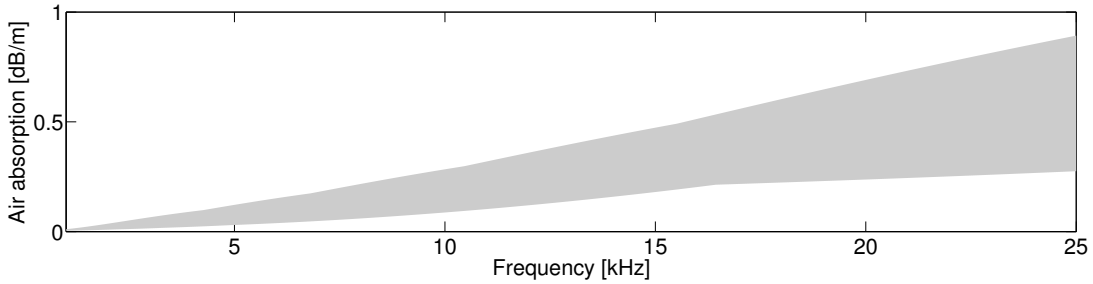

Figure 7.1: Range of values for the attenuation due to air absorption in dB/m, as a function of frequency. Calculation is based on the ANSI standard S1.26 [190]. Ambient temperature varies from 10 to 30°C and relative humidity from 20 to 70% (ambient pressure is assumed to be 1 atmosphere).

7.3 Description of the experimental protocol

The quantity used to assess the efficiency of the barrier we have been considering in this work is essentially the insertion loss, which is namely a ratio of pressure levels in the frequency domain, with and without the device, given a source and receiver positions and a given geometrical configuration. Assuming the desired configuration can be built, one still needs to choose the type of receiver to perform the measurement and the type of source to generate the signal.

7.3.1 Choice of the source: electrostatic spark source

Figure 7.2: Spark source Grozier GTS 51. The generator charges a capacitance, which can then be discharged across close electrodes. The electrodes are located at the end of a wand attached to the generator. Left: spark generator itself. Right: zoom on the electrodes, located at the end of the wand. Spacing between the electrodes is of the order of 3 mm.

In our numerical calculations, the source has been assumed omni-directional (point source), and therefore one needs to meet this condition as much as possible in practice in order to compare calculations and measurements. Besides, the source should be able to produce a significant output in the considered frequency range at the reduced scale (1 kHz - 20 kHz in our case). Typical sources that have been used for scale model measurements are audio tweeters [11], audio speakers coupled with circular pipes [188] and mostly electrostatic spark sources [5, 81, 129]. Pressurized air jets [123] have been used as well for higher reduction ratios and hence higher frequency ranges (up to 80 kHz).

The main advantage of using speakers or tweeters is that the signal that is fed to the source is well-defined (typically digitally generated), and therefore the measurement is repeatable and can be refined using classical digital signal processing techniques. However, those sources are inherently directive due to their dimensions in the considered frequency range (above 10 kHz), which can induce a significant error when comparing measurements with numerical simulations. On the other hand, for spark sources the volume where the spark is generated is small, typically of the order of 1 mm (see figure 7.2), which theoretically ensures the spark to be omni-directional at least up to 20 kHz ($ka \approx 0.4$ with $a = 1\,\text{mm}$ at 20 kHz).

Nevertheless, the spark is not strictly repeatable, which is a problem when measuring a noise barrier insertion loss since two separate measurements must be performed with and without the device, although the use of a reference microphone to correct the difference between spark signals can help tackle this issue [5]. Some authors also measured that the difference between sparks was sufficiently small to be neglected [81, 191]. This has been measured as well for the spark source we used for which we found, when the microphone is in front of the wand, that the different spark generated time waveforms have similar shape and that standard deviation of the spectrum is usually less than 1 dB up to 20 kHz (see figure 7.3). We also found that this variability is slightly higher in the plane perpendicular to the wand, but remains below 2 dB in this frequency

range. Nevertheless, as was done by Baulac et al. [5], we will use a reference microphone to correct for spark variability.

Concerning the frequency content itself of the generated signal, one can see that the signal has a significant energy between 2 kHz and 20 kHz, but quite a bit less below 2 kHz. We therefore expect measurements not to be as accurate below 200 Hz at the full scale.

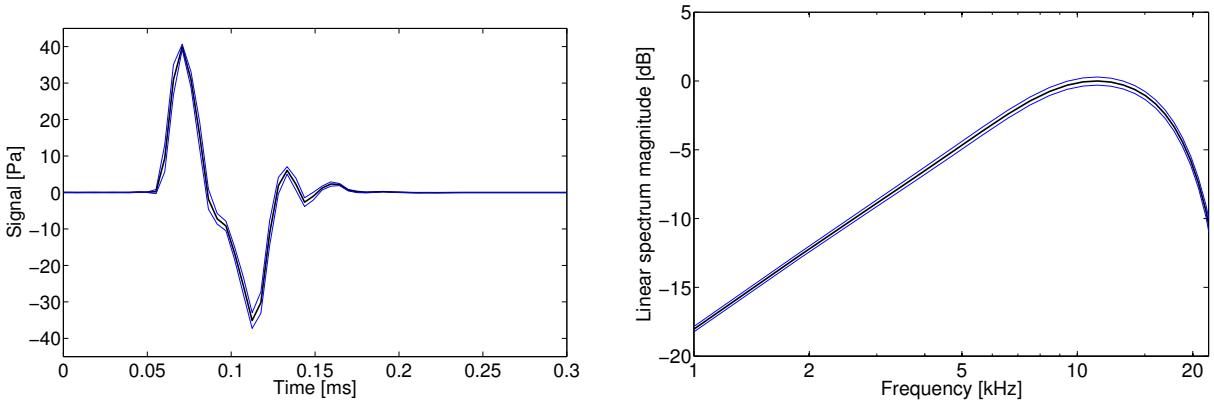

Figure 7.3: Mean and dispersion (plus and minus a standard deviation) of the signal generated by the spark, based on 10 recorded sparks in free field conditions approximately 1 m in front of the wand (sampling frequency of 192 kHz). Left - time domain signal in Pa ; right - linear spectrum magnitude in dB (the reference corresponds to the maximum value of the mean spectrum). Black thick line - mean quantity ; thin blue lines - mean plus and minus one standard deviation.

7.3.2 Measurement room and signal selection by time windowing

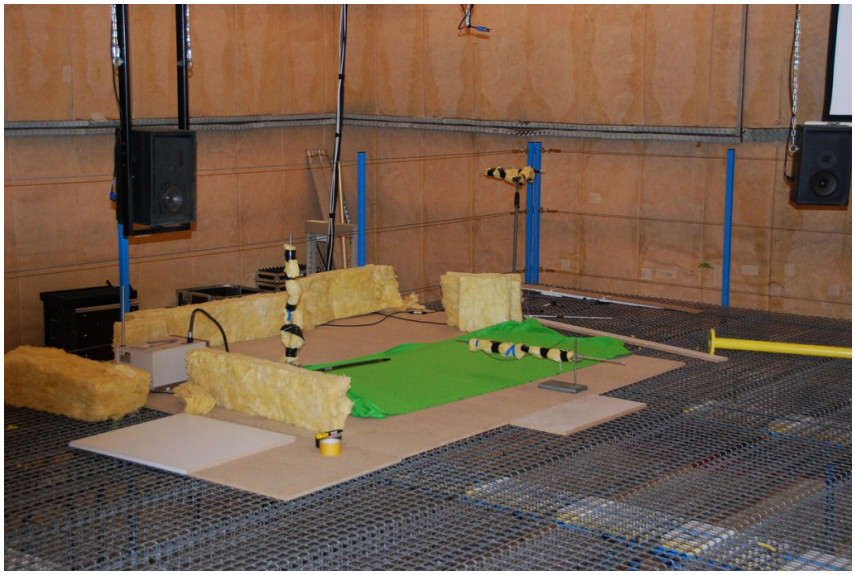

Figure 7.4: Overview of the experimental set up in the "scale model room" at the CSTB Grenoble. The walls of the room are covered with absorptive glass wool, which makes the room rather dry. Besides, the noise floor is low thanks to good insulation.

The room in which the measurements have been performed is the so-called "scale model room" at the CSTB in Grenoble, France. It is a large dry room with walls, floor and ceiling covered with absorptive glass wool. The main support structure is a simple metal grille, and

large pressed woods boards are used to represent a rigid ground (see figure 7.4).

This room is not anechoic and does have a few surrounding objects that could provide unwanted reflections to the measurement. However, since the room is rather large and the objects placed sufficiently far apart, those unwanted reflections will arrive long enough after the significant part of the signal and can therefore be windowed out. An example of this process is given in figure 7.5. Here one can extract the direct arrival or the direct and reflected pulses, and remove unwanted later arrivals.

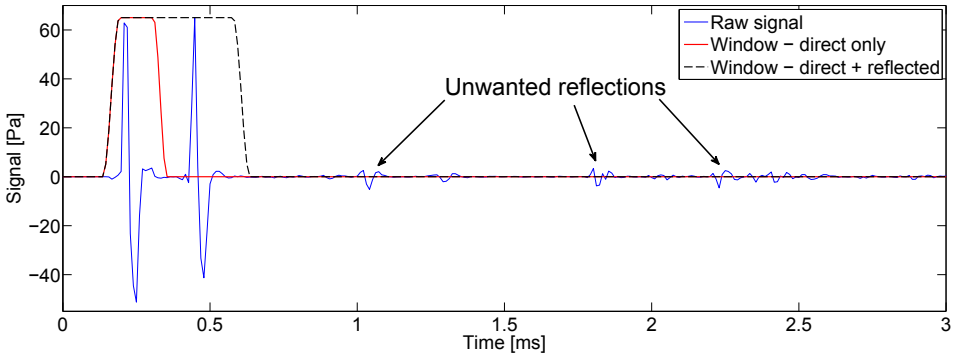

Figure 7.5: Recorded pressure signal in the case of a reflection above a rigid ground. Source and receiver are $z = 14.5\,\text{cm}$ above the ground and distant of $r = 49.5\,\text{cm}$ horizontally. One can clearly distinguish the direct arrival and the reflected pulse, as well as some extra unwanted reflections. The relevant part of the signal can then be extracted by multiplication of a specifically adjusted window function.

The considered window has been chosen as follows: the first rising half of a Hanning window, followed by a flat portion, and finally the second fading half of a Hanning window (this window is close to the so-called Adrienne window [11]). The time reference of the window is the instant of direct arrival t_{dir}, which is here defined as the instant at which the signal reaches 10% of the peak magnitude $|x|_{\max}$. Four time parameters are then needed to describe the window: the duration of the rising part Δt_{rise}, the duration of the flat portion before the direct arrival $\Delta t_{\text{flat},1}$, the duration of the flat portion after the direct arrival $\Delta t_{\text{flat},2}$, and finally the duration of the fading part Δt_{end} (see figure 7.6). Those parameters are manually chosen to extract the relevant part of the signal. For instance, it has been found that the following parameters can be used when one would like to extract a single direct arrival without any reflections (free-field conditions):

$$\Delta t_{\text{rise}} = 0.05\,\text{ms} \quad \Delta t_{\text{flat},1} = 0\,\text{ms} \quad \Delta t_{\text{flat},2} = 0.12\,\text{ms} \quad \Delta t_{\text{end}} = 0.05\,\text{ms}$$

Moreover, in order to smooth out the spectrum curve, the windowed signals are zero-padded so that each extracted signal has the same total number of points. Typically 2048 points were used, which at a sampling frequency of 192 kHz yields a frequency spacing of about 100 Hz, that is 10 Hz at full scale.

7.3.3 Receiver locations and microphones

The microphones used in this measurement must meet the requirement to have a flat frequency response in the considered frequency range and to be sufficiently small not to disturb the acoustic

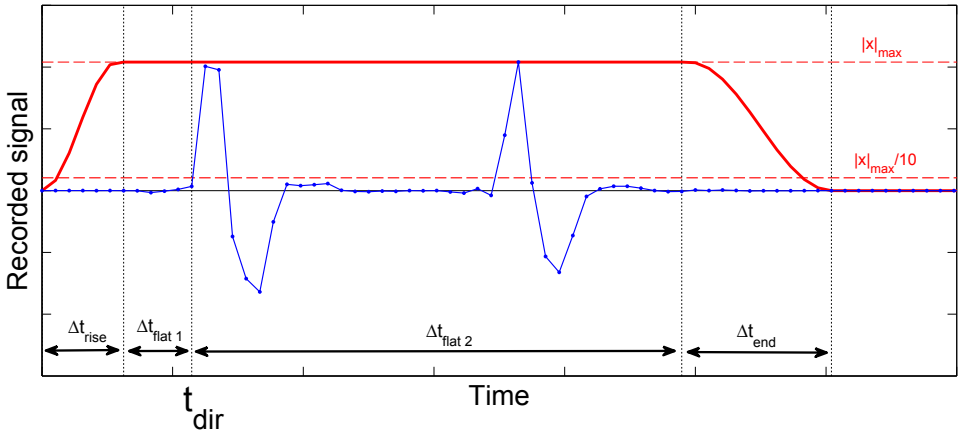

Figure 7.6: Definition of the parameters defining the time window used to extract the signal from the raw recording. t_{dir} is the instant of direct arrival, Δt_{rise} the duration of the rising part, $\Delta t_{\mathrm{flat},1}$ and $\Delta t_{\mathrm{flat},2}$ the durations of the flat parts respectively before and after the direct arrival, and Δt_{end} the duration of the fading part.

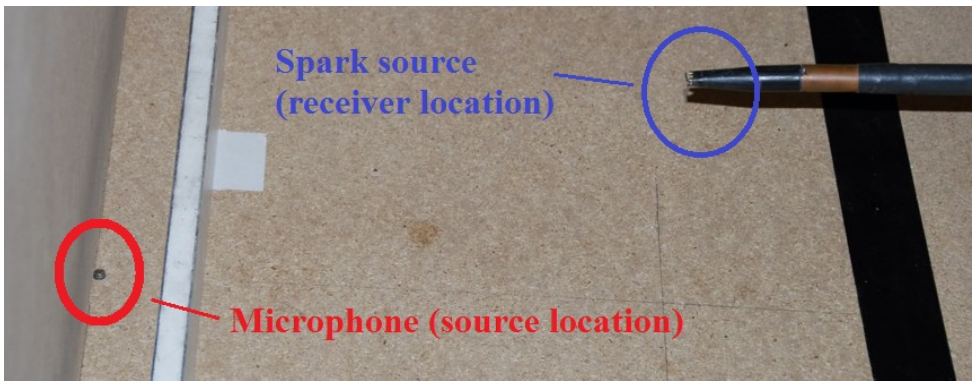

Figure 7.7: Spark source and microphone positions in the scale model measurement. Using reciprocity, source and receiver positions have been exchanged, so that the B&K 1/4" microphone lies at the ground level and represents the actual source, whereas the spark is generated at the actual receiver position, behind the barrier.

field. Brüel & Kjær quarter-inch type 4136 capsules mounted on type 2633 pre-amplifiers were chosen since they meet both requirements. Those capsules are pressure microphones, and since there is no correction for the diffraction induced by their presence, one should pay attention to their location. In our context, reciprocity states that source and receiver can be exchanged without changing the measured signal. Therefore, it has been chosen to put one microphone through the "ground" in place of the source located on the ground, which implies that the source (electrodes at the end of the wand) will be put in place of the receiver (see figure 7.7). This choice was mostly based on the fact that, if the source signal was actually generated on the ground, it would have been difficult to extract a direct arrival only at the reference microphone due to the confinement between the source, the tramway side and the barrier. Besides, the microphone inserted in the ground has little influence on the sound field and therefore the use of a pressure microphone makes sense in this context.

Moreover, the reference microphone, as a pressure microphone used in a free-field context, should be oriented perpendicular to the sound propagation direction. Also, at the reference, only the direct arrival signal should be recorded, which can be achieved by properly windowing

the recording signal (as explained in section 7.3.2). Finally, the reference microphone cannot be placed too close to the spark to avoid saturation (either at the pre-amplifier or at the digital conversion level).

7.3.4 Scale model representation of the tramway

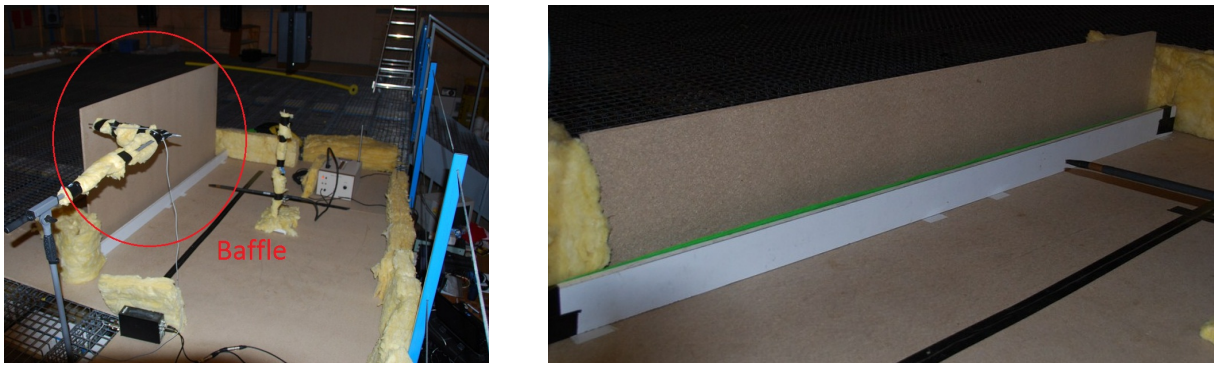

Figure 7.8: Wooden structure used to approximate the effect of the tramway. Left: "infinite" baffle configuration, 1 m high wooden board (10 meters in full scale). Right: tram configuration, 30 cm high board (3 m at full scale). The structure can be lifted up to reproduce the gap between the bottom of the tramway body and the ground (typically 1.6 cm was used in the model, 16 cm at full scale).

As stated in previous chapters, the presence of the tramway has an important effect on the efficiency of the barrier due to the multi-reflections happening between the tramway side and the barrier. To approximate this effect, a simple assembly of two pressed wood boards has been made (see figure 7.8). Both boards are 2 m long, one is 30 cm wide (3 m at full scale, which is a typical height for a tramway) and the other about 1 m wide (10 m at full scale). This second board can be used to approximate an "infinite" baffle, and therefore the effect of this idealization can be measured as well to some extent. The boards can be held raised up in order to reproduce the gap between the bottom of the tramway body and the ground. In our model, the boards were held 1.6 cm above the ground, which corresponds to 16 cm at full scale.

7.3.5 Data acquisition system and sampling frequency

Figure 7.9: Fireface UFX soundboard used to acquire the signals from the receiver microphone and the reference microphone. Maximum sampling frequency is $f_s = 192\,\text{kHz}$.

The two microphones and their pre-amplifiers are powered by a Brüel & Kjær power supply type 5935. No gain is applied since the peak value of the spark signal is rather high. The two

signals are then digitalized by a Fireface UFX soundboard (line entry) and then recorded thanks to the Reaper software. The soundboard has several sampling frequencies available, up to 192 kHz. The spark signal, which is impulsive (see figure 7.3), has a rather large bandwidth typically related to the inverse of the shortest rise time, which is about 15 μs. Therefore, one can expect a bandwidth of about 60 kHz, which requires a sampling frequency at least twice this value, 120 kHz. Simply from the signal shape, it seems like a 192 kHz sampling rate would be necessary. Indeed, one can compare the spectrum of the spark signal obtained when sampling at 96 kHz and 192 kHz (see figure 7.10). One can notice that even at 20 kHz, aliasing causes the two spectra to differ by more than 2 dB in magnitude. All recordings will therefore be made at a sampling rate of 192 kHz.

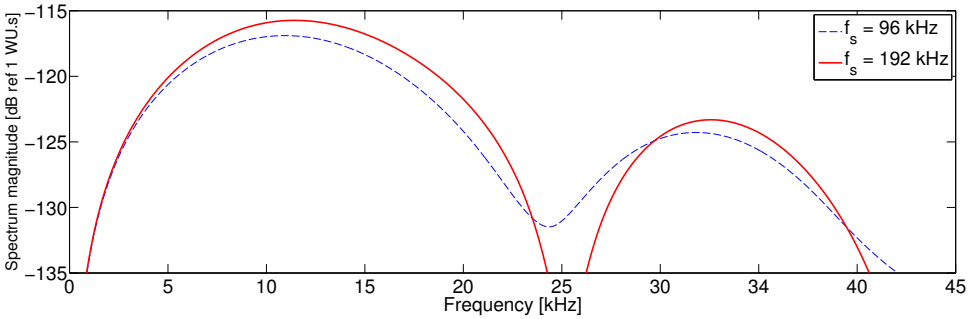

Figure 7.10: Comparison of the linear spectrum magnitude (in dB ref 1 WU.s) of the spark signal sampled at 96 kHz and 192 kHz, recorded in free-field conditions at a distance of about 1 m.

7.3.6 Measurement set-up overview and insertion loss calculation

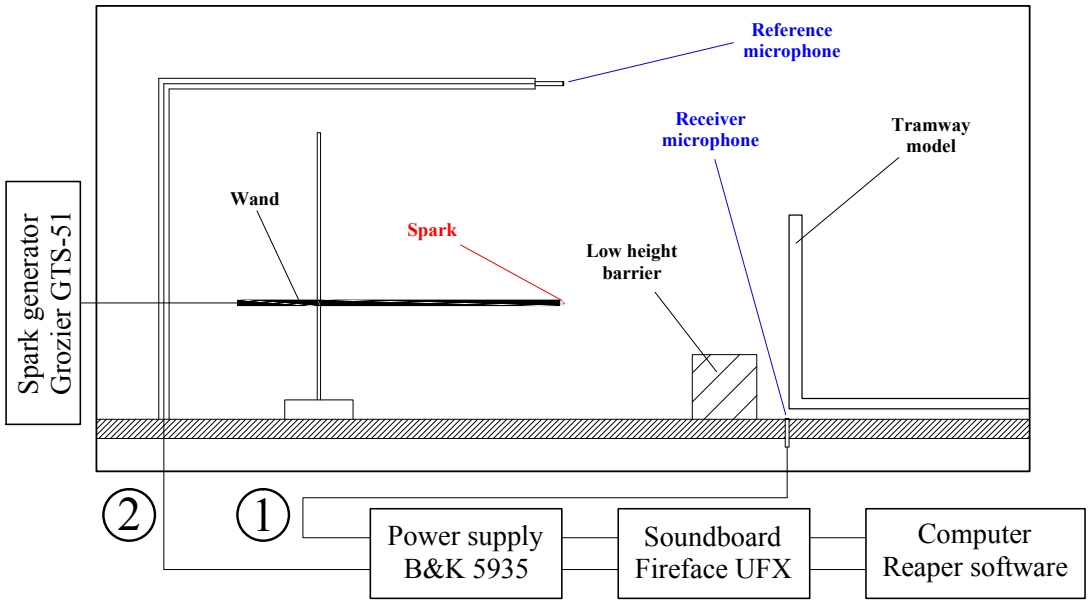

Figure 7.11: Schematic representing the whole measurement set up and the data acquisition chain.

The measurement set up as well as the data acquisition system is summarized schematically in figure 7.11. In addition, the typical geometrical configuration of the measurement is shown in

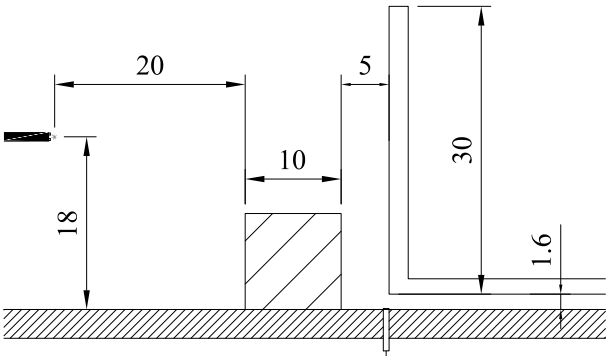

Figure 7.12: Chosen geometrical configuration for a given noise barrier insertion loss calculation. Dimensions are here in centimeters at the reduced scale.

figure 7.12. The receiver location (where the spark is generated) has been chosen as the highest and closest point to the barrier of the receiver zone considered in the BEM calculations, which is where the barrier is expected to have the smallest effect.

7.3.6.1 Insertion loss calculation

First, the chosen noise barrier scale model is set up, as well as the tramway scale model (we will only present results in the "tramway" case, as explained in section 7.3.4, since this is what we are mostly interested in). The recording at 192 kHz is started by the operator in the Reaper software, who then fires the spark (with a remote switch), and then stops the recordings. Typically five sparks were recorded for each configuration to allow some averaging process. Each recorded WAV file contains two signals, one from the so-called receiver microphone and the other from the reference microphone. WAV files are then imported in Matlab for windowing and treatment. The ambient temperature is also recorded so to know the speed of sound at the measurement instant (which is needed in the numerical calculation). The speed of sound as a function of the ambient temperature T in degrees kelvin is simply given by:

$$c = \sqrt{\frac{\gamma R T}{M}}$$

with $\gamma = 1.4$ is the ratio of specific heats for air, $R = 8.314\,\mathrm{J.mol^{-1}.K^{-1}}$ is the universal gas constant and $M = 28.97\ 10^{-3}\,\mathrm{kg.mol^{-1}}$ is the molecular mass of air.

To measure the insertion loss of a given barrier, a recording is made with the barrier, which yields two signals: x measured at the receiver microphone, and x_{ref} at the reference microphone. The barrier is then removed, and a recording is made again. The recorded signals are referred to in this case as x_{in} and $x_{\mathrm{in,ref}}$. Proper windowing is applied to each signal which are all zero-padded in order to have the same total number of points (typically 2048). The linear spectrum is calculated for each of the windowed signals, which yields the four quantities: X^w, $X^{\mathrm{w}}_{\mathrm{ref}}$, $X^{\mathrm{w}}_{\mathrm{in}}$ and $X^{\mathrm{w}}_{\mathrm{in,ref}}$. The measured insertion loss is then defined as follows:

$$\mathrm{IL} = -20\,\log\left|\frac{X^w}{X^{\mathrm{w}}_{\mathrm{in}}}\,\frac{X^{\mathrm{w}}_{\mathrm{in,ref}}}{X^{\mathrm{w}}_{\mathrm{ref}}}\right|$$

7.4 Simple validation tests

From now on, unless specified, dimensions and frequencies will be given at full scale. For instance, if a barrier height is actually 10 cm in the scale model, it will be written as its equivalent in full scale, which is 1 m. The frequency range of interest will also mostly be from now 100 Hz to 2000 Hz (as opposed to the frequency range actually used in the measurements, which is 1 kHz to 20 kHz).

7.4.1 Reflection on a rigid ground

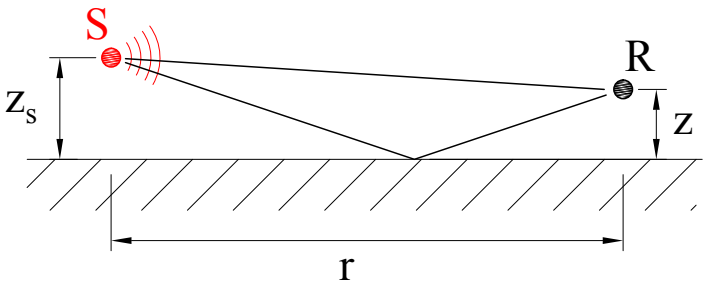

Figure 7.13: Geometrical configuration of the first test case. The source and receiver are located at height $z = z_s = 1.45\,\mathrm{m}$ and are separated by a horizontal distance $r = 4.95\,\mathrm{m}$ (full scale).

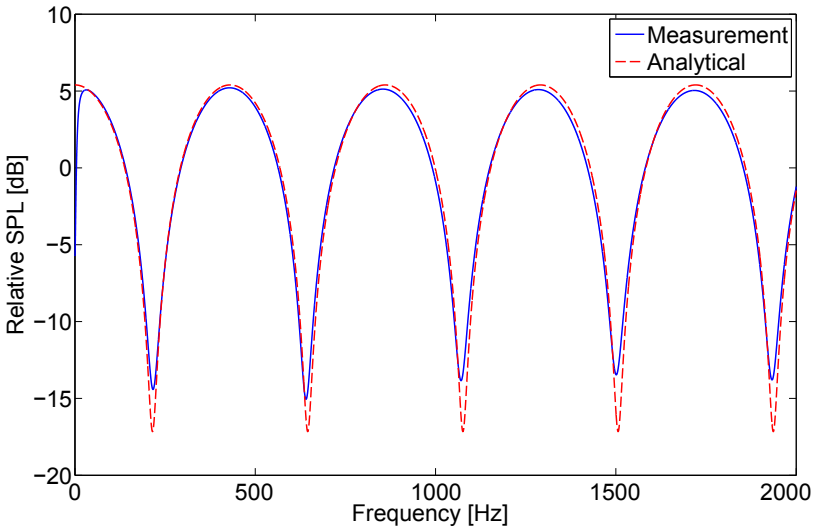

Figure 7.14: Comparison between measured and calculated relative SPL in dB as a function of frequency for the case described in figure 7.13.

The experimental protocol explained in section 7.3 is here tested in simple cases in order to assess its validity. First, a simple reflection on a rigid ground configuration is considered (see figure 7.13). The recorded signal at the microphone is shown in figure 7.5. In this case one can easily window the direct contribution p_{in} only, and separately the total field p, direct plus reflected contribution. From this one can calculate a measured relative sound pressure level ΔL_{meas} given by:

$$\Delta L_{\mathrm{meas}} = 20 \log \frac{P}{P_{\mathrm{in}}}$$

with P and P_{in} the spectra of p and p_{in}. In this simple case, assuming a perfectly rigid ground, the relative SPL is also given analytically by the following expression:

$$\Delta L_{\text{calc}} = 20 \log\left|1 + \frac{R_1}{R_2} e^{ik(R_2 - R_1)}\right|$$

with $R_1 = \sqrt{r^2 + (z - z_s)^2}$ is the direct path length and $R_2 = \sqrt{r^2 + (z + z_s)^2}$ is the reflected path length. Comparison between measurement and calculation is shown in figure 7.14. Agreement is excellent, which a posteriori justifies the fact that the pressed wood board used as the ground is indeed close to being perfectly rigid.

7.4.2 Diffraction by a straight wall

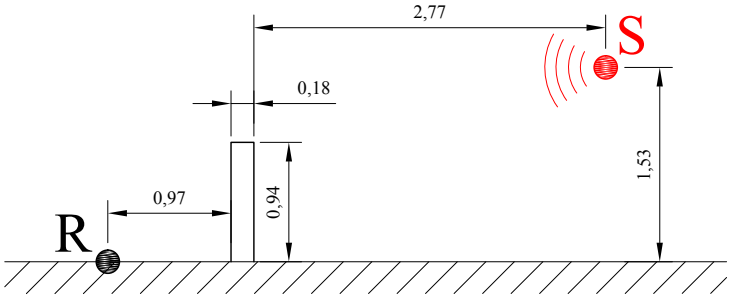

Figure 7.15: Geometrical configuration of the second test case, which is a simple diffraction by a straight wall with source on the ground. Dimensions are in meters (full scale).

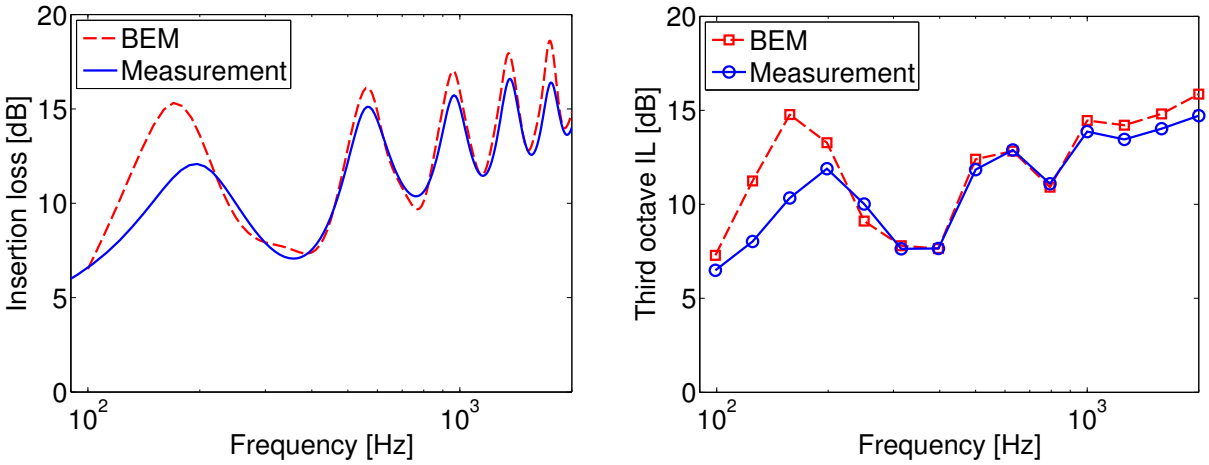

Figure 7.16: Comparison between measured and calculation insertion loss in the case of a simple straight wall (geometry given in figure 7.15). Left: insertion loss curve on a fine frequency spectrum - right: third-octave insertion losses. Solid line: measurements - dashed line: BEM calculations.

The second test case is the diffraction by a simple straight wall without the tramway. The geometrical configuration is shown in figure 7.15. The measured insertion loss is calculated using the process explained in section 7.3.6.1 and also with the boundary element method (BEM). Comparison is shown in figure 7.16 left part. One can notice overall a good agreement, especially in the insertion loss dips, even though there is a significant discrepancy at lower frequencies

(below 200 Hz) and at insertion loss peaks. The low frequency discrepancy could be due to a lack of energy in this low frequency range, as stated in section 7.3.1. Moreover, the discrepancy at insertion loss peaks is not surprising since those correspond to maximum destructive interference effects, which are usually not reproduced exactly in reality. This does not matter too much in our case since the A-weighted noise spectrum of the tramway source has little energy in the low frequency range, and also since the insertion loss peaks do not weight a lot when averaging over wide frequency bands. Indeed, comparing third octave band insertion losses (see figure 7.16 right part), the agreement is very good above 200 Hz up to 2000 Hz (within 1 dB).

7.5 Porous absorbing materials at the reduced scale: felt layers

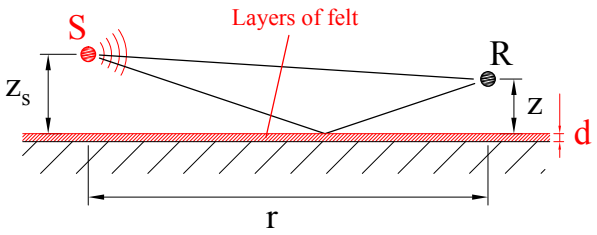

Figure 7.17: Geometrical configuration used for identification of the Delany-Bazley parameters of felt layers. Source and receiver heights are $z_s = 1.40\,\mathrm{m}$ and $z = 1.58\,\mathrm{m}$ and are separated by a horizontal distance $r = 5.45\,\mathrm{m}$ (full scale).

As previously stated in section 7.2.1, to represent a Delany-Bazley porous material of flow resistivity σ at the full scale, one needs a material of flow resistivity $\sigma^s = N\,\sigma$ at the reduced scale, which is typically a less absorbing material. Simple layers of felt can therefore be used to represent rather absorbing materials at full scale [5]. We proceed to the identification of the equivalent Delany-Bazley parameters by considering the simplest configuration in which the admittance of a surface matters: a reflection on a uniform impedant ground (see figure 7.17). In this case, the relative SPL can be easily measured and also calculated using the Weyl - Van der Pol solution [38]. In the case of a locally reacting plane of uniform normalized admittance β, the relative SPL can be approximately written as:

$$\Delta L_{\mathrm{calc}} = 20\,\log\left|1 + Q\,\frac{R_1}{R_2}\,e^{\mathrm{i}k(R_2-R_1)}\right| \qquad \text{with} \quad \begin{cases} Q = R_p + (1-R_p)\,F(d) \\ R_p = \dfrac{\sin\theta - \beta}{\sin\theta + \beta} \\ F(d) = 1 + \mathrm{i}\sqrt{\pi}\,d\,e^{-d^2}\left(1 - \mathrm{erf}(d)\right) \\ d = \sqrt{\dfrac{\mathrm{i}kR_2}{2}}\,(\beta + \sin\theta) \end{cases} \tag{7.2}$$

with $R_1 = \sqrt{(r-r_s)^2 + (z-z_s)^2}$ and $R_2 = \sqrt{(r-r_s)^2 + (z+z_s)^2}$ are the direct and reflected propagation distances, θ is the incidence angle defined by $\sin\theta = (z+z_s)/R_2$, d the so-called "numerical distance", erf the error function, F the boundary loss factor and R_p and Q the plane wave and spherical reflection coefficients. The normalized admittance β is calculated following the rigid-backed Delany-Bazley model (see in section 1.6.1), which depends on two parameters:

flow resistivity σ and thickness d (expressed here at full scale). For a given geometrical configuration, the calculated value of relative SPL ΔL_{calc} only depends on frequency and those two parameters, which can therefore be numerically fitted to match measured values of relative SPL as closely as possible. This process has been done for one to four layers of felt. Results of the identification is summarized in table 7.1. Measured and curve-fitted calculated relative SPL are also shown in figure 7.18.

Table 7.1: Fitted rigid-backed Delany-Bazley layer model parameters for one to four layers of felt (full scale).

Number of layers	Delany-Bazley layer parameters	
	Flow resistivity [kPa.s/m^2]	Thickness [m]
1	300	∞
2	150	∞
3	84	∞
4	66	0.04

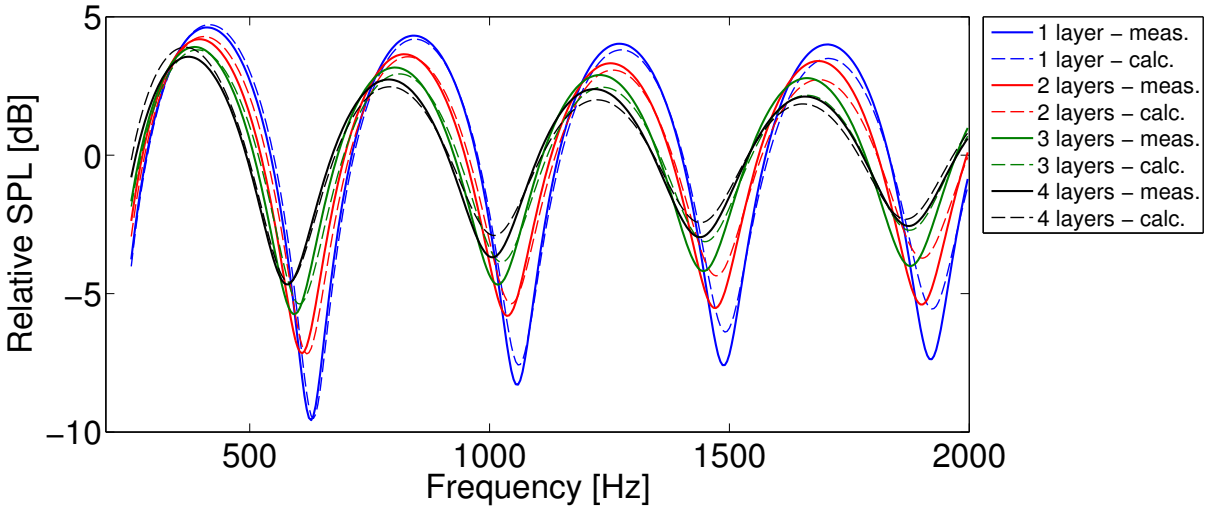

Figure 7.18: Comparison of measured and calculated relative SPL in dB in the case of a reflection on a uniform plane covered with one to four layers of felt. The calculation is based on the Weyl - Van der Pol solution given in equation (7.2), assuming the geometry given in figure 7.17. The admittance of the layer is calculated using the rigid-backed Delany-Bazley layer model. The parameter values used in the calculation are given in table 7.1. Continuous thick line: measurement - dashed thin line: calculation.

First one can notice than the more layers one uses, the more absorbent the equivalent porous material becomes since the effective flow resistivity decreases with the number of layers. This can also be seen in comparing the relative SPL curves (see figure 7.18), since the level at the constructive interference peaks decreases as the number of layers increases. The change of impedance also induces a phase change, which induces a frequency shift in the interference dips. Both effects are quite well reproduced by the Delany-Bazley model, although in the higher frequency range this model overestimates the absorption effect in the case of one to three layers. The match is however significantly better in the case of four layers. Further, the finite thickness of the layer does not seem to allow a much better match, except in the four layers case. For one to three layers of felt, one can therefore consider the equivalent porous layer infinitely thick.

We will therefore use four layers to represent an absorbing porous treatment on the scale

model barrier. Indeed, the value of 66 kPa.s/m^2 for the flow resistivity found in this section to characterize four layers of felt is rather close to the assumed value in chapter 6 - 50 kPa.s/m^2 - , which corresponds to a rather absorptive fiberglass type material. One can for instance calculate the absorption coefficient in both cases (see figure 7.19) and notice that they are indeed similar in the considered frequency range.

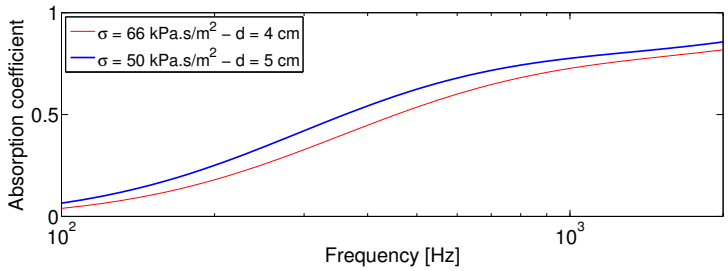

Figure 7.19: Comparison of the calculated absorption coefficient of two Delany-Bazley layers. Thin line: equivalent layer corresponding to four layers of felt (parameters $\sigma = 66\,\mathrm{kPa.s/m^2}$ and $d = 4\,\mathrm{cm}$) - thick line: fibrous absorbing material assumed in chapter 6 (parameters $\sigma = 50\,\mathrm{kPa.s/m^2}$ and $d = 5\,\mathrm{cm}$).

7.6 Measured performance of a T-shape barrier with absorbing treatment

In this section a few applications of the measurement protocol that has been explained in section 7.3 are presented. We chose to focus on the T-shape geometry, which is relatively easy to build, and to study the effect of different amount of absorbing treatment on the performance of the low-height barrier. In the following, the absorbing material in the scale model is made of four layers of felt (as explained in section 7.5).

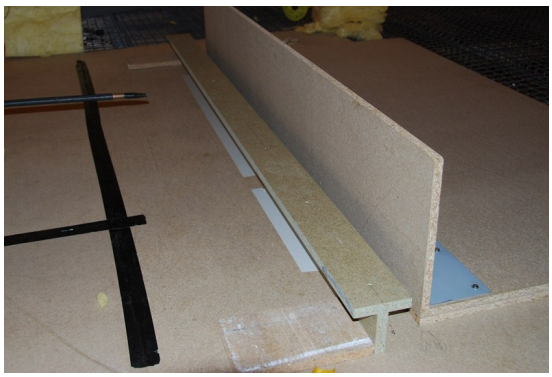

Figure 7.20: Photograph of the T-shape barrier scale model, made of two pressed wood boards.

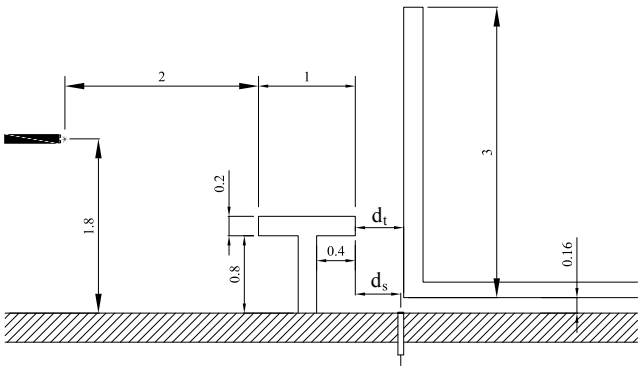

Figure 7.21: Geometrical configuration for the T-shape barrier measurement. Dimensions are in meters (full scale).

The scale model of the T-shape barrier is made of two pressed wood boards (see figure 7.20). The boards are 19 mm thick, and assuming a density of 600 kg/m^3 for the pressed wood, the transmission loss across the board based on the mass law is about 40 dB at 1000 Hz (100 Hz at full scale). This suggests the boards can be considered as acoustically rigid in our measurements.

Several absorbing treatments are considered, detailed in figure 7.22. The different locations of porous treatments have been chosen in order to emphasize the effect of such treatment on

attenuating multiple reflections. Those multiple reflections can be clearly seen in the signal recorded at the microphone in the case of a rigid barrier, shown in figure 7.23. One can notice the many reflections happening after the direct arrival due to the presence of the tramway, which in the end diminishes the efficiency of the barrier, as pointed out for instance in chapter 5.

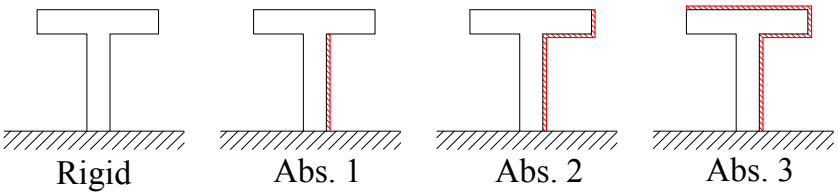

Figure 7.22: Considered configurations of absorbing treatment placed on the T-shape barrier and their denominations: rigid, Abs. 1, Abs. 2 and Abs. 3 (the tram is located on the right).

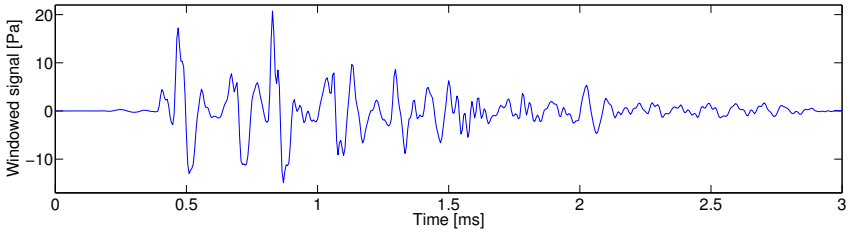

Figure 7.23: Windowed signal at the receiver microphone in the case of a rigid T-shape barrier.

7.6.1 Comparisons between measurements and BEM calculations

For a given configuration, the measured insertion loss is calculated and compared to a 2D BEM calculation, performed with the geometry given in figure 7.21. However, preliminary calculations showed that better agreement in the interference dips was obtained when the distance between the barrier and the tramway side d_t and the distance between barrier and source d_s (as shown on figure 7.21) were slightly modified to $d_t = 0.47\,\mathrm{m}$ and $d_s = 0.44\,\mathrm{m}$ instead of $d_t = d_s = 0.5\,\mathrm{m}$. This correction could be understood from the fact that the microphone has a finite extent and that there is some uncertainty in the distances in the experimental set-up. Whereas in most cases this uncertainty does not have a significant effect, it seems like in this case, due to the confinement of the sound field between the barrier and the tramway, the effect is significant. This correction will however remain the same for all BEM calculations.

Third-octave insertion losses for the considered treatments are presented in figure 7.24, and broadband insertion losses in table 7.2. The agreement between calculated and measurement third-octave insertion losses is good, although a consistent discrepancy can be observed at low frequencies, which could be due to a lack of energy of the spark signal, as stated earlier. Some discrepancy also exists at higher frequencies in the presence of absorbing treatment, where the BEM actually underestimates the efficiency of the barrier. However, this discrepancy does not affect the broadband insertion loss in presence of absorbing treatment, which is in very good agreement with the measurements in the Abs.2 and Abs.3 case. In the rigid case however, the discrepancy is such that the broadband insertion loss is underestimated by 2 dB(A). This might be due to the fact that the insertion losses are rather low in this case because of the

multiple reflections which induce complicated interference effects at the receiver. Those effects are sensitive to the spatial coherence of the source and the fine details of the geometry, and it would make sense that results would be different between the idealized BEM model (point source and point receiver) as opposed to the scale model set-up (finite extend of the of the source and receiver).

Table 7.2: Comparison of calculated and measured broadband insertion losses in the frequency range 100-1800 Hz in dB(A) for the T-shape barrier and the considered treatments.

	Broadband IL [dB(A)]	
	BEM	Measurement
Rigid	3.8	5.8
Abs. 1	7	8.4
Abs. 2	10.3	10.4
Abs. 3	14.0	14.0

7.7 Conclusion

An experimental protocol to measure the insertion loss of a low-height noise barrier close to a tramway at a reduced scale (here 1/10th) using an impulsive spark source is proposed and tested. The impulsive nature of the signal generated by the spark source allows accurate signal selection thanks to time domain windowing. Besides, the spectral content of this type of signal allows measurement in the range 100 - 1800 Hz at full scale, which is appropriate for tramway noise abatement applications.

Based on theoretical considerations on the admittance similarity during the scale change, one can identify equivalent properties of porous materials at the reduced scale (using for instance felt layers), which allows one to study for instance the effect of different amounts of absorbing materials.

After validation of the measurement protocol in simple configurations, it is applied to study the effect of absorbing treatments on a T-shape barrier. First, in the case of a rigid barrier, the multi-reflection phenomenon between the tramway side and the barrier can be clearly observed in the measured time domain signal. Corresponding insertion loss curves show that in this case the attenuation of the barrier is rather low - about 6 dB(A). However, placing absorbing treatment on the barrier side directly exposed to the source adds 4 dB(A) to the performance, whereas adding treatment on top yields another increase of 4 dB(A). 2D BEM calculations reproduce this observation very well. Overall the agreement is good between BEM calculations and measurements, even though the BEM tends to slightly underestimate the insertion loss at low and high frequencies.

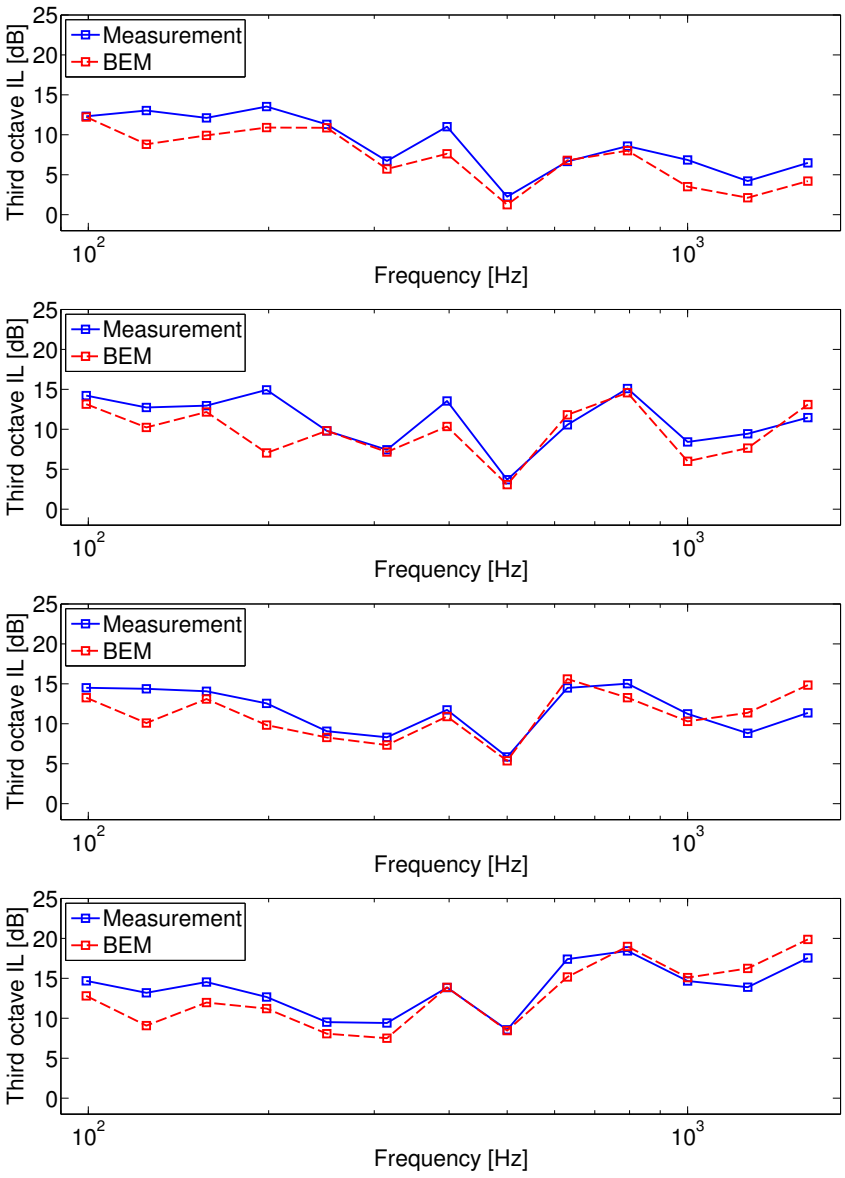

Figure 7.24: Comparison of calculated and measured third-octave insertion losses for the T-shape barrier and the three considered treatments. Continuous line: measurement - dashed line: BEM calculation. From top to bottom: rigid, abs.1, abs.2 and abs.3 configurations (as defined in figure 7.22).

Chapter 8

In situ measurements of a full scale low height barrier prototype

The assessment of a noise barrier performance based on numerical calculations or even scale model measurements is intrinsically biased. This is firstly due to the barrier design itself which in reality will never exactly match what has been assessed numerically, but it is also due to the idealization of the physical and geometrical features of a potential implementation site. For instance, in the scale model measurement set-up as well as numerical calculations, only one source on the ground was considered, whereas the actual noise sources of a tramway are a lot more complex due to their spatial distribution and directivity [26]. Moreover, apart from the fact that the geometrical model of the tram itself is extremely simple, modeling it as a rigid body is an approximation simply from the consideration that there is acoustic transmission inside the tramway.

It is unclear how much those approximations matter for the actual performance of the barrier, especially in the case of low-height noise barriers. It seemed therefore necessary to actually build and set-up a full scale prototype in a real situation in order to assess what actual noise reduction performance can be obtained by such a barrier, and also to evaluate if numerical predictions and scale model measurements yield a reasonable approximation of the in situ performance.

8.1 Preliminary considerations

8.1.1 Choice of the implementation site

The city of Grenoble and its nearby towns have developed in the past few years several tramway lines, and therefore it seemed natural to set up a low-height barrier prototype close to one of them.

Then, the choice of the implementation site for the prototype was based essentially on a background noise consideration. Let us recall that our goal is to evaluate the performance of a low-height barrier in a realistic environment, which we will characterize by an insertion loss, that is a difference of level at a given receiver point with and without the barrier. However, this difference in level will be related to the effect of the barrier only if other surrounding sources

of noise - which would not be attenuated by the barrier, such as cars, birds or pedestrians - do not influence the measured level too much. For this reason the background noise level of the implementation site should be sufficiently smaller than the measured level during the pass-by of a tramway, with and without the barrier. It is equivalent to state that the signal to noise ratio (SNR) should be sufficiently high, the *signal* referring here to the part of a recording due to the pass-by of a tramway, with and without the barrier, and the *noise* referring to the part of a recording due to other surrounding sources in the environment.

A corollary of this consideration is that we should choose a site where the level due to the pass-by of a tramway is as high as possible, since this would enhance the SNR. This in turn means that the speed of the tramway at the site should also be as high as possible, since there is a strong correlation between tramway noise power levels and speed [26], as for most transportation noise sources.

Finally, for practical reasons, assembling and disassembling of the prototype and measurements had to happen within one day only. Since the prototype itself has been built at the CSTB Grenoble site, the implementation site had to be not too far away to shorten transportation time.

Figure 8.1: View of the implementation site, in Saint-Martin-d'Hères (France). The tramway tracks are those of the B line, between the stops Les Taillées - Universités and Grand Sablon. In the background the tracks run over a bridge across the Isère river. The street opposite the bike trail is Antoine Polotti street.

Based on these considerations, we chose to set up the prototype on an asphalt bicycle trail running along the B line of the Grenoble tramway system, between the stops Les Taillées - Universités and Grand Sablon, opposite Antoine Polotti street in the town of Saint-Martin-d'Hères. A view of the site is shown in figure 8.1. The environment is relatively quiet since this site is next to a residential area, with few cars passing on Antoine Polotti street. However tram pass-bys are quite loud, as we will see later. This loudness is due to the fact that trams roll at relativity high speeds in this area, and probably also to the type of track, as it has been shown that this has a major influence on tram noise power levels [26].

One can also notice the presence of a safety fence running along the tracks. This fence is

an advantage for setting up the prototype since it will be easy to secure the installation of the noise barrier onto the fence in order to eliminate any risk of the prototype falling on the tracks. It is also believed that this safety fence has a negligible influence on the sound field.

It also turned out that inhabitants of this area have complained about noise emissions from the trams, and it therefore seems that this site would also be a good choice for installation of a long-term barrier, although this was not a requirement for the purpose of this work, which again is the evaluation of the performance of a low-height barrier prototype in a realistic environment.

8.1.2 Choice of the design

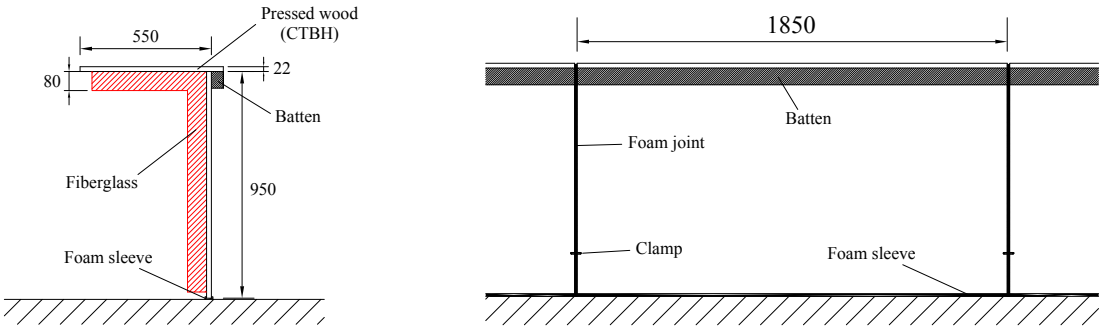

Figure 8.2: Schematic of the low-height barrier prototype. The barrier is made of treated pressed wood and fiberglass. Left: Gamma-shape cross section. Right: back view of one element and joint system between elements (dimensions are given in mm).

Due to time and feasibility constraints, the design of the noise barrier had to be much simpler than the optimized designs found in the previous chapters. Nevertheless, from the results of the previous chapters, it seems essential to cover the face of the barrier directly exposed to the noise sources radiation with absorptive materials in order to attenuate the multiple reflections happening between the tramway body and the barrier.

Based on the T-shape design, a simpler Gamma-shape covered on its interior part by fiberglass is hence proposed (see in figure 8.2). Indeed, preliminary calculations showed that the difference between the two shapes has a limited influence on the acoustic performance, however the Gamma-shape barrier is significantly easier to handle and to transport. Besides, one can point out that if a long-term barrier was set-up, it would be necessary to consider a sustainable absorptive material or to properly package the fiberglass in order to avoid any health hazard related to its presence. However in our case, since the prototype was meant to stay in place for a few hours only, it was found unnecessary to take such precautions.

The length of the barrier also had to be limited namely for ease of transport and installation. The barrier therefore consists of 12 elements, each 1.85 m long, for a total length of a little more than 22 m. Trams running on the B line are Alstom Citadis 402 trams which are 43 m long, and therefore the barrier covers at most half of the tramway length, as shown in figure 8.3.

Each element is made of a simple assembly of two pressed wood boards - one 60 cm wide, the other 95 cm wide - bound together to form a right angle thanks to shelf brackets and a batten. The boards are 22 mm thick, which was chosen to ensure the board to be considered

Figure 8.3: View of the noise barrier prototype with a Alstom Citadis 402 tramway of the Grenoble B line passing-by. The length of the barrier is about 22 m, whereas the tram is about 43 m long.

acoustically rigid. Indeed, the bulk density of the pressed wood is about $\rho = 700\,\mathrm{kg/m^3}$, and based on a simple mass law criterion, the transmission loss across the board at 100 Hz (lowest frequency of interest) is:

$$\mathrm{TL} = 20\,\log\left(\frac{\rho e \omega}{2\rho_0 c_0}\right) = 21\ \mathrm{dB}$$

with $e = 22\,\mathrm{mm}$ is the layer thickness, $\omega = 2\pi f$ the angular frequency, $\rho_0 = 1.21\,\mathrm{kg/m^3}$ is the density of air and $c_0 = 343\,\mathrm{m/s}$ is the speed of sound. This loss is sufficiently large to neglect any transmission through the board in the frequency range of interest.

Each element is bound to the next via a simple joint system: a rectangular piece of dense foam is glued on the side of the pressed wood boards, and several tied plastic clamps ensure compression of the joint, thus preventing strong acoustic leaks. Similarly, an insulating foam sleeve is put at the bottom of the structure to prevent leaks at the ground level. The compression in this case naturally happens thanks to the weight of the structure. Pictures of the barrier cross section and joint system are shown in figure 8.4.

Figure 8.4: Views of the low-height barrier prototype. Left: cross section. Right: joint system between elements.

8.2 Performed measurements

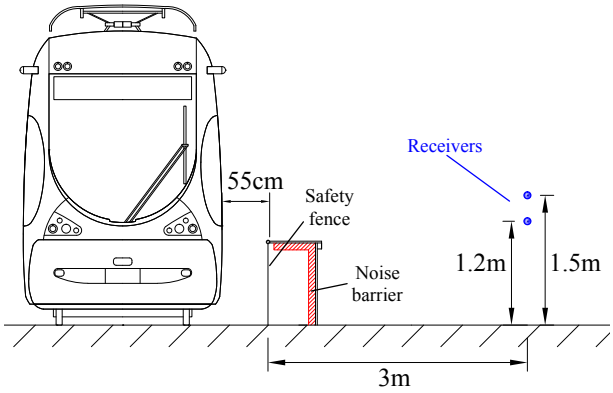

Figure 8.5: Cross sectional schematic showing relative positions of the tram, low-height noise barrier prototype and receivers.

In this work, we are interested in assessing the benefit of the presence of a low-height barrier for a close receiver, typically a pedestrian or a cyclist, while a tramway is passing by. We therefore mostly need to measure the level at a receiver point typically corresponding to the ears position of a passer-by. Two heights have been considered: 1.5 m, corresponding to an average ears position for a person standing, and 1.2 m, corresponding to the ear position of a person sitting on a bench for instance. The horizontal distance from the safety barrier is 3 m, which corresponds to a distance of about 3.5 m to the tramway side (see in figure 8.5). Finally the receivers are located in the vertical plane cutting the barrier in the middle of its length, which is where the noise barrier has the most important effect.

Pressure signals and levels were recorded by a B&K model 2250 sound level meter (SLM) at the receiver locations. The SLM was set up to record the pressure signal in a WAV file (sampled at 48 kHz) and the equivalent A-weighted levels $L_{\mathrm{Aeq,T}}$ over successive time periods of duration $T = 100$ ms, which have been defined in section 1.2.3. Binaural measurements were also made, although this type of measurement was not exploited in this work. Besides, we used an auxiliary microphone (embedded in a cellphone) which was placed very close to the tracks, away from the shadow zone of the barrier, and meant to record the pass-by of the train without any influence of the barrier, which would allow us to determine the speed of the tram during the pass-by (more details will be given in section 8.2.1). The different devices are shown in figure 8.6.

Figure 8.6: Devices used in the measurements. Left: B&K type 2250 sound level meter and binaural head. Right - cellphone LG P970 used as an auxiliary microphone for speed measurement.

Finally, SLM measurements are performed over a constant time interval of 15 s, each measurement being started manually by an operator whenever a tram is approaching. Besides, measurements are done for *close* trams - running the closest to the barrier, going from Grand Sablon to Les Taillées - and *far* trams - running the opposite way farthest from the barrier, towards the bridge over the Isère river (see in figure 8.7).

We therefore have 8 different configurations of measurements for which the analysis will be performed, depending on:

- Receiver height: 1.5 m or 1.2 m.
- Presence of the noise barrier (we will refer to each case as *with* or *without* barrier).
- Proximity of the tram: close or far.

Figure 8.7: Views of two tram pass-bys. Left: close tram, rolling towards the foreground of the picture. Right: far tram, rolling towards the background of the picture (towards the bridge over the Isère river).

8.2.1 Speed measurement from auxiliary microphone signal

Speed is an important parameter in pass-by levels measurements since it is highly correlated with the noise sources' power levels, as already pointed out. To avoid any bias in the evaluation of the noise reduction due to the barrier, as well as to study this correlation, it therefore seemed necessary to evaluate the speed of the tram during each measured pass-by. One approach is to determine the pass-by duration and to use the known length of the tram to calculate the speed. Durations can be measured with infrared cells, as done in [26], but one can also use the time history of the pass-by given by the $L_{\mathrm{Aeq,T}}$. Indeed, the passage of a bogie close to the microphone generates a bump in level which can be detected. From the knowledge of the corresponding instants, one can measure time intervals between the passage of the different bogies, and finally the speed assuming the distances between the bogies are known. However when the barrier is present, this bump is strongly attenuated, and therefore the measurement of the speed is more difficult. This is why we needed an extra microphone, located close to the tracks and away from the shadow zone of the barrier. Besides, the quality of the recording is

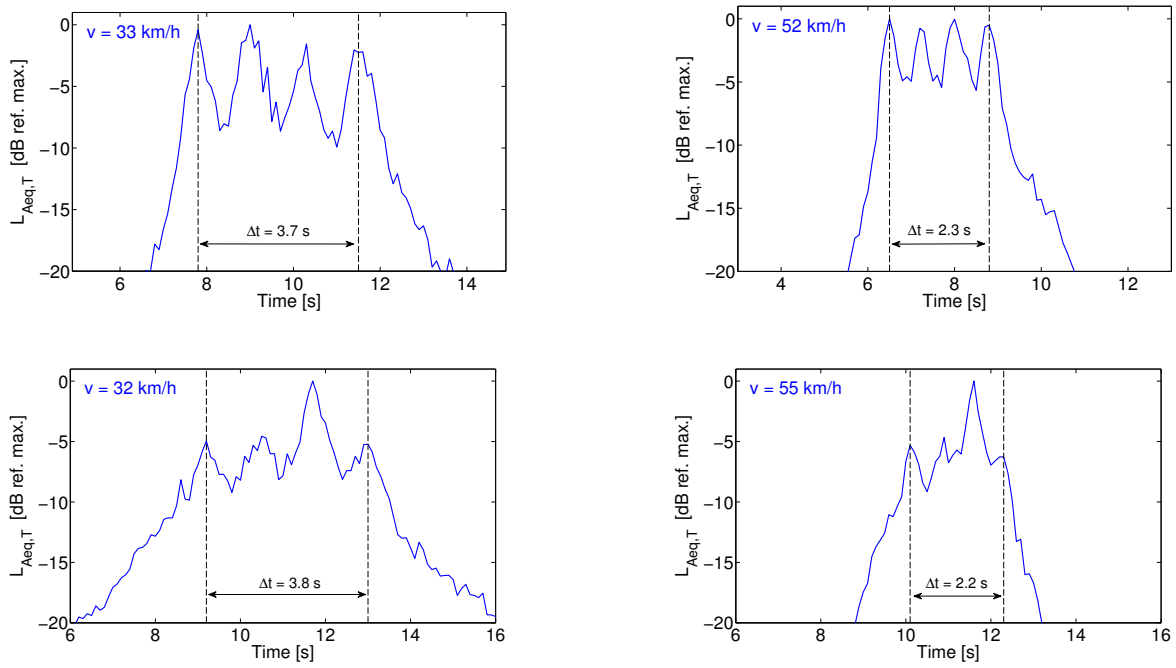

Figure 8.8: Examples of A-weighted levels $L_{\mathrm{Aeq,T}}$ time histories in dB(A) (referenced to the maximum value) during tram pass-bys, with $T = 100\,\mathrm{ms}$, recorded with the auxiliary microphone. For each signal, the passage of the four bogies in front of the microphone is identified, which yields a time interval Δt corresponding to the passage of the first and last bogie. From the known distance between the two extreme bogies ($d_1 = 33.5\,\mathrm{m}$ for Citadis 402 trams, see in figure 8.9), one can estimate the speed as $v = d_1/\Delta t$, indicated in blue on each plot. Top: close trams. Bottom: far trams.

not extremely important for this application, which is why using a simple cellphone microphone was sufficient.

A few examples of this process are shown in figure 8.8. From the recorded WAV file, the signal is extracted and the $L_{\mathrm{Aeq,T}}$ calculated by applying the A filter and averaging over intervals of 100 ms. All time histories present several bumps, corresponding to the pass-by of the bogie areas, since these sources emit more noise than the rail itself. This allows one to identify the instant at which each bogie passed in front of the microphone, which yielded the time interval Δt between the pass-by of the first and last bogie. For the Citadis 402 tram, the bogies are separated by a distance of 11.15 m, and therefore the distance between the first and last is $d_1 = 33.45\,\mathrm{m}$ (see in figure 8.9). Assuming the speed is constant during this interval, it can be calculated simply by $v = d_1/\Delta t$.

There is of course uncertainty in this measurement since the bumps might not be easily identifiable (see for instance in the figure 8.8 bottom plots) and since the time interval Δt is known with a precision of 0.1 s only. Measured time intervals typically vary between 2.0 and 4.0 s, hence the error varies between 2.5 and 5%. This yields a precision of 1 to 3 km/h in the speed, which for the purpose of this work is sufficient. Besides, it was found that taking a shorter averaging period made in general the identification of the bogie pass-bys more difficult.

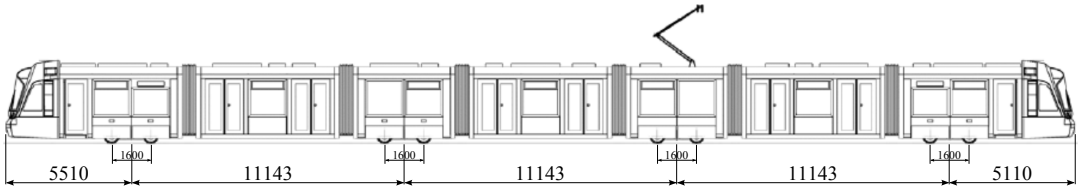

Figure 8.9: Longitudinal schematic of the Alstom Citadis 402 tram. Dimensions are given in mm. The distance between the first and last bogie centers is about $3 \times 11.15 = 33.45\,\text{m}$, and the total length of the tram is about 43.65 m.

8.3 Measurement analysis and barrier effect

In this section different analyses of the measured data are proposed in order to evaluate the effect of the low-height noise barrier prototype in terms of noise reduction: first based on the equivalent pass-by level, then on the time histories of the $L_{\text{Aeq,T}}$ during the pass-bys, and finally on the spectrum of the recorded signals.

8.3.1 Pass-by equivalent level and speed dependence

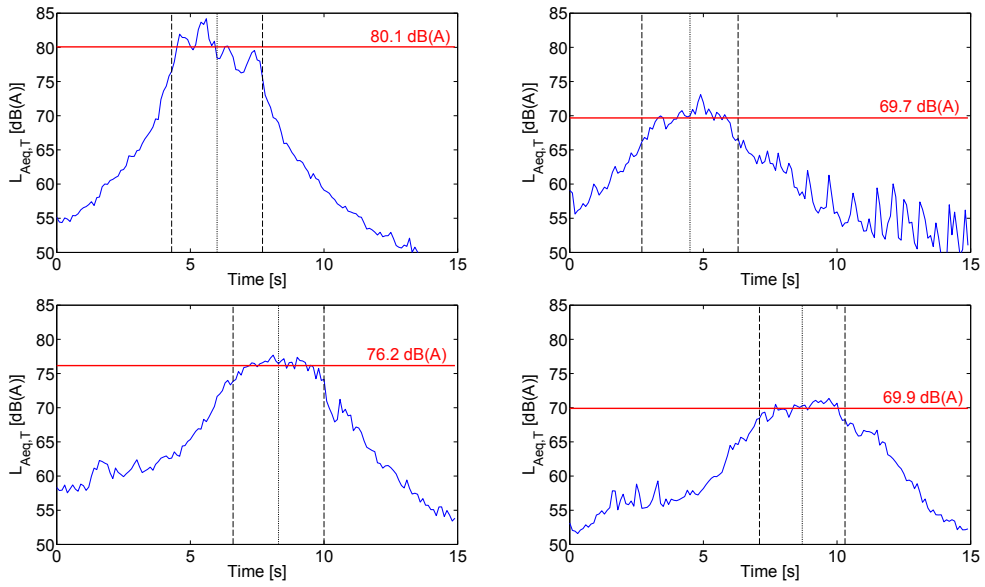

Figure 8.10: Examples of time histories of $L_{\text{Aeq,T}}$ in dB(A) during tram pass-bys, with $T = 100\,\text{ms}$, recorded with the SLM. The dotted line corresponds to the center time, and the two dashed lines correspond to the initial and final instants of the tram pass-by. The pass-by level $L_{\text{Aeq,pass}}$ is the mean level during the pass-by period and is indicated in red. Top left: close tram, without barrier. Top right: close tram, with barrier. Bottom left: far tram, without barrier. Bottom right: far tram, with barrier.

First the correlation between noise level and speed is studied, in each measurement configuration. The equivalent A-weighted sound pressure level is chosen to quantify the level during the pass-by, but one has to determine the time period of integration. Since the speed v of the tram is known for each pass-by, we set the period over which the equivalent level is calculated as the duration of the whole tram pass-by in front of the SLM, given by $\tau = d_2/v$ and $d_2 = 43\,\text{m}$ is approximately the total length of the tram (see in figure 8.9). The result is referred to as the

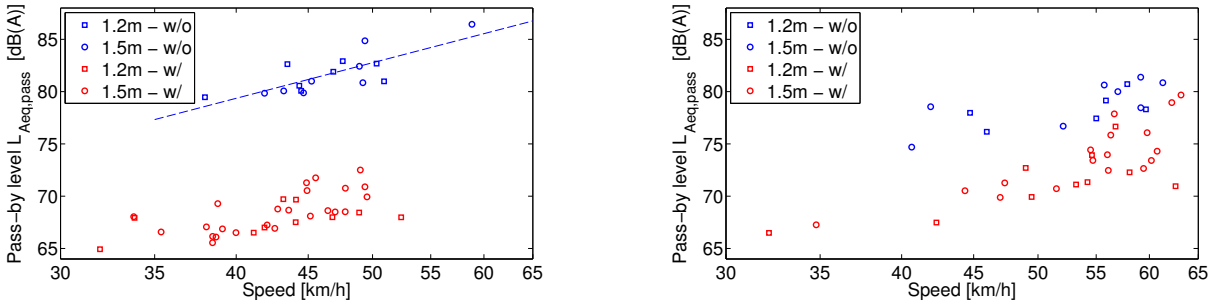

Figure 8.11: Tram pass-by A-weighted equivalent levels as a function of speed for all measurement configurations. The dotted line corresponds to the function $L_{\mathrm{Aeq,pass,ref}} + \alpha \log(v/v_{\mathrm{ref}})$ with $L_{\mathrm{Aeq,pass,ref}} = 79.3\,\mathrm{dB(A)}$, $\alpha = 35$ and $v_{\mathrm{ref}} = 40\,\mathrm{km/h}$, which is a regression on the levels for close trams without the barrier. Left - close trams; right - far trams. Color coding: blue - without noise barrier; red - with noise barrier. Symbols: squares - SLM height of 1.2 m; circles - SLM height of 1.5 m.

Table 8.1: Coefficients $L_{\mathrm{Aeq,pass,ref}}$ and α and their uncertainty based on the regression of A-weighted pass-by levels with speed, assuming a dependence of the form $L_{\mathrm{Aeq,pass}} = L_{\mathrm{Aeq,pass,ref}} + \alpha \log(v/v_{\mathrm{ref}})$ with $v_{\mathrm{ref}} = 40\,\mathrm{km/h}$, in all configurations. Broadband insertion losses in dB(A) (differences of reference pass-by levels at v_{ref}) are also shown.

Configuration		$L_{\mathrm{Aeq,pass,ref}}$ [dB(A)]	Speed-dependence coefficient α	Barrier insertion loss estimate at 40 km/h [dB(A)]
Close - 1.2 m	without barrier	80.3 ± 0.6	19 ± 10	12.8 ± 1
	with barrier	67.5 ± 0.4	12 ± 6	
Close - 1.5 m	without barrier	78.4 ± 0.7	48 ± 10	10.6 ± 0.8
	with barrier	67.7 ± 0.3	29 ± 6	
Far - 1.2 m	without barrier	76.1 ± 1.2	18 ± 11	7.5 ± 1.5
	with barrier	68.7 ± 1.0	26 ± 9	
Far - 1.5 m	without barrier	75.9 ± 1.1	25 ± 9	7.5 ± 1.5
	with barrier	68.4 ± 1.0	40 ± 7	

pass-by A-weighted equivalent level, written as $L_{\mathrm{Aeq,pass}}$, and calculated by logarithmic summation of the $L_{\mathrm{Aeq,T}}$ in the corresponding time interval (see examples of this calculation in figure 8.10).

The pass-by levels can then be plotted as a function of speed, for all configurations (see in figure 8.11). The range of tram speeds does vary depending on the configuration, with far trams typically rolling faster (from 40 to 65 km/h) than close trams (from 35 to 55 km/h). There also seems to be a little bias when the barrier was set up, since close trams rolled on average at 46.7 km/h without the noise barrier, but at 42.9 km/h with the barrier. Proper evaluation of the barrier performance therefore requires a correction of this effect.

Although there seems to be significant variability between the trams pass-bys, there is a positive correlation between levels and speeds in all cases. One can for instance assume a simple power-law dependence of the received power on speed, which in terms of the pass-by level in dB can be written as:

$$L_{\mathrm{Aeq,pass}} = L_{\mathrm{Aeq,pass,ref}} + \alpha \log(v/v_{\mathrm{ref}})$$

with $v_{\mathrm{ref}} = 40\,\mathrm{km/h}$ is the reference speed and $L_{\mathrm{Aeq,pass,ref}}$ the reference level. The regression coefficients $L_{\mathrm{Aeq,pass,ref}}$ and α and their uncertainties have been calculated as explained in appendix H and are tabulated in table 8.1 for all configurations. One can notice the coefficients α vary a lot and have a large uncertainty, which suggests pass-by levels do not depend only on

speed. Indeed defects in the tram can cause a great variability in levels between the different bogies, as seen for instance in the figure 8.8 bottom plots. In addition, propagation effects (due to the ground and the barrier) may affect the coefficients as well.

However, we will assume that tramway noise source power levels depend only on speed, as done in [26]. However, in order to evaluate the dependence of the power levels, one needs to avoid as much of the influence of the propagation effects as possible. Specifically, the configuration in which propagation will have the smallest effect is for the close tram without the noise barrier. We will therefore assume that the dependence of the source power levels can be approximated by the dependence of the pass-by levels for close trams (for both receiver positions). This yields a coefficient of $\alpha = 35 \pm 8$, which is in good agreement with the value of 32.7 measured by Pallas et al. for a modern tram in the case of soft pads and pavings [26], although the uncertainty is still important in our case. From now on, we will define the speed-corrected value of any A-weighted level L_A at $v_{\text{ref}} = 40\,\text{km/h}$ as:

$$L'_A = L_A - 35 \log \frac{v}{v_{\text{ref}}}$$

Finally, one can evaluate the speed-independent effect of the barrier in each configuration by comparing the $L_{\text{Aeq,pass,ref}}$ with and without the barrier (see the last column of table 8.1), which is a reduction on average of more than 10 dB(A) for close trams, and 7.5 dB(A) for far trams. One can already state that the effect of the barrier prototype, although its length is only half of that of the tram, is significant.

8.3.2 Analysis of the $L_{\text{Aeq,T}}$ time histories

Another way of measuring the effect of the barrier is to analyze the measured $L_{\text{Aeq,T}}$ time histories (again here $T = 100\,\text{ms}$). This will allow one to have a closer look at the noise reduction effect considering a time dependence. However, since the measurements were not synchronized, one first has to process the histories in order for them to have a similar center time (instant at which the center of the tram is the closest to the SLM). Besides, one needs to correct for the effect of speed, both on time and level. This will then allow one to make an elementary statistical analysis of the time histories, by considering the mean and the dispersion of the levels as a function of time.

The center time t_c of each time history is evaluated as the center time of the tram pass-by as defined in section 8.3.1. The *centered* time τ is then defined for each pass-by as $\tau = t - t_c$. The $L_{\text{Aeq,T}}$ levels and centered time τ are then corrected due to the speed dependence as:

$$L'_{\text{Aeq,T}} = L_{\text{Aeq,T}} - 35 \log\Big(\frac{v}{v_{\text{ref}}}\Big) \qquad \tau' = \frac{v}{v_{\text{ref}}}\,\tau$$

Since the corrected histories are no longer defined on the same instants, a linear interpolation in time is made. An example of this process is shown in figure 8.12.

Mean and dispersion calculations are then made at each instant on the corrected history, based on the different pass-bys for all measurement configurations. Results are shown in figure 8.13. One can also notice that there is a strong variability of the levels, even after the speed

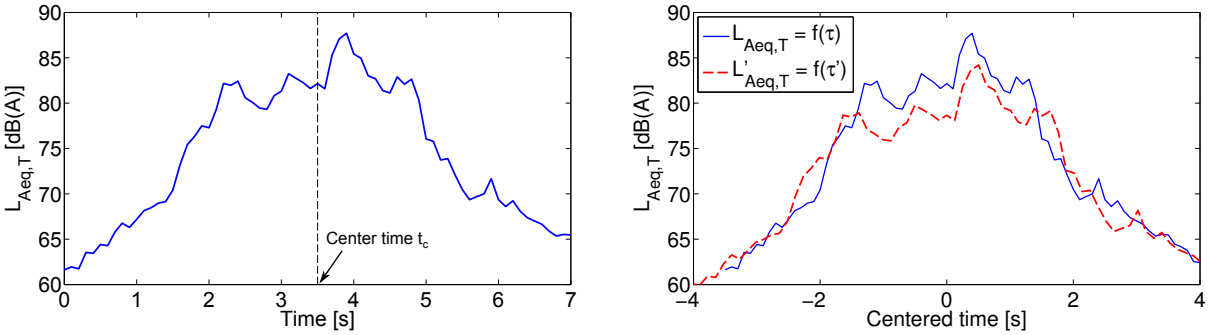

Figure 8.12: Example of a $L_{\mathrm{Aeq,T}}$ time history (close tram - 1.20 m - without barrier) and application of the speed correction on time and level. Left: measured time history and center time t_c. Right: measured time history of the $L_{\mathrm{Aeq,T}}$ as a function of centered time $\tau = t - t_c$ (solid line) and corrected time history of the $L'_{\mathrm{Aeq,T}}$ as a function of corrected centered time τ' (dashed line).

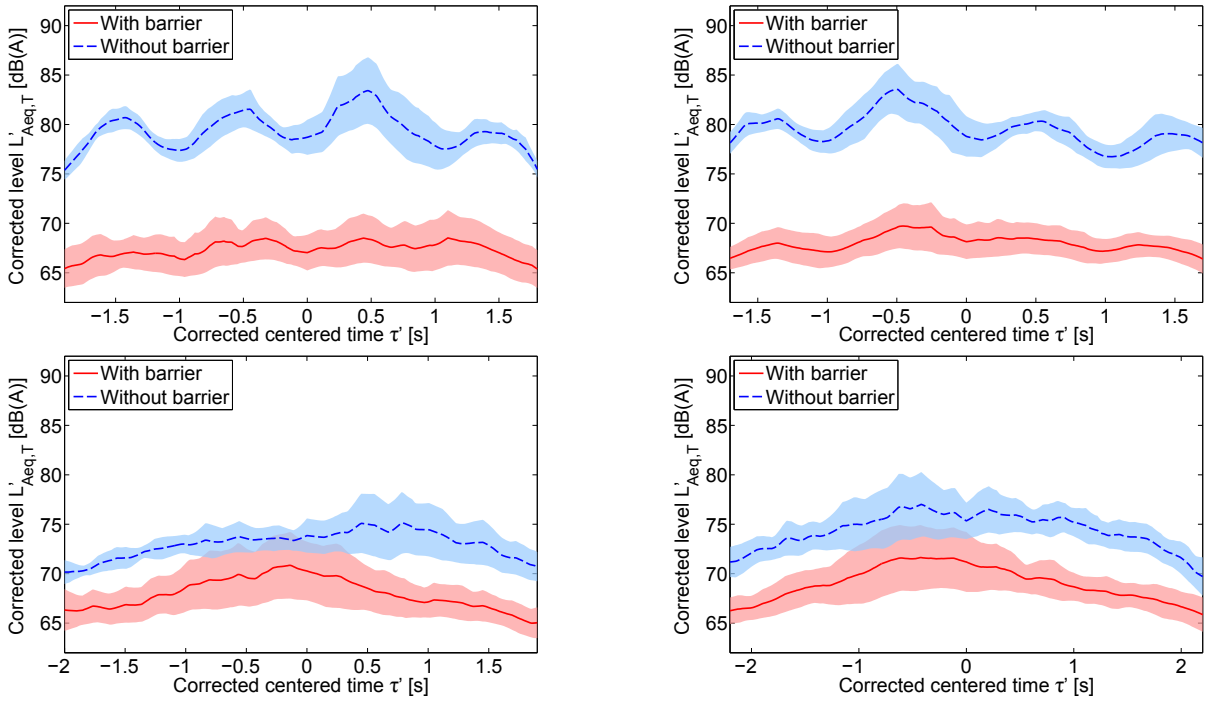

Figure 8.13: Mean and dispersion interval (plus and minus one standard deviation from the mean) of corrected levels $L'_{\mathrm{Aeq,T}}$ time histories in dB(A) during tram pass-bys as a function of corrected centered time τ', with (solid line) and without (dashed line) the noise barrier. Top left: close tram, height of 1.20 m. Top right: close tram, height of 1.50 m. Bottom left: far tram, height of 1.20 m. Bottom right: far tram, height of 1.50 m.

correction is applied, which is certainly related to the different trams having different defects as pointed out earlier. Nevertheless, the main result from this approach is that, at the considered receiver locations, the noise reduction effect of the barrier is effective during the whole pass-by (attenuation of 4-7 dB(A) for far trams, and of 9-15 dB(A) for close trams), despite the small length of the barrier compared to that of the tram. Indeed, when τ is large in absolute value, a smaller portion of the tram - which as a first approximation can be approximated as the region where most of the noise is generated - is "hidden" by the noise barrier (see in figure 8.14), and therefore one might have observed a negligible noise reduction effect. This aspect also strongly depends on the directivity of the sources in the horizontal plane, which is difficult to evaluate

directly with simple SLM measurements. However, based on the fact that the barrier does have an effect even at large values of τ, it seems like the main noise sources of this type of tram - namely wheel radiation and rolling noise - do present a significant horizontal directivity. One can also point out that the issue of noise reduction limitation due to the finite size of a noise barrier will be more important if the receiver was further away from the track, but in this case even without any noise barrier the received level would be smaller and therefore the pass-by of a tram might not cause as much of a nuisance.

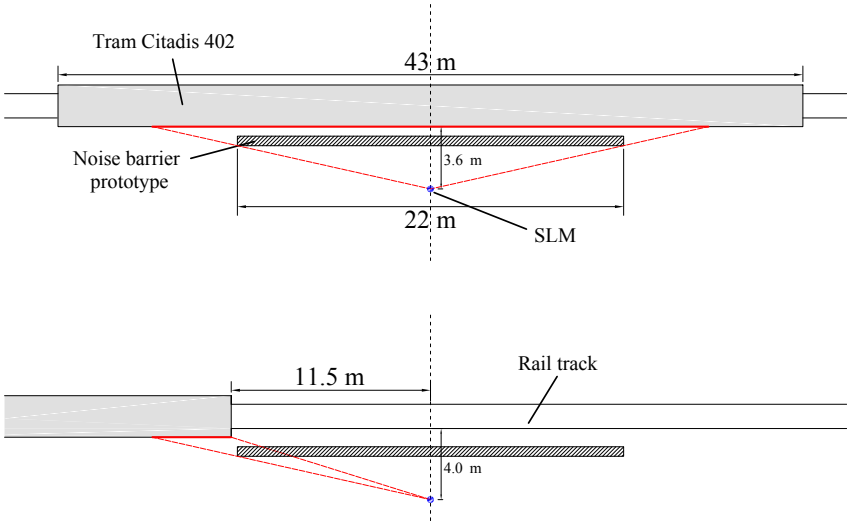

Figure 8.14: Schematic top view of the noise barrier prototype in case of the pass-by of a close tram. The thick red lines delimit the approximate part of the noise source region which the barrier can attenuate, based on purely geometrical considerations. The top plot corresponds to a value of $\tau = 0\,\mathrm{s}$, for which most of the source region is geometrically hidden by the barrier. The bottom plot corresponds to value of $\tau = -2\,\mathrm{s}$ (the tram is assumed to roll at 40 km/h), in which only a small portion of the region is geometrically hidden.

8.3.3 Spectral analysis and third-octave insertion losses

The attenuation provided by the low-height noise barrier is of course strongly dependent on frequency, as it has been shown in previous chapters. One therefore needs to evaluate the insertion loss of the noise barrier as a function of frequency, which would also allow us to compare the measurement with BEM calculations.

However, as stated above, the presence of background noise in the surrounding environment can bias the evaluation of the low-height barrier insertion loss, typically averaged on different third-octave bands. Although the site was relatively quiet, which means that broadband levels such as the $L_{\mathrm{Aeq,T}}$ were sufficiently above the background levels, this might not be true any more depending on which third-octave band is considered. We will therefore first analyze the data to find the frequency range in which the SNR was sufficiently good to evaluate the insertion loss accurately.

8.3.3.1 Effect of noise on insertion loss evaluation and considered frequency range

First of all, one can theoretically evaluate what is the influence of background noise on the evaluation of the insertion loss. Let P_{w} and P_{wo} be typical pressure spectrum values at a given

receiver location and in a given frequency band - they can be for instance the square root of the integrated value of the power spectral density (PSD) over a third-octave band -, with and without the noise barrier, in an ideal environment without any background noise. The ideal attenuation provided by the barrier is then $A = P_{\mathrm{w}}^2/P_{\mathrm{wo}}^2$ and the insertion loss $\mathrm{IL} = -10\log A$. However, in reality, what is measured is an approximate attenuation given by:

$$\tilde{A} = \frac{P_{\mathrm{w}}^2 + N_{\mathrm{w}}^2}{P_{\mathrm{wo}}^2 + N_{\mathrm{wo}}^2}$$

with N_{w} and N_{wo} typical spectra of uncorrelated background noises, which may be different between the measurement made with the barrier compared to that made without. Now define the dimensionless numbers $s_{\mathrm{w}} = P_{\mathrm{w}}^2/N_{\mathrm{w}}^2$ and $s_{\mathrm{wo}} = P_{\mathrm{wo}}^2/N_{\mathrm{wo}}^2$. These quantities are related to the signal-to-noise ratios $\mathrm{SNR_w}$ and $\mathrm{SNR_{wo}}$ by $\mathrm{SNR_w} = 10\log s_{\mathrm{w}}$ and $\mathrm{SNR_{wo}} = 10\log s_{\mathrm{wo}}$. Then the ratio of the measured attenuation to the ideal attenuation is:

$$\frac{\tilde{A}}{A} = \frac{1 + 1/s_{\mathrm{w}}}{1 + 1/s_{\mathrm{wo}}} \tag{8.1}$$

Due to the sound attenuation provided by the noise barrier, one typically has $P_{\mathrm{w}} < P_{\mathrm{wo}}$. Besides if one assumes the background noise levels to be similar, that is $N_{\mathrm{w}} \approx N_{\mathrm{wo}}$, one has $s_{\mathrm{w}} < s_{\mathrm{wo}}$ (which also means $\mathrm{SNR_w} < \mathrm{SNR_{wo}}$) and therefore from equation (8.1):

$$\frac{\tilde{A}}{A} > 1 \quad \Leftrightarrow \quad \widetilde{\mathrm{IL}} < \mathrm{IL}$$

where $\widetilde{\mathrm{IL}}$ is the estimated insertion loss in the presence of noise. This means that in most situations, the insertion loss measured in the presence of the noise will be under-evaluated.

Now, suppose that we can ensure the two SNRs are above a certain value $\mathrm{SNR_{min}}$. It is equivalent to state that $s_{\mathrm{w,wo}} > s_{\mathrm{min}}$ with $s_{\mathrm{min}} = 10^{(\mathrm{SNR_{min}}/10)}$. Using this relationship on equation (8.1), we have:

$$\frac{\tilde{A}}{A} < 1 + \frac{1}{s_{\mathrm{smin}}}$$

Defining the error on the measured insertion loss as $\Delta\mathrm{IL} = \mathrm{IL} - \widetilde{\mathrm{IL}} > 0$, this last equation can be rewritten as:

$$\Delta\mathrm{IL} < \Delta\mathrm{IL_{max}} \qquad \text{with} \quad \Delta\mathrm{IL_{max}} = 10\log\Big(1 + \frac{1}{s_{\mathrm{min}}}\Big) = 10\log\Big(1 + \frac{1}{10^{(\mathrm{SNR_{min}}/10)}}\Big)$$

$\Delta\mathrm{IL_{max}}$ is an indicator of the error on the insertion loss measured value, which is related to the minimum SNR. This relationship can therefore be used to find an appropriate value of $\mathrm{SNR_{min}}$ in order to have a limited error on the insertion loss. Suppose we would like the error on the insertion loss to be less than $\Delta\mathrm{IL_{max}} = 0.5\,\mathrm{dB}$, then the corresponding minimum SNR will be:

$$\mathrm{SNR_{min}} = -10\log\Big(10^{(\Delta\mathrm{IL_{max}}/10)} - 1\Big) = 9\,\mathrm{dB}$$

We can therefore use this criterion to select the frequency bands in which the barrier insertion

loss will be evaluated correctly (within 0.5 dB), without too much influence of the background noise. We evaluated the SNR over each third-octave by considering the *signal* portion of each recording as the tram pass-by (as defined in section 8.3.1) and the *noise* portion as the initial or last two seconds of the recording (depending on the pass-by center time). The third-octave levels of the signal are calculated by integration of the PSD of the signal portion over the corresponding band. Similar calculations are performed to evaluate the third-octave levels of the background noise. An example is shown in figure 8.15. Applying this process for all the recordings, it has been found that for 90% of them the SNR was above 9 dB in the frequency range [200 Hz - 2500 Hz], which will be the range of study in the rest of this section. Indeed, it has been noticed that tramway noise emissions at low frequencies are usually comparable to typical background noise. Besides, at higher frequencies, the measurement is limited by birds singing, which mostly contribute to the background noise at 3 and 4 kHz.

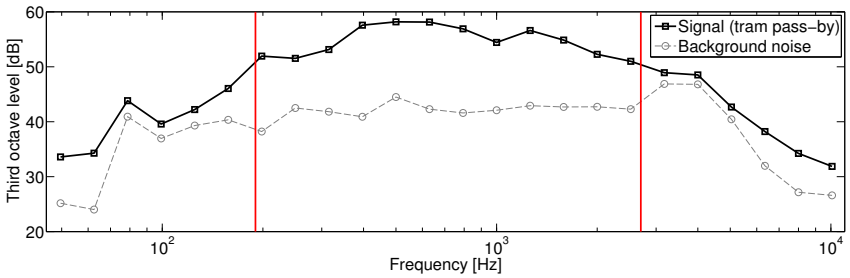

Figure 8.15: Examples of signal and background noise third-octave levels in dB ref. 20 μPa (far tram - SLM height of 1.20 m - with barrier). The red lines delimit the frequency range in which the SNR is sufficiently high (above 9 dB). The bump in the background noise spectrum at 3 and 4 kHz corresponds to birds singing. Thick solid line: signal - dashed thin line: background noise.

8.3.3.2 Measured third-octave insertion losses

Now that the trusted frequency band has been determined, one can calculate for a given configuration the insertion loss of the low-height barrier from the third octave levels without the barrier, averaged over all measurements, minus the averaged third octave levels with the barrier. Apart from the uncertainty due to the background noise, there is some variability in this evaluation which can be quantified by classical uncertainty calculations. Results are presented in figure 8.16. First of all, it is clear that the low-height barrier provides attenuation over the whole considered frequency range, both for close and far trams, although the attenuation is a lot higher for close trams. One can also notice that at the receiver height of 1.20 m, the performance of the noise barrier for far trams is increased at high frequencies compared to that measured at 1.50 m. This is correlated to the fact that at a height of 1.50 m, for far trams, the receiver is barely in the geometrical shadow zone of the barrier, whereas at 1.20 m the receiver is deeper in the shadow zone (see in figure 8.17). This difference between the two receiver heights is however smaller for close trams, since both receivers are well into the shadow zone in this case.

One can then consider a broadband insertion loss in dB(A) in the considered frequency range. Levels are first converted to dB(A) by applying the A-weighting correction to the third octave

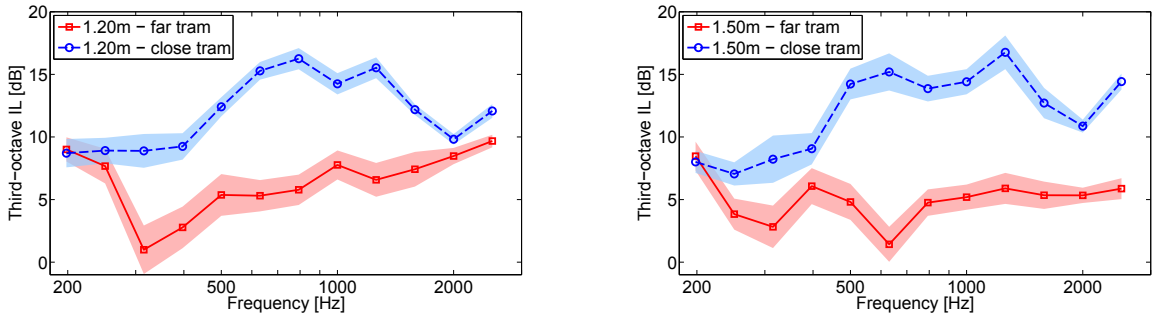

Figure 8.16: Mean values and uncertainty interval of measured third-octave insertion losses in dB in the different configurations in the frequency range 200-2500 Hz. Left: SLM height of 1.20 m - right: SLM height of 1.50 m. Solid line: far tram - dashed line: close tram.

Table 8.2: Mean value and uncertainty of broadband insertion losses in the 200-2500 Hz range based on A-weighted third-octave levels with and without the barrier, for all configurations.

Configuration	Broadband IL [dB(A)] (200-2500 Hz range)
Close tram - 1.2 m	13.3 ± 0.6
Close tram - 1.5 m	13.8 ± 1.2
Far tram - 1.2 m	5.5 ± 1.2
Far tram - 1.5 m	4.3 ± 1.1
Average (all config.)	8.6 ± 0.8

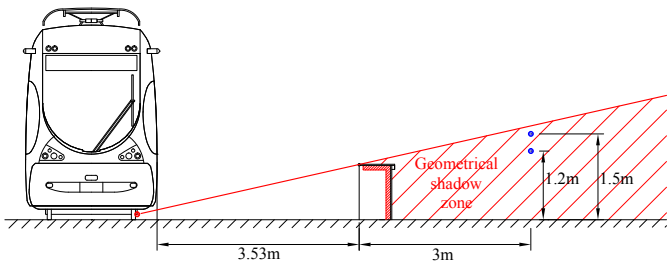

Figure 8.17: Schematic representing the geometrical shadow zone provided by the barrier for far trams. At a height of 1.20 m, the receiver is significantly deeper in the shadow zone than at a height of 1.50 m, which in turns increases the insertion loss mostly at high frequencies.

levels. The broadband insertion loss is then evaluated as:

$$\mathrm{IL} = 10\,\log\Big(\sum_j 10^{(L^{\mathrm{wo}}_{A,j}/10)}\Big) - 10\,\log\Big(\sum_j 10^{(L^{\mathrm{w}}_{A,j}/10)}\Big)$$

in which $L^{\mathrm{wo}}_{A,j}$ (resp. $L^{\mathrm{w}}_{A,j}$) are the A-weighted third-octave levels in the band of index j without the barrier (resp. with the barrier). The corresponding uncertainties are evaluated as well. Results for each configuration and on average for all configurations are shown in table 8.2. As already mentioned, the difference between the two receiver heights is significant for far trams, but not for close trams. It is however surprising that, in the close tram case, the mean insertion loss is smaller at 1.2 m than at 1.5 m. Let us recall that there is significant uncertainty in the evaluation of the measured broadband performance and therefore these results should be considered accordingly.

Notice that these results are a little different than the first estimate of the broadband insertion loss shown in section 8.3.1, which might be due to the fact that no speed correction was applied

on the third-octave levels, and also since the evaluation based directly on the measured pass-by levels was evaluated over a larger frequency band, but was also more subject to error due to the background noise implicitly present in the levels estimation. The choice not to apply a speed correction on the third-octave levels was based on the fact that such a correction should be dependent on the considered third-octave band (as done by Pallas et al. [26]), but in our case it has been found that the uncertainty on the regression coefficients was very high for most frequency bands, and therefore the coefficients not meaningful.

8.4 Comparison with BEM calculations

The third-octave insertion losses calculated in the previous section can now be compared to BEM calculations. It is expected that the results of the BEM predictions will be different from the measurements since the situation modeled in the simulations is a lot simpler than the real environment: infinitely extended geometry, omnidirectional coherent line source, position of the sources, approximate geometry, approximate acoustic properties of the surrounding surfaces (ground, tram and low-height barrier). It seems however interesting to estimate this difference.

Due to the lack of more accurate data, the ground, the tram and the pressed wood boards in which the barrier is made will be assumed perfectly rigid. The fiberglass is assumed to be a fibrous layer of admittance modeled by a Delany and Bazley layer of flow resistivity $\sigma = 30\,\text{kPa.s/m}^2$. Two sources located at each rail are considered, and their contributions are summed incoherently. Two receivers located at heights of 1.20 m and 1.50 m are considered, similarly to what has been done in the measurements. The geometries used in the simulations are presented in figure 8.18. The spectral content of the sources is not important to estimate the third-octave insertion losses, but will be added when evaluating the broadband insertion loss. Calculations are performed once again with the software MICADO, presented in chapter 2.

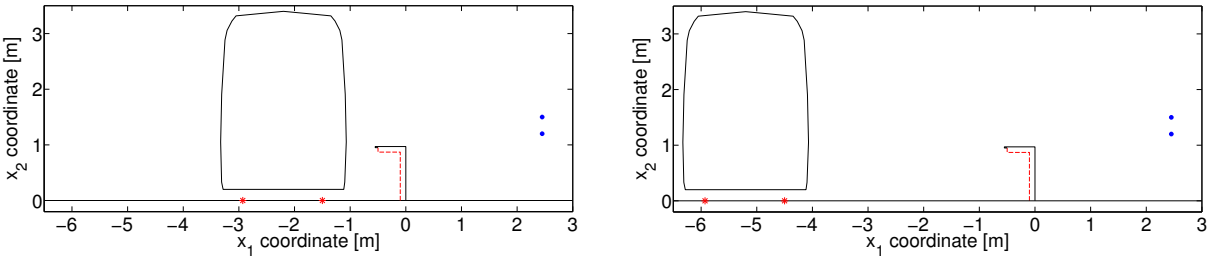

Figure 8.18: Considered geometries for 2D BEM calculations. The geometry is assumed infinitely extended in the direction orthogonal to the vertical plane. The blue dots are the receiver locations, and the red stars are the sources. Boundary color coding: black line - rigid; dashed red line - fibrous layer (Delany and Bazley model with parameters $\sigma = 30\,\text{kPa.s/m}^2$ and $d = 8\,\text{cm}$). Left: close tram; right: far tram.

Comparisons between the BEM and measured third octave insertion losses are presented in figure 8.19. Although significant differences exist, one can notice the general trends are relatively well-represented in the BEM calculation. Nevertheless, in the close tram case, the performance is largely overestimated at low and high frequencies. There is also a uniform overestimation of the BEM in the far tram case, which may be due to a ground effect happening in reality which is not taken into account in the calculation (since the ground has not been characterized

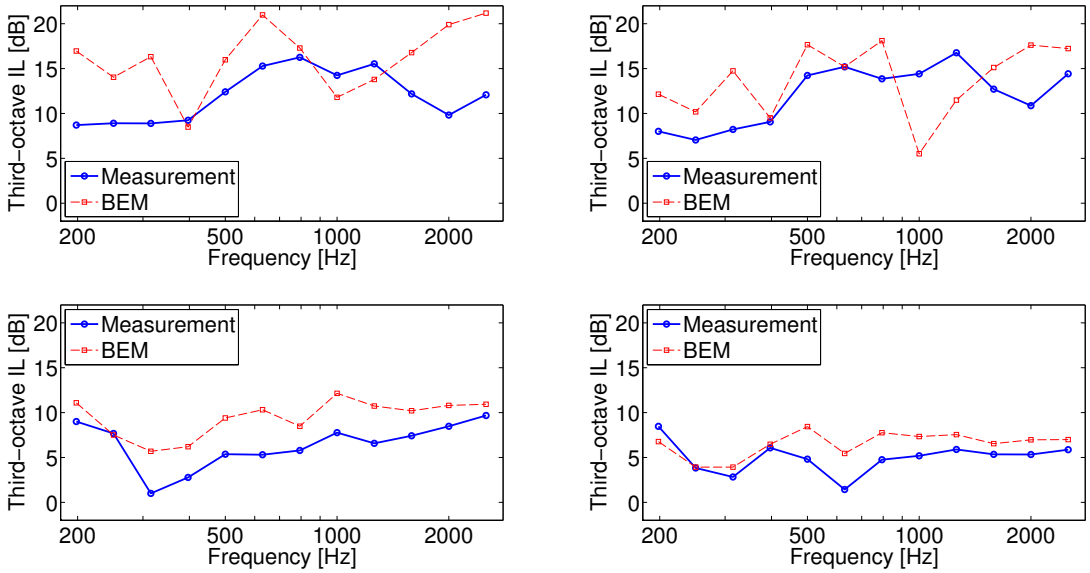

Figure 8.19: Comparison of mean measured values and BEM calculated values of third octave insertion losses. BEM calculations are done using the geometry given in figure 8.18. Thick solid line: measurement; thin dashed line: BEM calculation. Top left: close tram - SLM at 1.2 m; top right: close tram - SLM at 1.5 m; bottom left: far tram - SLM at 1.2 m; bottom right: far tram - SLM at 1.5 m.

Table 8.3: Measured and calculated broadband insertion losses in the 200-2500 Hz range, for all configurations. The calculation is done using equation (8.2).

Configuration	$IL_{200\text{-}2500}$ [dB(A)]	
	Measurement	BEM calculation
Close tram - 1.2 m	13.6	14.8
Close tram - 1.5 m	13.7	11.3
Far tram - 1.2 m	6.1	9.7
Far tram - 1.5 m	4.5	6.8

properly on site), or to the finite extent of the barrier. Besides, some peaks and dips in the insertion loss curve, probably related to interference effects, are typically more marked in the BEM calculation compared to reality, which is probably related to the simple modeling of the noise sources (coherent line source).

Furthermore, one can evaluate a broadband insertion based on the BEM predicted insertion losses, using a measured spectrum. Let $L_{A,j}^{\text{in}}$ be the mean A-weighted levels measured without the barrier for a given configuration, taken as an estimate of the power spectrum of the source. One can then evaluate the broadband insertion loss in the 200-2500 Hz range based on this spectrum and third-octave insertion losses IL_j as:

$$\text{IL}_{200\text{-}2500} = 10\,\log\Big[\sum_j 10^{(L_{A,j}^{\text{in}}/10)}\Big] - 10\,\log\Big[\sum_j 10^{(L_{A,j}^{\text{in}}/10)}\,10^{(-\text{IL}_j/10)}\Big] \tag{8.2}$$

The values IL_j can be taken as measured values or calculated values. For the BEM predictions, calculations are made with 20 frequencies per third-octave using the geometry shown in figure 8.18, with and without the low-height barrier. Besides, in each case the two source contributions are summed incoherently. Results are summarized in table 8.3. Measured values are slightly different from those given in table 8.2 since in this section the evaluation is based on an average

source spectrum and average attenuations, whereas the evaluation in section 8.3.3.2 was based on the difference between broadband average levels. This distinction was necessary since BEM calculations cannot predict broadband levels directly (due to the 2D approximation). In order to compare measured and predicted performances, one therefore has to use third-octave insertion losses and one source spectrum, as done in equation (8.2).

One can notice in the far tram case a difference of about 3-4 dB(A) between the measured and calculated broadband insertion losses for both receiver heights. This difference is smaller in the close tram case (1-2 dB(A)). Furthermore, although the BEM predicts a significant difference in the close tram case between the two receiver positions, which is consistent with the fact that one of them is deeper in the shadow zone, this is not observed in the measurement as pointed out in the previous section.

The main result of this comparison between attenuations obtained from simple BEM calculations and from in situ measurements is that, even though many features of the problem are not reproduced in the model, calculations yield results which are at least consistent with the in situ measurements - that is within a few dB(A) -, especially for the close tram case which is the one we are mostly interested in. This suggests that BEM numerical predictions are likely to represent the in situ performance - that is the broadband insertion loss - of such low height noise barriers, with an accuracy of a few dB(A). Therefore, one can hope that the predicted performance of the optimized low height barriers presented in the previous chapters of this work are accurate as well, within a few dB(A).

8.4.1 Numerical comparison of the barrier prototype with other designs

We end this section by comparing numerically, using the simplified BEM model given in the previous section, the performance of the chosen prototype barrier with other designs: a simple rigid straight wall, a straight wall with absorbing treatment on the source side and a fully optimized design. This will allow us to evaluate - at least numerically - how much more improvement could be obtained in the performance of such a tramway low-height noise barrier by optimizing further the design, and also how much better the chosen prototype performs than a simple solution. The fully optimized design is taken from the results of section 6.4.2, and is a wall of shape-optimized absorbing source side and optimized MPP resonator on top. The four designs are shown in figure 8.20.

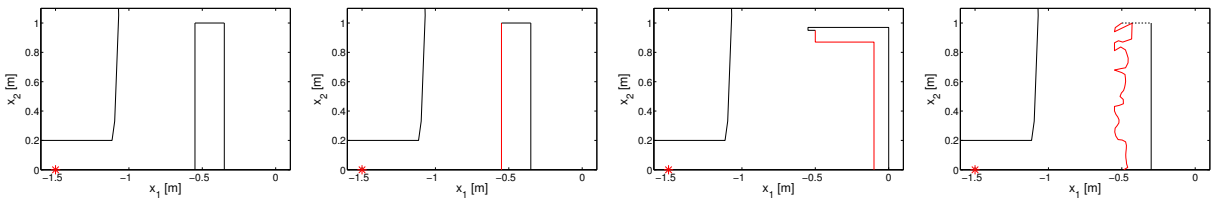

Figure 8.20: Considered low-height barrier designs used to evaluate the relative performance of the tested prototype. From left to right: straight rigid wall; straight wall with absorbing source side; tested prototype (Gamma-shape barrier with absorbing material on the source side); fully optimized design (wall with shape-optimized absorbing source side and optimized MPP resonator on top). Surface treatment color coding: rigid (thin black solid line); fibrous layer modeled with the Delany-Bazley model with parameters $\sigma = 30\,\mathrm{kPa.s/m^2}$ and $d = 10\,\mathrm{cm}$ (thick red solid line); MPP resonator of parameters $s = 0.162$, $a_0 = 3.6\,\mathrm{mm}$, $l_0 = 9.5\,\mathrm{mm}$ and $D = 9.8\,\mathrm{cm}$ (thick black dotted line).

Predicted third-octave insertion losses for the four considered designs are given in figure 8.21 and broadband insertion losses using equation (8.2) and based on the measured average tramway spectrum (as done in the previous section) are given in table 8.4. First, numerical predictions suggest that the chosen design for the full scale prototype performs much better than a simple rigid wall, essentially over the whole frequency range of interest (see in figure 8.21), yielding a broadband improvement of more than 6 dB(A) for the close tram case, and more than 3 dB(A) for the far tram case. But, the performance of the prototype is similar to that obtained with a straight wall with the source side covered with fiberglass. It could be pointed out however that the Gamma-shape was easier to set up than a straight wall in our case, since no fixation on the ground was necessary (the Gamma-shape was supported against the safety fence), and that the top of the Gamma-shape could protect the source side treatment from weather damage more efficiently.

However, BEM calculations also suggest that the prototype design is far from optimal, since another shape-optimized barrier has a higher performance, especially in the mid frequency range and for the close tram case. Even though BEM calculations typically over-estimate the performance, as shown in the previous section, it is likely that some difference of in situ performance between the prototype and a fully optimized design would remain, at least in the close tram case. For the far tram case however, the design of the barrier might not be as important, as suggested by the BEM predictions (difference smaller than 2 dB(A) between the prototype design and the fully optimized design). It should be recalled however that this type of low-height tramway noise barrier is mostly made to attenuate the noise emitted by a close tram.

Those results suggest that optimizing further the design of a tramway low-height barrier is probably worth it, in the sense that at least several dB(A) of improvement of the actual in situ performance could be achieved compared to the prototype that has been studied in this chapter.

Table 8.4: Calculated broadband insertion losses in the 200-2500 Hz range, for the four designs given in figure 8.20. The calculation is done using equation (8.2).

Configuration	$IL_{200\text{-}2500}$ [dB(A)]			
	Straight rigid wall	Straight absorbing wall	Prototype	Fully optimized wall
Close tram - 1.2 m	6.0	14.1	14.8	18.2
Close tram - 1.5 m	5.2	14.2	11.3	16.9
Far tram - 1.2 m	6.3	9.8	9.7	11.8
Far tram - 1.5 m	3.6	7.4	6.8	8.8

8.5 Conclusion

A full scale prototype of a tram low height noise barrier has been built and implemented in a real environment, along the B line of the Grenoble tramway system. A simple Gamma-shape design made of pressed wood and fiberglass, for a length of 22 m, is proposed. The design of the noise barrier as well as its length were chosen essentially to cope with feasibility and time constraints. A series of pass-by measurements were performed at a close location from the tram track, at two different heights, with and without the noise barrier. The tram speed has also been measured using an auxiliary microphone located very close to the track.

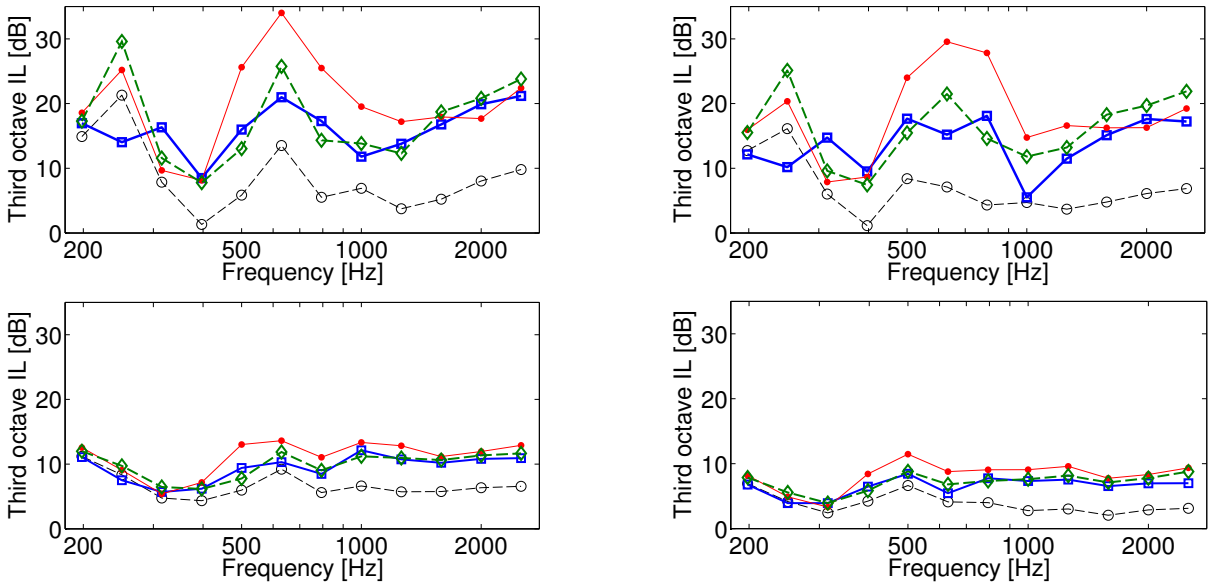

Figure 8.21: Predicted third-octave insertion losses between 200 and 2500 Hz, for the three designs given in figure 8.20, and in the four different configurations of tram and receiver positions. Top left: close tram, SLM at 1.20 m ; top right: close tram, SLM at 1.50 m ; bottom left: far tram, SLM at 1.20 m ; bottom right: far tram, SLM at 1.50 m. Line coding: straight rigid wall (thin dashed black line) ; straight wall with absorbing source side (thick dashed green line) ; prototype barrier (thick solid blue line) ; fully optimized design (thin solid red line).

First, a positive correlation has been found between pass-by equivalent level and speed, in agreement with previous studies. This was used to approximately correct for the speed in pass-by equivalent levels and time histories. Although a significant variability is found between the different trams, it is shown that the barrier provides on average an attenuation of more than 10 dB(A) for close trams, and of more than 5 dB(A) for far trams, during the whole pass-by, and not only when the barrier covers most of the tram length.

The effect of the noise barrier in the frequency domain has been studied as well. It is found that the barrier provides attenuation in the whole frequency range 200-2500 Hz (which is the range in which the effect of the barrier could be evaluated accurately), which yields a broadband insertion loss in this range of 13 dB(A) for close trams, 5 dB(A) for far trams and 8.5 dB(A) on average. BEM calculations are made as well, and it is found that although the environment is highly idealized in the calculations, the predictions yield rather good estimates of the actual in situ performance, within a few dB(A), especially for the close tram case. It is hence suggested that numerical predictions made in the rest of this work may be reasonably close to what would be actually measured in a real environment.

Finally, extra numerical calculations suggest that, although relatively efficient, the proposed design for the prototype could be further improved to gain several dB(A) of performance by treating the top of the barrier and by shape-optimizing the source side. Of course, actual implementation of more complicated designs such as the ones that have been numerically studied in the previous chapters of this work would raise feasibility and cost issues which should be studied extensively. Decision makers should in the end state if the benefit in terms of noise reduction performance is worth the extra cost of such optimized low-height noise barriers.

Chapter 9

Conclusions

9.1 Summary of findings

As a main tool in environmental noise control, noise barriers have been extensively studied in the second half of the 20^{th} century, both from a practical implementation viewpoint and from a research perspective. Nevertheless, they have mostly been looked at as a means to mitigate highway and railway noise. There is however an increasing concern to reduce noise exposure in urban areas as well, since noise is considered as a main nuisance by urban dwellers, and since many means of transport coexist in urban areas. Adapting a noise barrier design so that it can be implemented close to a noisy transportation system seems therefore promising towards urban noise reduction for pedestrians and cyclists, and as a side effect for surrounding buildings. Typically the height of these devices will have to be limited say to one meter, hence the name of low-height barriers. Application to tramway noise mitigation seems particularly interesting since this means of transportation has been rapidly developing in many cities, and since most of the emitted noise comes from the tracks and wheels, which are close to the ground, and which can therefore be efficiently mitigated. Moreover, published tramway noise power spectra suggests most of the A-weighted energy is contained between 100 and 2500 Hz, which has been chosen as the frequency range of study.

In an urban area, distances between noise sources and receivers are of the order of a few meters, which is different than for the more typical highway case, in which distances are much larger. Arguments are given that meteorological effects can probably be neglected in this case, and therefore the atmosphere can be considered homogeneous. The efficiency of the device - measured by a weighted attenuation taking into account the spectral content of tramway noise sources - is consequently mostly controlled by geometrical features, related to the presence of objects in the vicinity of the barrier such as the tramway body (which can induce the multiple reflections phenomenon), the ground properties and the design of the screen itself. Because of this dependence and because complex reflection and diffraction effects are involved, automatic optimization of the barrier design is likely to provide a significant increase of its efficiency.

Calculation of the sound field has been achieved with the boundary element method (BEM), which is one of the only prediction methods that can take precisely into account complex geo-

metrical effects as well as arbitrary distributions of admittance. Several assumptions have been made to make BEM calculations faster, which was necessary to limit computation time as the optimization algorithm has to evaluate the sound field multiple times. Hence a rigid ground has been assumed, and the effect of the reflection on the tramway body is idealized by considering a vertical baffle, which in turn is equivalent to introducing an image barrier. The mesh is considerably reduced with this method, as is the computational effort. Besides the diffraction problem has been only considered two-dimensional, which implicitly assumes that the geometry is infinitely extended in one direction and that the source is a coherent line source. However, this assumption is known to be accurate when predicting attenuation when the source is an actual 3D point source, which is what is used in the objective function.

In this work, both the shape and the surface treatment of the barrier are optimized. Although it is sometimes possible to describe the shape of a noise barrier with a small number of parameters corresponding to specific features of the design, it has been chosen here to consider a general representation of the geometry using an arbitrary set of control nodes. The variables describing the shape are therefore the coordinates of the control nodes. One should however ensure that the generated geometry is feasible, in the sense that the surface (or the curve in 2D) describing the boundary of the barrier does not fold over itself (the curve must be injective). Regarding the surface treatment, two types of materials have been considered in this work: a porous layer, which typically absorbs high frequencies well, and a reactive treatment, which can be tuned to be efficient in a given frequency band. Furthermore, two types of porous materials have been considered: a sound insulating fibrous material (such as fiberglass) and a hemp concrete layer, which is a more sustainable material. The fibrous material has been modeled with the Delany-Bazley model, whereas hemp concrete has been modeled with a Johnson-Zwikker-Kosten hybrid model, according to the literature. The chosen reactive treatment is the micro-perforated panel resonator (MPPR), and its admittance is modeled with the so-called Crandall-Sivian-Fok model.

A line-search sensitivity-based optimization method has been chosen to carry out the optimization of the control node coordinates and of the parameters describing the admittance of the chosen acoustic treatments. The sensitivity information is efficiently calculated, using an adapted version of the adjoint state approach to the acoustic scattering problem. Using a sensitivity-based method implies that one is only able to find a local solution of the optimization problem, however the number of function evaluations is dramatically smaller than with a global search method such as the genetic algorithm. Rather than finding *optimal* designs, the proposed algorithm therefore aims at finding *optimized* designs, meaning solutions with *better* performance than simple designs. Besides, due to the different types of constraints applied to the admittance parameters compared to the shape parameters (bounds constraints vs. shape injectivity constraint), it has been chosen to use different methods to optimize each type of parameters: a Sequential Quadratic Programming (SQP) method for admittance parameters, and an adapted steepest descent method for shape parameters. Indeed, whereas the SQP has a faster convergence rate, the steepest descent allows more control on the current estimate, which makes it easier to ensure the shape feasibility constraint.

First the optimization algorithm is applied to barriers assumed acoustically rigid, which would be the case if they were made out of concrete. Indeed, although acoustic surface treat-

ments can be efficient in increasing the performance of the barrier, they usually have a stronger environmental footprint than rigid materials. Several starting geometries are used in the shape optimization algorithm, including a medium wall, a Gamma-shape wall and a T-shape wall. In all cases, convergence was achieved rapidly, within a few dozens iterations. Whereas initial designs with straight geometries had low insertion loss, typically below 6 dB(A), the efficiency of optimized barriers are all above 11 dB(A) and can reach 14 dB(A), mostly due to an increase of attenuation at higher frequencies (above 500 Hz). It is also found that optimized geometries present irregularities on the side of the barrier directly exposed to the source radiation and the reflections on the tramway body. Intensity calculations suggest that this increase of attenuation is due to a redirection of the acoustic energy in the upwards direction, away from the shadow zone. Irregularities seem therefore to act against the multiple reflections happening between the tramway and the barrier.

Then, barriers covered with an absorbing fibrous material are shape-optimized. Again, convergence is achieved rapidly, and shape optimization is found to provide 5 dB(A) of extra efficiency (the predicted efficiency of shape-optimized absorbing designs reaches more than 20 dB(A)). However in this case, the geometry is less modified on the source side and more on the top side. This suggests that when multiple reflections are greatly attenuated thanks to an absorbing material, shape-optimization can still enhance the efficiency by acting on diffraction effects, which essentially happen in the top region of the barrier. Tuned MPPRs can also enhance the attenuation in the mid frequency range. Furthermore, it is found that similar attenuations of shape-optimized barriers can be obtained using hemp concrete instead of the initially considered highly absorptive fibrous material.

Further, extra calculations have been made for the found optimized designs to assess the validity of the different approximations assumed in the optimization. To do so, the tramway has been replaced by a more realistic cross-section, the ground has been considered as potentially absorbing, and the source has been modeled as a 3D point source, several incoherent point sources (approximating a finite incoherent line source of length equal to that of a tramway, that is 43 meters) or an infinite incoherent line source, using 2.5D modeling. Due to the increased complexity of the model, the attenuation has been calculated up to 1800 Hz only. First it is found that the efficiency calculated assuming an incoherent line source of all the considered designs is much lower than with the finite incoherent line source, and since considering the source finite is clearly more realistic, the results from the incoherent line source model are disregarded in our case.

For all other source models, predictions of the broadband efficiencies and insertion losses showed that the predicted benefit of the optimized barrier is lowered by about 1 dB(A) due to a more realistic cross section for the tram, and lowered by another 2-4 dB(A) due to a strongly absorbing ground. Consideration of the source spatial incoherence also decreases the efficiency of the barriers, especially in the low frequency range, although in all cases the efficiency of the optimized designs remain significant, especially in the case of a rigid ground: 9-12 dB(A) for shape-optimized rigid barriers, 16-19 dB(A) for shape-optimized barriers with optimized surface treatments. Furthermore, the benefit of using an absorbing treatment is evaluated to be of the order of 5 dB(A), even when the shape is optimized, whereas the presence of tuned MPPRs can

yield an improvement of 1 to 3 dB(A).

As a complement to the numerical simulations, a method to measure the insertion loss of a low-height barrier close to a tramway using scale models (at the 1/10th scale) has been developed and validated in simple cases. An impulsive method has been used, using a spark source and appropriate time windowing for signal selection. The spectral content of this source has been found to be significant and repeatable in the range 200-1800 Hz at full scale. Felt layers have been used to represent fibrous absorbing treatment in the model. The method has been applied to the T-shape design with different amount of absorbing materials covering the source side. Overall the agreement is good between BEM calculations and measurements, since for instance the poor performance of the rigid barrier due to the multiple reflections effect, as well as the benefit of using an absorbing treatment on the source side, are clearly confirmed by the measurements. Nevertheless, one should point out that the BEM tends to slightly underestimate the insertion loss at the low and high frequencies.

Finally, a full scale low height barrier prototype has been built and set up temporarily close to one line of the Grenoble tramway system. The prototype was made of a Gamma-shape assembly of pressed wood boards covered on the source side with fibrous absorbing material, and covers a length of 22 meters. The prototype has been set up in a residential area in which the tram rolls at relatively high speed - up to 60 km/h - and therefore measurements could be performed with good signal-to-noise ratio. A series of pass-by measurements were made at a location corresponding to the typical height of human ears, close to the track (1.5 m above the ground and 3 m away from the track), with and without the device. The tram speed has been measured as well using an auxiliary microphone located very close to the track.

A significant variability in pass-by levels has been found between the different trams, even when applying an approximate correction for speed. However it is shown that the barrier provides on average an attenuation of more than 10 dB(A), during the whole pass-by, and this even though the length of the barrier prototype was only half of that of the tramway. Spectral analysis of the recorded signals has been performed as well, and showed that the measured insertion loss of the prototype was about 13 dB(A) in the range 200-2500 Hz. Furthermore, comparisons between measurements and BEM calculations have shown that, although the environment is highly idealized in the calculations, predictions can yield rather good estimates of the actual in situ performance, especially for the close tram case. Extra numerical calculations however suggest that the performance of such a low height barrier could be improved further.

Finally, one can conclude that the design of low-height urban noise protections, as a relatively new topic of interest in the outdoor noise control community, is at the same time challenging and important since it could radically change the way of living in a dense urban area. Based on the numerical optimization results and the experimental data collected during this work, one can state that low height noise barriers can be efficient solutions to attenuate tramway noise for close receivers, namely pedestrians and cyclists. It is also likely that this type of noise protection could be efficient as well against any urban noise source located close to the ground, as long as it can be placed close to the source. Careful design of the device is particularly important for low height barriers, especially if the source of noise is surrounded by objects which might induce multiple reflections, since it may influence the efficiency significantly. Optimization methods such as the

one presented in this work are hence helpful design tools for low height noise barriers since they can help identify what are the features impacting the efficiency of the device the most.

9.2 Future work

Several improvements could be made to the approach described in this work. From a numerical modeling standpoint, one could for instance study the effect of removing some of the many assumptions used in the calculations. For instance, vertical source directivity effects could possibly change the generated optimized designs, although we believe the general trends that have been found in this work - benefit of irregular geometries and of an absorbing treatment - would probably remain. In three-dimensional modeling, it would be however interesting to study those directivity effects in the horizontal plane as well, since this would have a significant impact on the predictions when extended incoherent sources are considered. Rather accurate modeling of the actual sources of a tramway could certainly be achieved, even within a 2.5D BEM framework. Another possibility would be to use full 3D BEM calculations for the predictions, which would greatly extend the realism of the simulations, although one would certainly need a more advanced approach such as the fast multipole method to achieve this kind of simulation. Nevertheless, shape and admittance sensitivity calculations could probably be generalized to the 3D case rather easily since they essentially require the knowledge of the pressure field values on the boundary. Furthermore, when modeling surface treatments, a major assumption that should probably be looked at in details is the local reaction approximation, which is implicit when modeling the treatment with a surface admittance. Modeling the longitudinal sound propagation inside the materials would certainly be more accurate and could be achieved with proper BEM calculations as well.

Besides, the optimization strategy itself could also be further explored. Although arguments have been made towards the utilization of gradient-based optimization methods for our application, it would be interesting to compare our results to solutions obtained with global search methods (genetic algorithms for instance), in terms of efficiency and in terms of computational effort. One could even imagine coupling the two approaches, for instance by starting with a "coarse" optimization using a global search method and then running a local search with a sensitivity-based method. The question of variables representation would however require a lot of attention in this context.

Regarding shape optimized barriers as presented in this work, it also seems essential to evaluate in detail the feasibility of such somewhat complicated geometries. Extruded concrete might be a manufacturing option to build shape optimized rigid barriers, but this of course would require detailed investigation. Shaping absorbing treatments in irregular geometries also seems rather challenging.

Last but not least, following a holistic approach taking into account all aspects of sustainability (economical cost, environmental footprint, social benefit, health effects and so on) and not only the acoustic performance, seems absolutely necessary to evaluate properly the benefit of low height noise barriers. Nevertheless, even though from a holistic point of view the present

study is a small step, we are convinced that this type of noise protection is a promising tool towards a better quality of life in urban areas, and we can only hope this concept will be further developed in the near future.

Appendix

A Tangential differential operators

We give in this section a few definitions and properties regarding tangential differential operators. More comprehensive analyses of these operators can be found in [136, 149, 192]. Although those operators are defined in general in 3D, we also give more specific properties for the 2D case.

Let Γ is a smooth curve in 2D (or a smooth surface in 3D) and $\mathbf{n}$ the normal vector on Γ. Given a differentiable scalar function p defined in a neighborhood of Γ, one can define the surface gradient ∇_Γ at a point on Γ as:

$$\nabla_\Gamma p = \nabla p - \frac{\partial p}{\partial n}\,\mathbf{n}$$

Then the surface rotational is defined as: $\mathbf{rot}_\Gamma\, p = \nabla_\Gamma p \wedge \mathbf{n}$.

Similarly, if $\mathbf{u}$ is a vector field defined in a neighborhood of Γ, the surface divergence div_Γ of $\mathbf{u}$ can be defined as:

$$\mathrm{div}_\Gamma\, \mathbf{u} = \mathrm{div}\, \mathbf{u} - \mathbf{n} \cdot \nabla \mathbf{u} \cdot \mathbf{n}$$

The surface rotational of a vector field is then defined as: $\mathrm{rot}_\Gamma\, \mathbf{u} = \mathrm{div}_\Gamma\, (\mathbf{u} \wedge \mathbf{n})$.

Several properties - similar to those involving usual differential operators - can be derived. In particular:

$$\mathrm{div}_\Gamma\, \mathbf{rot}_\Gamma p = 0 \qquad \mathrm{rot}_\Gamma\, \nabla_\Gamma p = 0$$

Besides, one has the following integration by parts properties (given p and q smooth scalar valued functions and $\mathbf{u}$ a smooth vector valued function):

$$\begin{aligned}
\int_\Gamma \nabla_\Gamma p \cdot \mathbf{u}\, \mathrm{d}\Gamma &= -\int_\Gamma p\, \mathrm{div}_\Gamma \mathbf{u}\, \mathrm{d}\Gamma \\
\int_\Gamma \mathbf{rot}_\Gamma p \cdot \mathbf{u}\, \mathrm{d}\Gamma &= \int_\Gamma p\, \mathrm{rot}_\Gamma \mathbf{u}\, \mathrm{d}\Gamma \\
\int_\Gamma p\, \mathbf{rot}_\Gamma q\, \mathrm{d}\Gamma &= -\int_\Gamma q\, \mathbf{rot}_\Gamma p\, \mathrm{d}\Gamma
\end{aligned}$$

Furthermore, in the 2D case, there is essentially one tangential operator which is the tangential derivative. At any smooth point on Γ, the gradient of a scalar function p can be broken

down on the local normal and tangent vector $\mathbf{n}$ and $\mathbf{t}$:

$$\nabla p = (\nabla p \cdot \mathbf{n})\,\mathbf{n} + (\nabla p \cdot \mathbf{t})\,\mathbf{t} = \frac{\partial p}{\partial n}\mathbf{n} + \frac{\partial p}{\partial t}\mathbf{t}$$

Therefore one has:

$$\nabla_\Gamma p = \frac{\partial p}{\partial t}\mathbf{t}$$

which yields:

$$\mathbf{rot}_\Gamma\, p = \frac{\partial p}{\partial t}\,\mathbf{t} \wedge \mathbf{n} = \frac{\partial p}{\partial t}\,\mathbf{e}_3$$

where $\mathbf{e}_3$ is the unit vector along the x_3 direction (normal to the vertical plane, as defined in figure 2.1). In particular, this implies:

$$\mathbf{rot}_\Gamma\, p \cdot \mathbf{rot}_\Gamma\, q = \frac{\partial p}{\partial t}\,\frac{\partial q}{\partial t}$$

B Uniqueness of Jean's integral equation solution

In this section we derive the fact that equation (2.12) has a unique solution for all wavenumbers if the admittance β has a nonzero real part everywhere. The derivation follows closely the approach used in [139].

Let us consider the corresponding homogeneous equation:

$$Np_\Gamma + D^*(\mathrm{i}k\beta p_\Gamma) + \mathrm{i}k\beta\, Dp_\Gamma + \mathrm{i}k\beta\, S(\mathrm{i}k\beta p_\Gamma) = 0 \tag{B.1}$$

Since equation (2.12) is linear, the only thing to prove is that the homogeneous equation (B.1) only admits the solution $p_\Gamma = 0$.

Let p_Γ be a solution of equation (B.1). Define $v = Dp_\Gamma + S(\mathrm{i}k\beta p_\Gamma)$. By properties of the integral operators [136], v satisfies the homogeneous Helmholtz equation in Ω^i and Ω^e:

$$-(\nabla^2 + k^2)\, v = 0 \quad \text{in } \Omega^i \cup \Omega^e$$

as well as the radiation condition at infinity. Also, we have the following expressions for the interior and exterior traces v_i and v_e of v on Γ, and those of the interior and exterior normal derivatives $\partial v/\partial n|_i$ and $\partial v/\partial n|_e$:

$$\begin{aligned} v_i &= -\frac{1}{2}\,p_\Gamma + Dp_\Gamma + S(\mathrm{i}k\beta p_\Gamma) \\ \frac{\partial v}{\partial n}\Big|_i &= \frac{1}{2}\,\mathrm{i}k\beta p_\Gamma + Np_\Gamma + D^*(\mathrm{i}k\beta p_\Gamma) \\ v_e &= \frac{1}{2}\,p_\Gamma + Dp_\Gamma + S(\mathrm{i}k\beta p_\Gamma) \end{aligned}$$

$$\frac{\partial v}{\partial n}\Big|_e = -\frac{1}{2}\,\mathrm{i}k\beta p_\Gamma + Np_\Gamma + D^*(\mathrm{i}k\beta p_\Gamma)$$

Finally, the jump relations at the boundary Γ are given by:

$$p_\Gamma = v_e - v_i \qquad ik\beta p_\Gamma = \frac{\partial v}{\partial n}\Big|_i - \frac{\partial v}{\partial n}\Big|_e \tag{B.2}$$

One can therefore rewrite equation (B.1) as:

$$0 = \frac{\partial v}{\partial n}\Big|_i - \frac{1}{2}\,\mathrm{i}k\beta p_\Gamma + \mathrm{i}k\beta\left(v_i + \frac{1}{2}\,p_\Gamma\right) = \frac{\partial v}{\partial n}\Big|_i + \mathrm{i}k\beta v_i \tag{B.3}$$

Similarly, one can show that the same boundary condition holds for the exterior traces:

$$\frac{\partial v}{\partial n}\Big|_e + \mathrm{i}k\beta v_e = 0 \tag{B.4}$$

Now, applying Green's second identity [136, 139] to v and its complex conjugate v^* in the interior domain Ω^i, one has :

$$\int_\Gamma \left(v_i\,\frac{\partial v^*}{\partial n}\Big|_i - v_i^*\,\frac{\partial v}{\partial n}\Big|_i\right)\mathrm{d}\Gamma = \int_{\Omega^i}(v\,\nabla^2 v^* - v^*\,\nabla^2 v)\,\mathrm{d}\Omega \tag{B.5}$$

Applying equation (B.3), the left hand side of equation (B.5) becomes:

$$\int_\Gamma \left(v_i\,\frac{\partial v^*}{\partial n}\Big|_i - v_i^*\,\frac{\partial v}{\partial n}\Big|_i\right)\mathrm{d}\Gamma = \int_\Gamma \left(v_i\,(-\mathrm{i}k\beta v_i)^* - v_i^*\,(-\mathrm{i}k\beta v_i)\right)\mathrm{d}\Gamma = 2\mathrm{i}k\int_\Gamma \left(\mathrm{Re}(\beta)\,|v_i|^2\right)\mathrm{d}\Gamma$$

Besides, since v satisfies the homogeneous Helmholtz equation in Ω^i, the right hand side of equation (B.5) becomes:

$$\int_{\Omega^i}(v\,\nabla^2 v^* - v^*\,\nabla^2 v)\,\mathrm{d}\Omega = \int_{\Omega^i}(-k^2\,|v|^2 + k^2\,|v|^2)\,\mathrm{d}\Omega = 0$$

Therefore, equation (B.5) becomes:

$$\int_\Gamma \left(\mathrm{Re}(\beta)\,|v_i|^2\right)\mathrm{d}\Gamma = 0$$

Provided that $\mathrm{Re}(\beta) \neq 0$ everywhere on Γ, this yields $v_i = 0$, and recalling equation (B.3), yields $\partial v/\partial n|_i = 0$ as well.

We can also write Green's second identity in Ω^e. The surface integral term at infinity vanishes due to the radiation condition, and therefore, recalling the boundary condition (B.4)

and following the same process, one can show:

$$\int_\Gamma \Big(\mathrm{Re}(\beta) \, |v_e|^2 \Big) \, \mathrm{d}\Gamma = 0$$

Again, this implies $v_e = 0$ due to the constraint on β. Finally, recalling the first trace relationship given in equation (B.2), this yields $p_\Gamma = 0$, which concludes the proof.

C Static kernels properties and regularization of the Kirchhoff-Hemholtz integral equation

In this section an approach which allows to regularize the classical Kirchhoff-Helmholtz equation (2.10) and its derivative (2.11) is presented, using properties of the static integral operators introduced in section 2.3.1. This approach is essentially inspired by Duhamel [137] and Liu and Rizzo [193]. The main advantage of such a technique is that integration of regular functions only are required to build the system satisfied by the boundary pressure field.

C.1 Integral properties of static kernels

As stated in section 2.3.2, the integral representation theorem is also valid in the "static" case, that is when $k = 0$. This will allow to derive important properties about the static operators, which we will write with a superscript ^{0} (such as S^0, D^0, and so on). The results obtained in this section are similar to those derived by Liu and Rudolphi [194].

Consider the field $\hat{p}$ of constant value 1 in Ω^i and of value 0 in Ω^e. This function, as a piecewise constant function, satisfies the Laplace equation in $\Omega^i \cup \Omega^e$ and the radiation condition. The jumps across Γ are in this case: $\mu = 1$ and $\lambda = 0$. Application of equations (2.8) and (2.9) yields:

$$D^0 1 = \begin{cases} 0 & \text{in } \Omega^e \\ -\dfrac{1}{2} & \text{in } \Gamma \\ -1 & \text{in } \Omega^i \end{cases} \qquad \text{and} \qquad N^0 1 = 0 \quad \text{in } \Omega^e \cup \Gamma \cup \Omega^i$$

The fact that $N^0 1 = 0$ everywhere is not surprising considering the expression of the operator N given in equation (2.7) since $\mathbf{rot}_\Gamma 1 = 0$.

Another simple function that satisfies the Laplace equation and the radiation condition is the linear function y_i equal to one coordinate x_i, with $i = 1, 2$, in Ω^i and 0 in Ω^e. The notation y_i is used since $\mathbf{y}$ has been and will be the main variable of integration in this section. In this case $\mu = y_i$ and $\lambda = n_i$, n_i being the i^{th} component of the normal vector $\mathbf{n}$. Application of the

integral representation theorem yields the following relationships:

$$S^0 n_i - D^0 y_i = \left\{ \begin{array}{rcl} 0 & \text{in} & \Omega^e \\ \frac{1}{2} y_i & \text{in} & \Gamma \\ y_i & \text{in} & \Omega^i \end{array} \right\} = -y_i \, D^0 1$$

Rewriting this under vector form, one has at any point in space:

$$S^0(\mathbf{n}) = D^0(\mathbf{y}) - \mathbf{x} \, D^0(1) = D^0(\mathbf{y} - \mathbf{x}) \tag{C.6}$$

This can also be written out as:

$$(\forall \mathbf{x} \in \Omega^i \cup \Gamma \cup \Omega^e) \qquad \int_\Gamma G^0(\mathbf{x}, \mathbf{y}) \, \mathbf{n}(\mathbf{y}) \, \mathrm{d}\Gamma(\mathbf{y}) = \int_\Gamma \frac{\partial G^0}{\partial n_y}(\mathbf{x}, \mathbf{y}) \, (\mathbf{y} - \mathbf{x}) \, \mathrm{d}\Gamma(\mathbf{y})$$

Application of the integral representation of the gradient yields (transforming in vector form directly):

$$D^{0*} \mathbf{n} - N^0 \mathbf{y} = \left\{ \begin{array}{rcl} 0 & \text{in} & \Omega^e \\ \frac{1}{2} \mathbf{n} & \text{in} & \Gamma \\ \mathbf{1} & \text{in} & \Omega^i \end{array} \right.$$

with $\mathbf{1} = (1, 1)$. Since $N^0 1 = 0$, this can be rewritten as:

$$D^{0*} \mathbf{n} - N^0(\mathbf{y} - \mathbf{x}) = \left\{ \begin{array}{rcl} 0 & \text{in} & \Omega^e \\ \frac{1}{2} \mathbf{n} & \text{in} & \Gamma \\ \mathbf{1} & \text{in} & \Omega^i \end{array} \right.$$

C.2 Regularization using static kernels

We are now considering the two equations (2.10) and (2.11) which are combined together to form either Burton and Miller's integral equation or Jean's integral equation, which is then solved numerically. Although integrability of the different expressions is theoretically ensured, one may wish to form more regular integrals which can be evaluated more easily in a numerical implementation. For instance, although the kernel involved in the single layer potential is integrable, it is unbounded when the integration point approaches the current point, which makes the numerical integration more difficult. We give here an approach to circumvent this issue, essentially inspired by Duhamel [137] and Liu and Rizzo [193].

The basic idea is to consider an auxiliary function, solution of another scattering problem, and to use the integral equations satisfied by this auxiliary function to regularize the initial integral equations, typically equations (2.10) and (2.11). Let p^0 a function solution of the Laplace equation in Ω^i and of zero value in Ω^e. In this case the two distributions λ and μ are

respectively the interior traces of $\partial p^0/\partial n$ and p^0 on Γ, and therefore the trace relationships given in equation (2.9) yield:

$$\begin{cases} \dfrac{1}{2}\, p_\Gamma^0 + D^0 p_\Gamma^0 - S^0 \dfrac{\partial p^0}{\partial n}\Big|_\Gamma = 0 \\ \dfrac{1}{2}\, \dfrac{\partial p^0}{\partial n}\Big|_\Gamma + N^0 p_\Gamma^0 - D^{0*} \dfrac{\partial p^0}{\partial n}\Big|_\Gamma = 0 \end{cases}$$

Let us now recall the two equations (2.10) and (2.11) satisfied by p_Γ and its normal derivative:

$$\begin{cases} \dfrac{1}{2}\, p_\Gamma - D p_\Gamma + S \dfrac{\partial p}{\partial n}\Big|_\Gamma = p^{\text{in}}|_\Gamma \\ \dfrac{1}{2}\, \dfrac{\partial p}{\partial n}\Big|_\Gamma - N p_\Gamma + D^* \dfrac{\partial p}{\partial n}\Big|_\Gamma = \dfrac{\partial p^{\text{in}}}{\partial n}\Big|_\Gamma \end{cases}$$

Adding those two sets of equations together, one obtains:

$$\begin{cases} \dfrac{1}{2}\,(p_\Gamma + p_\Gamma^0) - (D p_\Gamma - D^0 p_\Gamma^0) + \Big(S \dfrac{\partial p}{\partial n}\Big|_\Gamma - S^0 \dfrac{\partial p^0}{\partial n}\Big|_\Gamma \Big) = p^{\text{in}}|_\Gamma \\ \dfrac{1}{2}\, \Big(\dfrac{\partial p}{\partial n}\Big|_\Gamma + \dfrac{\partial p^0}{\partial n}\Big|_\Gamma \Big) - (N p_\Gamma - N^0 p_\Gamma^0) + \Big(D^* \dfrac{\partial p}{\partial n}\Big|_\Gamma - D^{0*} \dfrac{\partial p^0}{\partial n}\Big|_\Gamma \Big) = \dfrac{\partial p^{\text{in}}}{\partial n}\Big|_\Gamma \end{cases}$$

which can be further rewritten as:

$$\begin{cases} \dfrac{1}{2}\,(p_\Gamma + p_\Gamma^0) - \Big((D - D^0) p_\Gamma + D^0 (p_\Gamma - p_\Gamma^0) \Big) \\ \qquad + \Big((S - S^0) \dfrac{\partial p}{\partial n}\Big|_\Gamma + S^0 \dfrac{\partial (p - p^0)}{\partial n}\Big|_\Gamma \Big) = p^{\text{in}}|_\Gamma \end{cases} \tag{C.7}$$

$$\begin{cases} \dfrac{1}{2}\, \Big(\dfrac{\partial p}{\partial n}\Big|_\Gamma + \dfrac{\partial p^0}{\partial n}\Big|_\Gamma \Big) - \Big((N - N^0) p_\Gamma + N^0 (p_\Gamma - p_\Gamma^0) \Big) \\ \qquad + \Big((D^* - D^{0*}) \dfrac{\partial p}{\partial n}\Big|_\Gamma + D^{0*} \dfrac{\partial (p - p^0)}{\partial n}\Big|_\Gamma \Big) = \dfrac{\partial p^{\text{in}}}{\partial n}\Big|_\Gamma \end{cases} \tag{C.8}$$

Such a rewriting is convenient since the operators minus their static equivalent $S - S^0$, $D - D^0$ and $D^* - D^{0*}$ involve more regular kernels and are therefore more convenient to evaluate numerically. The term $N - N^0$ requires a little more rewriting:

$$\begin{aligned} (N - N^0) p_\Gamma &= -\text{rot}_\Gamma\, S(\mathbf{rot}_\Gamma p_\Gamma) + k^2\, S(p_\Gamma \mathbf{n}) \cdot \mathbf{n} + \text{rot}_\Gamma\, S^0(\mathbf{rot}_\Gamma p_\Gamma) \\ &= -\text{rot}_\Gamma \left[(S - S^0) \mathbf{rot}_\Gamma p_\Gamma \right] + k^2 \left(S - S^0 \right)(p_\Gamma \mathbf{n}) \cdot \mathbf{n} \\ &\quad + k^2\, S^0\big((p_\Gamma - p_\Gamma^1) \mathbf{n} \big) \cdot \mathbf{n} + k^2\, S^0 (p_\Gamma^1 \mathbf{n}) \cdot \mathbf{n} \end{aligned} \tag{C.9}$$

where p_Γ^1 can be an arbitrary function defined on Γ.

Now there mostly remain terms involving the static operators acting on $p_\Gamma - p_\Gamma^0$ or its normal derivative. The static kernels have essentially the same behavior as the dynamic kernels, which means that there are still unbounded as the integration point approaches the current point. However if p_Γ^0 is chosen in order to mimic the behavior of p_Γ close to the current point on Γ

- which we will call from now on $\mathbf{x}$ -, $p_\Gamma - p^0_\Gamma$ can compensate for the singularity of the static kernels.

One can choose for instance a linear approximation of p close to the point $\mathbf{x}$. The function p^0 is therefore defined as:

$$p^0(\mathbf{y}) = \begin{cases} p_\Gamma(\mathbf{x}) + \nabla p(\mathbf{x})|_\Gamma \cdot (\mathbf{y}-\mathbf{x}) & \text{in } \Omega^i \\ 0 & \text{in } \Omega^e \end{cases}$$

This choice for the function p^0 requires the solution to be sufficiently regular at $\mathbf{x}$ in order to ensure that the gradient is well defined at this point. This is usually true, but as it has been seen in section 2.4, this requirement will fail at a geometrical singularity (a corner for instance).

p^0 satisfies the radiation condition and, as a piecewise linear function, is indeed a solution of the Laplace equation. The interior trace on the boundary Γ of p^0 can then be written as:

$$\begin{aligned} (\forall \mathbf{y} \in \Gamma) \qquad p^0_\Gamma(\mathbf{y}) &= p_\Gamma(\mathbf{x}) + \frac{\partial p}{\partial n}(\mathbf{x})\, \mathbf{n}(\mathbf{x}) \cdot (\mathbf{y}-\mathbf{x}) + \nabla_\Gamma p(\mathbf{x}) \cdot (\mathbf{y}-\mathbf{x}) \\ &= p_\Gamma(\mathbf{x}) - \mathrm{i}k\beta(\mathbf{x}) p_\Gamma(\mathbf{x})\, \mathbf{n}(\mathbf{x}) \cdot (\mathbf{y}-\mathbf{x}) + \nabla_\Gamma p(\mathbf{x}) \cdot (\mathbf{y}-\mathbf{x}) \end{aligned}$$

where the normal derivative of p has been replaced using the boundary condition. The interior trace of the normal derivative of p^0 is given by:

$$(\forall \mathbf{y} \in \Gamma) \qquad \frac{\partial p^0}{\partial n}\Big|_\Gamma(\mathbf{y}) = -\mathrm{i}k\beta(\mathbf{x}) p_\Gamma(\mathbf{x})\, \mathbf{n}(\mathbf{x}) \cdot \mathbf{n}(\mathbf{y}) + \nabla_\Gamma p(\mathbf{x}) \cdot \mathbf{n}(\mathbf{y})$$

Finally, since the gradient of p^0 is constant of value $\nabla p^0 = \nabla p(\mathbf{x})$ in Ω^i, the interior traces of the surface gradient and rotational of p^0 are constant as well of value:

$$\nabla_\Gamma p^0 = \nabla_\Gamma p(\mathbf{x}) \quad \text{and} \quad \mathbf{rot}_\Gamma p^0 = \mathbf{rot}_\Gamma p(\mathbf{x})$$

Another function p^1_Γ has been introduced in the rewriting of $N - N^0$. Recalling equation (C.9), it should be chosen so that $p_\Gamma - p^1_\Gamma$ vanishes at $\mathbf{x}$ but can be here chosen constant. Defining $p^1_\Gamma = p_\Gamma(\mathbf{x})$, equation (C.9) becomes:

$$\begin{aligned} (N-N^0)p_\Gamma = &- \mathrm{rot}_\Gamma\left[(S-S^0)\mathbf{rot}_\Gamma p_\Gamma\right] + k^2\left(S-S^0\right)(p_\Gamma \mathbf{n}) \cdot \mathbf{n} \\ &+ k^2\, S^0\big[\big(p_\Gamma(\mathbf{y}) - p_\Gamma(\mathbf{x})\big)\mathbf{n}\big] \cdot \mathbf{n} + k^2\, p_\Gamma(\mathbf{x})\, S^0(\mathbf{n}) \cdot \mathbf{n} \end{aligned}$$

Again here $\mathbf{x}$ is the point which the equation is evaluated at, and $\mathbf{y}$ is a dummy integration variable used in the evaluation of the integral operators (this type of somewhat abusive notation will be used extensively in the rest of this section). Recalling equation (C.6), this finally yields:

$$(N-N^0)p_\Gamma = -\mathrm{rot}_\Gamma\left[(S-S^0)\mathbf{rot}_\Gamma p_\Gamma\right] + k^2\left(S-S^0\right)(p_\Gamma \mathbf{n}) \cdot \mathbf{n}$$

$$+ k^2\, S^0\big[\big(p_\Gamma(\mathbf{y}) - p_\Gamma(\mathbf{x})\big)\mathbf{n}\big]\cdot\mathbf{n} + k^2\, p_\Gamma(\mathbf{x})\, D^0(\mathbf{y}-\mathbf{x})\cdot\mathbf{n}$$

Under this form, it is clear that all the involved integrands are regular since $p_\Gamma(\mathbf{y}) - p_\Gamma(\mathbf{x})$ and $\mathbf{y}-\mathbf{x}$ vanish when $\mathbf{y}$ goes to $\mathbf{x}$. Therefore, with this choice of auxiliary functions, equation (C.9) involves regular integrands only.

Substituting the expressions for p^0 and p^1 in equations (C.7) and (C.8) and using the boundary condition, one obtains, for any point $\mathbf{x}\in\Gamma$:

$$\begin{cases} p_\Gamma - (D-D^0)p_\Gamma - D^0\big(p_\Gamma(\mathbf{y})-p_\Gamma(\mathbf{x})\big) - \mathrm{i}k\beta p_\Gamma\,\mathbf{n}\cdot D^0(\mathbf{y}-\mathbf{x}) \\ \qquad - \big(S-S^0\big)(\mathrm{i}k\beta p_\Gamma) - S^0\big(\mathrm{i}k\beta(\mathbf{y})p_\Gamma(\mathbf{y}) - \mathrm{i}k\beta(\mathbf{x})p_\Gamma(\mathbf{x})\,\mathbf{n}(\mathbf{x})\cdot\mathbf{n}(\mathbf{y})\big) \\ \qquad + \nabla_\Gamma p(\mathbf{x})\cdot\big(D^0(\mathbf{y}-\mathbf{x}) - S^0(\mathbf{n})\big) = p^{\mathrm{in}}|_\Gamma \\ -\mathrm{i}k\beta p_\Gamma - (N-N^0)p_\Gamma + \mathrm{rot}_\Gamma\, S^0\big(\mathbf{rot}_\Gamma p_\Gamma(\mathbf{y}) - \mathbf{rot}_\Gamma p_\Gamma(\mathbf{x})\big) \\ \qquad - (D^*-D^{0*})(\mathrm{i}k\beta p_\Gamma) - D^{0*}\big(\mathrm{i}k\beta(\mathbf{y})p_\Gamma(\mathbf{y}) - \mathrm{i}k\beta(\mathbf{x})p_\Gamma(\mathbf{x})\mathbf{n}(\mathbf{y})\cdot\mathbf{n}(\mathbf{x})\big) \\ \qquad - \nabla_\Gamma p\cdot D^{0*}\mathbf{n} = \dfrac{\partial p^{\mathrm{in}}}{\partial n}\Big|_\Gamma \end{cases}$$

Besides, the term $\nabla_\Gamma p(\mathbf{x})\cdot D^{0*}\mathbf{n}$ can be regularized as follows:

$$\nabla_\Gamma p(\mathbf{x})\cdot D^{0*}\mathbf{n} = \nabla_\Gamma p(\mathbf{x})\cdot D^{0*}\big(\mathbf{n}(\mathbf{y})-\mathbf{n}(\mathbf{x})\big) + \underbrace{\nabla_\Gamma p(\mathbf{x})\cdot\mathbf{n}(\mathbf{x})}_{=0} D^{0*}1 = \nabla_\Gamma p(\mathbf{x})\cdot D^{0*}\big(\mathbf{n}(\mathbf{y})-\mathbf{n}(\mathbf{x})\big) \tag{C.10}$$

Recalling equation (C.6) and (C.10), one can rewrite equations (C.7) and (C.8) as:

$$\begin{cases} p_\Gamma - (D-D^0)p_\Gamma - D^0\big(p_\Gamma(\mathbf{y})-p_\Gamma(\mathbf{x})\big) - \mathrm{i}k\beta p_\Gamma\,\mathbf{n}\cdot D^0(\mathbf{y}-\mathbf{x}) \\ \qquad - \big(S-S^0\big)(\mathrm{i}k\beta p_\Gamma) - S^0\big(\mathrm{i}k\beta(\mathbf{y})p_\Gamma(\mathbf{y}) - \mathrm{i}k\beta(\mathbf{x})p_\Gamma(\mathbf{x})\,\mathbf{n}(\mathbf{x})\cdot\mathbf{n}(\mathbf{y})\big) = p^{\mathrm{in}}|_\Gamma \end{cases} \tag{C.11}$$

$$\begin{cases} -\mathrm{i}k\beta p_\Gamma - (N-N^0)p_\Gamma + \mathrm{rot}_\Gamma\, S^0\big(\mathbf{rot}_\Gamma p_\Gamma(\mathbf{y}) - \mathbf{rot}_\Gamma p_\Gamma(\mathbf{x})\big) \\ \qquad - (D^*-D^{0*})(\mathrm{i}k\beta p_\Gamma) - D^{0*}\big(\mathrm{i}k\beta(\mathbf{y})p_\Gamma(\mathbf{y}) - \mathrm{i}k\beta(\mathbf{x})p_\Gamma(\mathbf{x})\mathbf{n}(\mathbf{y})\cdot\mathbf{n}(\mathbf{x})\big) \\ \qquad - \nabla_\Gamma p\cdot D^{0*}\big(\mathbf{n}(\mathbf{y})-\mathbf{n}(\mathbf{x})\big) = \dfrac{\partial p^{\mathrm{in}}}{\partial n}\Big|_\Gamma \end{cases} \tag{C.12}$$

All the terms of equations (C.11) and (C.12) involve regular integrands only. One can now consider a complex combination of equation (C.11) and (C.12) to obtain a Burton and Miller - like equation or a regularized version of Jean's equation, as done in section 2.3.3. For instance, one can consider the combination (C.12)+i$k\beta$(C.11), multiply by an arbitrary weighting function q_Γ defined on Γ and integrate over Γ. Using the variational expression for N and N^0 in 2D given in section 2.3.1.2 and regrouping terms yields the following equation under its variational form:

$$\int_\Gamma\int_\Gamma \mathrm{d}\Gamma(\mathbf{y})\mathrm{d}\Gamma(\mathbf{x}) \\ \Bigg(\big(G-G^0\big)(\mathbf{x},\mathbf{y})\Big[-\frac{\partial p_\Gamma}{\partial t}(\mathbf{y})\,\frac{\partial q_\Gamma}{\partial t}(\mathbf{x}) + k^2\,\big(\mathbf{n}(\mathbf{y})\cdot\mathbf{n}(\mathbf{x}) - \beta(\mathbf{y})\,\beta(\mathbf{x})\big)\,p_\Gamma(\mathbf{y})\,q_\Gamma(\mathbf{x})\Big]$$

$$
\begin{aligned}
&+ G^0(\mathbf{x},\mathbf{y}) \Big[-\big(\frac{\partial p_\Gamma}{\partial t}(\mathbf{y}) - \frac{\partial p_\Gamma}{\partial t}(\mathbf{x})\big)\, \frac{\partial q_\Gamma}{\partial t}(\mathbf{x}) + k^2 \left(p_\Gamma(\mathbf{y}) - p_\Gamma(\mathbf{x})\right) q_\Gamma(\mathbf{x})\, \mathbf{n}(\mathbf{y})\cdot\mathbf{n}(\mathbf{x}) \\
&\qquad\qquad -k^2 \left(\beta(\mathbf{y}) p_\Gamma(\mathbf{y}) - \beta(\mathbf{x}) p_\Gamma(\mathbf{x})\, \mathbf{n}(\mathbf{x})\cdot\mathbf{n}(\mathbf{y})\right) \beta(\mathbf{x})\, q_\Gamma(\mathbf{x}) \Big] \\
&+ \Big(\frac{\partial G}{\partial n_y}(\mathbf{x},\mathbf{y}) - \frac{\partial G^0}{\partial n_y}(\mathbf{x},\mathbf{y})\Big)\, \mathrm{i}k\, \beta(\mathbf{x})\, p_\Gamma(\mathbf{y})\, q_\Gamma(\mathbf{x}) \\
&+ \frac{\partial G^0}{\partial n_y}(\mathbf{x},\mathbf{y}) \Big[\big(p_\Gamma(\mathbf{y}) - p_\Gamma(\mathbf{x})\big)\, \mathrm{i}k\, \beta(\mathbf{x}) + k^2\, (\mathbf{y}-\mathbf{x})\cdot\mathbf{n}(\mathbf{x})\, \big(1-\beta(\mathbf{x})^2\big) p_\Gamma(\mathbf{x}) \Big]\, q_\Gamma(\mathbf{x}) \\
&+ \Big(\frac{\partial G}{\partial n_x}(\mathbf{x},\mathbf{y}) - \frac{\partial G^0}{\partial n_x}(\mathbf{x},\mathbf{y})\Big)\, \mathrm{i}k\, \beta(\mathbf{y})\, p_\Gamma(\mathbf{y})\, q_\Gamma(\mathbf{x}) \\
&+ \frac{\partial G^0}{\partial n_x}(\mathbf{x},\mathbf{y}) \Big[\frac{\partial p_\Gamma}{\partial t}(\mathbf{x})\, \mathbf{t}(\mathbf{x}) \cdot \big(\mathbf{n}(\mathbf{y}) - \mathbf{n}(\mathbf{x})\big) + \mathrm{i}k \left(\beta(\mathbf{y})\, p_\Gamma(\mathbf{y}) - \beta(\mathbf{x})\, p_\Gamma(\mathbf{x})\, \mathbf{n}(\mathbf{y})\cdot\mathbf{n}(\mathbf{x})\right) \Big]\, q_\Gamma(\mathbf{x}) \Bigg) \\
&= \int_\Gamma h^{\mathrm{in}}(\mathbf{x})\, q_\Gamma(\mathbf{x})\, \mathrm{d}\Gamma(\mathbf{x})
\end{aligned}
$$

with h^{in} defined as in equation (2.2). Unfortunately this equation does not seem to be symmetrical with respect to p and q because of the term $\nabla_\Gamma p\, q_\Gamma$, but nonetheless could probably be implemented and readily solved. This has not been achieved in this work and is presented here again as an example of how to theoretically use the properties of static kernels to regularize integral equations.

D Shape optimization algorithm details

In this section the steepest descent method used for the shape optimization is outlined. This method is called by the main algorithm presented in section 3.5 at a given iteration i.

This method is essentially a line search strategy (the search direction being the opposite of the gradient at the current estimate), however the step-size is chosen automatically thanks to a simple backtracking algorithm. This simply consists in starting with a large step-size (for instance $\alpha_0 = 0.5$), and decreasing it exponentially by multiplying it by a contraction constant $\rho < 1$ until some conditions are met. This can be used to ensure at the same time a sufficient decrease of the objective function (which is quantified here by the Armijo condition [147]) and that the shape is injective at each iteration. Indeed, thanks to the backtracking algorithm, given that the shape the algorithm started with was indeed feasible, even if the current shape is not for a certain step-size, one can ensure that by decreasing it enough the new shape will be injective again (this is ensured theoretically by the fact that the set of continuous injective functions form an open set). An outline of the shape optimization algorithm is:

Given ϵ_Γ (shape optimization convergence tolerance)
Given ρ , c , α_0 (backtracking algorithm constants)
Given $\mathbb{P}$ (bound constraints projection operator)
Given $\mathbf{x}_\Gamma^i$, $\mathbf{x}_\beta^{i+1}$ (current variable estimates)
Given e_β^{i+1} , $\mathbf{g}_\beta^{i+1}$ (current objective function and gradient values)

$k = 0$, $\mathbf{x}_\Gamma^k = x_\Gamma^i$, $\mathbf{x}_\beta = \mathbf{x}_\beta^{i+1}$, $e^k = e_\beta^{i+1}$, $\mathbf{g}^k = \mathbf{g}_\beta^{i+1}$

while $\Big($**not** $\big(|e^{k+1} - e^k| < \epsilon_\Gamma\big)$ or $k = 0\Big)$
  Step-size selection (backtracking algorithm)
  $\alpha = \alpha_0$, $\mathbf{x}_b = \mathbb{P}(\mathbf{x}_\Gamma^k - \alpha\, \mathbf{g}^k)$, $e_b = e(\mathbf{x}_\beta, \mathbf{x}_b)$
  while $\Big($**not** $\big(e_b < e^k - c\,||\mathbf{g}^k||^2$ (sufficient decrease condition)$\big)$ or **not** $\big(\Gamma(\mathbf{x}_b)$ is injective$\big)\Big)$
    $\alpha \leftarrow \rho\, \alpha$
    $x_b \leftarrow \mathbb{P}(\mathbf{x}_\Gamma^k - \alpha\, \mathbf{g}^k)$, $e_b = e(\mathbf{x}_\beta, \mathbf{x}_b)$
  end
  $\alpha_k = \alpha$

  Current shape parameters update
  $\mathbf{x}_\Gamma^{k+1} = \mathbb{P}(\mathbf{x}_\Gamma^k - \alpha_k\, \mathbf{g}_k)$
  $e^{k+1} = e\big(\mathbf{x}_\beta, \mathbf{x}_\Gamma^{k+1}\big)$, $\mathbf{g}^{k+1} = \nabla e\big(\mathbf{x}_\beta, \mathbf{x}_\Gamma^{k+1}\big)$
  $k \leftarrow k + 1$
end

Typically one can choose the following values for the constants: $\epsilon_\Gamma = 10^{-4}$, $\rho = 0.5$ and $c = 10^{-4}$. The projection operator is given in section 3.3.2.2.

D.1 Loop detection algorithm

Finally, we give a straightforward method used to ensure that the curve defining the shape is injective. Mostly this method aims at detecting loops.

From the current vector of shape parameters $\mathbf{x}_\Gamma$, one can extract the current set of control nodes $(\mathbf{x}^{(0)}, ..., \mathbf{x}^{(N)})$. Then one can state the whole curve Γ obtained after linear interpolation is injective if every pair of distinct elements do not cross. More specifically, given two indexes i and j with $|j - i| > 1$ (which means the elements do not follow each other), we consider the two segments $[\mathbf{x}^{(i)}, \mathbf{x}^{(i+1)}]$ and $[\mathbf{x}^{(j)}, \mathbf{x}^{(j+1)}]$. One can calculate the determinant of the two vectors as:

$$d_{ij} = \Delta x_2^{(i)}\, \Delta x_1^{(j)} - \Delta x_1^{(i)}\, \Delta x_2^{(j)} \qquad \text{with} \quad \Delta x_n^{(m)} = x_n^{(m+1)} - x_n^{(m)}$$

Assuming d_{ij} is non zero, which means the two elements are non parallel, one can determine the intersection between the two lines emanating from each segment. Those two lines, referred to as l_i and l_j, can be parametrized as:

$$l_i = \{\mathbf{x}^{(i)} + t\,(\mathbf{x}^{(i+1)} - \mathbf{x}^{(i)}) \quad : \quad t \in \mathbb{R}\} \qquad ; \qquad l_j = \{\mathbf{x}^{(j)} + u\,(\mathbf{x}^{(j+1)} - \mathbf{x}^{(j)}) \quad : \quad u \in \mathbb{R}\}$$

The parameters corresponding to the intersection point are given by:

$$t_{ij} = \frac{1}{d_{ij}} \Big(-\Delta_2^{(j)}\, (x_1^{(j)} - x_1^{(i)}) + \Delta_1^{(j)}\, (x_2^{(j)} - x_2^{(j)})\Big)$$
$$u_{ij} = \frac{1}{d_{ij}} \Big(-\Delta_2^{(i)}\, (x_1^{(j)} - x_1^{(j)}) + \Delta_1^{(i)}\, (x_2^{(j)} - x_2^{(i)})\Big)$$

Finally, one can state that the two elements do not cross each other if t_{ij} and u_{ij} are not in

the segment $[0,1]$. Otherwise, if both parameters were in that segment, it would mean the intersection would belong to both elements, which would precisely correspond to a loop. If such a loop is detected, the injectivity test called in the backtracking algorithm returns a false value.

The case of following elements - meaning $j = i+1$ - can be treated as well, by ensuring $t_{i,i+1}$ does not belong to $[0,1)$ and $u_{i,i+1}$ does not belong to $(0,1]$.

Finally, the case of parallel elements can be treated as well quite easily, by either ensuring a finite distance between l_i and l_j, or by making sure two elements do not overlap.

E Shape derivative of a boundary integral defined on a piecewise smooth curve

In this section we derive the formula given in equation (4.12). Following the notations introduced above, the functional G can then be written as:

$$G = \sum_{i=1}^{N} \int_{\Gamma_i} f \,\mathrm{d}\Gamma = \sum_{i=1}^{N} \int_0^1 f(\mathbf{x}_i(t))\, J_i(t)\,\mathrm{d}t$$

where $\mathbf{x}_i$ is a smooth map of each part Γ_i parametrized by $t \in [0,1]$ and $J_i = \sqrt{x_{i1}'^2 + x_{i2}'^2}$ is the Jacobian. The derivative applied to the velocity field $\boldsymbol{\theta}(t) = \big(\theta_1(t), \theta_2(t)\big)$ on each part Γ_i is given by:

$$\frac{\partial}{\partial\Gamma}\left[\int_0^1 f(\mathbf{x}_i)\, J_i \,\mathrm{d}t\right]\cdot\boldsymbol{\theta} = \int_0^1 \boldsymbol{\nabla} f\cdot\boldsymbol{\theta}\, J_i \,\mathrm{d}t + \int_0^1 f\,\frac{\mathbf{x}_i'\cdot\boldsymbol{\theta}'}{J_i}\,\mathrm{d}t$$

Since $\boldsymbol{\theta}$ and $\mathbf{x}_i$ are smooth on Γ_i, one can use an integration by parts on the second integral to remove the derivative on $\boldsymbol{\theta}$:

$$\frac{\partial}{\partial\Gamma}\left[\int_0^1 f(\mathbf{x}_i)\, J_i \,\mathrm{d}t\right]\cdot\boldsymbol{\theta} = \left[f\,\frac{\mathbf{x}_i'\cdot\boldsymbol{\theta}}{J_i}\right]_0^1 + \int_0^1 \left(\boldsymbol{\nabla} f\cdot\boldsymbol{\theta}\, J_i - \boldsymbol{\nabla} f\cdot\mathbf{x}_i'\,\frac{\mathbf{x}_i'\cdot\boldsymbol{\theta}}{J_i} - f\,\frac{\mathbf{x}_i''\cdot\boldsymbol{\theta}}{J_i} + f\,\frac{(\mathbf{x}_i'\cdot\boldsymbol{\theta})(\mathbf{x}_i''\cdot\mathbf{x}_i')}{J_i^3}\right)\mathrm{d}t$$

Now, on each part Γ_i one can define the tangent vector $\mathbf{t}_i = \mathbf{x}_i'/J_i$ and the normal vector $\mathbf{n_i}$ as the orthogonal vector to $\mathbf{t}_i$ pointing inside Ω so that $\boldsymbol{\theta}$ can be written on Γ_i as $\boldsymbol{\theta} = \theta_n\,\mathbf{n}_i + \theta_t\,\mathbf{t}_i$. By definition of $\mathbf{n}_i$ and $\mathbf{t}_i$, we have $\mathbf{x}_i'\cdot\boldsymbol{\theta} = \theta_t\, J_i$. Besides, the curvature H can be written in terms of the map $\mathbf{x}_i$ as :

$$H = -\frac{\mathbf{x}_i''\cdot\mathbf{n}_i}{J_i^2} = \frac{\det[\mathbf{x}_i', \mathbf{x}_i'']}{J_i^3}$$

Making this substitution in the expression of the sensitivity and simplifying yields:

$$\frac{\partial}{\partial\Gamma}\left[\int_0^1 f(\mathbf{x}_i)\, J_i \,\mathrm{d}t\right]\cdot\boldsymbol{\theta} = \int_0^1 \Big(\frac{\partial f}{\partial n} + Hf\Big)\theta_n\, J_i \,\mathrm{d}t + [f\theta_t]_0^1 = \int_{\Gamma_i} \Big(\frac{\partial f}{\partial n} + Hf\Big)\theta_n \,\mathrm{d}\Gamma + [f\theta_t]_{\Gamma_i}$$

where $[.]_{\Gamma_i}$ is the difference between the end and start values of a function on Γ_i. Now, by summing over all smooth parts, one can see that we recover the expression for a smooth curve

Γ, plus an extra term related to the jumps at the ends of each smooth part. This yields:

$$\frac{\partial G}{\partial \Gamma} \cdot \boldsymbol{\theta} = \int_\Gamma \Big(\frac{\partial f}{\partial n} + Hf \Big) \theta_n \, \mathrm{d}\Gamma - \sum_{i=1}^{N-1} [\![f\theta_t]\!]^{(i)} + (f\theta_t)^{(N)} - (f\theta_t)^{(0)}$$

where $[\![.]\!]^{(i)}$ is the jump of a function at the point $\mathbf{x}^{(i)}$, defined as the limiting value after the jump minus the limiting value before the jump.

F Derivatives of considered admittance models with respect to the parameters

In order to compute the sensitivity of the pressure field with respect to changes in the admittance parameters, we also need to compute the derivatives of the admittance function with respect to each parameter. Recalling equation (1.5), for the MPPR model, this yields:

$$\begin{aligned}
\frac{\partial \beta_{\mathrm{MPPR}}}{\partial s} =& - \mathrm{i}\, \beta_{\mathrm{MPPR}}^2 \left[\frac{k l_0}{s^2} \left(\frac{1}{\Theta(x')} + \frac{16}{3\pi} \frac{a_0}{l_0} \frac{\Psi(\xi)}{\Theta(x)} \right) - \frac{k a_0}{s} \frac{16}{3\pi} \frac{\Psi'(\xi)}{2\xi\, \Theta(x)} \right] \\
\frac{\partial \beta_{\mathrm{MPPR}}}{\partial a_0} =& \mathrm{i}\, \beta_{\mathrm{MPPR}}^2 \frac{k l_0}{s} \left[-\frac{x'}{a_0} \frac{\Theta'(x')}{\Theta(x')^2} + \frac{16}{3\pi} \frac{\Psi(\xi)}{l_0} \left(\frac{1}{\Theta(x')} - \frac{\Theta'(x)\, x}{\Theta(x)^2} \right) \right] \\
\frac{\partial \beta_{\mathrm{MPPR}}}{\partial l_0} =& \mathrm{i} \frac{k}{s} \beta_{\mathrm{MPPR}}^2 \frac{1}{\Theta(x')} \\
\frac{\partial \beta_{\mathrm{MPPR}}}{\partial d} =& \frac{\mathrm{i}k}{\sin^2(kd)} \beta_{\mathrm{MPPR}}(f)^2
\end{aligned}$$

where the derivatives of the two functions Θ and Ψ given by:

$$\begin{aligned}
\Psi'(\xi) =& \sum_{m=1}^{8} m\, u_m\, \xi^{m-1} \\
\Theta'(w) =& \frac{2}{w} \left(\frac{J_2(w\sqrt{\mathrm{i}})}{J_0(w\sqrt{\mathrm{i}})} - \frac{J_1(w\sqrt{\mathrm{i}})^2}{J_0(w\sqrt{\mathrm{i}})^2} \right)
\end{aligned}$$

For the rigid-backed Delany & Bazley model, recalling equations (1.3) and (1.2), we have:

$$\begin{aligned}
\frac{\partial \beta_{\mathrm{DBL}}}{\partial \sigma} =& - \beta_{\mathrm{DBL}}^2 \left[\coth(-\mathrm{i}k_{\mathrm{DB}}d) \left(0.75 \times 0.0511 \frac{1}{f} \left(\frac{\sigma}{f} \right)^{0.75-1} + \mathrm{i}\, 0.73 \times 0.0768 \frac{1}{f} \left(\frac{\sigma}{f} \right)^{0.73-1} \right) \right. \\
& \left. + z_{\mathrm{DB}} \frac{\mathrm{i}k_0 d}{\sinh^2(-\mathrm{i}k_{\mathrm{DB}}d)} \frac{1}{f} \left(1 + 0.7 \times 0.0858 \left(\frac{\sigma}{f} \right)^{0.7-1} + \mathrm{i}\, 0.59 \times 0.175 \left(\frac{\sigma}{f} \right)^{0.59-1} \right) \right] \\
\frac{\partial \beta_{\mathrm{DBL}}}{\partial d} =& - \beta_{\mathrm{DBL}}^2 \frac{\mathrm{i}z_{\mathrm{DB}}\, k_{\mathrm{DB}}}{\sinh^2(-\mathrm{i}k_{\mathrm{DB}}d)}
\end{aligned}$$

G Shape smoothing algorithm

We here give the details of the shape smoothing algorithm used in chapter 5 to test the effect of irregularities on the performance of a shape.

We consider a set of $N+1$ nodes $\mathbf{x}^{(i)} = (x_1^{(i)}, x_2^{(i)})$, $i \in [0:N]$, and it is assumed that the initial and last nodes lie on the ground (with means $x_2^{(0)} = 0$ and $x_2^{(N)} = 0$). One can first of all define the symmetrical shape with respect to the ground, and therefore consider two vectors of coordinates X_1 and X_2 as follows:

$$\begin{cases} X_1 = (x_1^{(0)}, x_1^{(1)}, ..., x_1^{(N-1)}, x_1^{(N)}, x_1^{(N-1)}, ..., x_1^{(1)}) \\ X_2 = (x_2^{(0)} = 0, x_2^{(1)}, ..., x_2^{(N-1)}, x_2^{(N)} = 0, -x_2^{(N-1)}, ..., -x_2^{(1)}) \end{cases}$$

The original shape and its image have hence $2N$ nodes. Those two vectors represent periodic functions and are therefore well-suited for Fourier analysis. The smoothing will indeed simply consist in low-pass filtering the two vectors of coordinates in the spatial frequency domain. However, the definition of the Fourier transform of a discrete signal usually assumes that the spacing between the different samples is constant. If one describes the coordinates as a function of the curvilinear coordinate, this is not true (the spacing between following points corresponding to the length of each element, which is in general not constant). One can however approximate the actual vector of curvilinear coordinate by a uniformly spaced vector. To do so, first let us define the curvilinear coordinate of each node s_i (calculated on the original shape only for now) recursively as follows:

$$\begin{cases} s_0 = 0 \\ (\forall i \in [1:N]) \quad s_i = s_{i-1} + l_i \qquad \text{with} \quad l_i = ||\mathbf{x}^{(i)} - \mathbf{x}^{(i-1)}|| \end{cases}$$

The approximate curvilinear coordinate defined on the shape and its image is then simply taken as:

$$(\forall i \in [0:2N-1]) \quad \tilde{s}_i = i\,\Delta s \qquad \text{with} \quad \Delta s = \frac{s_N}{N}$$

Δs is the approximate spacing of the coordinates vectors. One can then define a sampling spatial frequency as $k_s = 1/\Delta s$ and a set of spatial frequencies:

$$(\forall m \in [0:2N-1]) \quad k_m = m\,\frac{k_s}{2N}$$

The approximate spatial spectrum Y_1 and Y_2 of each coordinate vector is calculated by:

$$(\forall m \in [0:2N-1]) \quad \begin{cases} Y_{1,m} = \sum_{n=0}^{2N-1} x_1^{(n)}\, e^{-2\mathrm{i}\pi mn/(2N)}\, \Delta s \\ Y_{2,m} = \sum_{n=0}^{2N-1} x_2^{(n)}\, e^{-2\mathrm{i}\pi mn/(2N)}\, \Delta s \end{cases}$$

Those expressions can be evaluated by classical FFT algorithms.

Smoothing the original shape can be achieved by applying a filter on the spectrum coordinates. Let us assume that one would want to smooth the geometrical details of size typically smaller than a characteristic length l. This can be done by low-pass filtering the coordinate spectra up to $k_l = 1/l$ - the spatial frequency corresponding to the maximum detail size - by multiplying Y_1 and Y_2 by a window function of value 1 up to for instance $0.9\,k_l$, a taper function decreasing from 1 to 0 between $0.9\,k_l$ and k_l and 0 above. The taper is used to avoid non physical oscillations that could happen with an abrupt change. The window should also be symmetrical about $k_s/2$ in order to keep the symmetry of the spectrum. An example is given in figure A.1.

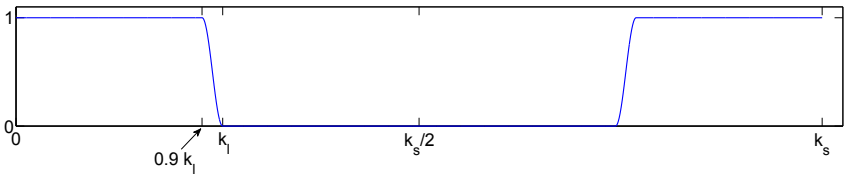

Figure A.1: Example of window function used in the shape smoothing low-pass filter, expressed as a function of spatial frequency k and for a signal sampled at k_s. The cut-off frequency is $k_l = 1/l$ with l is the characteristic filtering size.

Multiplying the two spectra by the window functions yields two new spectra Y_{1f} and Y_{2f}, and by taking the inverse Fourier transform one obtains two new sets of coordinates X_{1f} and X_{2f}. The generated shape is still symmetrical with respect to the ground and therefore one should keep only the first N generated points.

An example of this process with different values of the low-pass characteristic length l is shown in figure A.2.

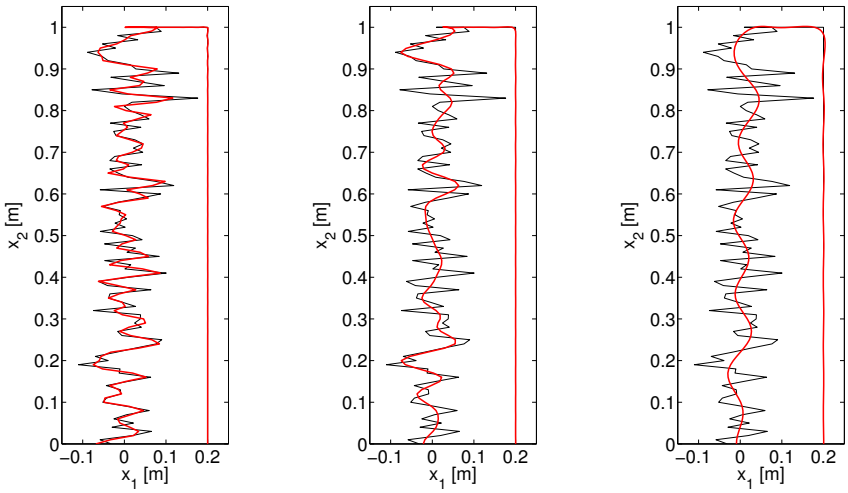

Figure A.2: Example of smoothed versions of a randomly generated shape for different low-pass characteristic lengths. The think black line is the original shape and the thick red line is the smoothed shape. Left: $l = 0.1\,\mathrm{m}$ - middle: $l = 0.2\,\mathrm{m}$ - right: $l = 0.5\,\mathrm{m}$.

H Uncertainty evaluation of linear regression parameters

We briefly review here some results of linear regression analysis that were used in chapter 8 to estimate linear dependence coefficients as well as their uncertainties. All the results given in this section are rather standard and can be found for instance in a set of lecture notes [195].

We consider a set of n points of coordinates (x_i, y_i) and we assume the variable y can be described approximately as a linear function of x of the form: $y = ax + b$. We wish to find the most appropriate values of a and b as well as the corresponding uncertainties.

Let $\bar{x}$ and $\bar{y}$ the mean value of x and y, and σ_x and σ_y their standard deviation:

$$\bar{x} = \frac{1}{n}\sum_i x_i \quad , \quad \bar{y} = \frac{1}{n}\sum_i y_i$$
$$\sigma_x^2 = \frac{1}{n}\sum_i (x_i - \bar{x})^2 \quad , \quad \sigma_y^2 = \frac{1}{n}\sum_i (y_i - \bar{y})^2$$

It is well-known that the value of a and b which minimize the squared error between y and $ax+b$ are given by:

$$\begin{cases} a = \dfrac{1}{n\,\sigma_x^2}\displaystyle\sum_i (x_i - \bar{x})(y_i - \bar{y}) \\ b = \bar{y} - a\bar{x} \end{cases}$$

The regression coefficient is given by:

$$r^2 = a\,\frac{\sigma_x}{\sigma_y}$$

Now define the standard error of the residuals S as:

$$S^2 = \frac{1}{n-2}\sum_i (y_i - ax_i - b)^2$$

The standard error e_a and e_b on the regression coefficient a and b can be then calculated as follows:

$$e_a = \frac{a}{\sqrt{n-2}}\sqrt{\frac{1}{r^2} - 1} \qquad e_b = S\sqrt{\frac{1}{n} + \frac{\bar{x}^2}{n\sigma_x^2}}$$

Confidence intervals for a and b can then be taken as $[a - \alpha e_a, a + \alpha e_a]$ and $[b - \alpha e_b, b + \alpha e_b]$, with α a coefficient related to the level of confidence of the interval and the number of points n. αe_a and αe_b are therefore the uncertainties of the regression coefficients a and b. Typically, when assuming normally distributed independent residuals and for a sufficient large value of n (typically greater than 10), taking $\alpha = 1$ yields a level of confidence of about 65%, and $\alpha = 2$ a level above 90%. In this work, for simplicity the uncertainty is evaluated to be the standard error (which means α is taken to be equal to 1), hence the considered confidence level is about 65%.

References

[1] Jolibois, A. (2013) *A sensitivity-based approach to optimize the surface treatment of a low-height tramway noise barrier*, Ph.D. thesis, The Pennsylvania State University (University Park, PA, USA). 2, 17, 18, 57, 68, 110

[2] "World Health Organization, Regional Office for Europe website," .
URL `http://www.euro.who.int/en/health-topics/environment-and-health/noise/data-and-statistics` 5

[3] *Burden of disease from environmental noise*, *Tech. rep.*, World Health Organization, Regional office for Europe and the European Commission.
URL `http://www.euro.who.int/__data/assets/pdf_file/0008/136466/e94888.pdf` 5

[4] Baulac, M. (2006) *Optimisation des Protections Anti-bruit Routières de Forme Complexe (Optimization of Complex Traffic Noise Barriers)*, Ph.D. thesis, Université du Maine (Le Mans, France). 7, 22, 44, 55, 61, 109

[5] Baulac, M., J. Defrance, P. Jean, and F. Minard (2006) "Efficiency of noise protections in urban areas: prediction and scale model measurements," *Acta Acust. united Ac.*, **92**, pp. 530–539. 22, 111, 112, 113, 121

[6] Baulac, M., J. Defrance, and P. Jean "Optimization of low height noise protections in urban areas," in *Forum Acousticum 2005, Budapest, Hungary*, pp. 1075–1080. 22, 55, 109

[7] Baulac, M., A. Guillou, J. Defrance, and P. Jean (2008) "Calculations of low height noise barriers efficiency by using Boundary Element Method and optimisation algorithms," in *Proc. Acoustics'08, Paris, France*.

[8] Horoshenkov, K., D. C. Hothersall, and S. E. Mercy (1999) "Scale modelling of sound propagation in a city street canyon," *J. Sound Vib.*, **223**(5), pp. 795–819. 15, 22

[9] Thorsson, P. J. (2000) "Optimisation of low-height noise barriers using the equivalent sources method," *Acta Acust.*, **86**, pp. 811–820. 22, 55

[10] ——— (2003) "Combined effects of admittance optimisation on both barrier and ground," *Appl. Acoust.*, **64**, pp. 693–711. 22, 55, 85, 88

[11] Koussa, F. (2012) *Evaluation de la performance acoustique des protections antibruit innovantes utilisant des moyens naturels : application aux transports terrestres (Evaluation of the acoustic efficiency of innovative noise barriers using natural means: application to ground transportation systems)*, Ph.D. thesis, Ecole Centrale de Lyon (Lyon, France). 22, 23, 55, 61, 109, 112, 114

[12] Koussa, J., J. Defrance, P. Jean, and P. Blanc-Benon (2012) "Transport noise reduction by low height sonic crystal noise barriers," in *Proc. Acoustics 2012, Nantes, France*. 23

[13] Koussa, F., J. Defrance, P. Jean, and P. Blanc-Benon (2013) "Acoustic performance of gabions noise barriers: numerical and experimental approaches," *Appl. Acoust.*, pp. 189–197. 23, 109

[14] Ding, L., T. Van Renterghem, and D. Botteldooren (2011) "Estimating the effect of semi-transparent low-height road traffic noise barriers with ultra weak formulation," *Acta Acust. united Ac.*, **97**, pp. 391–402. 22

[15] Fernandez, P., I. Diez, J. L. Eguiguren, and I. Aspuru (2013) "Noise barriers customized to abate non conventional noise sources," in *Proc. Internoise 2013, Innsbruck, Austria.* 7

[16] Defrance, J., P. Jean, F. Koussa, L. T., K. Attenborough, S. Taherzadeh, D. Botteldooren, T. Van Renterghem, K. Horoshenkov, A. Khan, H. Bemkreira, J. Forssén, J. Kang, J. Mandon, and A. Rohr (2010) *Innovative barriers exploiting natural materials: state of the art of experience and models*, *Deliverable 2.1*, Collaborative Project HOSANNA (FP7/2007-2013 grant agreement n 234306). 7

[17] Defrance, J., K. Attenborough, K. Horoshenkov, F. Koussa, P. Jean, and T. Van Renterghem (2011) *Innovative barriers exploiting natural materials: choice and adaptation of models*, *Deliverable 2.2*, Collaborative Project HOSANNA (FP7/2007-2013 grant agreement n 234306).

[18] Defrance, J., P. Jean, F. Koussa, K. Horoshenkov, A. Khan, H. Benkreira, T. Van Renterghem, J. Kang, J. Smyrnowa, and J. Forssén (2013) *Innovative barriers exploiting natural materials: application to innovations*, *Deliverable 2.3*, Collaborative Project HOSANNA (FP7/2007-2013 grant agreement n 234306).

[19] Defrance, J., P. Jean, F. Koussa, K. Horoshenkov, A. Khan, H. Benkreira, T. Van Renterghem, J. Kang, and J. Smyrnowa (2013) *Innovative barriers exploiting natural materials: analysis and recommendations*, *Deliverable 2.4*, Collaborative Project HOSANNA (FP7/2007-2013 grant agreement n 234306). 7

[20] Rylander, R., Björkman, U. Åhrlin, and S. Sörensen (1977) "Tram noise in city traffic," *J. Sound Vib.*, **51**(3), pp. 353–358. 7

[21] Wijnia, Y. K. (1988) "Noise emission from trams," *J. Sound Vib.*, **120**(2), pp. 281–286.

[22] Miedama, H. M. E. and R. Van den Berg (1988) "Community response to tramway noise," *J. Sound Vib.*, **120**(2), pp. 341–346. 7

[23] Mandula, J., B. Salaioá, and M. Koval'aková (2002) "Prediction of noise from trams," *Appl. Acoust.*, **63**, pp. 373–389. 7

[24] Philipps-Bertin, C., P. Champelovier, C. Trindade, and J. Lambert (2006) *Caractérisation des sources et évaluation de la perception du bruit et des vibrations des tramways (Source identification and perception evaluation of tramway noise and vibrations)*, *Tech. rep.*, INRETS-LTE (ADEME grant number 04.03.C0053). 7

[25] Pallas, M.-A., J. Lelong, and R. Chatagnon (2008) "Tram noise emission: spectral analysis of the noise source contribution," in *Proc. Acoustics'08, Paris, France.*

[26] Pallas, M. A., J. Lelong, and R. Chatagnon (2011) "Characterization of tram noise emission and contribution of the noise sources," *Appl. Acoust.*, **72**, pp. 437–450. 7, 59, 85, 89, 127, 128, 132, 136, 142

[27] Sandrock, S., B. Griefahn, T. Kaczmarek, H. Hafke, A. Preis, and T. Gjestland (2008) "Experimental studies of annoyance causes by noises from trams and buses," *J. Sound Vib.*, **313**, pp. 908–919. 7

[28] Duhamel, D. (1996) "Efficient calculation of the three-dimensional sound pressure field around a noise barrier," *J. Sound Vib.*, **197**(5), pp. 547–571. 10, 40, 41, 60, 88, 89

[29] Van Renterghem, T., E. M. Salomons, and D. Botteldooren (2005) "Efficient FDTD-PE model for sound propagation in situations with complex obstacles and wind profiles," *Acta Acust. united Ac.*, **91**, pp. 671–679. 10, 17

[30] Kaseloo, P. A. and K. O. Tyson *Synthesis of Noise Effects on Wildlife Populations*, *Tech. rep.*, US Department of Transportation, Federal Highway Administration. 12

[31] Hanson, C. E. (2008) "High Speed Train Noise Effects on Wildlife and Domestic Livestock," in *Noise and Vibration Mitigation for Rail Transportation Systems*, vol. 99, Springer Berlin Heidelberg, pp. 26–32. 12

[32] Fields, J. M. and J. G. Walker (1982) "Comparing the relationship between noise levels and annoyance in different surveys: a railway noise vs. aircraft and road traffic comparison," *J. Sound Vib.*, **81**(1), pp. 51–80. 12

[33] Öhrström, E. (1991) "Psycho-social effects of traffic noise exposure," *J. Sound Vib.*, **151**(3), pp. 513–517. 12

[34] Ouis, D. (2001) "Annoyance from road traffic noise: a review," *J. Environ. Psychol.*, **21**, pp. 101–120. 12

[35] Öhrström, E. and R. Rylander (1982) "Sleep disturbance effects of traffic noise - a laboratory study on after-effects," *J. Sound Vib.*, **84**(1), pp. 87–103. 12

[36] Carter, N. L. (1996) "Transportation noise, sleep and possible after-effects," *Environ. Int.*, **22**(1), pp. 105–116. 12

[37] Hong, J., J. Kim, C. Lim, K. Kim, and S. Lee (2010) "The effects of long-term exposure to railway and road traffic noise on subjective sleep disturbance," *J. Acoust. Soc. Am.*, **128**(8), pp. 2829–2835. 12

[38] Attenborough, K., K. M. Li, and K. Horoshenkov (2007) *Predicting outdoor sound*, Taylor and Francis. 13, 14, 121

[39] Salomons, E. M. (2001) *Computational atmospheric acoustics*, Springer. 13, 17

[40] Embleton, T. F. W. (1996) "Tutorial on sound propagation outdoors," *J. Acoust. Soc. Am.*, **100**(1), pp. 31–48. 13, 14

[41] Scholes, W. E., A. C. Salvidge, and J. W. Sargent (1971) "Field performance of a noise barrier," *J. Sound Vib.*, **16**(4), pp. 627–642. 13, 109

[42] Rasmussen, K. B. (1996) "Sound propagation over screened ground under upwind conditions," *J. Acoust. Soc. Am.*, **100**(6), pp. 3581–3586. 13, 109

[43] Barrière, N. and Y. Gabillet (1999) "Sound propagation over a barrier with realistic wind gradients. Comparison of wind tunnel experiments with GFPE computations," *Acta Acust. united Ac.*, **85**, pp. 325–334. 13, 109

[44] Salomons, E. M. (1999) "Reduction of the performance of a noise screen due to screen-induced wind-speed gradients. Numerical computations and wind-tunnel experiments," *J. Acoust. Soc. Am.*, **105**(4), pp. 2287–2293. 13

[45] Salomons, E. M. and K. B. Rasmussen (2000) "Numerical computation of sound propagation over a noise screen based on an analytic approximation of the wind speed field," *Appl. Acoust.*, **60**, pp. 327–341. 13

[46] Daigle, G. A. (1982) "Diffraction of sound by a noise barrier in the presence of atmospheric turbulence," *J. Acoust. Soc. Am.*, **71**(4), pp. 847–854. 13

[47] Forssén, J. (1998) "Calculation of sound reduction by a screen in a turbulent atmosphere using the parabolic equation method," *Acta Acust. united Ac.*, **84**, pp. 599–606. 13

[48] Forssén, J. and M. Ögren (2002) "Thick barrier noise-reduction in the presence of atmospheric turbulence: measurements and numerical modelling," *Appl. Acoust.*, **63**, pp. 173–187.

[49] Wilson, D. K., V. E. Ostashev, G. H. Goedecke, and H. J. Auvermann (2004) "Quasi-wavelet calculations of sound scattering behind barriers," *Appl. Acoust.*, **65**, pp. 605–627. 13

[50] Attenborough, K., I. Bashir, and S. Taherzadeh (2011) "Outdoor ground impedance models," *J. Acoust. Soc. Am.*, **129**(5). 14, 18

[51] Rudnick, I. (1947) "The propagation of an acoustic wave along a boundary," *J. Acoust. Soc. Am.*, **19**(2), pp. 348–356. 14

[52] ——— (1948) "Erratum: The propagation of an acoustics wave along a boundary," *J. Acoust. Soc. Am.*, **20**(2), pp. 149–149.

[53] Chien, C. F. and W. W. Soroka (1975) "Sound propagation along an impedance plane," *J. Sound Vib.*, **43**(1), pp. 9–20.

[54] Nobile, M. A. and S. I. Hayek (1985) "Acoustic propagation above an impedance plane," *J. Acoust. Soc. Am.*, **78**(4), pp. 1325–1336. 14

[55] Weyl, H. (1919) "Ausbreitung elektromagnetischer wellen über einem ebenen Leiter (propagation of electromagnetic waves over a flat conductor)," *Ann. Phys. - Berlin*, **60**, pp. 481–500. 14

[56] Van der Pol, B. and K. F. Niessen (1930) "Über die Ausbreitung elektromagnetischer Wellen über eine ebene Erde (on the propagation of electromagnetic waves over a flat ground)," *Ann. Phys. - Berlin*, **6**, pp. 273–294. 14

[57] Jonasson, H. G. (1972) "Sound reduction by barriers on the ground," *J. Sound Vib.*, **22**(1), pp. 113–126. 14, 16

[58] Isei, T., T. F. W. Embleton, and J. E. Piercy (1980) "Noise reduction by barriers on finite impedance ground," *J. Acoust. Soc. Am.*, **67**(1), pp. 46–58. 14

[59] Hutchins, D. A., H. W. Jones, and L. T. Russell (1984) "Model studies of barrier performance in the presence of ground surfaces. Part I - thin, perfectly reflecting barriers," *J. Acoust. Soc. Am.*, **75**(6), pp. 1807–1816. 14, 85, 87

[60] ——— (1984) "Model studies of barrier performance in the presence of ground surfaces. Part II - different shapes," *J. Acoust. Soc. Am.*, **75**(6), pp. 1817–1826. 14, 15

[61] Davies, H. G. (1978) "Multiple-reflection diffuse-scattering model for noise propagation in streets," *J. Acoust. Soc. Am.*, **64**(2), pp. 517–521. 15

[62] Kang, J. (1999) "Sound propagation in street canyons: comparison between diffusely and geometrically reflecting boundaries," *J. Acoust. Soc. Am.*, **107**(3), pp. 1394–1404. 15

[63] Li, K. M. and S. H. Tang (2003) "The predicted barrier effects in the proximity of tall buildings," *J. Acoust. Soc. Am.*, **114**(2), pp. 821–832. 15

[64] Li, K. M., M. P. Pwok, and M. K. Law (2008) "A ray model for hard parallel noise barriers in high-rise cities," *J. Acoust. Soc. Am.*, **123**(1), pp. 121–132. 15

[65] Li, K. M., M. K. Law, and M. P. Kwok (2008) "Absorbent parallel noise barriers in urban environments," *J. Sound Vib.*, **315**, pp. 239–257. 15

[66] May, D. N. and M. M. Osman (1980) "The performance of sound absorptive, reflective and T-profile noise barriers in Toronto," *J. Sound Vib.*, **71**(1), pp. 65–71. 15, 21

[67] Watts, G. R., D. H. Crombie, and D. C. Hothersall (1994) "Acoustic performance of new designs of traffic noise barriers: full scale tests," *J. Sound Vib.*, **177**(3), pp. 289–305. 15, 21, 109

[68] Morgan, P. A., D. C. Hothersall, and S. N. Chandler-Wilde (1998) "Influence of shape and absorbing surface - a numerical study of railway noise barriers," *J. Sound Vib.*, **217**(3), pp. 405–417. 15, 16

[69] Sommerfeld, A. (1896) "Mathematische Theorie der Diffraction (geometrical theory of diffraction)," *Mathematische Annalen*, **47**(2-3), pp. 317–374. 16

[70] MacDonald, H. M. (1915) "A class of diffraction problems," *P. Lond. Math. Soc.*, **14**, pp. 410–427. 16

[71] Keller, J. B. (1962) "Geometrical theory of diffraction," *J. Opt. Soc. Am.*, **52**(2), pp. 116–130. 16

[72] Pierce, A. D. (1974) "Diffraction of sound around corners and over wide barriers," *J. Acoust. Soc. Am.*, **55**(5), pp. 941–955. 16

[73] Pierce, A. D. and W. J. Hadden, Jr. (1978) "Plane wave diffraction by a wedge with finite impedance," *J. Acoust. Soc. Am.*, **63**(1), pp. 17–27. 16

[74] Rasmussen, K. B. (1985) "On the effect of terrain profile on sound propagation outdoors," *J. Sound Vib.*, **98**(1), pp. 35–44. 16

[75] Haek, S. I. (1990) "Mathematical modeling of absorbent highway noise barriers," *Appl. Acoust.*, **31**, pp. 77–100.

[76] De Jong, B. A., A. Moerkerken, and J. D. Van der Toorn (1983) "Propagation of sound over grassland and over and earth barrier," *J. Sound Vib.*, **86**(1), pp. 23–46. 16

[77] Medwin, H. (1981) "Shadowing by finite noise barriers," *J. Acoust. Soc. Am.*, **69**(4), pp. 1060–1064. 16

[78] Lam, Y. W. and C. Roberts (1993) "A simple method for accurate prediction of finite barrier insertion loss," *J. Acoust. Soc. Am.*, **93**(3), pp. 1445–1452. 16

[79] Maekawa, Z. (1968) "Noise reduction by screens," *Appl. Acoust.*, **1**(3), pp. 157–173. 16

[80] Kurze, U. J. and G. S. Anderson (1971) "Sound attenuation by barriers," *Appl. Acoust.*, **4**, pp. 35–53. 16

[81] Menounou, P. (2001) "A correction to Maekawa's curve for the insertion loss behind barriers," *J. Acoust. Soc. Am.*, **110**(4), pp. 1828–1838. 16, 109, 112

[82] Defrance, J., E. Salomons, I. Noordhoek, D. Heimann, B. Lovsing, G. Watts, H. Jonasson, X. Zhang, E. Premat, I. Schmich, F. Aballea, M. Baulac, and F. de Roo (2007) "Outdoor sound propagation reference model developed in the European Harmonoise project," *Acta Acust. united Ac.*, **93**, pp. 213–227. 17

[83] Pierce, A. D. (1989) *Acoustics: an introduction to its physical principles and applications*, Acoustical Society of America. 17

[84] Poulain, K. (2011) *Numerical propagation of aircraft en-route noise*, Master's thesis, The Pennsylvania State University (University Park, PA, USA). 17

[85] Gilbert, K. E. and M. J. White (1989) "Application of the parabolic equation to sound propagation in a refracting atmosphere," *J. Acoust. Soc. Am.*, **85**(2), pp. 630–637. 17

[86] Gilbert, K. E. (1993) "A fast Green's function method for one-way sound propagation in the atmosphere," *J. Acoust. Soc. Am.*, **94**(4), pp. 2343–2352. 17

[87] Aballéa, F.-E. (2004) *Propagation acoustique en milieu extérieur : application de l'équation parabolique rapide au couplage d'effets météorologiques et de topographies complexes (Outdoor sound propagation: application of the fast parabolic equation method to the coupling of meteorological and complex terrain effects)*, Ph.D. thesis, Université du Maine (Le Mans, France). 17

[88] Aballéa, F.-E. and J. Defrance (2007) "Single and multiple reflections in plane obstacle using the parabolic equation method with a complementary Kirchhoff approximation," *Acta Acust. united Ac.*, **93**, pp. 22–30. 17

[89] Van Renterghem, T. (2003) *De eindige-differenties-in-het-tidjsdomein-methode voor de simulatie van geluidspropagatie in een bewegend medium (the finite-difference time-domain method for simulation of sound propagation in a moving medium)*, Ph.D. thesis, Ghent University (Belgium). 17

[90] Van Renterghem, T. and D. Botteldooren (2007) "Prediction-step staggered-in-time FDTD: an efficient numerical scheme to solve the linearised equations of fluid dynamics in outdoor sound propagation," *Appl. Acoust.*, **68**, pp. 201–216. 17

[91] Premat, E. (2000) *Prise en compte d'effets météorologiques dans une méthode d'éléments finis de frontière (consideration of meteorological effects in a boundary element method)*, Ph.D. thesis, Institut National des Sciences Appliquées de Lyon (Lyon, France). 17

[92] Premat, E. and Y. Gabillet (2000) "A new boundary-element method for predicting outdoor sound propagation and application to the case of a sound barrier in the presence of downward refraction," *J. Acoust. Soc. Am.*, **108**(6), pp. 2775–2783. 17

[93] Coifman, R., V. Rokhlin, and S. Wandzura (1993) "The fast multipole method for the wave equation: a pedestrian description," *IEEE Antenn. Propag. M.*, **35**, pp. 7–12. 17

[94] Delany, M. E. and E. N. Bazley (1970) "Acoustical properties of fibrous absorbent materials," *Appl. Acoust.*, **3**, pp. 105–116. 18

[95] Wassilieff, C. (1996) "Sound absorption of wood-based materials," *Appl. Acoust.*, **48**(4), pp. 339–356. 18

[96] Glé, P., E. Gourdon, and L. Arnaud (2011) "Acoustical properties of materials made of vegetable particles with several scales of porosity," *Appl. Acoust.*, **72**, pp. 249–259. 18

[97] ——— (2012) "On the acoustical properties of hemp concrete," in *Proc. Internoise 2012, New York City, NY, USA*. 18

[98] Johnson, D. L., J. Koplik, and R. Dashen (1987) "Theory of dynamic permeability and tortuosity in fluid-saturated porous media," *J. Fluid Mech.*, **176**, pp. 379–402. 18

[99] Zwikker, C. and C. W. Kosten (1949) *Sound absorbing materials*, Elsevier, New York. 18

[100] Asdrubali, F. and G. Pispola (2007) "Properties of transparent sound-absorbing panels for use in noise barriers," *J. Acoust. Soc. Am.*, **121**(1), pp. 214–221. 19

[101] Baulac, M. and J. Defrance (2008) "Optimisation with genetic algorithm of the acoustic performance of T-shaped noise barriers with a reactive top surface," *Appl. Acoust.*, **69**, pp. 332–342. 55

[102] Auerbach, M., A. Bockstedte, O. Zaleski, and O. Von Estorff (2010) "Numerical and experimental investigations of noise barriers with Helmholtz resonators," in *Proc. Noise-Con 2010, Baltimore, MD, USA (joint with the 159th ASA meeting)*. 22, 109

[103] Fujiwara, K., D. C. Hothersall, and C. Kim (1998) "Noise barriers with reactive surfaces," *Appl. Acoust.*, **53**(4), pp. 255–272. 22, 109

[104] Volz, R. (2000) "Headpieces with quarter-wavelength resonators to improve sound barriers - various contours," in *Proc. 7th International Congress on Sound and Vibration, Garmisch-Partenkirchen, Germany*. 22

[105] Monazzam, M. R. and Y. W. Lam (2005) "Performance of profiled single noise barriers covered with quadratic residue diffusers," *Appl. Acoust.*, **66**, pp. 709–730. 22

[106] ——— (2008) "Performance of T-shape barriers with top surface covered with absorptive quadratic residue diffusers," *Appl. Acoust.*, **69**, pp. 93–109. 22

[107] Naderzadeh, M., M. R. Monazzam, P. Nassiri, and S. M. Fard (2011) "Application of perforated sheets to improve the efficiency of reactive profiled noise barriers," *Appl. Acoust.*, **72**, pp. 393–398. 19, 22

[108] Maa, D.-Y. (1975) "Theory and design of microperforated panel sound-absorbing constructions," *Sci. Sinica*, **18**(1), pp. 55–71. 19

[109] ——— (1998) "Potential of microperforated panel absorber," *J. Acoust. Soc. Am.*, **104**(5), pp. 2861–2866.

[110] Melling, T. H. (1975) "The acoustic impedance of perforates at medium and high sound pressure levels," *J. Sound Vib.*, **29**(1), pp. 1–65. 19

[111] Sobolev, A. F. (2007) "A semi-empirical theory of a one-layer cellular sound-absorbing lining with a perforated face panel," *Akusticheskii Zhurnal (Soviet Physics-Acoustics Journal)*, **53**(6), pp. 762–771.

[112] Randeberg, R. T. (2000) *Perforated panel absorbers with viscous energy dissipation enhanced by orifice design*, Ph.D. thesis, Norwegian University of Science and Technology (Trondheim, Norway). 19

[113] Crandall, I. B. (1926) *Theory of vibrating systems and sound*, Van Nostrand. 19

[114] Sivian, L. J. (1935) "Acoustic impedance of small orifices," *J. Acoust. Soc. Am.*, **7**, pp. 94–101. 19

[115] Fok, V. A. (1941) "Teoreticheskoe issledovanie provodimosti kruglogo otverstiya v peregorodke, postavlennoi poperek truby (Theoretical study of the conductance of a circular hole in a partition across a tube)," *Doklady Akademii Nauk SSSR (Soviet Physics Doklady)*, **31**(9), pp. 875–882. 19, 20

[116] Rzhevkin, S. N. (1963) *A course of lectures on the theory of sound*, Pergamon Press, London. 19, 20

[117] Hothersall, D. C., D. H. Crombie, and S. N. Chandler-Wilde (1991) "The performance of T-profile and associated noise barriers," *Appl. Acoust.*, **32**, pp. 269–287. 20

[118] Hothersall, D. C., S. N. Chandler-Wilde, and M. N. Hajmirzae (1991) "Efficiency of single noise barriers," *J. Sound Vib.*, **146**, pp. 303–322. 85, 86

[119] Ishizuka, T. and K. Fujiwara (2004) "Performance of noise barriers with various edge shapes and acoustical conditions," *Appl. Acoust.*, **65**, pp. 125–141. 20, 21

[120] Jean, P. (1998) "A variational approach for the study of outdoor sound propagation and application to railway noise," *J. Sound Vib.*, **212**(2), pp. 275–294. 20, 25, 35, 36, 39, 60

[121] Morgan, P. A., D. C. Hothersall, and S. N. Chandler-Wilde (1998) "Influence of shape and absorbing surface - a numerical study of railway noise barriers," *J. Sound Vib.*, **217**(3), pp. 405–417. 20

[122] May, D. N. and M. M. Osman (1980) "Highway noise barriers: new shapes," *J. Sound Vib.*, **71**(1), pp. 73–101. 20, 21, 109

[123] Hothersall, D. C., K. V. Horoshenkov, P. A. Morgan, and M. J. Swift "Scale modelling of railway noise barriers," *J. Sound Vib.*, **234**(2), pp. 207–223. 20, 109, 112

[124] Watts, G. R. and P. A. Morgan (1996) "Acoustic performance of an interference-type noise-barrier profile," *Appl. Acoust.*, **49**(1), pp. 1–16. 21, 109

[125] Watts, G. R., P. A. Morgan, and M. Surgand (2004) "Assessment of the diffraction efficiency of novel barrier profiles using an MLS-based approach," *J. Sound Vib.*, **274**, pp. 669–683. 21

[126] Ekici, I. and H. Bougdah (2003) "A review of research on environmental noise barriers," *Build. Ac.*, **10**(4), pp. 289–323. 21

[127] Watts, G. R. (1996) "Acoustic performance of a multiple edge noise barrier profile at motorway sites," *Appl. Acoust.*, **47**, pp. 47–66. 21, 109

[128] Baulac, M., J. Defrance, and P. Jean (2007) "Optimization of multiple edge barriers with genetic algorithms coupled with a Nelder-Mead local search," *J. Sound Vib.*, **300**, pp. 71–87. 21, 44, 45, 48, 55

[129] Ho, S. S. T., J. Busch-Vishniac, and D. T. Blackstock (1997) "Noise reduction by a barrier having a random edge profile," *J. Acoust. Soc. Am.*, **101**(5), pp. 2669–2676. 21, 109, 112

[130] Shao, W., H. P. Lee, and S. P. Lim (2001) "Performance of noise barriers with random edge profiles," *Appl. Acoust.*, **62**, pp. 1157–1170.

[131] Menounou, P. and J. H. You (2004) "Experimental study of the diffracted sound field around jagged edge noise barriers," *J. Acoust. Soc. Am.*, **116**(5), pp. 2843–2854. 21

[132] Obuko, T. and K. Fujiwara (1998) "Efficiency of a noise barrier on the ground with an acoustically soft cylindrical edge," *J. Sound Vib.*, **98**(5), pp. 771–790. 21, 55

[133] ——— (1999) "Efficiency of a noise barrier with an acoustically soft cylindrical edge for practical use," *J. Acoust. Soc. Am.*, **105**(6), pp. 3326–3335. 21

[134] Möser, M. and R. Volz (1999) "Improvement of sounds barriers using headpieces with finite acoustic impedance," *J. Acoust. Soc. Am.*, **106**, pp. 3049–3060. 21, 55

[135] Morgan, P. A. (1999) *Boundary element modelling and full scale measurement of the acoustic performance of outdoor noise barriers*, Ph.D. thesis, Brunel University (London, United Kingdom). 21

[136] Terrasse, I. and T. Abboud (2007) *Modélisation des phénomènes de propagation d'ondes (Modeling of wave propagation phenomena)*, Ecole Polytechnique. 25, 29, 30, 32, 64, 153, 154, 155

[137] Duhamel, D. (1994) *L'acoustique des problèmes couplés fluide-structure: application au contrôle actif du son (coupled fluid-structure problems in acoustics: application to active noise control)*, Ph.D. thesis, Ecole Nationale des Ponts et Chaussées (Marne-la-Vallée, France). 30, 32, 156, 157

[138] Lin, T.-C. (1984) "A proof for the Burton and Miller integral equation approach for the Helmholtz equation," *J. Math. Anal. Appl.*, **103**, pp. 565–574. 32

[139] Burton, A. J. and J. F. Miller (1971) "The application of integral equation methods to the numerical solution of some exterior boundary-value problems," *P. R. Soc. London*, **323**(1553), pp. 201–210. 34, 35, 154, 155

[140] Hamdi, M. A. (1982) *Formulation variationnelle par équations intégrales pour le calcul de champs acoustiques linéaires proches et lointains (variational formulation by integral equations for linear acoustics near-field and far-field calculations)*, Ph.D. thesis, Université de Technologie de Compiègne (Compiègne, France). 35

[141] Dauge, M. (1988) *Elliptic boundary value problems on corner domains - Smoothness and asymptotics of solutions*, Springer. 37

[142] Abramovitz, M. and I. A. Stegun (1964) *Handbook of mathematical functions*, National Bureau of Standards, Applied Mathematics. 37

[143] Duhamel, D. and P. Sergent (1999) "Sound propagation over noise barriers with absorbing ground," *J. Sound Vib.*, **218**(5), pp. 799–823. 40, 41, 89

[144] Jean, P., J. Defrance, and Y. Gabillet (1999) "The importance of source type in the assessment of noise barriers," *J. Sound Vib.*, **226**(2), pp. 201–216. 41, 88, 89, 91

[145] Leissing, T., F. Grannec, J. Defrance, P. Jean, D. Lutgendorf, C. Heinkele, and J.-P. Clairbois (2012) "Holistic optimisation of noise reducing devices," in *Proc. Acoustics 2012, Nantes, France.* 44

[146] Allaire, G. (2007) *Conception optimale des structures (optimal design of structures)*, Springer. 44, 46, 49, 52, 53, 54, 61, 78

[147] Nocedal, J. and S. J. Wright (2006) *Numerical optimization*, Springer. 46, 47, 51, 52, 161

[148] Nelder, J. A. and R. Mead (1965) "A simplex method for function minimization," *Comput. J.*, **7**, p. 308313. 46, 47

[149] Bonnet, M. (1995) "BIE and material differentiation applied to the formulation of obstacle inverse problems," *Eng. Anal. Bound. Elem.*, **15**, pp. 121–136. 50, 56, 63, 64, 66, 68, 78, 153

[150] He, L., S. Kindermann, and M. Sini (2009) "Reconstruction of shapes and impedance functions using few far-field measurements," *J. Comput. Phys.*, **228**, pp. 717–730. 50, 56, 61, 63, 64, 68

[151] MATLAB (2010) *version 7.10.0 (R2010a)*, The MathWorks Inc., Natick, Massachusetts (USA). 52

[152] Eiben, A. E. and J. E. Smith (2003) *Introduction to evolutionary computing*, Springer. 53

[153] Meric, R. A. (1995) "Differential and integral sensitivity formulations and shape optimization by BEM," *Eng. Anal. Bound. Elem.*, **15**, pp. 181–188. 54

[154] Bonnet, M. (1995) "Regularized BIE formulations for first- and second-order shape sensitivity of elastic fields," *Comput. Struct.*, **56**(5), pp. 799–811. 54

[155] Belegundu, A. D. and S. D. Rajan (1988) "A shape optimization approach based on natural design variables and shape functions," *Comput. Method Appl. M.*, **66**, pp. 87–106. 54

[156] Rajan, S. D. and A. D. Belegundu (1989) "Shape optimal design using fictitious loads," *J. AIAA*, **27**(1), pp. 102–107.

[157] Tai, K. and R. T. Fenner (1996) "Optimum shape design and positioning of features using the boundary integral equation method," *Int. J. Numer. Meth. Eng.*, **39**, pp. 1985–2003.

[158] Belegundu, A. D. and T. R. Chandrupatla (2011) *Optimization concepts and applications in engineering*, Cambridge University Press, Second Edition. 54

[159] Mohamadi, B. . and O. Pironneau (2000) *Applied shape optimization for fluids*, Oxford University Press. 54

[160] Yang, Y. and C. K. Soh (2002) "Automated optimum design of structures using genetic programming," *Comput. Struct.*, **80**, pp. 1537–1546. 54

[161] Nava, G. P., Y. Yasuda, Y. Sato, and S. Sakamoto (2009) "On the in situ estimation of surface acoustic impedance in interiors of arbitrary shape by acoustic inverse methods," *Acoust. Sci. Tech.*, **30**(2), pp. 100–109. 54

[162] Watson, W. R., M. G. Jones, and T. L. Parott (1999) "Validation of an impedance eduction method in flow," *J. AIAA*, **37**(7), pp. 818–824. 54

[163] Watson, W. R. (2002) "Three-dimensional rectangular duct code with application to impedance eduction," *J. AIAA*, **40**(2), pp. 217–226.

[164] Jones, M. G. and W. R. Watson (2013) "Validation of an improved experimental method for use in impedance eduction," *J. AIAA*, **51**(1), pp. 186–199. 54

[165] Chang, Y.-C., L.-J. Yeh, M.-C. Chiu, and G.-J. Lai (2005) "Shape optimization on constrained single-layer sound absorber by using GA method and mathematical gradient methods," *J. Sound Vib.*, **286**, pp. 941–961. 55

[166] Chang, Y.-C., L.-J. Yeh, and M.-C. Chiu (2005) "Optimization of constrained composite absorbers using simulated annealing," *Appl. Acoust.*, **66**, pp. 341–352. 55

[167] Ruiz, H., P. Cobo, and F. Jacobsen (2011) "Optimization of multiple-layer microperforated panels by simulated annealing," *Appl. Acoust.*, **72**, pp. 772–776. 55

[168] Campos, L. M. B. C. and J. M. G. S. Oliveira (2004) "On the optimization of non-uniform acoustic liners on annular nozzles," *J. Sound Vib.*, **275**, pp. 557–576. 55

[169] Astley, R. J., R. Sugimoto, and P. Mustafi (2011) "Computational aero-acoustics for fan duct propagation and radiation. Current status and application to turbofan liner optimisation," *J. Sound Vib.*, **330**, pp. 3832–3845. 55

[170] Reimann, C. A. (2007) *Development of a general methodology for optimizing acoustic treatment using an equivalent source method*, Ph.D. thesis, North Carolina State University. 55

[171] Duhamel, D. (2006) "Shape optimization of noise barriers using genetic algorithms," *J. Sound Vib.*, **297**, pp. 432–443. 55

[172] Grubeša, S., K. Jambrošić, and H. Domitrović (2012) "Noise barriers with varying cross-section optimized by genetic algorithms," *Appl. Acoust.*, **73**, pp. 1129–1137.

[173] Jambrošić, K., S. Grubeša, and H. Domitrović (2013) "Optimization of noise barrier efficiency using genetic algorithms," in *Proc. Internoise 2013, Innsbruck, Austria.* 55

[174] Van der Aa, B. and J. Forssén (2013) "Shape-optimal design of graded index sonic crystal noise barriers with line defects," in *Proc. Internoise 2013, Innsbruck, Austria.* 55

[175] Mun, S. and Y.-H. Cho (2009) "Noise barrier optimization using a simulated annealing algorithm," *Appl. Acoust.*, **70**, pp. 1094–1098. 55

[176] Kane, J. H., S. Mao, and G. C. Everstine (1991) "A boundary element formulation for acoustic shape sensitivity analysis," *J. Acoust. Soc. Am.*, **90**(1), pp. 561–573. 55

[177] Koo, B.-U., J.-G. Ih, and B.-C. Lee (1998) "Acoustic shape sensitivity analysis using the boundary integral equation," *J. Acoust. Soc. Am.*, **104**(5), pp. 2851–2860.

[178] Zheng, C., T. Matsumoto, T. Takahashi, and H. Chen (2012) "A wideband fast multipole boundary element method for three dimensional acoustic shape sensitivity analysis based on direct differentiation method," *Eng. Anal. Bound. Elem.*, **36**, pp. 361–371. 55

[179] Barbieri, R. and N. Barbieri (2005) "Finite element acoustic simulation based shape optimization of a muffler," *Appl. Acoust.*, **67**, pp. 346–357. 55

[180] Horváth, G., C. Kirisits, and I. Sachpazidis (2013) "Inverse optimization of noise barriers," in *Proceedings of the Internoise 2013 conference in Innsbruck, Austria.* 55

[181] Feijóo, G. R., A. A. Oberai, and P. M. Pinsky (2004) "An application of shape optimization in the solution of inverse acoustic scattering problems," *Inverse Probl.*, **20**, pp. 199–228. 56

[182] Dühring, M., J. S. Jensen, and O. Sigmund (2009) "Acoustic design by topology optimization," *J. Sound Vib.*, **317**, pp. 557–575. 56

[183] Abe, K., T. Fujiu, and K. Koro (2010) "A BE-based shape optimization method enhanced by topological derivative for sound scattering problems," *Eng. Anal. Bound. Elem.*, **34**, pp. 1082–1091.

[184] ——— (2010) "Shape optimization with topological derivative and its application to noise barrier for railway viaducts," in *Advances in Boundary Element Techniques XI, Proc. 11th International Conference, Berlin, Germany*, vol. 34, pp. 1082–1091. 56

[185] Feijoo, G. R. (2004) "A new method in inverse scattering based on the topological derivative," *Inverse probl.*, **20**, pp. 1819–1840. 56

[186] Nemitz, N. and M. Bonnet (2008) "Topological sensitivity and FMM-accelerated BEM applied to 3D acoustic inverse scattering," *Eng. Anal. Bound. Elem.*, **32**, pp. 957–970. 56

[187] Petryk, H. and Z. Mroz (1986) "Time derivatives of integrals and functionals defined on varying volume and surface domains," *Arch. Mech.*, **38**, pp. 694–724. 63, 64

[188] Jin, B.-J., H.-S. Kim, H.-J. Kang, and J.-S. Kim (2001) "Sound diffraction by a partially inclined noise barrier," *Appl. Acoust.*, (62), pp. 1107–1121. 109, 112

[189] International Organization for Standards (1993) "Acoustics - attenuation of sound during propagation outdoors - Part 1: calculation of the absorption of sound by the atmosphere," *ISO 9613-1*. 111

[190] American National Standards Institute (1995 - revised in 2009) "Method for calculation of the absorption of sound by the atmosphere," *ANSI S1.26*. 111

[191] Picaut, J. and L. Simon (2001) "A scale model experiment for the study of sound propagation in urban areas," *Appl. Acoust.*, **62**, pp. 327–340. 112

[192] Hoppe, R. H. W., "Script for the Computational Electromagnetics class, Fall 2003, University of Houston, USA," .
URL `http://www.math.uh.edu/~rohop/fall_03/index.html` 153

[193] Liu, Y. and F. J. Rizzo (1992) "A weakly singular form of the hypersingular integral equation applied to 3-D acoustic wave problems," *Comput. Method Appl. M.*, **96**, pp. 271–287. 156, 157

[194] Liu, Y. and T. J. Rudolphi (1991) "Some identities for fundamental solutions and their applications to weakly singular boundary element formulations," *Eng. Anal. Bound. Elem.*, **8**(6), pp. 301–311. 156

[195] Kirchner, J. W., "Data analysis toolkits, provided for the Analysis of Environmental Data class, Fall 2001, University of California, Berkeley, USA," .
URL `http://seismo.berkeley.edu/~kirchner/eps_120/EPSToolkits.htm` 167

Publication list

[1] Jolibois, A. (2013) *A sensitivity-based approach to optimize the surface treatment of a low-height tramway noise barrier*, Ph.D. thesis, The Pennsylvania State University (University Park, PA, USA).

[2] Jolibois, A., D. Duhamel, V. W. Sparrow, J. Defrance, and P. Jean (2012) "Scattering by a cylinder covered with an arbitrary distribution of impedance and application to the optimization of a tramway noise abatement system," *J. Sound Vib.*, **331**, pp. 5597–5622.
URL `http://www.sciencedirect.com/science/article/pii/S0022460X1200510X`

[3] ——— (2012) "Scattering of a cylinder covered with an arbitrary distribution of admittance and application to the design of a tramway noise abatement system," in *Proc. Acoustics 2012, Nantes, France*, pp. 4055–4060.
URL `http://hal.archives-ouvertes.fr/hal-00782251`

[4] ——— (2012) "Application of admittance optimization to the design of a low-height tramway noise barrier," in *Proc. Internoise 2012, New York City, NY, USA.*
URL `http://hal.archives-ouvertes.fr/hal-00781159`

[5] ——— (2013) "Sensitivity-based shape optimization of a rigid tramway low-height noise barrier," in *Proc. Internoise 2013, Innsbruck, Austria.*
URL `http://hal.archives-ouvertes.fr/hal-00869855`

Résumé

Le bruit est devenu une nuisance importante en zone urbaine au point que selon l'Organisation Mondiale de la Santé, 40% de la population européenne est exposée à des niveaux de bruit excessifs, principalement dû aux transports terrestres. Il devient donc nécessaire de trouver de nouveaux moyens de lutter contre le bruit en zone urbaine.
Dans ce travail, on étudie une solution possible à ce problème : un écran bas antibruit. Il s'agit d'un écran de hauteur inférieure à un mètre placé près d'une source, conçu pour réduire le niveau de bruit pour les piétons et les cyclistes à proximité. Ce type de protection est étudié numériquement et expérimentalement. Nous nous intéressons particulièrement aux écrans adaptés au bruit du tramway puisque dans ce cas les sources sont proches du sol et peuvent être atténuées efficacement.
La forme ainsi que le traitement de surface de l'écran sont optimisés par une méthode de gradient couplée à une méthode 2D d'éléments finis de frontière. Les variables à optimiser sont les coordonnées de nœuds de contrôle et les paramètres servant à décrire l'impédance de surface. Les sensibilités sont calculées efficacement par la méthode de l'état adjoint.
Les formes générées par l'algorithme d'optimisation sont assez irrégulières mais induisent une nette amélioration par rapport à des formes simples, d'au moins 5 dB(A). Il est également montré que l'utilisation de traitement absorbant du côté source de l'écran peut améliorer la performance sensiblement. Ce dernier point est confirmé par des mesures effectuées sur modèle réduit.
De plus, un prototype à l'échelle 1 d'écran bas antibruit a été construit et testé en conditions réelles, le long d'une voie de tramway à Grenoble. Les mesures montrent que la protection réduit le niveau de 10 dB(A) pour un récepteur proche situé à hauteur d'oreilles. Ces résultats semblent donc confirmer l'applicabilité de ces protections pour réduire efficacement le bruit en zone urbaine.

Mots-clés : Écrans antibruit de faible hauteur, Bruit de tramway, Conception optimale par méthode de gradient, Éléments finis de frontière, Mesures sur modèles réduits, Mesures sur prototype en conditions réelles

Abstract

Noise has become a main nuisance in urban areas to the point that according to the World Health Organization 40% of the European population is exposed to excessive noise levels, mainly due to ground transportation. There is therefore a need to find new ways to mitigate noise in urban areas.
In this work, a possible device to achieve this goal is studied: a low-height noise barrier. It consists of a barrier typically less than one meter high placed close to a source, designed to decrease the noise level for nearby pedestrians and cyclists. This type of device is studied both numerically and experimentally. Tramway noise barriers are especially studied since the noise sources are in this case very close to the ground and can therefore be attenuated efficiently.
The shape and the surface treatment of the barrier are optimized using a gradient-based method coupled to a 2D boundary element method (BEM). The optimization variables are the node coordinates of a control mesh and the parameters describing the surface impedance. Sensitivities are calculated efficiently using the adjoint state approach.
Numerical results show that the shapes generated by the optimization algorithm tend to be quite irregular but provide a significant improvement of more than 5 dB(A) compared to simpler shapes. Utilizing an absorbing treatment on the source side of the barrier is shown to be efficient as well. This second point has been confirmed by scale model measurements.
In addition, a full scale low height noise barrier prototype has been built and tested in situ close to a tramway track in Grenoble. Measurements show that the device provides more than 10 dB(A) of attenuation for a close receiver located at the typical height of human ears. These results therefore seem to confirm the applicability of such protections to efficiently decrease noise exposure in urban areas.

Keywords: Low-height noise barriers, Tramway noise, Gradient-based optimal design, Boundary element method, Scale model measurements, In situ measurements of a prototype device